DEVELOPMENT OF TOOLS AND PARADIGMS TO ASSESS BRAIN CORTICAL ACTIVITY DURING COGNITIVE TASKS

Romain Aubonnet

December 2022

Department of Engineering, School of Technology

Reykjavík University

Ph.D. Dissertation

Development of tools and paradigms to assess brain cortical activity during cognitive tasks

by

Romain Aubonnet

Dissertation submitted to the Department of Engineering, School of Technology
at Reykjavík University in partial fulfillment
of the requirements for the degree of
Doctor of Philosophy

December 2022

Thesis Committee:

Paolo Gargiulo, Supervisor
Professor, Reykjavík University, Iceland

Mahmoud Hassan, Co-advisor
Assistant Professor, Reykjavík University, Iceland

Hannes Petersen, Co-advisor
Professor, University of Iceland, Iceland

Giorgio Di Lorenzo, Co-advisor
Professor, University of Rome, Italy

Luigi Bianchi, Examiner
Associate Professor, University of Rome, Italy

The undersigned hereby certify that they recommend to the Department of Engineering, School of Technology, Reykjavík University, that this dissertation entitled **Development of tools and paradigms to assess brain cortical activity during cognitive tasks**, submitted by **Romain Aubonnet**, be accepted as partial fulfilment of the requirements for the degree of **Doctor of Philosophy (Ph.D.) in Engineering**
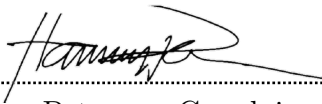
22.12.2022
....
date

....
Paolo Gargiulo, Supervisor
Professor, Reykjavík University, Iceland

....
Mahmoud Hassan, Co-advisor
Assistant Professor, Reykjavík University, Iceland

....
Hannes Petersen, Co-advisor
Professor, University of Iceland, Iceland

....
Giorgio Di Lorenzo, Co-advisor
Professor, University of Rome, Italy

....
Luigi Bianchi, Examiner
Associate Professor, University of Rome, Italy

The undersigned hereby grants permission to the Reykjavík University Library to reproduce single copies of this Dissertation entitled **Development of tools and paradigms to assess brain cortical activity during cognitive tasks** and to lend or sell such copies for private, scholarly or scientific research purposes only.

The author reserves all other publication and other rights in association with the copyright in the Dissertation, and except as herein before provided, neither the Dissertation nor any substantial portion thereof may be printed or otherwise reproduced in any material form whatsoever without the author's prior written permission.

22.12.2022
....
date

....
Romain Aubonnet
Doctor of Philosophy

x

Development of tools and paradigms to assess brain cortical activity during cognitive tasks

Romain Aubonnet

December 2022

Abstract

Monitoring brain cortical activity is essential to decipher and understand neurophysiological behaviour. A wide amount of tools and experimental setups has been developed to stimulate, record and analyze brain activity. The identification of quantitative metrics to assess this activity during specific tasks remains an essential requirement, as it could lead to improve diagnostics, describe objectively self-assessed condition, or track variation during long-term studies.

This thesis introduces the development of tools and paradigms to assess brain cortical activity during cognitive tasks. It introduces a complete set of analyses based on EEG signals, under two main scopes, schizophrenia and postural control. The first part of the work evaluates the impact of a potential therapeutic solution for patients with schizophrenia. A longitudinal study case is introduced, where psychometrics data are compared with three types of analysis from EEG data: temporal, spectral and connectivity. The small sample size prevents us to draw definitive conclusion, however, this work reveals the interest to use EEG-based metrics to complete the standard psychometrics assessment.

The second part of the work focuses on postural control, using a novel measurement setup, called BioVRSea, combining virtual reality and a moving platform. The brain cortical activity of more than 150 healthy individuals have been investigated during this experiment. A robust neurophysiological reference has been identified using power spectral density. Moreover, combining brain connectivity and microstate segmentation, network dynamics reveal a coherent brain remodeling throughout the acquisition, strengthening our current knowledge regarding complex postural control.

The current work highlights the concrete benefit of using EEG signal to decipher brain cortical activity. The tools developed in this thesis are of interest to build a neurophysiological signature of specific cognitive tasks, that will be crucial for a further understanding of neurodegenerative disease.

Keywords: EEG, Brain connectivity, Spectral analysis, Schizophrenia, Postural control

Þróunn tóla og hugmyndafræði til að meta heilaberka starfsemi við vitræn verkefni

Romain Aubonnet

desember 2022

Útdráttur

Að fylgjast með starfsemi heilaberki er nauðsynlegt til að útskýra og skilja tauga-lífeðlisfræðilega hegðun. Fjölbreytt útval af tólum og tilraunauppsetningum hefur verið þróað til að örva, vista og greina heilastarfsemi. Það er nauðsynleg krafa að finna magnmælingu til að greina þessa starfsemi í ákveðnu verkefni, því það gæti leitt að beturumbættu greiningarferli, útskýrt hlutlægu sjálfsmats ástandi, eða fylgst með breytingum í lang-tíma rannsóknum.

Þessi ritgerð kynnir þróunn tóla og hugmyndafræði til að meta heilaberka starfsemi við vitræn verkefni. Ritgerðinn kynnir heilt safn af greiningum byggt á EEG merkj-um, í tvem megin sviðum, geðklofa og líkamsstöðustjórnun. Fyrsti hluti verkefnisins metur áhrifin af mögulegum meðferðarlegum lausnum fyrir sjúklinga með geðklofa. Kynnt er langtímarannsóknartilvik, þar sem þar sem sálfræðigögn eru borin saman við þrenns konar greiningar úr heilarita gögnum: tímabundnum, litrófs- og tengingum. Lítil úrtaksstærð kemur í veg fyrir að við getum dregið endanlegar ályktanir, en þessi vinna sýnir áhugann á því að nota heilalínuritaða mælikvarða til að ljúka stöðluðu sálfræðimati.

Annar hluti verksins fjallar um líkamsstöðustýringu, með því að nota nýja mæling-aruppsetningu, sem kallast BioVRSea, sem sameinar sýndarveruleika og hreyfanlegan vettvang. Heilabarkarvirkni af meira en 150 heilbrigðra einstaklinga hefur verið rann-sökuð í þessari tilraun. Öflug taugalífeðlisfræðileg tilvísun hefur fundist með því að nota kraftrófsþéttleika. Þar að auki, með því að sameina heilatengingu og örstöðu-skiptingu, sýnir netverkun samfellda endurgerð heilans í gegnum tökuna, sem styrkir núverandi þekkingu okkar varðandi flókna líkamsstöðustjórnun.

Þessi rannsókn undirstrikar raunverulegan ávinning af því að nota EEG merki til að ráða virkni heilabarka. Tólin sem þróuð eru í þessari ritgerð eru mikilvæg til að byggja upp taugalífeðlisfræðilega undirskrift ákveðinna vitræna verkefna, sem mikilvæg eru fyrir frekari skilning á taugahrörnunarsjúkdómum.

Efnisorð: EEG, Heila tengingar, Litrófar greining, Geðklofi, Líkamsstöðustjórnun

I dedicate this work to my loved ones, their continuous and essential support, for which I could not be more grateful.

Acknowledgements

Preface

This dissertation is original work by the author, Romain Aubonnet.

I graduated as a biomedical engineer of Telecom Physique Strasbourg (France) in 2015. During my studies, I underwent an internship in the Institute of Biomedical and Neural Engineering of Reykjavik University, under the supervision of Paolo Gargiulo.

After my graduation, I worked for three years as a QA/test engineer in Lyon, France. However, I was missing the biomedical aspect in this job, and contacted Paolo to commence a new adventure, that began in August 2019. I was interested to work in research again, and especially to focus my effort in understanding and deciphering brain mechanisms. Thanks to Paolo, I had the opportunity, after a few months in his lab, to start a PhD focusing on the development of methodologies to quantify brain cortical activity, that led to the work detailed in the present dissertation.

Publications

The following work has been adapted from several publications listed below of which I, Romain Aubonnet, am an author. All publications have been submitted for peer-review during the duration of my doctoral studies.

- R. Aubonnet, O. C. Banea, R. Sirica, et al., "P300 analysis using high-density eeg to decipher neural response to rtms in patients with schizophrenia and auditory verbal hallucinations", *Frontiers in Neuroscience*, vol. 14, 2020, issn: 1662-453X. doi: `10.3389/fnins.2020.575538`. [Online]. Available: `https://www.frontiersin.org/articles/10.3389/fnins.2020.575538`.

- M. Recenti, C. Ricciardi, R. Aubonnet, et al., "Toward predicting motion sickness using virtual reality and a moving platform assessing brain, muscles, and heart signals", *Frontiers in Bioengineering and Biotechnology*, vol. 9, 2021, issn: 2296-4185. doi: `10.3389/fbioe.2021.635661`. [Online]. Available: `https://www.frontiersin.org/article/10.3389/fbioe.2021.635661`.

- D. Jacob, I. S. Unnsteinsdottir Kristensen, R. Aubonnet, et al., "Towards defining biomarkers to evaluate concussions using virtual reality and a moving plat- form (biovrsea)", *Scientific Reports*, vol. 12, no. 1, p. 8996, 2022, issn: 2045- 2322. doi: `10.1038/s41598-022-12822-0`. [Online]. Available: `https://doi.org/10.1038/s41598-022-12822-0`.

- S. Stehle, R. Aubonnet, M. Hassan, M. Recenti, D. Jacob, H. Petersen, and P. Gargiulo, "Predicting postural control adaptation measuring EEG, EMG, and center of pressure changes: BioVRSea paradigm", *Frontiers in Human Neuroscience*, 2022. (`https://doi.org/10.3389/fnhum.2022.1038976`)

- R. Aubonnet, A. Shoykhet, D. Jacob, G. Di Lorenzo, H. Petersen, and P. Gargiulo, "Postural control paradigm (biovrsea): Towards a neurophysiological signature", *Physiological Measurement*, 2022. DOI: `https://doi.org/10.1088/1361-6579/ac9c43`.

- R. Aubonnet, M. Hassan, A. Mheich, G. Di Lorenzo, H. Petersen, and P. Gargiulo, "Brain network dynamics during a complex postural control task", *Journal of Neural Engineering*, 2022. (***Under review***)

- F. K. Ciliberti, L. Guerrini, A. E. Gunnarsson, et al., "Ct- and mri-based 3d reconstruction of knee joint to assess cartilage and bone", *Diagnostics*, vol. 12, no. 2, 2022, issn: 2075-4418. doi: `https://doi.org/10.3390/diagnostics12020279`.

- R. Aubonnet, J. Ramos, M. Recenti, et al., "Towards new assessment of knee cartilage degeneration", *Cartilage*, 2022. DOI: `https://doi.org/10.1177/19476035221144746`.

Contents

List of Figures

List of Tables

List of Abbreviations

AHS	Auditory Hallucinations Subscale
AUD	Auditory network
AVH	Auditory Verbal Hallucinations
BNS	brain network state
CG	Control Group
CNS	Central nervous system
CT	Computed tomography
DAN	Dorsal attention network
DASS	Depression Anxiety Stress Scale
DMN	Default mode network
EEG	Electroencephalogram
ERP	Event-related Potential
fMRI	Functional magnetic resonance imaging
fNIRS	Functional near-infrared spectroscopy
GEV	Global explained variance
MEG	Magnetoencephalogram
MOT	Motor network
MRI	Magnetic resonance imaging
MS	Motion sickness
MSP	Motion sickness prone
MSS	Motion sickness symptoms
MSSQ	Motion sickness susceptibility questionnaire
NMSP	Not motion sickness prone
OA	Osteoarthritis
PC	Participation coefficient (Chapter 3)
PC	Postural control (Chapters 2, 4 and 5)
PLV	Phase-locking value
PSD	Power Spectral Density
PSYRATS	Psychotic Symptom Rating Scales
QoLS	Quality of Life Scale
ROI	region of interest
RSN	Resting-state network
rTMS	Repetitive Transcranial Magnetic Stimulation
SAN	Salience network
TG	Treatment Group
TMS	Transcranial Magnetic Stimulation
VIS	Visual network
VR	Virtual reality
wMNE	weighted minimum-norm estimation

Chapter 1

Prologue

The human brain is often described as one of the most complex and sophisticated entity ever analyzed by mankind. As of today, it continuously generated plenty of questions and fascination regarding its structure, its mechanisms, its processes.

This organ is the fundamental piece of the nervous system. It monitors and commands the majority of the actions of the body, conscious or not, from information processing to decision making, remaining constantly active throughout our whole life.

To deepen our understanding of this organ, research base their work on multidisciplinary sciences. Neurophysiology, defined as a branch of physiology and neurosciences, aims to study the function of the central and peripheral nervous systems, through experimental and clinical techniques. More specifically, literature shows that the use of clinical neurophysiology, that records brain bioelectrical activity to analyse nervous systems, is more and more preponderant to assist diagnosis, assessment and rehabilitation of pathological conditions. It is a valuable asset to provide objective quantities in complement of scales, that can be self-assessed, often subjective, or lack repeatability. However, quantitative metrics extracted from neurophysiological studies need to be reliable, accurate, and it is therefore necessary to provide a robust methodology and a thorough data analysis. Moreover, it has to be validated through a sufficient number of subjects, through different studies, to set those quantities as biomarkers of a condition. For those reasons, the use of those metrics in the clinical environment remains rare. The development of workflows and the identification potential biomarkers is an imperative step to strengthen this application in the clinical field. It is a milestone towards the establishment of tools and solution for diagnosis and prevention of neurodegenerative diseases.

This thesis proposes a methodology to quantify brain cortical activity, based on electroencephalography (EEG), under two main research scopes: schizophrenia (chapter 3) and postural control (chapter 4). Different EEG signals analyses have been performed to elicit a guideline workflow that can be used for EEG studies, with a final aim to define reliable biomarkers, based on quantitative metrics. For both research scopes, the employed methodology highlighted substantial features, that could, on one hand, characterize a reference behaviour, and on the other hand describe the cognitive processes associated with this behavior.

Contributions The remainder of this thesis is structured in five chapters. Chapter 2 is an introduction to brain anatomy and function and the way to analyse it. The main input of this work is presented in chapters 3 and 4, where the findings are reviewed and discussed for future directions in chapter 5. Chapter 6 presents the parallel work pursued during this thesis, regarding cartilage degeneration, and should be considered

as an annex chapter. Finally, chapter 7 is a global conclusion of this dissertation. Chapters 3, 4 and 6 are built on a set of publications written during the time of the thesis. It has to be noted that chapters 3 and 4 are presenting research studies in a chronological order; it highlights the progression of the reflection during this thesis, on how the methodology started as a proof of concept and was then elaborated in more details to make it as robust as possible. The main contributions of chapters 3 to 6 are summarized below:

- **Chapter 2:** introduces basic information about brain anatomy and functions, as well as the different methodologies and concepts used to evaluate brain cortical activity.

- **Chapter 3:** presents the work done on the schizophrenia. It investigates the impact of rTMS in patients with schizophrenia, based on an evoked potential paradigm, the P300. It is a study case comparing results from patients of a treatment group and a control sham group, on the temporal, spectral, and functional connectivity domain.

- **Chapter 4:** presents the work performed on postural control, based on a complex postural paradigm BioVRSea, combining virtual reality and a moving platform. It is divided in three parts. The first part is composed of three different exploratory studies using a multimetrics assessment. The first exploratory works aimed to quantify motion sickness a proof of concept of the BioVRSea paradigm. The second exploratory work studies the impact of concussion on postural control, and the third work aimed to predict postural control stimulation based on measured biosignals. The second part of this chapter aims to define a reference neurophysiological behaviour of BioVRSea paradigm. It studies the spectral EEG features from 190 individuals, throughout the different phases of the experiment. The last part of this chapter presents a novel approach to decipher brain network dynamics during BioVRSea paradigm. It combines two EEG analysis techniques; functional networks reconstructed from 158 individuals' EEG times-series, and microstate segmentation. This investigation led to a dynamic distribution of what will be called brain network states, highlighting the dynamic remodeling of the brain.

- **Chapter 5:** is a short discussion of the main contributions presented in this thesis.

- **Chapter 6:** presents the parallel work performed during this PhD work, focusing on the knee cartilage to extract new metrics to quantify cartilage degeneration. Two studies are presented, pointing out the benefit of using measurements from 2D and 3D datasets to improve the assessment of cartilage degeneration.

- **Chapter 7:** is a general conclusion of the work.

Chapter 2

Introduction

This chapter is divided in two main parts. The first part is an overview of brain anatomy and functions, and a description of the methodologies used in the dissertation to analyse it. The second part introduces the two main research areas investigated in this thesis, where the developed methodology has been applied to assess brain cortical activity.

2.1 Brain

2.1.1 Anatomy and function

The human brain is a complex organ, that governs the majority of the activities of the body, from breathing, body regulation, to motor skills, thought, emotion, memory. It gathers, processes and coordinates the information received by the sensory organs, and take decisions as a list of instruction to the body. Brain and spinal cord jointly composes the central nervous system (CNS). It is located within the skull, and is protected by the skull bones, meninges and cerebro-spinal fluid ([1]). The human brain weighs on average around 1.4kg, which represent 2% of the total body weight ([2]). It is divided into three main components: the cerebrum, the cerebellum, and the brainstem (figure 2.1) [3].

2.1.1.1 Cerebrum

The cerebrum is the largest part of the brain. It is divided in two hemispheres (left and right). The outerpart of the cerebrum is called cerebral cortex. Its particular structure is composed of gyri (ridges) and sulci (furrows). These gyri can be used as basis to design brain atlas, dividing the cortex is a certain amount of regions grouping gyri, such as the Desikan-Killiany atlas [4]. The cerebral cortex is partitioned in four lobes: frontal, parietal, occipital and temporal (figure 2.2) [3]. Each lobes and regions are associated with specific task. Overall, the cerebrum takes part in a wide range of actions linked with cognition: thinking, decision making, memory, information processing; sensory perception: visual, auditory, olfactory,...; speech and language; voluntary motor activities, and much more. Here we will detail the specific role of each lobe.

Frontal lobe   The frontal lobe is the largest of the four lobes, and is located in the front part of each hemisphere. It is covered by what we call the frontal cortex. This
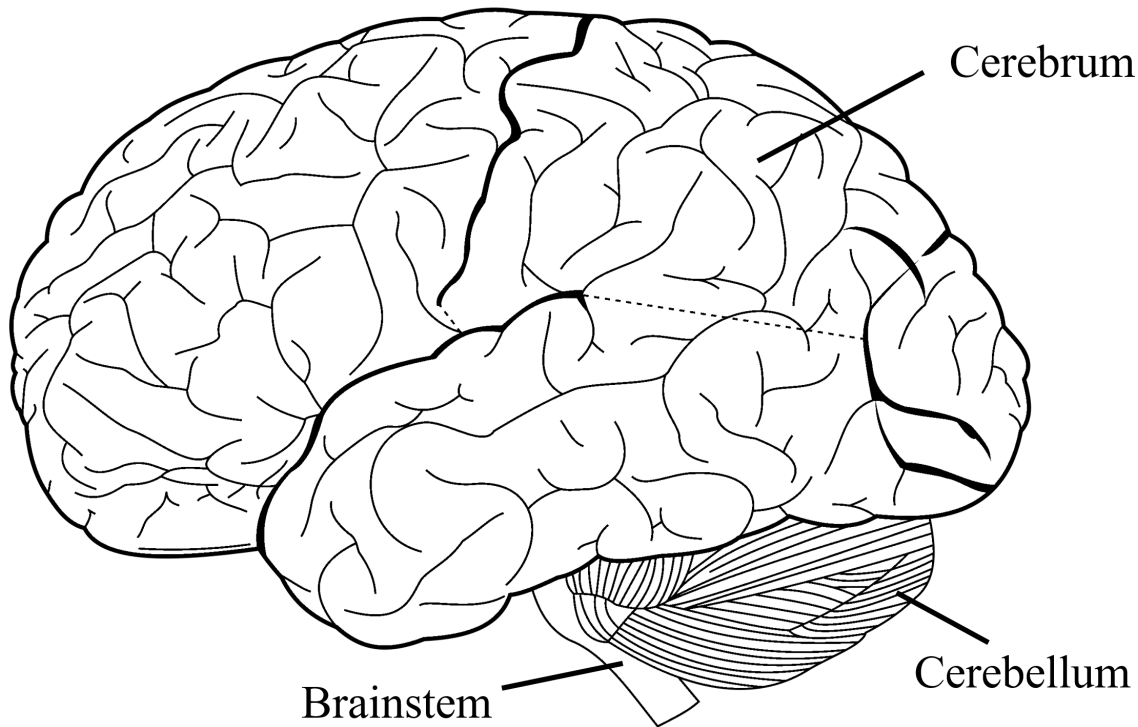
Figure 2.1: Main parts of the human brain

cortex has been known for a long time for its involvement in all tasks related with motor actions, such as eye or body movement, but also its preponderance in speech and language [5]. However, further researches highlighted its complex role, and its implication in decision making, memory, conscious mental thoughts and reasoning, in what is called the prefrontal cortex, which is the biggest part of the frontal lobe. Moreover, recent works show that the cognitive processes associated with this cortex are intricately linked with emotions, personality, and are therefore related with our social and moral thinking [6]. On the clinical aspect, frontal lobe impairment or injury can be related with different pathologies or conditions, such as depression, aphasia, tremor, gait abnormality, eating disorder, and can be linked with Parkinson's or Alzheimer's disease.

Parietal lobe   The parietal lobe is located behind the frontal one and above the temporal. This cortex is essential for all tasks needing coordination. It merges information from external stimulus and internal sensory feedback from all parts of the body. It is crucial for spatial localization and representation. This cortex is involved in information processing, from the sense of touch [7], but also in the visuospatial aspect [8]. It is therefore associated with motor functions, such as understanding of intention, of the goal of an action, and the perception associated with this action [9]. On the clinical aspect, parietal lobe impairment can be associated with seizures, dyslexia, apraxia, or spatial disorientation.

Occipital lobe   The occipital lobe is located in the back of the brain, and is responsible for visual proccessing [10], [11]. It is divided in several visual areas, that are all playing a role regarding visual processing, from color and shape recognition, to motion perception. It also plays a role in orientation, spatial information, and visual memory. Occipital lobe impairment can lead to visual hallucinations, and can be related with

color or movement agnosia, or even blindness. Moreover, epilepsy can be related with occipital lobe seizures.

Temporal lobe The temporal lobe is located beneath the parietal and frontal lobes. The temporal lobe is mainly associated with memory processing [12]. It is involved in long-term memory, sensory processing from visual or auditory inputs, and memory storage and creation. The temporal lobe contains the auditory cortex [13], and is also implicated in language comprehension (oral or written) [14]. Damages to the temporal lobe are associated with visual agnosia, auditory impairment, and could be related to schizophrenia.
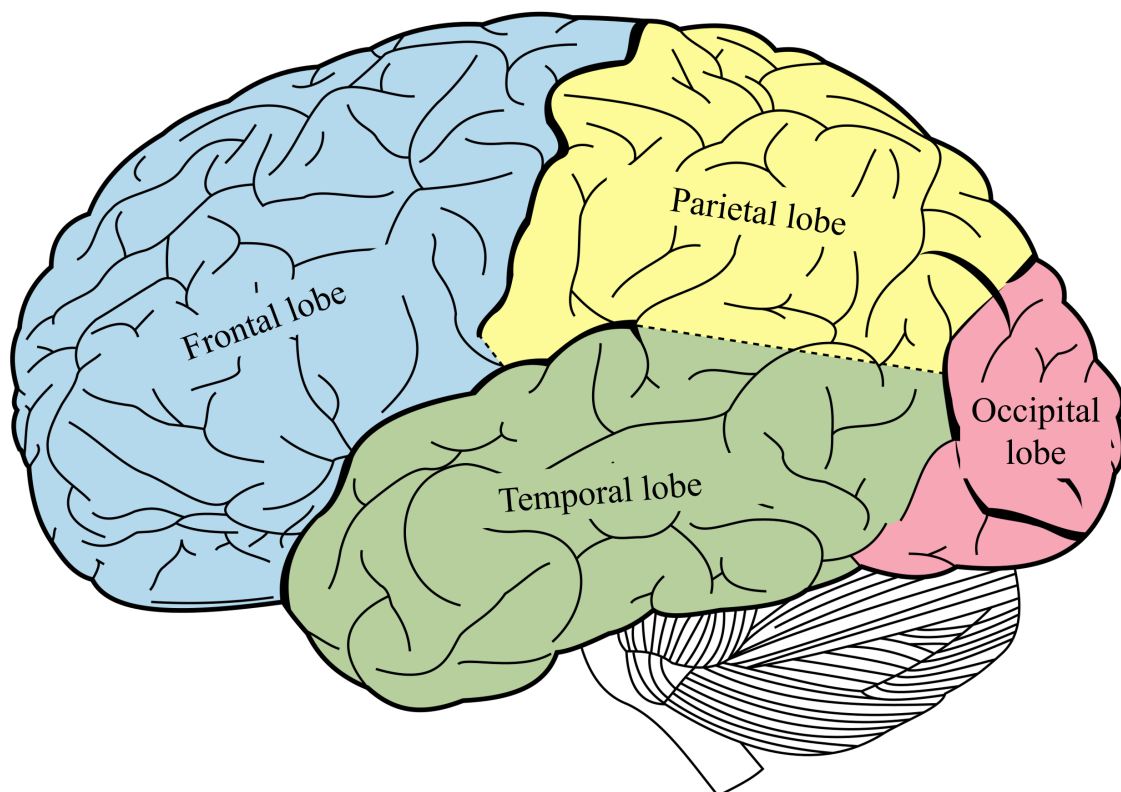
Figure 2.2: Lobes of the cerebral cortex

2.1.1.2 Cerebellum

The cerebellum is a smaller region located in the lower part of the brain, underneath the occipital lobe of the cerebrum. It is interconnected with the cerebral cortex, and regulates and controls several types of actions, from motor movements, associated with balance for instance, to cognition linked with emotion [15].

2.1.1.3 Brainstem

The brainstem is the lowest part of the brain, located beneath the cerebrum, connecting this part with the spinal cord. Its role is crucial for information relay: all information going to the body from the cerebrum and cerebellum, and the other way around goes through the brainstem. Moreover, the brainstem is vital for the good functioning of the body, as it is in charge of all the unconscious and autonomic tasks, including cardiovascular system control (heart beating for instance), respiratory control (breathing),

(a) Anatomy of a neuron

(b) Synaptic transmission
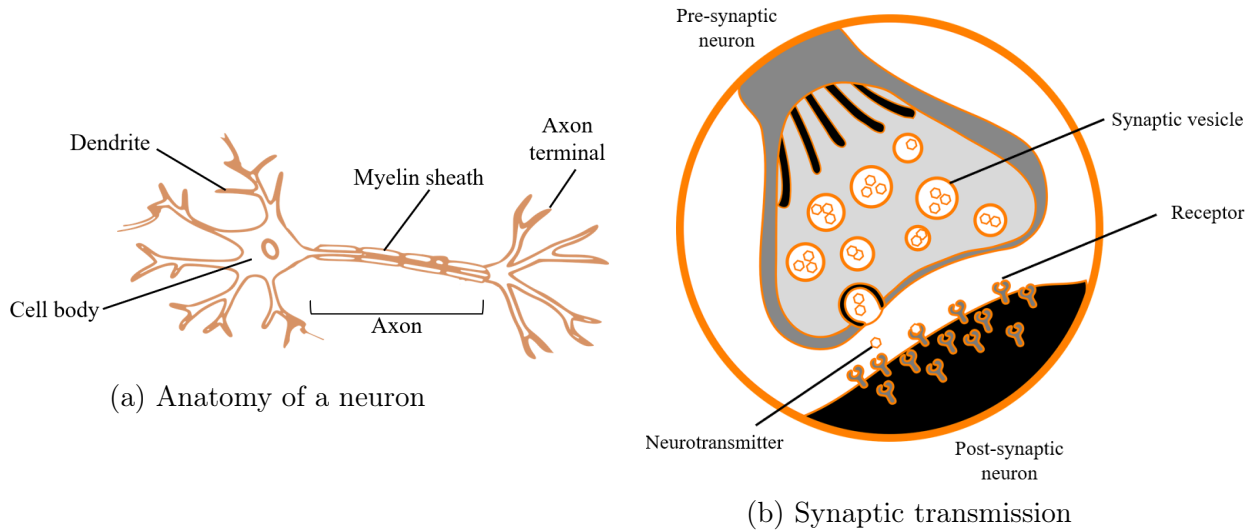
Figure 2.3: Illustration of a neuron anatomy and synaptic transmission

consciousness, pain sensitivity control [16], [17]. Any type of brainstem impairment is life-threatening.

2.1.2   Measuring brain cortical activity

Brain activity can be described from changes associated with neural activity. The brain contains around 86 billions of neurons, from which 16 billions are located in the cerebral cortex [18]. Neurons are the principal elements of the nervous system, whose role is to process and transmit cellular signals. They are supported by glial cells, that are not conducting nerve impulses, but protect the neuron and maintain their environment [19]. A neuron is typically composed of a cell body (called soma), dendrites, and axons, that are terminated by synapses (figure 2.3).

When a neuron send an information, it generates an action potential, due to an electrical depolarization, that is transmitted to other cells through synapses; indeed, the electrical impulse generated by the neuron induce the transfer of neurotransmitters from one cell to another, by activating specific postsynaptic receptors [20]. This process is commonly called neuronal firing. Thus, neurotransmission generates electrical activity. However, due to the several layers composing the head (tissue, bone, skin), it is difficult to monitor strong enough electrical activity. This is why most of the recorded electrical activity comes from pyramidal neurons, that are located in the cortical regions [20]. This electrical activity induces magnetic fields, that can be measured as well, but also changes in blood flow as neuronal firing consumes energy in the form of sugar and oxygen. Monitoring the changes in brain cortical activity is then crucial to decipher and understand in depth brain mechanisms, for healthy persons, but also neurodegenerative diseases, in different experimental situations. This is the basis for the development of referent neuromarkers, leading to the improvement of diagnostics, rehabilitation, prevention and cures solution.

2.1.3   Measurement devices

Studying the changes of brain cortical activity is a good way to have more insight and knowledge about brain function and mechanism. As mentioned in the previous

paragraph, neuronal firing generates electrical activity, induces magnetic fields and changes in blood flow. Different techniques and devices can be used to monitor this evolution. This section details the three main measurement techniques to record brain electrical activity.

2.1.3.1 fMRI

Functional magnetic resonance imaging (fMRI) measures brain activity by detecting changes in blood flow, underlining the need to aliment the cells in oxygen after a neuronal firing. fMRI monitors blood-oxygen-level dependent (BOLD) contrast, imaging the changes in blood flow to map neural activity [21]. fMRI provides an excellent spatial resolution, and gives more and more insight about brain functional organization, due to the emergence of more advanced setups [22]. Based on resting-state data, fMRI studies discovered fundamental observation regarding the communication between different brain regions, their activation, and the role it can play towards the understanding of pathological conditions such as Alzheimer's disease or schizophrenia for instance [23], by identifying reference networks called resting state networks (RSN) [24]. However, its acquisition settings and protocols causes some limitations. It suffers from a low temporal resolution, and does not measure direct neural activity, as it is based on a linear relation between neural activity and BOLD contrast, that remains not totally understood [25]. Moreover, fMRI is an expensive and stationary setup, leading to a high sensitivity to motion artefacts, a problem which is progressively address by research groups [26], [27]. It also requires a trained and licensed operator, and therefore lacks flexibility.

2.1.3.2 MEG

Magnetoencephalography (MEG) records the magnetic fields produced by the electrical activity from the neurons [28]. This technique provides a very good spatial and temporal resolution [29]. Unlike fMRI, it directly measures neural activity, and is able to give a dynamic temporal insight, regarding RSN for instance [30]. It has shown robust results in deciphering brain mechanism during cognitive tasks, such as face recognition [31]. However, like fMRI, it is an expensive and stationary device, and requires an adequate training. Acquiring, processing and analysing data is a complex and intensive task, that relies on a robust and adequate workflow [29].

2.1.3.3 EEG

Electroencephalography (EEG) measures brain electrical activity, using electrodes positioned on the scalp [32]. It provides a very accurate temporal resolution, enabling the precise tracking of brain activation and its dynamics [33]. It detects the direct changes in neural activity, identifying postsynaptic potentials of thousands of pyramidal cells [20]. Thus, using EEG is crucial to track and monitor cognitive events, that occurs within ten to hundreds of milliseconds [34]. It has to be noted that the measured signal oscillations are direct measures of neural activity, that is fundamental to interpret and understand specific brain evolution during cognitive processes. Moreover, from EEG time-series, an extensive variety of data can be extracted, from the temporal, spectral, and even connectivity domains. It allows the research to a complete overview of hypotheses testing, and to adapt and design a specific protocol. Compared to fMRI and MEG listed above, EEG is inexpensive and do not require an intensive training.

Moreover, it presents a great setup flexibility, and is adapted mobile and various acquisition processes. However, it suffers from a low spatial resolution, and is not suited for rigorous functional localization. EEG systems mostly rely on electrodes placed on the scalp. It requires an appropriate setup regarding electrodes positioning and signal amplifier [35]. Figure 2.4 shows an example of a basic EEG setup.

Figure 2.4: Basic EEG setup: EEG cap, amplifier, software and computer. From ANT-neuro, eego^{TM} mylab

Although it is sufficient to record data from the outer cortex, it is therefore very limited for subcortical or deep brain studies. Besides, the high-temporal resolution is useful for the fast-track of cognitive event, but it can be a disadvantage for the comprehension of slow temporal processes. Finally, similarly to MEG and fMRI, EEG is very sensitive to noise and motion artefacts during the recordings. It is very important to define a coherent and adapted setup while using those techniques, and to maintain an environment as neutral as possible during the acquisition. Moreover, before processing the recorded data, an extensive pre-processing workflow is required to clean the data from noise and artefacts.

The work developed in this thesis focus on brain cortical activity recorded by EEG. Its high flexibility in measurement setup, and its ease to use and its multidimensional approach fit the several experimental studies detailed in the following chapters, where specific paradigms are used to trigger fast cognitive responses. Moreover, it allows the use of mobile setups, as well as the tracking of dynamic changes in link with postural control. The following section details how EEG is used in the frame of neurophysiology, and how its signal is analysed.

2.2   Brain electrical activity

Clinical neurophysiology base its analysis on designed experimental setups to trigger and observe response from the brain, that is usually recorded through its electrical activity. It aims to obtain quantitative results and define norms in order to assist with diagnostics and patient's evaluation. Diverse paradigms are developed and used in

the frame of clinical neurophysiology, such as EEG, spectral feature extraction, evoked potentials, functional connectivity. The results can be applied in complement of other tests to verify or validate the patient's condition. However, the clinical application of EEG results remains limited, due to the difficulty of identifying but also validating quantitative biomarkers of a condition. It is crucial for research groups to propose and demonstrate the use of robust and reliable methodologies and analysis, that can be endorsed by the clinical field.

2.2.0.1 Brain rythms

As stated before, brain activity can be monitored through neurotransmission, that generates electrical activity. The related signal analysis revealed typical brain oscillations of different frequencies, that are called brain rhythms: delta (1-4Hz), theta (4-8Hz), alpha (8-13Hz), beta (13-30Hz), low-gamma (30-45Hz), and high-gamma (45+Hz) [36], [37] (see figure 2.5).

| Delta (1-4Hz) | Theta (4-8Hz) | Alpha (8-13Hz) | Beta (13-30Hz) | Low Gamma (30-45Hz) |
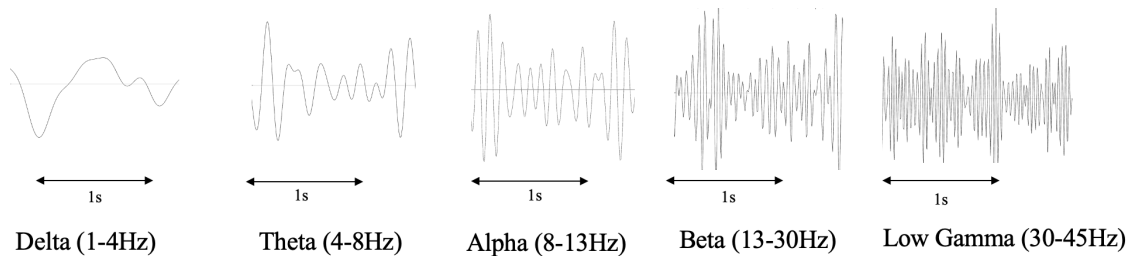
Figure 2.5: Illustration of the five main brain rhythms

They are correlated with cognition, but their mechanisms and associated physiology remain undefined [38], [39]. Depending on the type of stimulations, the brain areas it occurs, and the parameters extracted, several conclusion can be drawn [40]. The following paragraphs will quickly summarise the main findings regarding each brain rhythm.

Delta band Delta waves are the slowest emitted by the brain. They are usually associated with sleep, and all processes related to sleep, such as memory organization, as well as skills or information storage, but are also linked with motivation [41], [42].

Theta band Theta waves are associated with mental processes, such as working memory, information processing, focused attention, and the encoding of new information [43], [44].

Alpha band Alpha waves are related to several cognitive processes. It is first known to increase with relaxation. On the other hand, alpha inhibition is linked with mental and physical engagement to a task, during a focused attention towards a stimulus, showing information processing and attentional process [43], [45].

Beta band Beta waves is mostly known for its correspondence with motor tasks. It increases during movement planning and execution, but also during active thinking or concentration [46].

Low-gamma band   Low-gamma waves are still being investigated, as their definite role remains unclear [47]. However, studies show their importance in cortical activation or inhibition, information processing and memory tasks [48].

2.2.0.2   ERP

Event-related potentials (ERP) are a way to measure direct neural activity. They are time-locked EEG changes based on triggered stimulation provoked by cognitive, motor or sensory events [49]. The advantages of using ERP are their ease to implement and analyse to compare two different conditions; the study of latency, polarity or amplitude enables to characterize healthy from pathological responses for instance. ERP components are named with the letter 'P' in case of a positive polarity and 'N' in case of negative polarity. They trigger fast cognitive response and can be observed in high temporal resolution, making them very convenient to study with EEG. ERP have been widely studied and many experimental setups exist to trigger specific response [50], [51]. It is very simple to find methodologies to adapt and study specific phenomenons, such as using visual stimulus to target occipital response for instance [52]. However, it is way harder to interpret physiological processes from ERP studies, as literature lacks of exhaustive analyses [34]. Most of the time, ERP are studied under one domain, that limits the data analysis. Due to its short period and its averaging over trials, some cognitive process may not be observable with ERP, as it only captures phase-locked and time-locked activity. Nonetheless, ERP are considered in the clinical field [53], [54], underlining different reponse while comparing healthy patients against patients with depression, schizophrenia or dementia [55]. It is a usefool tool towards a deep understanding of this disorders [56].

2.2.0.3   Microstates

The analysis of EEG time series showed voltage topographies remain stable for a period of around 80-120ms. Those stable periods have been mentioned as functional microstates [57]. The study of microstates helped to comprehend brain states, and to characterize brain functions in several studies [58], [59]. More and more tools are available to process and analyze microstates. During dynamic tasks, the review of microstates is a promising tool to decode brain cortical remodeling.

2.2.0.4   Designing optimal experimental paradigms

Before starting an EEG study, it is critical to design an experiment that is adequate and exploitable. Based on previous studies, experience and objectives, the attention should be focused on what we want to measure, and how to do it. Should it be a dynamic or static environment, a longitudinal study, how many subjects group and with which characteristics? How to record the brain cortical response, is it a resting-state based study or based on specific triggers, or with several types of stimulation (auditory, visual, motor, combined,...) ?
Once those questions have been answered, methodological considerations apply to the EEG device.
The first consideration is the number of electrodes to use. Depending on the measurement goal, a sufficient number of electrodes is required to use spatial fiters, observe topographical results, or perform functional connectivity analysis. However, most of EEG caps require the use electroconductive gel placed in each electrode. The higher

the number of electrodes, the more time it takes to prepare, and the most discomfort is given to the subject. Moreover, a high number of electrodes require a higher storage, and therefore a longer processing time. A good compromise needs to be found to address all those issues. It is advised for good practice to use a minimum of 64 electrodes.

The second question concerns the sampling frequency. The adequate sampling rate should be considered depending on the type of data we want to observe, and the amount of information we need, as well as the storage and processing time that we have. It is always possible to downsample the datasets, so it is safer to take a higher sampling frequency and downsample it later if needed. For common practice, EEG data are usually acquired between 500 and 2000Hz.

Even though EEG is a very adequate technique to record brain cortical activity, an adapted workflow is needed to extract valuable metrics to quantify brain response. Figure 2.6 illustrates the global workflow reported in this dissertation. The following section will detail the concepts mentioned in the figure.
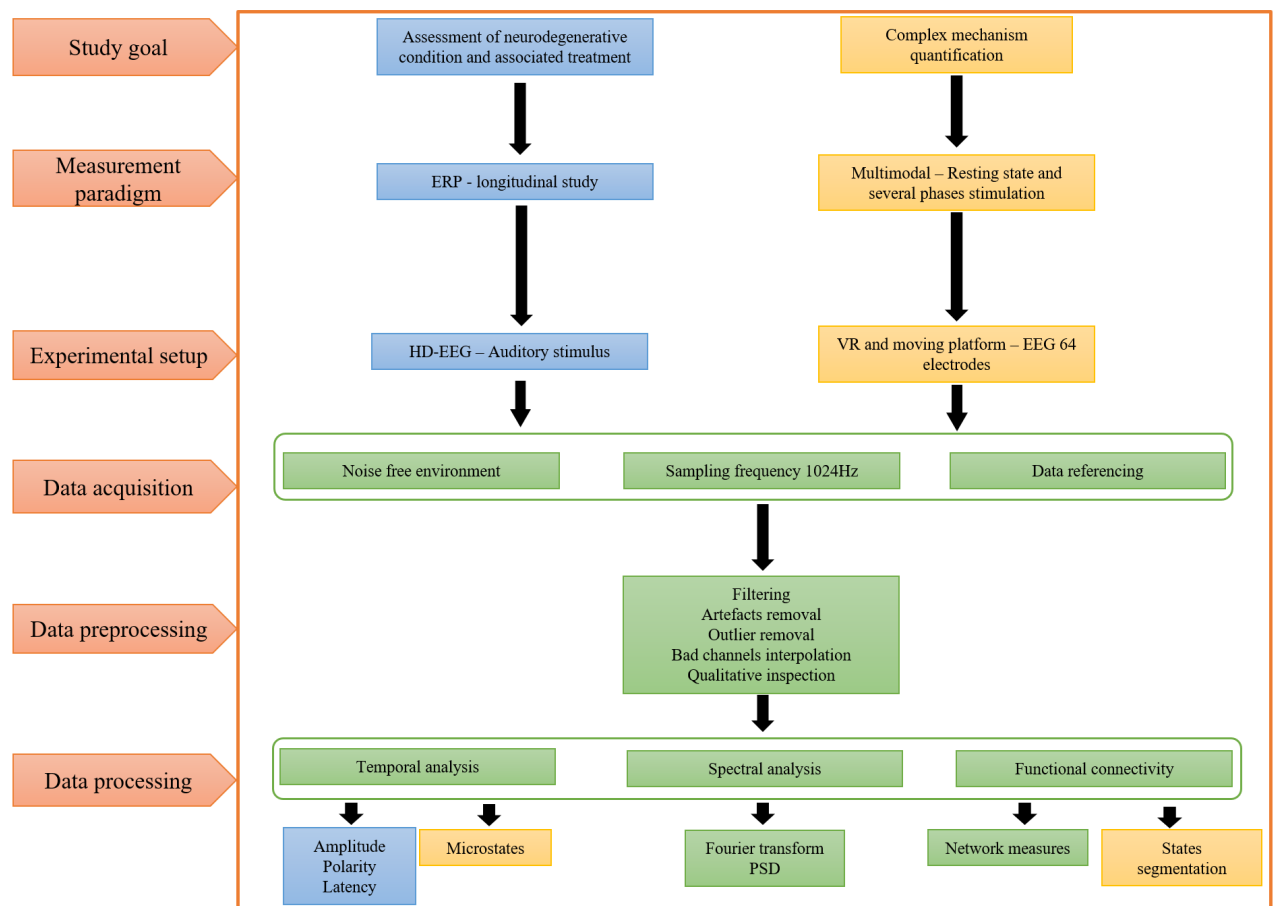
Figure 2.6: Summary of the global methodological workflow reported in the dissertation

(a) EEG signal before pre-processing   (b) EEG signal after pre-processing
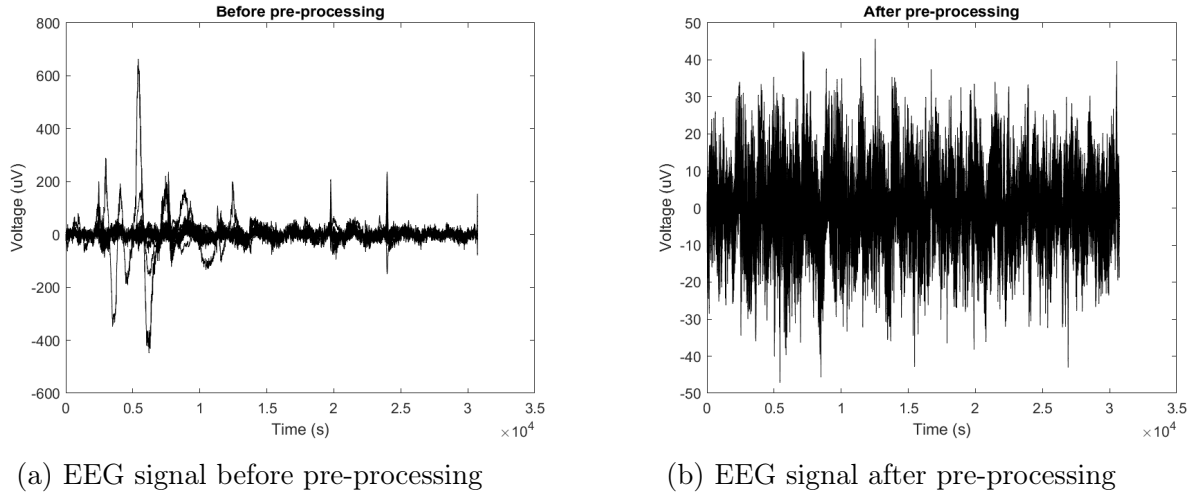
Figure 2.7: Comparison of 2 EEG signals before and after pre-processing

2.2.1   Methodology

2.2.1.1   Pre-processing

Like other imaging techniques, EEG is very sensitive to noise and artefacts. Before starting any type of analysis, a thorough pre-processing plan is necessary to clean the signals and obtain exploitable data [35]. The usual first step to pre-process the signal is to apply a band-pass filter. A notch filter is also necessary to remove noise due to powerline interference. Afterwards, the artefacts (visible due to a too high amplitude) need to be removed. This can be done trough the whole time series by removing the whole signal from an electrode, or by removing a particular time segment. For this, several technique exists, from manual inspection to variance based analysis, or independent component analysis. Once the signal is clean, bad channels are interpolated to obtain a full clean time-series. The different approaches used are detailed in the methods section of chapters 3 and 4. Figure 2.7 compares the same EEG signal before and after the pre-processing.

2.2.1.2   Time domain

EEG time-series provide a voltage value for each time point. When studying ERP, the signal is averaged through all the trials. The main parameters used to characterize ERP response are their polarity, the latency, and the amplitude [60]. The voltage can be seen on a scalp distribution at a certain point of time, to observe the repartition of cortical activity. To facilitate the visual inspection of the signal, a topographical variance graph can be plotted, based on the global field power (computation of the standard deviation over all electrodes at each point in time) [61]. The more brain regions become actives, the more global field power will increase. It is complementary with the amplitude analysis, and can help for the data quality assessment.
Time domain analysis can also rely on functional microstate segmentation. The clustering through time based on voltage topography is a powerful and robust tool for task-related and statistical analyses.

2.2.1.3 Spectral analysis

If we assume that their signal is stationary (meaning that mean and variance of data distribution do not depend on time), EEG time-series can be decomposed as a sum of sine waves of different frequencies, amplitudes and phases. Even though EEG is known to be non-stationary, the previous assumption is correct for short-time windows [62]. This is a crucial point as most signal processing methods relies on stationarity, such as Fourier transform (FT).

Fourier transform and power spectral density   FT is a mathematical operation that decomposes signal into frequency components. Usually, it is implemented using Fast Fourier Transform (FFT), an algorithm that computes the discrete Fourier transform (DFT) of a signal [63]:

$$X_k = \sum_{n=0}^{N-1} x_n \cdot e^{-\frac{i2\pi}{N}kn} \tag{2.1}$$

Where x_n is the nth sample of time-series of N elements, and X_k represents the Fourier coefficient

The power of a frequency component obtained by DFT can be computed by squaring the magnitude of this component. Then, the power spectral density (PSD) can be observed by plotting the power against the frequency axis. Figure 2.8 shows an example of several sine waves plotted through time and their associated Fourier power spectrum.
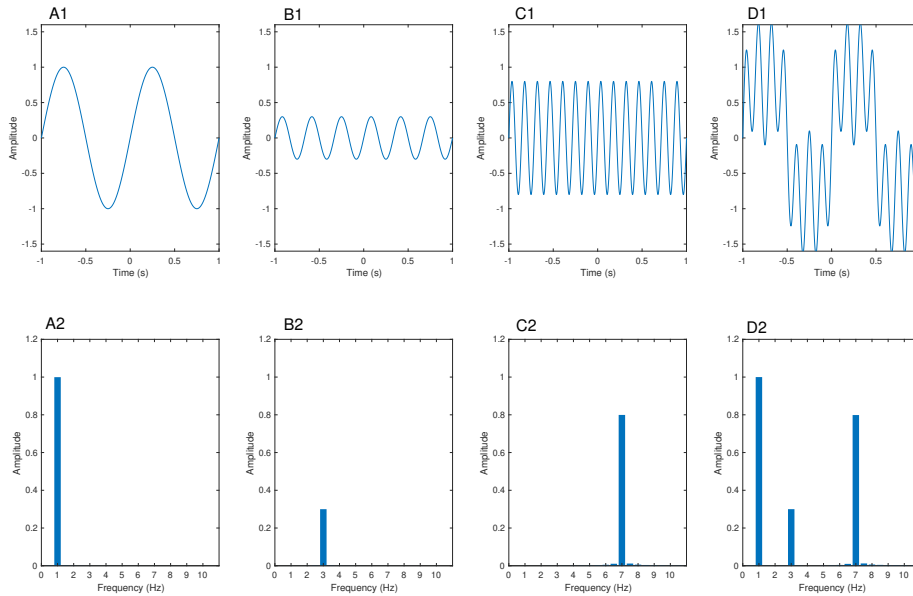
Figure 2.8: Sine waves of 1, 3 Hz and 7 Hz (panels A1, B1 and C1), and their sum (panel D1), with their related Fourier power spectrum represented in plots of frequency (x-axis) by amplitude (y-axis) (panels A2 to D2). The frequency of the sine wave is represented by the position on the x-axis, and the amplitude of the sine wave by the position on the y-axis.

As stated is its name, DFT works on discrete signal, which is not representative of real applications where the signal is continuous. Therefore, FFT considers the input signal as one period of a continuous periodic signal. This is problematic as our EEG time-series are segmented over one time period with a specific sampling frequency. Both extremities of the signal are then not likely to match, which can alter the spectrum estimate. This phenomenon is called spectral leakage, and can be addressed using windowing. Windowing is used to reduce the amplitude of the discontinuities in both edges of the acquired signal, multiplying the time-series by a finite length window that will adjust the edges towards zero. The most commonly used windowing approach is the Hanning window. However, since windowing is smoothing the data towards the edge, it leads to a loss of information and therefore inaccurate power estimate. To counter this problem, window segments are overlapped. This common approach has been developed by Welch, to estimate PSD using a periodogram method [64]; the EEG signal is split into a certain amount of segments with an overlap of 50%. Then, each overlapping segment is windowed, and the associated periodogram is computed by applying DFT and estimating the spectral density over the interval. Finally, the individual periodograms are averaged, leading to the signal's PSD estimate. From the PSD estimate, absolute and relative power can be obtained. Absolute power (AP) is computed by taking the integral of the all PSD values within a frequency range. Relative power (RP) is obtained by taking the percentage of AP in a frequency range over the sum of all frequency bands studies. AP and RP are valuable metrics as they enable to study the power evolution of the five main brain rhythms. They are essential to describe brain behaviour during cognitive processes.

Scalp distribution   EEG time-series represent the signal recorded over the scalp, for each electrode. The PSD estimation is then performed for each electrode as well. As EEG electrodes positioning is standardized, it is of common use to plot EEG power on topographical maps of the scalp, seen from above. Those maps are useful to compare data from different populations, different tasks or even the evolution through time [65], [66]. Figure 2.9 shows an example of a topological PSD scalp distribution.
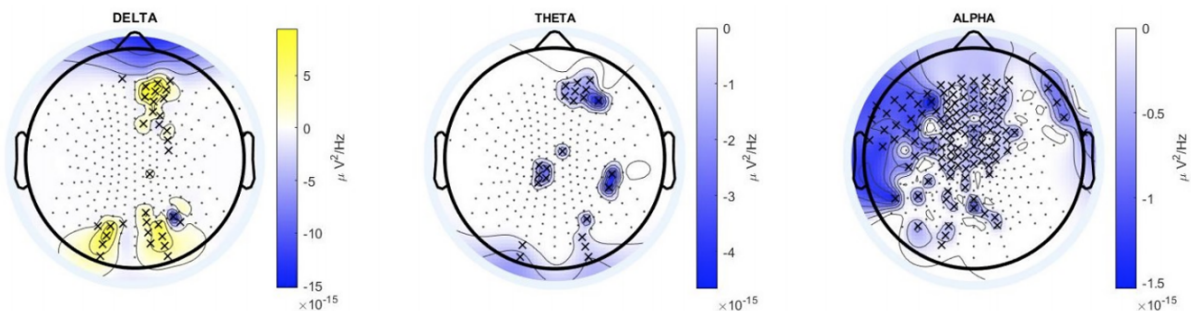
Figure 2.9: PSD scalp distribution for three frequency bands.

The different results evolution of each frequency band is also directly seen, making it easier to analyse and interpret. Moreover, it slightly compensates the poor spatial resolution of EEG, by giving an insight of which brain region testify to a power activation or suppression during a certain task.

2.2.1.4 Brain network

A novel approach has emerged in the last years, to understand brain behaviour not only at a single level, but how several brain areas interact with each other. This approach uses network analysis to study brain organization. This method aims to characterize the sequence of information running from one region to another, giving more highlight on how a cognitive process or a certain condition or disorder impacts these sequences. This methodology bases its mathematical concepts on graph theory [67]. Graph theory represents complex systems under the shape of a graph, a mathematical structure that model relations (edges) between objects (nodes). Figure 2.10a illustrates a network comporting 6 nodes and 7 edges, under its graph form and its associated matrix form.

(a) Graph form
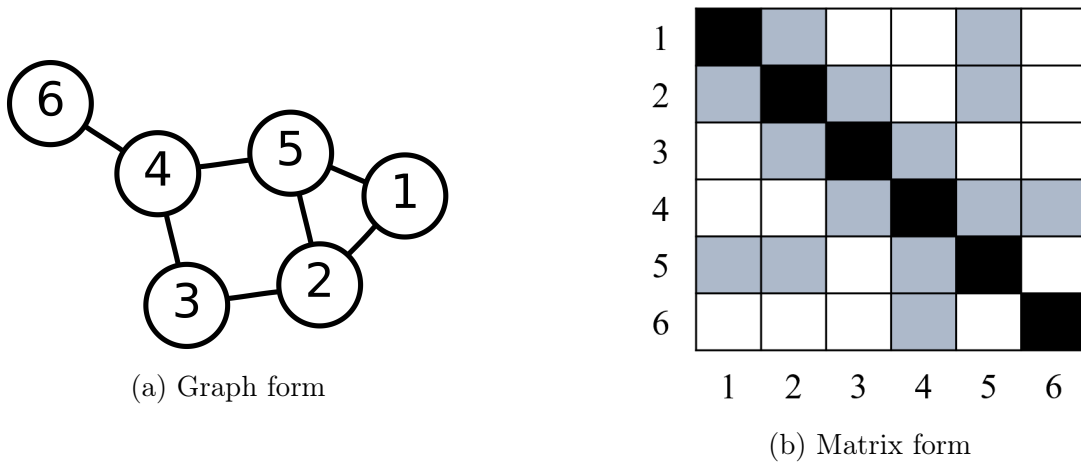
(b) Matrix form

Figure 2.10: Illustration of a network under the graph form and the matrix form

Thus brain network analysis illustrates the brain as graph (network), where brain cortical areas are considered as nodes, and the connections between areas are edges. This graph portrays the functional connectivity between brain cortical regions. Due to its excellent spatial resolution, fMRI is the most commonly used technique to study functional connectivity. However, its low temporal resolution does not enable to track fast changes in network, and prevent from studying brain network dynamics. EEG is the ideal candidate to address this problem, but some issues were raised to build a brain network from EEG. First, since the signal is recorded from the scalp, how is it possible to accurately estimate electrical activity from the brain regions, which is altered due to the volume conduction effect. Indeed, the electrical signals recorded from the scalp are passing through several tissue layers from the head, all of them comporting different electrical properties. Thus, the source of the recorded signal is not unique and direct from a cortical source, but mostly a mix of several tissue sources. The second issue is to measure the connectivity between those brain regions. To address this problem, a method has been used to estimate cortical sources from EEG channels, and therefore reconstruct cortical time-series. This method is called EEG source connectivity [68], and is based on two main steps: brain sources reconstruction, and source connectivity estimation.

Source reconstruction The reconstruction of cortical sources is based on finding the solution to the inverse problem, where source time-series are estimated from scalp time-series. It uses a current dipole model of the head, and appropriate constraints

to reduce the number of solutions [69], [70]. The current dipole model of the head is employed to simulate electrical activity propagation through the head tissues, and the applied constraints are based on several properties of the sources. A standard head model can be used, as there is no significant difference with the use of a subject-specific head model [71]. Thus, the relation between source and scalp time series can be expressed as a linear combination. To resolve the source estimate, the inverse solution matrix needs to be computed. Several algorithms exist to solve the inverse problem, such as weighted minimum norm estimate (wMNE) [72]. The final outcome of the inverse problem is the source time-series matrix, that can contain more than 1000 sources, depending on which head model is used. This number of sources is way too high for a network analysis, as each source would be a node. For this reason, the use of anatomical atlas is essential to focus on the regional level, and average sources over regions of interest (ROIs). One commonly used atlas is the Desikan-Killiany atlas [4], that divides the brain into 68 regions. Thus, the final output would a matrix of 68 ROI time-series (scouts) for instance, where the connectivity can be computed.

Functional Source connectivity   Functional connectivity will rely on the statistical relationships between cortical areas. This approach is weighted, as the connectivity value between two regions are not binary, and undirected, as the statistical dependency between two regions is symmetric. Several methods exist to compute brain connectivity, such as phase-locking value (PLV) [73]. It describes the neural synchronization between two signals, and is comprised between 0 (independent activity) and 1 (strong synchronisation of signal phase). The final connectivity matrix expresses the symmetric PLV value between each brain region, leading to a symmetric matrix that describes the network.

The source connectivity workflow presented in this thesis is based on wMNE and PLV algorithms, and is represented in figure 2.11. Other methods exist, but a previous study [74] showed that this combination presented the most reliable results.
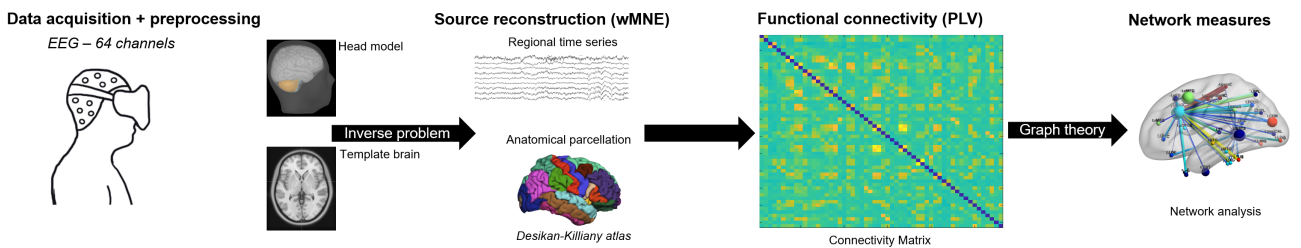
Figure 2.11: Source connectivity workflow: From the EEG time-series, sources are reconstructed using wMNE algorithm, based on a current dipole head model. Then, using Desikan-Killiany anatomical parcellation, the sources are regrouped in ROIs, from which the functional connectivity is computed using PLV. From this final matrix, brain networks can be analysed based on graph theory.

Network analysis   From the final connectivity matrix, different analyses can be performed, on the static or the dynamic aspect [75]. The static analysis is based only on one connectivity matrix, and aims to extract network characteristics in a specific condition, whereas the dynamic connectivity matrix will study several connectivity matrices computed through time, and observe how the network evolves over time.

The most studied properties of brain network in the static analysis are hubness (measured by strength), integration (measured by participation coefficient), and segregation (measured by clustering coefficient). Figure 2.12 illustrates a brain network with the associated vocabulary required for basic understanding.
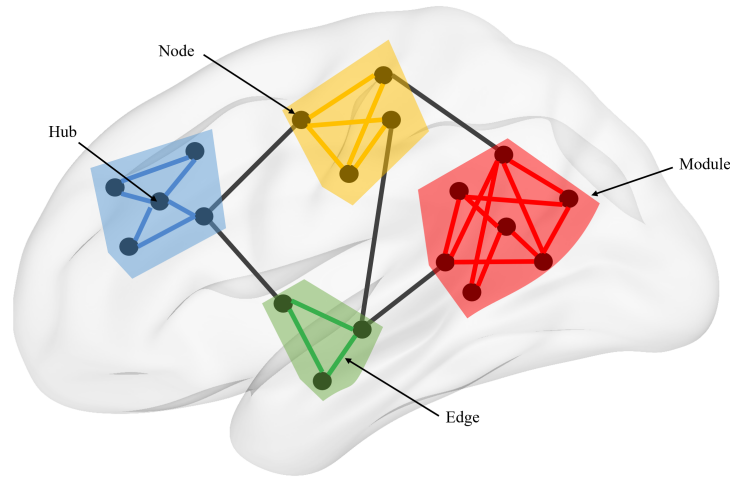
Figure 2.12: Illustration of brain network and basic terminology

Hubness studies the connections of nodes. A hub is a node with a high number of connections. They are essential for the network structure, showing the most active and solicited brain regions. The hubness of a node is computed by the strength, which is the sum of the weights of all edges linked to this node. The study of brain network integration and segregation is complementary. Network integration explains the organisation of the brain into a large functional structure to deal with a diverse and wide amount of information, and plan an adapted action. Network segregation describes the organisation of the brain into different modules separating the different type of information for specialised processes. Both of them testify to the modularity of the network, which is a crucial property of functional connectivity. Modules are subdivisions of the networks; they are groups of nodes that are strongly connected within other nodes of the same module, and weakly connected with the rest of the network. The study of modularity through time enables to identify the main structures of the brain and how they change over time, depending on the different conditions the brain is exposed to. It helps to characterize the how cortical areas organize themselves according to the cognitive process involved, and understand the underlying brain remodeling. Moreover, it helps to the interpretation of brain function depending on which cortical areas is involved.

Chapter 3

Assessment of rTMS as therapeutical solution for patients with schizophrenia

3.1 Background

3.1.1 Definition

Schizophrenia is a mental disorder defined by repeated episodes of psychosis, which has a lifetime prevalence of 1% [76], with an onset on early adulthood, that can lead to long-term life impairment [77]. The main symptoms are delusions, auditory verbal hallucinations (AVH), but it can also be manifested as demotivation, social withdrawal, and cognitive symptoms like deficiency in working memory, processing speed and execution [78].

3.1.2 Diagnostics methods

The diagnosis of schizophrenia relies on clinical assessment. Different methods are available, but are mainly based on psychometrics scale, and lack objective and quantitative data [79]. However, in the case of subjects with schizophrenia suffering from auditory verbal hallucinations, structural and physiological changes have been observed (grey matter volume, atypical connectivity on several brain regions) [80].

3.1.3 Treatment

The main way to treat schizophrenia is the use of antipsychotic medication. However, over a third of schizophrenia patients suffer from treatment-resistant hallucinations [81]. To address this issue, non pharmacological solutions have been implemented, among which repetitive transcranial magnetic stimulation (rTMS).

3.1.4 rTMs

Transcranial magnetic stimulation is non-invasive brain stimulation technique, using magnetic field to induce an electric current in a targeted area of the brain [82]. In the clinical aspect, rTMS has shown evidence of efficacy for disorders such as depression [83], mild cognitive impairment and Alzheimer's disease [84]. Some studies found

moderate to high effect for the use of rTMS as a treatment for AVH [85]. However, most of this analyses based their results from the psychometrics score.

3.1.5 EEG and schizophrenia

EEG has been used to understand the underlying mechanism of schizophrenia [86], [87]. The study of two main ERP paradigms, P50 and P300 revealed differences between patients with schizophrenia and control subjects [88]. Spectral analysis and graph-theory have shown promising results to evaluate schizophrenia's impact on brain response on one side [87], [89], but also to observed the impact of rTMS in disorders such as depression [90]. Therefore, EEG is a critical tool to assess the impact of rTMS as therapeutical solution for schizophrenia with AVH.

3.1.6 Context of the study

The study developed in this thesis aims to evaluate the use of rTMS as a potential treatment for patients with schizophrenia, on a longitudinal study. It will be detailed in chapter 3. It aimed to identify potential biomarkers of brain response to rTMS for patients with schizophrenia, based on an extensive set of metrics extracted from different EEG analyses. It has been published in *Frontiers in Neuroscience* ([91]).

3.2 Introduction

Hallucinations are sensory perceptions occurring in the absence of an external stimulus. Auditory verbal hallucinations (AVH) are positive psychotic symptoms of schizophrenia and a diagnostic feature in the pathology, occurring in an estimated 60%–70% of people with this disorder. An increased interaction among the auditory-language and striatal brain regions occurs while patients hallucinate([92]). Patients with AVH present evidence of structural brain alterations associated with these perceptions, such as reduced grey matter volume in the superior temporal gyrus ([93]), including the primary auditory cortex, and abnormal connectivity among the temporal, prefrontal and anterior cingulate regions ([94], [92]). Among the empirically supported theories of the origin of AVH, are a misinterpretation of inner speech ([95]) and aberrant activation of the auditory cortex ([96]). Almost one-third of patients with positive psychotic schizophrenia present treatment resistant symptoms ([97]) and there is a compelling need for novel treatments.

Transcranial magnetic stimulation (TMS) is a non-invasive method used over the past 25 years in the treatment of neurobehavioral disorders ([98]). It uses an alternating magnetic field to induce an electrical current in the brain, depolarizing neurons and generating action potentials. [99] and [100] reported that 1 Hz repetitive TMS (rTMS) reduces the excitability of cortical neurons in healthy individuals. Based on these effects, [101] hypothesized that 1Hz rTMS delivered to the left temporoparietal cortex reduced activity in receptive language areas associated with AVH in patients with schizophrenia. Neuroimaging studies of AVH showed an increased activation in the absence of an external stimulus in the left primary auditory cortex of subjects with this symptom ([102]).

Our goal was to establish a methodological tool to quantitatively assess the cognitive processes of people suffering with AVH. We aimed to develop an hypothesis

that can validate psychometric results with event related potential (ERP) morphology (time domain), power spectral density (frequency domain) and brain connectivity in patients undergoing ten sessions of low-frequency rTMS.

To date, the mechanism of the effect of rTMS on AVH has only been inferred from the hypothesis of left temporoparietal cortex dysfunction and the behavioral response is variable from patient to patient. Dozens of studies have used inhibitory low frequency rTMS over the T3-P3 EEG location as a treatment for pharmaco-resistant AVH with the effects measured mainly with psychometric scales ([103], [85]). Physiological measures linked to specific brain areas and biomarkers of target engagement and response are needed to optimize treatment. Indeed, response biomarkers are essential as predictors of treatment where behavioral outcomes can be variable. They may also be very useful for rTMS treatments, where multiple parameters, including frequency, train length, intensity, duration and treatment schedule can all influence effectiveness and should be optimized before full-scale clinical trials are attempted. Past studies indicate a relation between different frequency bands and cognitive processes ([104]). The power spectral density (PSD) changes observed in response to attentional demands can be of interest to monitor patients with schizophrenia behavior. Electroencephalographic (EEG) measures, including spectral density and evoked potentials ([105]), have been used as measures of the physiological response to TMS treatment. For instance, it has been observed that rTMS to the dorsolateral prefrontal area increased the P300 response in patients with schizophrenia, but not healthy controls ([106]).

The P300 first described by [49], mostly studied as a parameter of voluntary attention ([107]), is the leading Event Related Potential (ERP) correlate of target discrimination ([107]) and it has been largely employed to characterize schizophrenia ([108]). Previous studies have found that patients with auditory hallucinations exhibit reduced P300 amplitudes ([109], [110] [108]). Many works based on P300 also analyzed N100, the negative deflection that occurs approximately 100ms after the auditory stimulus, noting a relation with working memory ([111]). The mean amplitudes of the auditory N100 and P300 responses are decreased in patients with schizophrenia in comparison to healthy participants ([112], [113], [114]).

Here, we compared alterations in the P300 response after left temporal and vertex (used as a control in previous studies with schizophrenia and AVH ([115],[116],[117])) TMS in patients with schizophrenia using three different approaches : time, frequency and source-space connectivity. Patients also underwent a battery of neurobehavioral and tests before and after treatment. We remained descriptive in our analysis before and after treatment, at group and single levels.

3.3 Material and Methods

3.3.1 Participants

The patients were recruited from the psychiatric wards and outpatient clinics of the National Hospital of Iceland. They were diagnosed with schizophrenia, following the ICD-10 (International Classification of Diseases, Tenth Revision, Clinical Modification) schizophrenia classification (F20). Only those still experiencing persistent AVH after finishing at least two 6-8 week drug treatments were selected. Patients were excluded if they had history of seizures, were using cannabis or drinking more than three units of alcohol daily, were using any other illegal drugs within one month prior to the beginning

of the study, or showing TMS contraindications during the pre-treatment interview
([118]). Permission from the Health Research Ethics Committee at the University
Hospital of Iceland was obtained (approval no. 21.2018). Ten patients (7 men and 3
women, mean age = 32, SD = 6.41)) were selected for the study. All of them were
taking medications. Table 3.1 sums up the patient information.

Group	Id	Gender	Medication	Diagnosis
TG	T1	M	Clozapine, Fluoxetine, Bupropion	Paranoid Schizophrenia
TG	T2	M	Clozapine, Olanzapine, Perphenazine, Alprazolam, Levomepromazine, Oxazepam and Melatonin	Paranoid Schizophrenia
TG	T3	F	Sertraline, Quetiapine, Pregabalin and Zopiclone	Schizoaffective Disorder Depressive type
TG	T4	M	Clozapine and Flupenthixol	Paranoid Schizophrenia
TG	T5	M	Clozapine, Amisulpiride, Propranolol and Clonazepam	Paranoid Schizophrenia
CG	C1	M	Paliperidone, Quetiapine and Perphenazine	Paranoid Schizophrenia
CG	C2	F	Clozapine, Flupenthixol, Zopiclone, Mirtazapine, Escitalopram, Metoprolol and Chlorpromazine	Paranoid Schizophrenia
CG	C3	F	Aripiprazole, Olanzapine, Chlorprothixene and Pregabalin	Paranoid Schizophrenia
CG	C4	M	Clozapine, Olanzapine, Bupropion and Propranolol	Paranoid Schizophrenia
CG	C5	M	Clozapine, Pregabalin, Amisulpride	Hebephrenic Schizophrenia

Table 3.1: Socio-demographic information. (Group : TG : T3-P3 group, CG : Cz
group. Gender : M : man, F : woman.)

The patients were randomly assigned into two groups. Five patients (four men
and one woman, mean age 35.2, SD = 5.12,range 30-48) were included in the active
treatment group (TG). They received ten daily sessions of 15 minutes 1Hz frequency
rTMS (900 pulses/session) at 100% of abductor pollicis brevis resting motor threshold
(RMT) applied at T3-P3 location. Five patients (three men and two women, mean age
29.6, SD = 3.92, range 26-39) were included in the control group (CG) and received
rTMS at 100% RMT to the vertex of CG 10-20 location. The EEG and psychometric
data were acquired twice in each patient group; before the rTMS treatment (pre-
treatment) and within one week after completing ten sessions of rTMS treatment
(post-treatment). This produced 20 datasets: five pre-TMS TG, five post-TMS TG,
five pre-TMS CG and five post-TMS CG. Figure 3.1 shows the experimental set-up
and workflow designed for this study. Figure 3.2 shows the pre-processing and data
analysis pipeline used for this study.
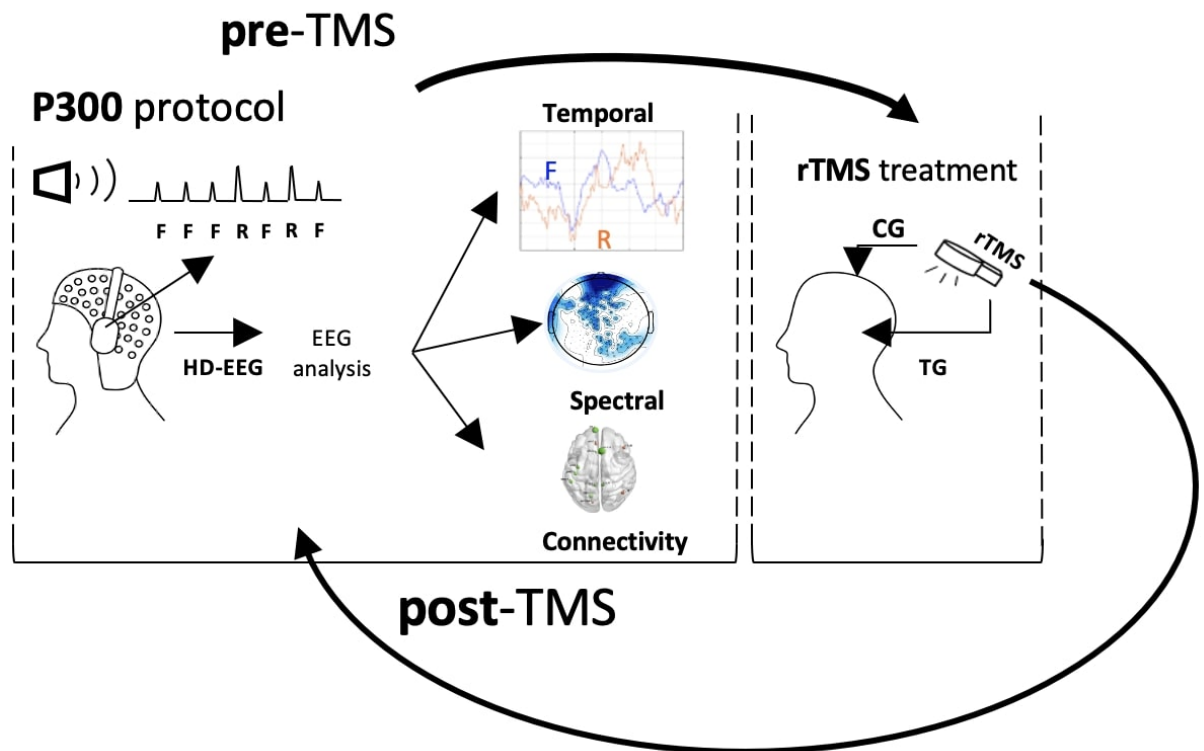
Figure 3.1: Data acquisition and processing workflow
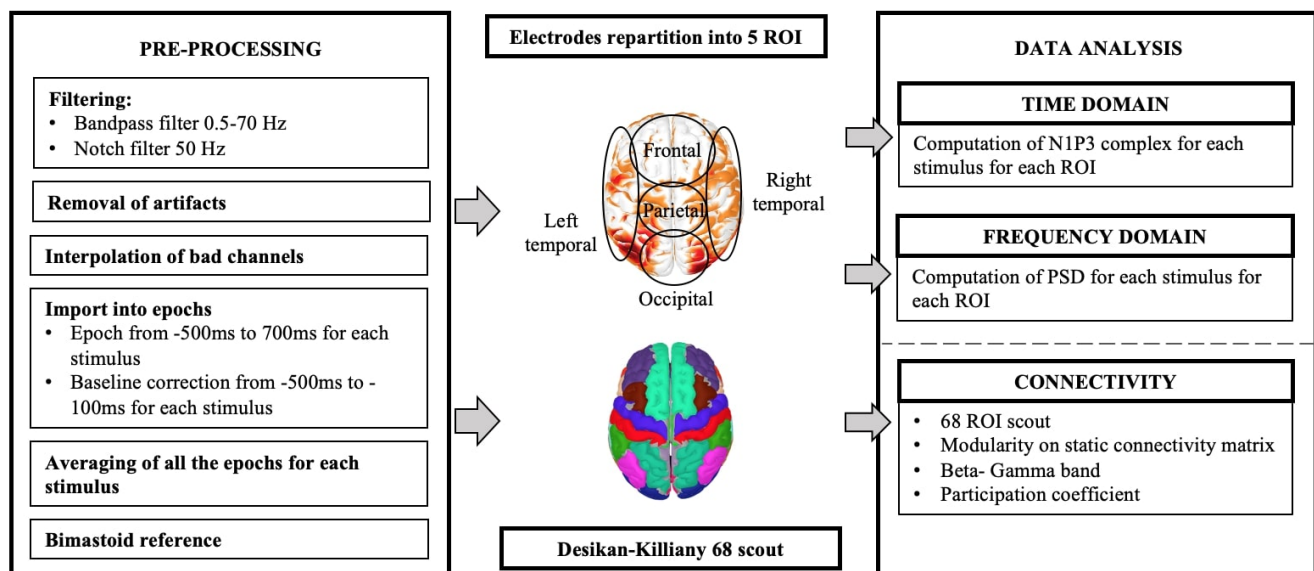
Figure 3.2: Pre-processing and analysis workflow

3.3.2 Psychometric Data

Three scales were used to collect clinical information pre- and post-treatment.

3.3.2.1 PSYRATS

Psychotic Symptom Rating Scales (PSYRATS) auditory hallucinations subscale (AHS) is an interview measuring auditory hallucinations using 11 items rated on a five-point ordinal scale (0-4). The scale measures the severity of AVH for the past week in eleven dimensions which are: frequency, duration, location, loudness, beliefs about origin, negative content, intensity of negative content, amount of distress, intensity of distress, disruption of life and control. PSYRATS has shown excellent inter-rater reliability and good discriminant and convergent validity for both chronic and first episode psychosis ([119]; [120]).

3.3.2.2 Quality of Life Scale (QoLS)

Quality of life was assessed with a 16 item self-report scale, consisting of five conceptual domains of quality of life: material and physical well-being, relationships with other people, social community and civic activities, personal development and fulfillment, and recreation. The scale has been shown to have good test-retest reliability and good convergent and discriminant validity ([121]).

3.3.2.3 Depression Anxiety Stress Scales (DASS)

The DASS is a measure of mental health focusing on the three traits of depression, anxiety and stress. It consists of 42 items, rated on a four point Likert type scale of how much that symptom occurred in the last week. In clinical samples the scale has shown excellent internal consistency and temporal stability as well as excellent discriminant validity and good convergent validity ([122]).

3.3.3 P300 recordings

P300 was measured with an auditory oddball paradigm attention task. The recordings took place between 11h00 and 14h00 for a duration of one hour. The subjects sat with their eyes closed. The frequent (F) and the rare (R) auditory stimuli were presented binaurally through headphones at an interstimulus interval between tones of constant 1.1 sec. The loudness was adjusted for each participant. For each subject, there was one trial of 200 tones, comporting a random tone occurrence with a probability of 0.2, leading to 160 frequent tones and 40 rare ([123]). We required the participants to focus on the rare stimuli without counting or moving a finger.

3.3.4 EEG pre-processing and analysis

The EEG was recorded using a 256 channel system (ANT Neuro, Netherlands) with an electrooculogram (EOG) electrode placed below the right eye and a ground electrode placed on the left side of the neck. Data pre-processing and analysis were performed with Brainstorm ([124]) and MATLAB 2018b (MathWorks, Inc., Natick, 158 Massachusetts, USA).

3.3.4.1 Pre-processing

The data were sampled at 1024 Hz and re-referenced to the average of left and right mastoid electrodes (R19R, L19L). A bandpass filter was set between 0.5-70 Hz and

notch filter from 49-51 Hz was used to remove undesired monomorphic artifacts from 50 Hz mains electricity. Bad channels were manually removed when EEG voltage was higher than ± 80 μV; if more than 10% of the channels showed too much noise or incorrect signal, the whole trial was rejected. The signals were digitized in epochs of 1200 ms, starting 500 ms before the presentation of each auditory stimulus (-500 to +700 ms). Baseline correction was performed using pre-stimulus 500 ms to pre-stimulus 100 ms window and channels marked as bad were removed and interpolated. Individual trials were visually inspected and rejected when indicative of excessive muscle activity, eye movements or other artifacts.

3.3.4.2 Data analysis

Time domain N100-P300 complex values of both frequent and rare stimuli were calculated and plotted via MATLAB 2018b for each subject (pre and post-treatment for patients groups).
The scalp was divided into 5 regions of interest (ROI), see figure 3.2. The 254 electrodes were partitioned as follows: 80 channels for the Frontal region (F), 59 for the Parietal region (P), 69 for the Occipital region (O), 23 for Right Temporal lobe (RT), and 23 for Left Temporal lobe (LT)([125]).
N1-P3 wave signals were calculated for the entire N100-P300 complex from the average of channels of every ROI as the difference between the most negative voltage value within time range of 80-150 ms (N100) and the most positive voltage value within time range of 250-500 ms (P300).
The differences between frequent and rare stimulus and pre- and post-treatment were also computed and plotted.

Frequency domain The power spectral density (PSD) was computed for each epoch with Welch's method, using Brainstorm, with the following frequency bands: delta (0.5–4 Hz), theta (4–8 Hz), alpha (8–13 Hz), beta (13–30 Hz), gamma (30–70 Hz). The PSD has been divided by the associated bandwidth for each frequency band.
Using the same scalp division as that of the time analysis, the PSD of electrodes within the same ROI were averaged for frequent and rare stimuli, pre- and post-treatment for each subject.
The PSD difference post-pre treatment and frequent - rare were computed for each subject.

Connectivity The connectivity has been computed at the cortical level using the "EEG source connectivity" method. It consists of estimating the brain sources (over 68 regions of interest -ROI-) and then computing the statistical coupling between these reconstructed sources. The weighted minimum norm estimate (wMNE) and the Phase Locking Value (PLV) were used to solve the inverse problem and compute the functional connectivity, respectively. This choice was based on previous comparative studies showing good performance of this combination on simulated and real data. ([126]; [74] ; [68]). The analysis has been performed only on the beta and gamma bands, due to window length constraints (here 700 ms). The source-space networks

were estimated for each trial, subject and conditions. To compare between conditions, the networks were quantified using network measures that allow the extraction of the topological properties of the networks. We made the choice here to focus on network integration as it is the most consistent network feature that changes due to electric/magnetic stimulation ([127]) or brain disorders ([128]). The network integration reflects the ability of the brain network to integrate information form different and distant brain regions, a key feature of efficient information processing. To quantify the network integration, we used the participation coefficient (PC), to calculate the interactions between brain modules (distant sub-networks), on the thresholded connectivity matrices (here 20%). We used the brain connectivity toolbox (BCT) ([129]) to compute the PC (https://sites.google.com/site/bcnet/).

3.4 Results

3.4.1 Group results

The analysis for each individual revealed general consistent results. The results picturing the evolution (increase or decrease) of the neurophysiological and psychometric data and are detailed in table 3.2 for the TG, and in table 3.3 for the CG. The associated numerical values are detailed in table 3.4 for the TG and in table 3.5 for the CG. The analysis of the psychometric tests revealed that four out of five subjects in TG (tables 3.2 and 3.4) and three out of five subjects in CG (tables 3.3 and 3.5) felt improved condition after the treatment, whereas the other subjects remained neutral or reported worse psychometric scores. In the time domain analysis, the N1-P3 amplitude was globally higher post-treatment than pre-treatment, for six subjects, two in TG (tables 3.2 and 3.4) and four in CG (tables 3.3 and 3.5). The PSD increased post-treatment mainly for the alpha band and beta band globally, for six subjects as well, two in TG (tables 3.2 and 3.4) and four in CG (tables 3.3 and 3.5) . No trends were detectable for the gamma and theta bands. In several subjects, the right temporal area showed an opposite behavior compared to the other regions. The connectivity results showed an increased network integration (increase in participation coefficient) during post-treatment for frequent, for the beta band especially, for seven subjects, four in CG (tables 3.3 and 3.5), three in TG (tables 3.2 and 3.4). Due to the small sample size and high variability of the results, we will discuss selected study cases individually. The following four patients were selected due to their interplay between psychometric score and neurophysiological results, independant of treatment. Two subjects (T2, in TG and C3, in CG) presented an improvement in the psychometric score post-TMS, and the two others presented a stagnation in the psychometric (C2, in CG) or a decrement (T5, in TG). The rest of the data are provided in the supplementary material. There were no significant changes on AVH severity measured with PSYRATS AHS, in QoL and DASS global scores after rTMS between TG and CG.

3.4.2 Study case 1 : improvement in psychometric score

The two patients detailed in this section presented an improvement in their psychometric score post-treatment. We chose to describe them in this section due to their

	N1-P3 amplitude (μV)					Connectivity Participation coefficient (%)	Psychometrics		
	F	P	O	LT	RT		QoL	DASS	PSYRATS
T1	↑↑	-↓	↑↓	↓↓	↑↓	↑	↑	-	↓
T2	↓↓	-↑	↓↓	↓↑	↓↓	↑	↑	↓	↓
T3	-↑	↑↑	↓↓	↓-	–	-	↑	↓	↓
T4	↑↑	↑↑	↑↑	↑↑	↑↑	-	-	-	↓
T5	↓↓	↓-	↓↓	↓↓	↓↓	↑	-	↑	↑

	Power Spectral Density																			
	PSD: THETA					PSD: ALPHA					PSD: BETA					PSD: GAMMA				
	F	P	O	LT	RT	F	P	O	LT	RT	F	P	O	LT	RT	F	P	O	LT	RT
T1	-↓	↓↓	↓↓	↓↓	↓↓	↓↓	↓↓	↓↓	↓↓	↓↓	↓↓	↓-	↓↓	↓↓	↓↓	↑-	↑↑	-↓	↓↓	↑↑
T2	↓↓	↓↓	↓-	↓↓	↓↑	↑↑	-↑	↑↑	↑↑	↑↑	↓↓	↓↓	↓↓	↓↓	↓↓	↓↓	↓↓	↓↓	↓↓	↓↓
T3	↓↓	↓↓	↓↓	↓↓	↓↑	↓↓	↓↓	↓↓	↓↓	↓↓	↓↓	↓↓	↓↓	↓↓	↓↓	↑↑	↑↑	↑↑	↑↑	↑↑
T4	↓↓	↓↓	-↓	↑-	↓↓	↑↑	↑↑	↑↑	↑↑	↓↓	↑↑	↑↑	↑↑	↑↑	↓↓	↑↑	↑↑	↑↑	↑↑	↑↑
T5	↑↑	↑↑	↑↑	↑↑	↓-	↑↑	↑↑	↑↑	–	↓↓	↑↑	↑↑	↑↑	↑↑	↓↑	↑↑	↑↑	↑↑	↑↑	↓↓

Table 3.2: Treated Group: Increase (↑), decrease (↓) or constancy (-) of the value after treatment of N1-P3, Connectivity, Psychometric and Power spectral density (PSD) of the frequent (blue) and rare (orange) stimuli (F: frontal; P: parietal; O: occipital; LT: left temporal; RT: right temporal). (QoLS: Quality of Life Scale,DASS: Depression Anxiety Stress Scale ,PSYRATS: Psychotic Symptom Rating Scales)

	N1-P3 amplitude (μV)					Connectivity Participation coefficient (%)	Psychometrics		
	F	P	O	LT	RT		QoL	DASS	PSYRATS
C1	↓↑	↓↑	↓↑	↓↑	↓↑	-	-	↓	-
C2	–	↓↓	-↑	↑↑	↑↑	↑	-	-	-
C3	↑↑	↑↑	↑↑	↑↓	↑↓	↑	↑	↓	-
C4	↓↓	↓↓	↓↓	↓↓	↓↓	↑	↓	↓	-
C5	↓↓	↓↓	↓↑	↓↑	↓↑	↑	↓	↑	-

	Power Spectral Density																			
	PSD: THETA					PSD: ALPHA					PSD: BETA					PSD: GAMMA				
	F	P	O	LT	RT	F	P	O	LT	RT	F	P	O	LT	RT	F	P	O	LT	RT
C1	-↑	↓↓	↓↓	↓↓	↓↑	↓↓	↓↓	↓↓	↓↓	↑↑	↑↑	↑↑	↑↑	-↑	↑↑	↑↑	↑↑	↓-	↓↓	↓↓
C2	↑↑	↑↑	↑↑	↑↑	↑↑	↓↑	-↑	-↑	↑↑	↑↑	↑↑	↑↑	↑↑	↑↑	-↑	↓↓	↓↓	↓↓	↓↓	↓↓
C3	↑↑	↑↑	↑↑	↑↑	↑↑	↑↑	↑↑	↑↑	↑↑	↓↓	↑↑	↑↑	↑↑	↑↑	↑↑	↑↑	↑↑	↑↑	↑↑	↑↑
C4	↓↓	↓↓	↓↓	↓↑	↓↓	↓-	–	-↑	↑↑	–	↓↓	↓↓	↓↓	↑↑	-↓	↓↓	↓-	↓↓	↓↑	↓↓
C5	↓↓	↓↓	↓↓	↓↓	↓↓	↓↓	↓↓	↓↓	↓↓	↓↓	↓↓	↓↓	↓↓	↓↓	↓↓	↓↓	↓↓	↓↓	↓↓	↓↓

Table 3.3: Control Group: Increase (↑), decrease (↓) or constancy (-) of the value after treatment of N1-P3, Connectivity, Psychometric and Power Spectral Density (PSD) of the frequent (blue) and rare (orange) stimuli(F: frontal; P: parietal; O: occipital; LT: left temporal; RT: right temporal). (QoLS: Quality of Life Scale,DASS: Depression Anxiety Stress Scale ,PSYRATS: Psychotic Symptom Rating Scales)

higher values post treatment in the neurophysiological data, (Figure 3.3A and Figure 3.4A)in order to find a potential correlation between those two outcomes.

| | Connectivity | | Psychometrics | | | | | |
| | Participation coefficient (%) | | QoL | | DASS | | PSYRATS | |
	Pre	Post	Pre	Post	Pre	Post	Pre	Post
T1	1	9	68	77	8	9	21	16
T2	6	13	55	75	92	85	32	25
T3	10	8	50	69	118	53	34	28
T4	9	10	94	91	5	4	30	23
T5	15	26	93	96	39	58	23	28

N1-P3 amplitude (uV)

| | Freq | | | | P | | | | O | | | | LT | | | | RT | | | |
| | Pre | | Post | | Pre | | Post | | Pre | | Post | | Pre | | Post | | Pre | | Post | |
	Freq	Rare	Freq	Rare	Freq	Rare	Freq	Rare	Freq	Rare	Freq	Rare	Freq	Rare	F	Rare	F	Rare	F	Rare
T1	3.52	6.91	4.12	7.33	5.05	10.08	4.85	7.85	3.91	5.58	4.37	2.77	6.50	10.49	5.15	8.60	5.25	8.32	6.03	7.42
T2	2.05	6.77	1.61	4.27	1.72	4.73	1.56	5.33	2.10	5.25	1.33	4.43	4.64	9.75	1.02	10.06	3.66	9.33	0.99	8.30
T3	5.24	5.17	5.36	10.14	5.59	8.93	6.68	10.02	5.50	7.03	4.67	5.78	5.98	10.81	5.40	10.79	5.40	9.53	5.18	9.81
T4	3.39	6.60	8.11	12.37	3.31	6.72	7.81	12.22	3.50	5.53	7.23	13.33	5.12	5.96	7.49	14.11	4.11	5.24	7.07	12.93
T5	2.68	4.58	2.47	4.10	3.51	5.06	2.72	5.15	3.82	5.08	3.15	4.48	5.20	6.70	3.42	4.42	5.22	6.21	3.39	4.46

Power spectral density : Theta band ($\mu V^2 /Hz$)x10^{-15}

| | Freq | | | | P | | | | O | | | | LT | | | | RT | | | |
| | Pre | | Post | | Pre | | Post | | Pre | | Post | | Pre | | Post | | Pre | | Post | |
	Freq	Rare	Freq	Rare	Freq	Rare	Freq	Rare	Freq	Rare	Freq	Rare	Freq	Rare	F	Rare	F	Rare	F	Rare
T1	172	338	105	235	152	244	94	255	145	262	95	208	124	228	109	356	196	225	166	259
T2	59	120	21	170	44	95	15	164	45	145	17	194	66	232	26	208	82	111	22	457
T3	88	130	47	292	59	102	19	139	43	107	17	171	58	66	27	527	77	424	70	599
T4	37	85	348	468	36	78	169	264	39	91	355	639	30	53	427	621	66	102	267	481
T5	112	379	83	317	197	378	44	148	279	386	47	134	113	261	95	322	364	504	69	303

Power spectral density : Alpha band ($\mu V^2 /Hz$)x10^{-15} 1

| | Freq | | | | P | | | | O | | | | LT | | | | RT | | | |
| | Pre | | Post | | Pre | | Post | | Pre | | Post | | Pre | | Post | | Pre | | Post | |
	Freq	Rare	Freq	Rare	Freq	Rare	Freq	Rare	Freq	Rare	Freq	Rare	Freq	Rare	F	Rare	F	Rare	F	Rare
T1	116	395	28	92	100	245	26	90	167	366	30	92	262	548	42	175	221	697	53	100
T2	67	348	40	484	65	217	37	393	66	241	62	490	32	295	61	521	203	340	106	1047
T3	109	304	44	493	84	111	22	176	120	178	43	273	87	278	55	332	300	573	97	413
T4	31	52	39	244	14	21	31	137	35	59	56	170	17	44	45	118	38	109	44	255
T5	24	86	11	45	34	136	9	31	45	198	9	27	19	87	14	32	61	235	17	40

Power spectral density : Beta band ($\mu V^2 /Hz$)x10^{-15}

| | Freq | | | | P | | | | O | | | | LT | | | | RT | | | |
| | Pre | | Post | | Pre | | Post | | Pre | | Post | | Pre | | Post | | Pre | | Post | |
	Freq	Rare	Freq	Rare	Freq	Rare	Freq	Rare	Freq	Rare	Freq	Rare	Freq	Rare	F	Rare	F	Rare	F	Rare
T1	7	28	6	37	6	19	5	37	15	48	6	40	16	69	7	27	15	44	11	129
T2	21	93	13	50	22	93	13	50	28	127	18	65	33	258	14	50	50	177	31	84
T3	29	138	10	99	20	103	4	59	33	218	8	113	54	405	13	108	43	339	21	282
T4	3	13	31	111	2	10	31	110	4	14	33	110	3	14	40	118	4	16	22	121
T5	9	47	3	8	9	45	3	6	11	46	3	7	11	46	3	11	15	68	3	7

Power spectral density : Gamma band ($\mu V^2 /Hz$)x10^{-15}

| | Freq | | | | P | | | | O | | | | LT | | | | RT | | | |
| | Pre | | Post | | Pre | | Post | | Pre | | Post | | Pre | | Post | | Pre | | Post | |
	Freq	Rare	Freq	Rare	Freq	Rare	Freq	Rare	Freq	Rare	Freq	Rare	Freq	Rare	F	Rare	F	Rare	F	Rare
T1	0.8	6	3	8	0.5	4	3	7	2	11	3	8	2	14	2	5	0.9	7	5	17
T2	10	46	1	3	11	49	1	3	12	54	1	4	14	59	1	2	14	67	2	5
T3	0.6	3	4	47	0.5	2	2	20	0.8	3	3	33	0.5	3	4	37	0.6	2	6	57
T4	1	3	16	51	1	2	15	52	1	4	19	63	2	4	19	68	2	4	14	52
T5	3	12	1	3	3	15	1	3	3	17	1	4	3	13	2	7	4	19	1	4

Table 3.4: Treatment Group: Values pre and post treatment of N1-P3, Connectivity, Psychometric and Power spectral density of the frequent (blue) and rare (orange) stimuli(F: frontal; P: parietal; O: occipital; LT: left temporal; RT: right temporal). (QoLS: Quality of Life Scale,DASS: Depression Anxiety Stress Scale ,PSYRATS: Psychotic Symptom Rating Scales)

	Connectivity		Psychometrics					
	Participation coefficient (%)		QoL		DASS		PSYRATS	
	Pre	Post	Pre	Post	Pre	Post	Pre	Post
C1	29	26	83	84	34	26	28	28
C2	11	15	68	69	52	56	31	29
C3	8	16	41	79	80	42	32	31
C4	13	20	86	78	89	81	31	30
C5	1	22	96	82	11	18	30	27

N1-P3 amplitude (μV)

	F				P				O				LT				RT			
	Pre		Post		Pre		Post		Pre		Post		Pre		Post		Pre		Post	
	Freq	Rare	Freq	Rare	Freq	Rare	Freq	Rare	Freq	Rare	Freq	Rare	Freq	Rare	Freq	Rare	Freq	Rare	Freq	Rare
C1	2.94	4.38	2.16	8.27	4.22	4.87	2.71	6.80	2.71	3.09	1.31	7.94	4.61	7.05	0.91	9.58	3.77	6.11	1.49	9.53
C2	8.79	10.26	7.93	10.7	9.54	15.23	8.03	10.98	7.04	7.89	7.67	10.49	5.75	6.22	7.90	14.49	5.84	5.33	7.76	10.88
C3	1.02	3.01	5.16	7.43	2.08	4.59	6.84	8.67	2.01	5.51	5.65	8.42	5.31	11.63	6.89	9.31	5.09	10.61	7.01	9.61
C4	6.49	4.38	1.65	2.15	6.09	5.50	1.63	2.18	5.86	6.83	1.16	1.69	5.97	10.90	1.23	2.01	5.62	10.07	1.22	1.58
C5	5.10	4.71	4.16	2.57	9.16	14.05	4.40	5.72	5.31	5.08	2.62	8.73	8.31	11.93	4.01	13.87	9.00	10.37	4.03	12.49

Power spectral density : Theta band ($\mu V^2/Hz$)x10^{-15}

	Freq				P				O				LT				RT			
	Pre		Post		Pre		Post		Pre		Post		Pre		Post		Pre		Post	
	Freq	Rare	Freq	Rare	Freq	Rare	Freq	Rare	Freq	Rare	Freq	Rare	Freq	Rare	F	Rare	F	Rare	F	Rare
C1	46	154	68	381	42	146	62	192	45	141	51	195	78	129	59	167	46	118	76	382
C2	647	1651	544	792	245	606	299	289	153	506	188	264	571	1484	156	754	212	1933	311	459
C3	34	42	61	85	29	48	53	79	44	64	73	105	14	86	40	150	80	137	119	102
C4	653	1580	38	175	506	1430	37	190	688	2157	78	216	577	3253	231	328	793	2011	38	225
C5	660	763	429	1919	748	847	281	1543	945	1078	317	1453	1759	1273	1425	3293	1251	1098	200	2306

Power spectral density : Alpha band ($\mu V^2/Hz$)x10^{-15}

	Freq				P				O				LT				RT			
	Pre		Post		Pre		Post		Pre		Post		Pre		Post		Pre		Post	
	Freq	Rare	Freq	Rare	Freq	Rare	Freq	Rare	Freq	Rare	Freq	Rare	Freq	Rare	F	Rare	F	Rare	F	Rare
C1	34	120	51	215	44	85	35	129	40	116	43	181	46	259	69	174	26	97	45	112
C2	165	849	196	207	97	304	142	156	152	227	174	191	424	563	199	187	162	756	120	325
C3	39	105	79	141	27	94	73	106	34	135	90	153	17	50	130	185	48	345	62	219
C4	139	229	10	73	66	188	10	79	116	238	24	170	306	580	87	391	131	192	10	85
C5	54	177	78	220	57	153	61	218	63	204	77	247	59	340	66	353	55	282	100	347

Power spectral density : Beta band ($\mu V^2/Hz$)x10^{-15}

	Freq				P				O				LT				RT			
	Pre		Post		Pre		Post		Pre		Post		Pre		Post		Pre		Post	
	Freq	Rare	Freq	Rare	Freq	Rare	Freq	Rare	Freq	Rare	Freq	Rare	Freq	Rare	F	Rare	F	Rare	F	Rare
C1	6	16	9	61	5	17	8	47	5	23	11	58	6	40	18	102	6	24	13	70
C2	18	32	34	29	8	16	21	17	6	19	13	20	17	27	22	43	15	57	28	28
C3	5	11	11	22	5	13	10	22	4	12	12	33	5	10	17	47	5	16	11	23
C4	25	102	4	11	16	60	4	11	23	83	6	23	38	178	14	40	21	76	6	12
C5	8	18	15	58	7	14	12	54	7	14	15	66	7	15	36	190	8	21	10	56

Power spectral density : Gamma band ($\mu V^2/Hz$)x10^{-15}

	Freq				P				O				LT				RT			
	Pre		Post		Pre		Post		Pre		Post		Pre		Post		Pre		Post	
	Freq	Rare	Freq	Rare	Freq	Rare	Freq	Rare	Freq	Rare	Freq	Rare	Freq	Rare	F	Rare	F	Rare	F	Rare
C1	2	7	3	21	2	5	2	20	3	8	3	21	5	23	6	48	4	9	3	18
C2	8	20	0.5	0.4	6	16	0.3	0.3	6	18	0.2	0.3	9	24	0.4	0.3	8	27	0.3	0.3
C3	3	7	6	24	3	8	6	24	3	9	8	30	6	19	13	42	4	11	5	27
C4	3	19	0.2	2	3	14	0.2	2	4	28	0.2	2	7	41	0.5	8	7	27	0.3	2
C5	2	4	1	7	2	4	1	5	1	4	1	7	2	4	4	13	3	7	1	5

Table 3.5: Control Group: Values pre and post treatment of N1-P3, Connectivity, Psychometric and Power spectral density of the frequent (blue) and rare (orange) stimuli(F: frontal; P: parietal; O: occipital; LT: left temporal; RT: right temporal). (QoLS: Quality of Life Scale,DASS: Depression Anxiety Stress Scale ,PSYRATS: Psychotic Symptom Rating Scales)

3.4.2.1 Patient T2

Patient T2 (Figure 3.3) is a man with paranoid schizophrenia, in the TG, who took part in the study while taking : clozapine, olanzapine, perphenazine, alprazolam, levomepromazine, oxazepam and melatonin.
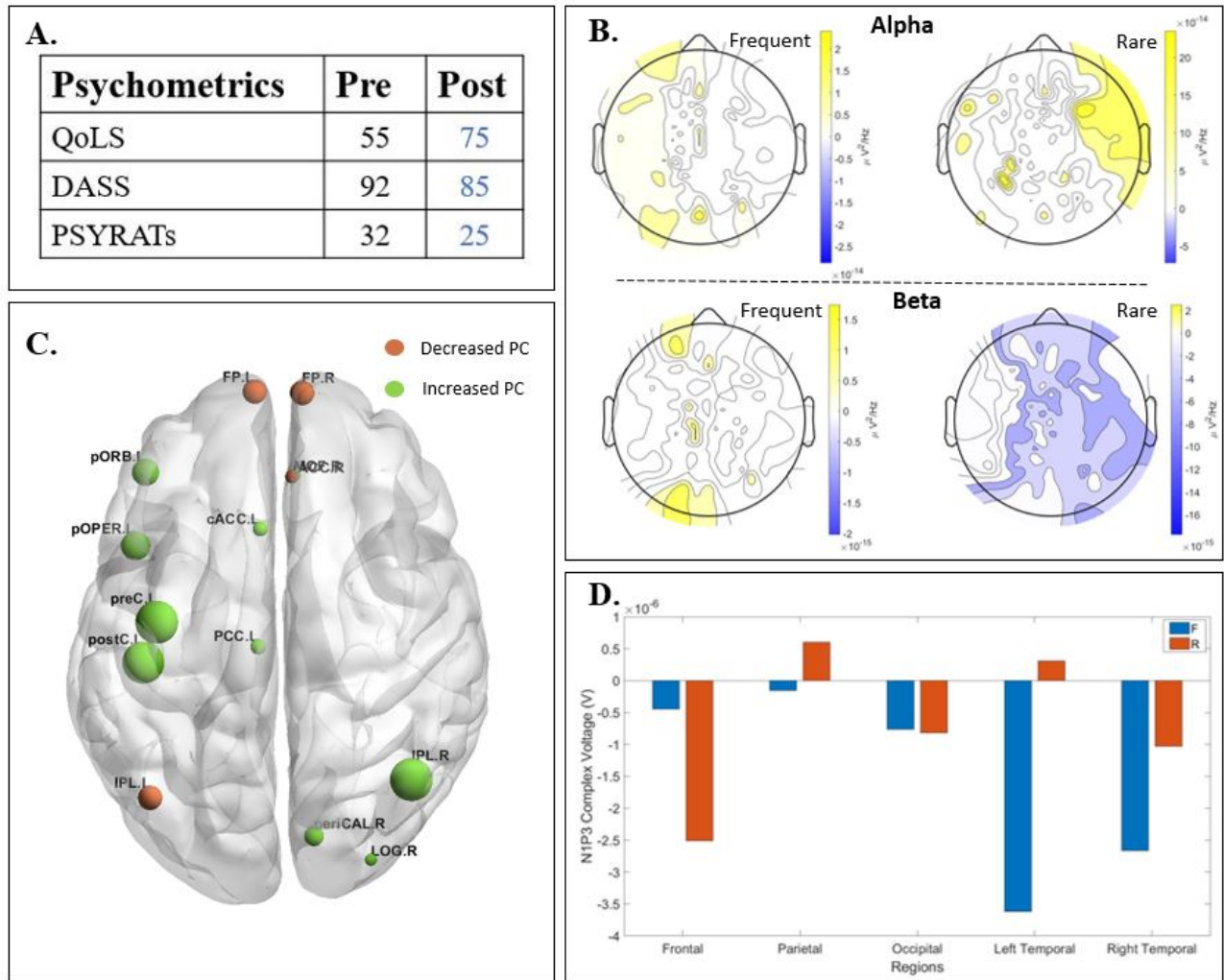
Figure 3.3: Results of patient T2 : A. psychometric; B. Scalp-level frequency analysis; C. Source-space connectivity; D. Scalp-level time analysis. The yellow areas in frequency analysis are related to a higher Power Spectral Density (PSD) post-treatment, whereas the blue ones are related to a higher PSD pre-treatment. The size of the node in the connectivity is related to the amount of increase (green) or decrease (orange) participation coefficient (PC) values. The positive bars in time analysis are related to a higher N1-P3 amplitude post-treatment. (QoLS: Quality of Life Scale,DASS: Depression Anxiety Stress Scale ,PSYRATS: Psychotic Symptom Rating Scales)

The psychometric tests (Figure 3.3A) show an improvement of the quality of life post-treatment, a decreased DASS after TMS and decreased PSYRATS post-treatment. The temporal analysis (Figure 3.3D) showed a lower N1-P3 amplitude post-treatment, except for the parietal and left temporal parts. The PSD (Figure 3.3B) showed higher alpha power post-TMS. However, the beta power is lower post-TMS. The connectivity (Figure 3.3C) revealed a clear higher participation coefficient (represented by the larger green nodes), especially in the left central, left orbito-frontal and the right occipital brain regions. The frontal area showed a relatively lower participation coefficient.

3.4.2.2 Patient C3

Patient C3 (Figure 3.4) is a woman with paranoid schizophrenia, in the CG, who tool part in the study while taking : aripriprazole, olanzapine, chloroprothixene and pregabalin.
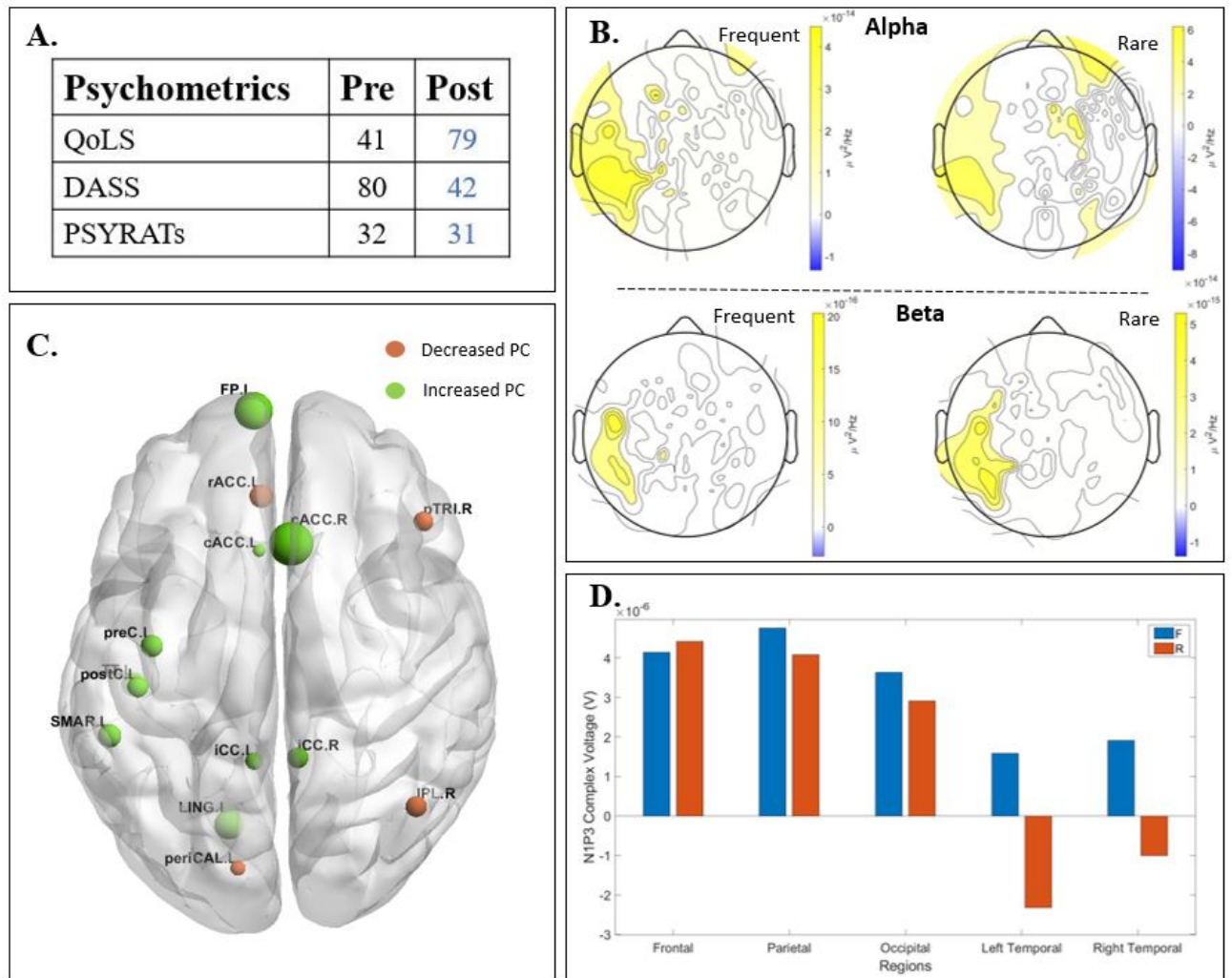
Figure 3.4: Results of patient C3 : A. psychometric; B. Scalp-level frequency analysis; C. Source-space connectivity; D. Scalp-level time analysis. The yellow areas in frequency analysis are related to a higher Power Spectral Density (PSD) post-treatment, whereas the blue ones are related to a higher PSD pre-treatment. The size of the node in the connectivity is related to the amount of increase (green) or decrease (orange) participation coefficient (PC) values. The positive bars in time analysis are related to a higher N1-P3 amplitude post-treatment. (QoLS: Quality of Life Scale,DASS: Depression Anxiety Stress Scale ,PSYRATS: Psychotic Symptom Rating Scales)

The psychometric outcome (Figure 3.4A) revealed an improvement after the treatment. The quality of life increased, the DASS decreased, while the PSYRATS did not change. The time domain analysis (Figure 3.4D) showed a higher amplitude of the N1-P3 complex after the treatment, except on the temporal regions for the rare stimulus. The PSD (Figure 3.4B) showed higher alpha power post-TMS, except from the right temporal region for both frequent and rare stimuli. The beta band also showed a

higher PSD post-TMS. Finally, the connectivity study (Figure 3.4C) displayed a globally improved participation coefficient, principally in the frontal, occipital and central areas of the brain.

3.4.3   Study case 2 : stagnation in psychometric score

The patient detailed in this section presented a stagnation in her psychometric score post treatment (Figure 3.5A). We chose to describe her in this section in order to find a potential correlation with the neurophysiological data.

3.4.3.1   Patient C2

Patient C2 (Figure 3.5) is a woman with paranoid schizophrenia, in the CG, who took part in the study while taking : clozapine, flupenthixol, zopiclone, mirtazapine, escitalopram, metoprolol and chlorpomazine.

The psychometric data (Figure 3.5A) showed that the treatment did not have a lot of impact on this scale. The quality of life, the DASS and the PSYRATS remained more or less the same. The time domain (Figure 3.5D) showed a global increase of N1-P3 amplitude post-TMS, except for the parietal region for both stimuli and the frontal region for the frequent stimulus. The PSD analysis (Figure 3.5B) showed higher alpha and beta power post-TMS (with the exception of frontal frequent stimulus responses in the alpha band). The connectivity analysis (Figure 3.5C) revealed a balanced participation evolution. Globally the left hemisphere (mainly the entorhinal and frontal) showed a decreased participation coefficient, and the right areas (mainly the frontal and occipital) showed an increased participation coefficients.

3.4.4   Study case 3 : decrease in psychometric score

The patient detailed in this section presented a decrease in their psychometric score post treatment. We chose to describe him due to his lower values in the neurophysiological data post treatment (Figure 3.6A), in order to find a potential correlation between those two outcomes.

3.4.4.1   Patient T5

Patient T5 (Figure 3.6) is a man with paranoid schizophrenia, in the TG, who took part in the study while taking : clozapine, flupenthixol, zopiclone, mirtazapine, escitalopram, metoprolol and chlorpomazine.

The psychometric data (Figure 3.6A) showed very little effect of treatment on this scale. The quality of life remained the same, the DASS increased and the PSYRATS slightly increased. The time domain (Figure 3.6D) showed a global decrease of N1-P3 amplitude post-TMS, except for the parietal region for the rare stimulus. The PSD analysis (Figure 3.6B) showed a lower alpha power post-TMS, except for the right temporal region. The beta power decreased as well, except for the right temporal region for the frequent stimulus. The connectivity analysis (Figure 3.6C) showed a
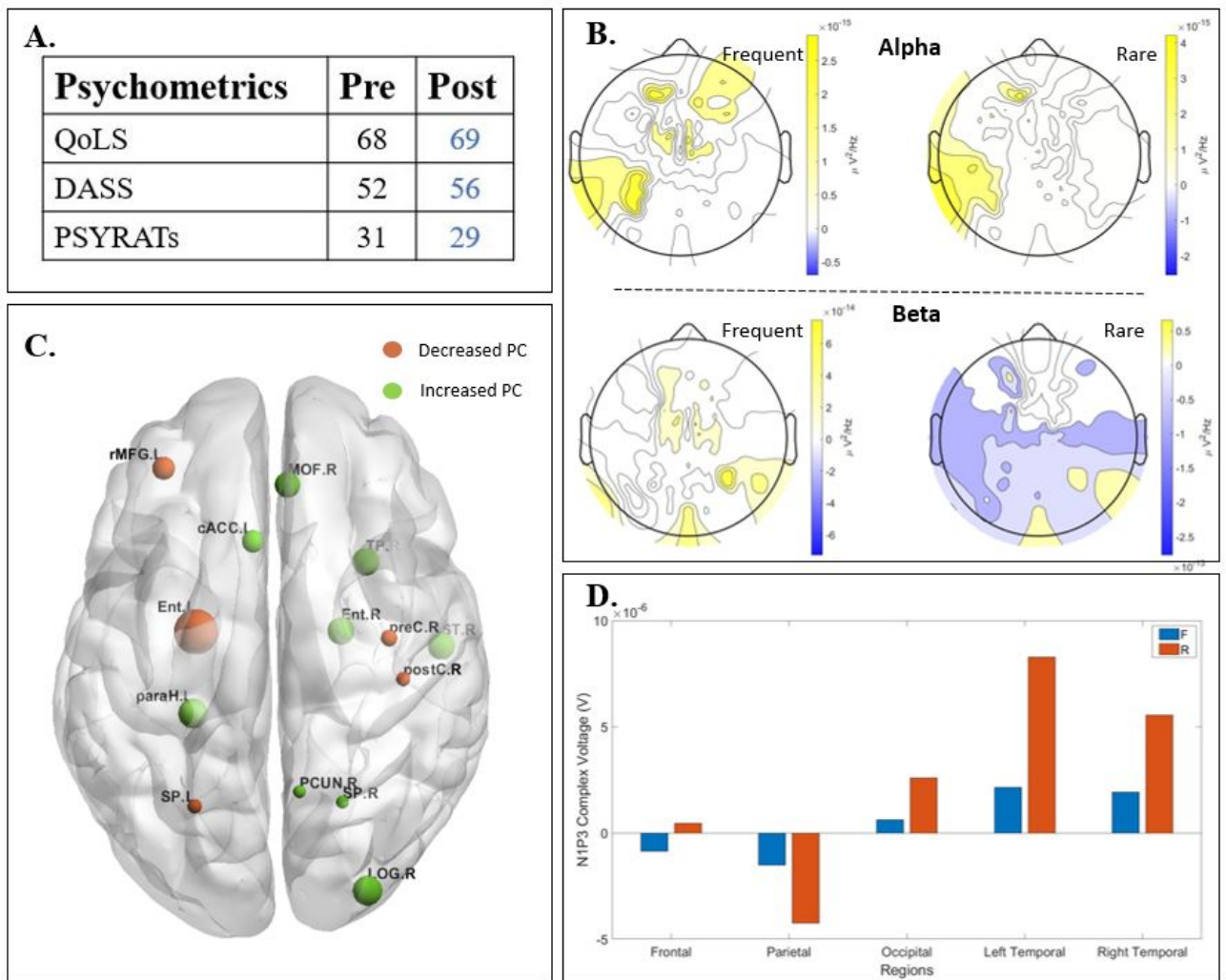
Figure 3.5: Results of patient C2 : A. psychometric; B. Scalp-level frequency analysis; C. Source-space connectivity; D. Scalp-level time analysis. The yellow areas in frequency analysis are related to a higher Power Spectral Density (PSD) post-treatment, whereas the blue ones are related to a higher PSD pre-treatment. The size of the node in the connectivity is related to the amount of increase (green) or decrease (orange) participation coefficient (PC) values. The positive bars in time analysis are related to a higher N1-P3 amplitude post-treatment. (QoLS: Quality of Life Scale,DASS: Depression Anxiety Stress Scale ,PSYRATS: Psychotic Symptom Rating Scales)

globally higher participation coefficient in the right frontal, left central and occipital brain regions.

3.5 Discussion

The present work aimed to develop hypothesis to assess the effects of TMS in schizophrenia with AVH, analysing EEG data and psychometric outcome. This was based on three different approaches : temporal size (with the calculation of N1P3 complex amplitude), spectral (with the evaluation of the PSD in several frequency bands (theta,
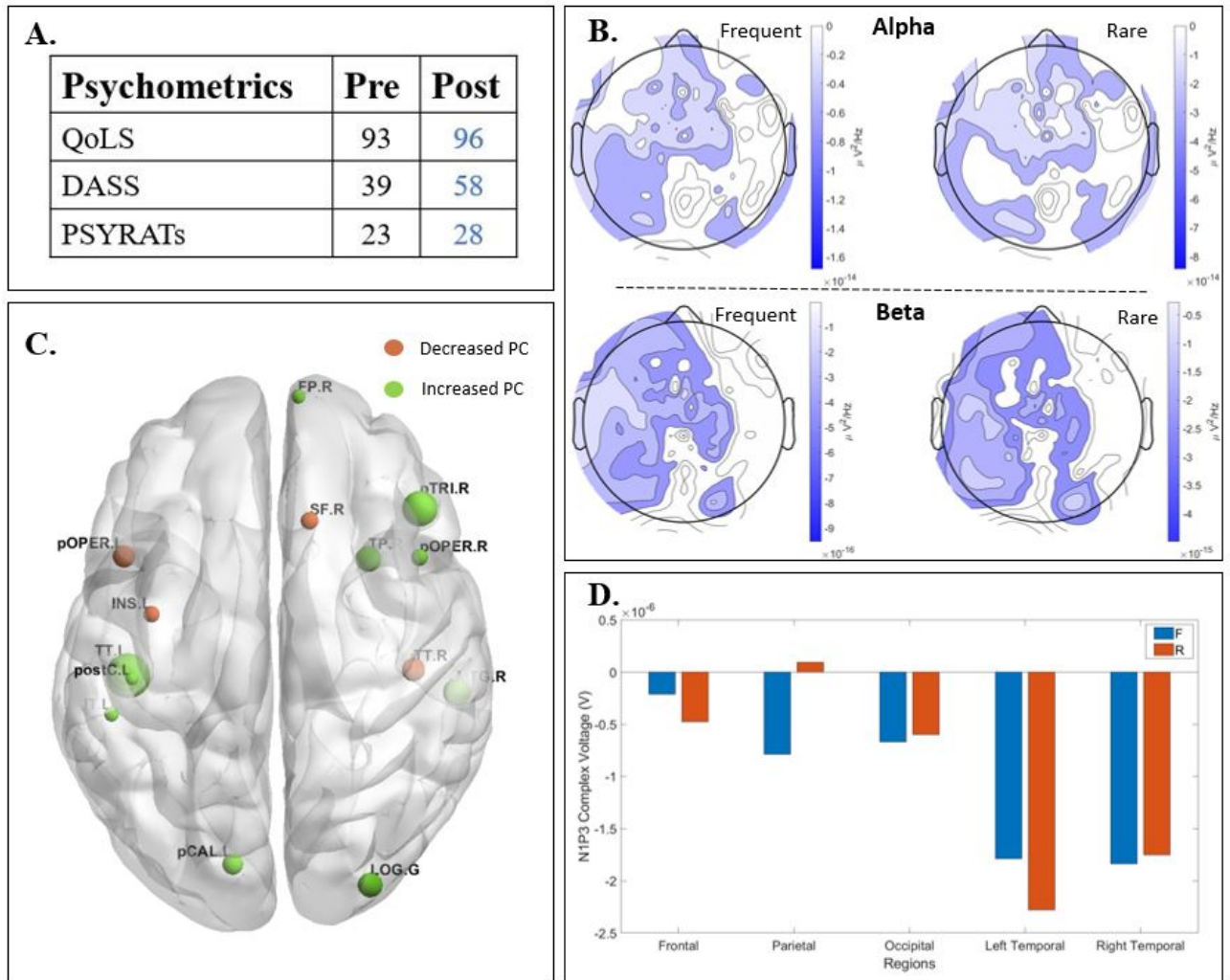
Figure 3.6: Results of patient T5 : A. psychometric; B. Scalp-level frequency analysis; C. Source-space connectivity; D. Scalp-level time analysis. The yellow areas in frequency analysis are related to a higher Power Spectral Density (PSD) post-treatment, whereas the blue ones are related to a higher PSD pre-treatment. The size of the node in the connectivity is related to the amount of increase (green) or decrease (orange) participation coefficient (PC) values. The positive bars in time analysis are related to a higher N1-P3 amplitude post-treatment. (QoLS: Quality of Life Scale,DASS: Depression Anxiety Stress Scale ,PSYRATS: Psychotic Symptom Rating Scales)

alpha, beta and gamma)) and connectivity, (with the calculation of the participation coefficient in beta and gamma band).

The general results from our study revealed a high variability between individuals, in both groups. This can be explained in several ways : Firstly, subjects were taking a range of medications all of which can interfere with the background neural activity and the generation of ERPs ([130]). Secondly, the long and tiring recording procedure (around one hour), and the different states of the patients during the protocol could also have led to varying data quality. Indeed, [131] highlights the fact that background EEG variation contributes significantly to a high P300 individual variability.

However, there were some indications of improvement in the psychometric results, in four out of five subjects in TG and three out of five in CG. Half of our subjects (six

out of ten, four CG, two TG) showed an increase of the N1-P3 amplitude after the treatment, especially for the rare stimulus. [110] and [108] established that patients with schizophrenia and AVH presented an inhibition to the P300 experiment. Thus, the clearer presence of N100 and P300 waves post-TMS, which is a known response to the auditory oddball task ([132]), suggested a response to TMS. Likewise, the spectral analysis displayed an increase of the PSD in alpha and beta bands for six subjects (4 in CG, 2 in TG). [133] demonstrated that those bands were directly linked to attention, focus, emotional and cognitive processes. A higher power in these bands could be indicative of a change in those mechanisms. Finally, our brain connectivity results showed a global increased participation coefficient in the beta band after treatment, for six subjects (3 in TG, 4 in CG). These results lead us to the conclusion that TMS seemed to have a positive impact on the patients, in both groups. However, it is not possible to assume that the location where the treatment was applied had a different impact on the brain function. The results in connectivity analysis show indeed an improved participation coefficient thus a better network integration independently from the group. Therefore, we discussed the results without regard to the patients' group. We chose to underline in the results section some patients that showed an agreement between the psychometric scores and our neurophysiological data.

It is interesting to note that for patient C3, where the psychometric results were better post-TMS, all three neurophysiological components used for this study revealed a higher value post-TMS. For this patient, there seems to be a clear link between clinical and neurophysiological outcomes. For T2, the trend is there, but is less obvious, with half of the neurophysiological results being in concordance with the improved psychometric score. Conversely, patient T5 had a deterioration in their psychometric post-TMS, and the same tendency is visible in their neurophysiological data,

Although there was significant dissociation between clinical and neurophysiological outcome, the participation coefficient from the connectivity analysis was the parameter that seemed to interact most closely with the psychometric results, followed by alpha power. Concerning the connectivity analysis, our results showed an increased network integration in some brain regions and a slight decrease in other regions, different for every patient. This reconfiguration of the brain network has been widely reported in the literature when stimulating the brain using electrical and magnetic means, and is also present in several brain disorders ([134]). The increased network integration may be related to better information processing in the human brain and more efficient networks. This increase in network integration was associated with a decrease in this same integration in other brain regions, reflecting the inter-subject variability. Although the small sample size did not allow us to test statistical significance, we showed a clear 'trend' of reshaping of the functional brain network between the different conditions. The frequency analysis revealed the most interesting changes in power spectrum, mainly in the alpha and beta bands. There was higher alpha power post-TMS, which is less prominent but still visible in the beta power. The gamma and theta power did not show any clear trends. The fact that alpha and beta bands are directly linked to attention, focus and emotional tasks ([133]) is interesting. A higher power post-TMS linked with a better score in the psychometric scale could indicate that the improvement of these cognitive mechanisms was directly linked to the progress of the patient's clinical condition. Due to our small sample size, this has to be put in perspective, and nothing definitive can be assessed. However, there was a "trend" of an increase in alpha and beta powers post-TMS that is linked with an improvement in the clinical outcome. Finally, the time domain was the area of analysis presenting the most vari-

ability. Half of the patients presented a higher N1-P3, especially in the rare stimuli, but no clear trend was established between this outcome and the clinical outcome. However, due to its conclusive results in studies related to schizophrenia with AVH ([112],[113],[114]), our small number of subjects, as well as its subject inter-variability ([131]), it is a paradigm that should be taken in account in further studies.

Considering the fact that psychometric tests are a semi-self assessment evaluation of patients condition, this work is a first step towards a development of a hypothesis to correlate and validate psychometrics with quantitative neurophysiological data. We suggest further investigation of any link between psychometrics and neurophysiological data under the umbrella of TMS, focusing mainly on the participation coefficient in the beta band and the power spectral density in alpha band. The beta power as well as the N1-P3 amplitude should also be considered of interest.

3.5.1 Limitations

The study has many limitations. Firstly, due to the very small sample size, it was not possible to assess our results definitively. Rather, we aimed to discover trends in order to generate hypotheses for further study. Secondly, the patients were also undergoing their usual treatment, including antipsychotic and sedative medications. This did not change between pre- and post-rTMS conditions but might have influenced the background neural activity and the generation of the ERPs ([130]). Thirdly, the experimental procedure was long (1 hour) and tiring and some patients had difficulty cooperating and maintaining task engagement, which may have affected data quality. Muscle and movement artifacts added noise to the EEG signal, requiring a thorough pre-processing and the exclusion of many trials. We encourage similar experiments with patients in the supine position to reduce the noise and improve the data quality, making them easier to process and analyze. Finally, in this study we only analyzed the oddball auditory paradigm. We recommend pursuing this work using other procedures as well, in order to have a more complete overview of the results.

3.5.2 Future directives

Future studies of rTMS and neurophysiological markers in schizophrenia should recruit larger number of participants than the present study. The possible association of AVH and other symptoms of schizophrenia with variations in P300, PSD and other EEG markers should be studied further. This may help to establish whether the PSD in the alpha and beta bands, the N1-P3 complex and the participation coefficient in beta bands are reliable biomarkers of the neural response to TMS in patients with schizophrenia and AVH.

3.6 Conclusion

After conducting TMS, most patients showed an evolution in psychometric data as well as on the neurophysiological quantitative data, independent of the stimulation site. We examined the interplay between the psychometric and the neurophysiological data. When the psychometric improved post-TMS, we could observe an increased network integration mainly, through the participation coefficient in the beta bands, a higher alpha and beta band power, and sometimes a higher N1-P3 amplitude. Due

to the small sample size, it is not possible to assess definitively the impact of TMS on the brain function in schizophrenia, nor the correlation between psychometric and neurophysiological data. However, our results suggest that brain connectivity, through the participation coefficient, alpha and beta power bands, were highly related with the psychometric score, and that N1-P3, despite his variability, should be investigated. This hypothesis will have to be verified in further studies, with a larger sample size, and an improved recording procedure, leading to a better data quality. This is a first step toward the definition of quantitative neurophysiological parameters to assess TMS treatment.

Chapter 4

Quantitative neurophysiological evaluation of postural control

4.1 Background

4.1.1 Definition

Postural control is a central nervous system (CNS) feedback control system that governs human upright stance and gives a platform for locomotion and task-driven behavior, as well as several autonomic responses [135]. Several studies have shown that PC can be affected by a lot of factors. General and local muscular fatigue is provoking PC disturbance, leading to compensating PC response to react to this fatigue [136]. Cognitive processing is mandatory to maintain balance and keep a good PC. The amount of processing depends on the required task. Alteration to a system (muscular, neural, or neurophysiological) involved in maintaining PC, due any type of condition, fatigue, or pathology, will concretely affect PC and lead to balance problem. There are significant differences in age-related PC studies, proving that older people get more postural instability , thus explaining the relationship between the amounts of falls and age [137], [138]. However, this problem can be counterbalanced by developing physical training strategies, as a study shows that targeting specific training helps to improve balance control system in dynamic and static tasks. Several diseases or pathologies are affecting the neural and muscular system, consequently provoking PC disturbance. Nonetheless, PC being a combination of several mechanisms, there are a lot of available tools to study, investigate and assess neurophysiological parameters during experiments triggering PC disturbance. First, as stated before, PC is a CNS system involving cognitive processing. Previous studies conducted in our lab showed the importance and role of cortical recruitment associated with PC tasks [139], [140]. Using EEG, brain signals are recorded during PC tasks. Those signals can be analyzed in terms of time, frequency, and network dynamics, to identify neurological markers of PC engagement.

4.1.2 Context of the research study

We developed a PC paradigm called BioVRSea. It consists of a multimetric platform based on a VR system that dynamically visualizes an open sea environment. The application CinetoVR is used to simulate the sea environment that the subject sees through VR glasses. To make the experience even more realistic, a combination of a

simulation platform from MotionSystems and two static force plates from Virtualis is currently used. Figure 4.1 illustrates the global setup.
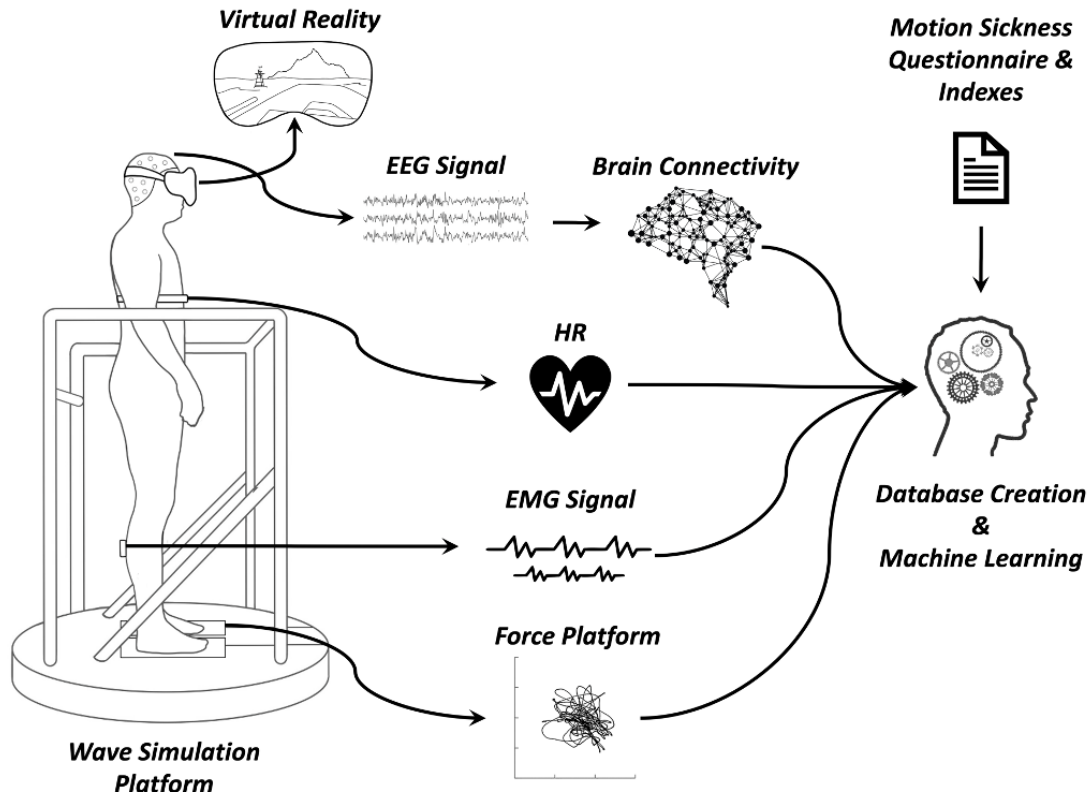
Figure 4.1: BioVRSea global setup

BioVRSea is a complex dynamic postural task, whose results will be presented in chapter 4. Our work focused on defining a reference neurophysiological behaviour based on a healthy population, as well as the development of novel metrics to quantify brain networks dynamics. It is a first step towards the development of tools with a further aim to assess and quantify subjects suffering from neurophysiological disorders affecting their balance.

4.2   Exploratory studies

This section relates the exploratory works performed during this thesis. They were investigated as a proof of concept of BioVRSea paradigm as multimetric solution to assess motion sickness, postural control, and how it can help in pathologies differentiation. Each subsection is adapted from a published or under review study. Those exploratory works comports several biosignals analysis, but only EEG will be detailed in the following sections. The other biosignals analyses can be found in the related publications.

4.2.1 Exploratory study 1: Toward Predicting Motion Sickness Using Virtual Reality and a Moving Platform Assessing Brain, Muscles, and Heart Signals

This work is adapted from a study published in *Frontiers in Bioengineering and Biotechnology* [141]. The aim of this study was to extract parameters from different biosignals (EEG, EMG and heart rate), and prediction motion sickness based on a questionnaire index.

4.2.1.1 Introduction

Postural control and motion sickness are intricately linked. Postural control is a central nervous system feedback control system, that regulates upright stance and carries out mobility and motor related tasks. It is based on the constant information obtained from viusal, vestibular, proprioceptive and somatosensory receptors [135]. Postural control system can be disturbed in several ways, and one of them is a physiological overstimulation, that can lead to motion sickness. Motion sickness is endured during passing travel, and one of its most famous occurrence is seasickness [142]. Motion sickness is a poly-symptomatic illness, from nausea and vomiting to salivation, sweating, dizziness [143]. Despite all the current knowledge regarding this condition, the cause of motion sickness remains uncertain, as two main theories emerged to identify its origin. The first one is the sensory conflict theory, stating that motion sickness relies on conflict between the visual, vestibular input and the somatosensory input [144]. For instance, in case of passive travel in a car, the physical motion experienced by the vestibular system does not match the visual input. The second theory is the postural control theory, stating that an extended period of postural control instability is causing motion sickness [145]. Nevertheless, since motion sickness and postural control are related to the central nervous system, it is possible to study those phenomenons by measuring the associated physiological signals. Studies have shown the use of EEG, EMG, heart rate, center of pressure to be of great use for evaluating motion sickness levels [146], [147]. On another hand, motion sickness susceptibility is usually assessed from a questionnaire, based on symptoms evolution or previous experiences of motion sickness [148], [149]. This study introduces a novel motion sickness and postural control paradigm called BioVRSea. This device aims to replicate the situation of a boat at sea, combining virtual reality and a moving platform (figure 4.2). This multimetric (EEG, EMG, heart rate) device tool is completed by a questionnaire self-assessing symptoms of motion sickness after the experiment. The aim of this exploratory work was to validate the use of BioVRsea in postural control and motion sickness studies, and to correlate motion sickness symptoms with biosignals metrics.

4.2.1.2 Material and methods

The biosensors used in this study are 64-channel EEG, 2-channel EMG, and HR chest monitor. This study is based on data acquired from 28 subjects (age: 23.8 $\pm$ 1.2), 22 women and 6 men (ethic approval by the Icelandic Bioethics Commission – Number: VSN-20-101 – May 2020). Each participant was measured three times (except one subject who underwent only two protocols) using different protocols based on the amplitude and frequency of the simulated waves. From each protocol, we extracted 19 parameters associated with HR, EEG, and EMG signals. After every protocol,
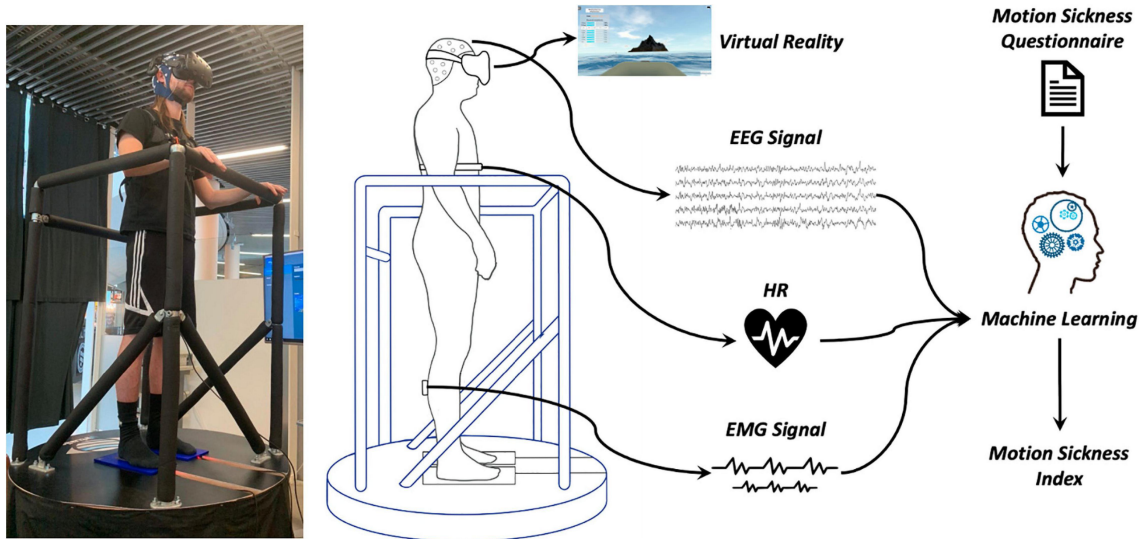
Figure 4.2: BioVRSea setup: the moving platform, shown in a photo with a subject on the left, is combined with a rough sea VR scenario and with EEG, EMG, and HR bio-signal acquisition.

the subject answers the Motion Sickness Susceptibility Questionnaire (MSSQ) [143] based on the self-evaluation of 13 different neurophysiological conditions. A total of 83 datasets [(28 × 3) - 1] constitute the final database of our study.

Measurement's protocols   Three different protocols were implemented in this study 4.3.
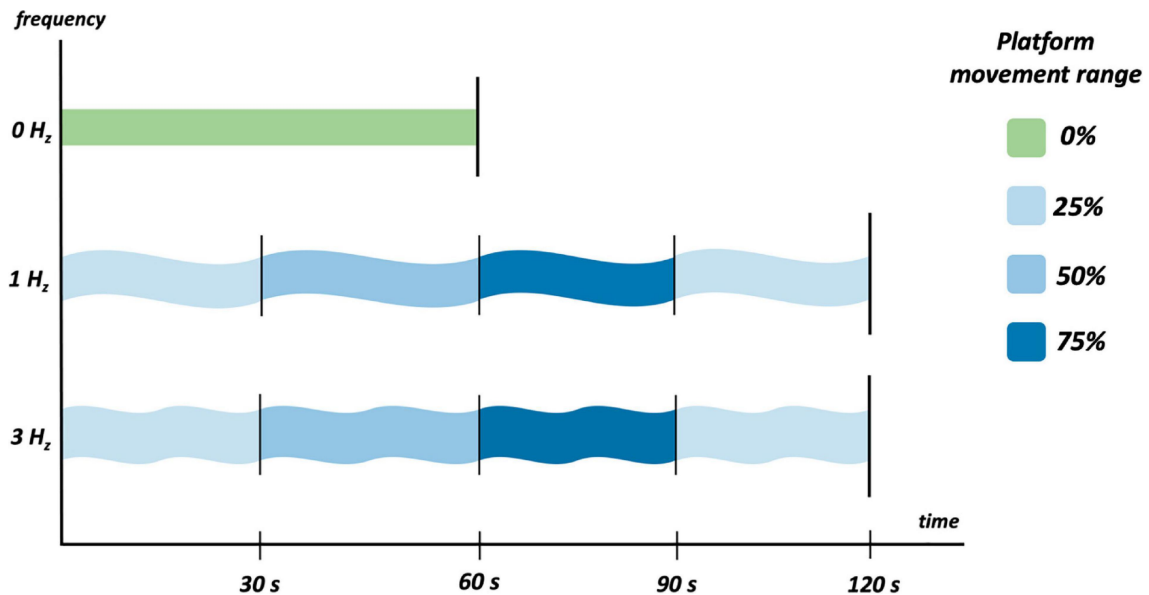
Figure 4.3: The three acquisition protocols that each patient has been subjected to.

• 0 Hz, null wave amplitude. Sea simulation is not performed during this protocol. The subject remains in an upright position on the platform for 60 s, observing mountains surrounded by lights in a dark environment through the goggles.

• 1 Hz, and wave amplitude = 0.6. This sea simulation protocol is divided into four parts, 30 s each with different platform movement amplitudes: 25, 50, 75, and

again 25%. Total time: 120 s.

- 3 Hz, and wave amplitude = 0.5. This sea simulation protocol is divided into four parts, 30 s each with different platform movement amplitudes: 25, 50, 75, and again 25%. Total time: 120 s.

The first protocol mentioned (0 Hz) is the non-movable (platform stable) pre-test (baseline) sampling where the subjects can relax. This is done before the other two protocols (1 and 3 Hz) where the subjects during the movements have to grab onto the protection bars that they have in front. The eyes must be opened during all the three protocols.

Data acquisition   During each protocol, heart, muscle, and brain data were acquired using the following technologies:

- HR was measured using a heart chest sensor (Polar Electro, Kempele, Finland, sampling frequency of 1,000 Hz). Two features were computed from this signal: mean and standard deviation.

- Muscle electrical activities from the lower limbs were acquired using two wireless EMG sensors (sampling frequency of 1,600 Hz) placed on the gastrocnemius of each leg (Kiso ehf, Reykjavik, Iceland). Twelve features were extracted from this signal.

- Brain electrical activity was measured using a 64-channel dry electrode cap (sampling frequency of 500 Hz) from AntNeuro, Hengelo, Netherlands.

EEG data pre-processing and analysis were performed with Brainstorm [124] and Matlab 2020b. The data were re-referenced using the common average reference. A high-pass and a low-pass filter were set, respectively, from 0.1 and 40 Hz. Bad channels were manually removed when EEG voltage was higher than 300 μV. If more than 20% of the channels showed too much noise or incorrect signal, the whole trial was rejected. The signals were digitized in segments of 30 s, within 1Hz and 3Hz protocols. DC offset correction was performed, and baseline correction was applied using the 0-Hz segment. Channels marked as bad were removed and interpolated. Individual trials were visually inspected and rejected when indicative of excessive muscle activity, eye movements, or other artifacts.

The PSD was computed for each epoch with Welch's method, with the following frequency bands: delta (0.5–4 Hz), theta (4–8 Hz), alpha (8–13 Hz), beta (13–35 Hz), and low gamma (LG) (35–40 Hz). The relative power of each band was then computed and averaged across all channels, obtaining a total of five EEG-related features.

Figure 4.4 sums up the 19 features extracted from the different biosignals.

Motion sickness Indexes   At the end of every protocol the subjects were asked to fill out a questionnaire regarding their MS symptoms. The questionnaire is based on the MSSQ proposed by Golding [143]. The subjects must give a score between zero and two for 13 typical MS symptoms: general discomfort, dizziness and vertigo, stomach awareness, sweating, nausea, salivation, burping, headache, fullness of head,

Biometric parameter	Description
EEG – Delta	Relative power spectra between frequency band 0.5–4 Hz
EEG – Theta	Relative power spectra between frequency band 4–8 Hz
EEG – Alpha	Relative power spectra between frequency band 8–13 Hz
EEG – Beta	Relative power spectra between frequency band 13–35 Hz
EEG – LG	Relative power spectra between frequency band 35–40 Hz
EMG – L area	Integral of the rectified EMG signal of left gastrocnemius divided by the sample size
EMG – R area	Integral of the rectified EMG signal of right gastrocnemius divided by the sample size
EMG – L 40-132	Left gastrocnemius relative PSD in the 40–132 Hz frequency band
EMG – L 132-224	Left gastrocnemius relative PSD in the 132–224 Hz frequency band
EMG – L 224-316	Left gastrocnemius relative PSD in the 224–316 Hz frequency band
EMG – L 316-408	Left gastrocnemius relative PSD in the 316–408 Hz frequency band
EMG – L 408-500	Left gastrocnemius relative PSD in the 408–500 Hz frequency band
EMG – R 40-132	Right gastrocnemius relative PSD in the 40–132 Hz frequency band
EMG – R 132-224	Right gastrocnemius relative PSD in the 132–224 Hz frequency band
EMG – R 224-316	Right gastrocnemius relative PSD in the 224–316 Hz frequency band
EMG – R 316-408	Right gastrocnemius relative PSD in the 316–408 Hz frequency band
EMG – R 408-500	Right gastrocnemius relative PSD in the 408–500 Hz frequency band
HR average	Heart rate average
HR std	Heart rate standard deviation

Figure 4.4: Description of the 19 biometric parameters that compose the database

blurred vision, fatigue, eye strain, and difficulty focusing. We define a total of eight binary indexes considering the MSSQ answers.

General discomfort (IGenDis, 1st) and Dizziness and Vertigo (IDizz, 2nd) are considered as independent and individual indexes. Stomach awareness, sweating, nausea, salivation, and burping are considered together as stomach-related to create the Stomach-related Index (IStom, 3rd). Headache, fullness of head, and blurred vision together produce the Head Index (IHead, 4th) while fatigue, eye strain, and difficulty focusing contribute to the Fatigue Index (IFatig, 5th). IStom, IFatig, and IHead are computed as binary indexes following these steps: first, we compute the average from the individual responses of each index; second, we calculate the maximum among the averages; and third, we divide the cohort into two groups (below and above 1/3 of the maximum). For IGenDis and IDizz, we apply only steps 2 and 3 using the direct response instead of the average.

Moreover, we established two more indexes, Physiological/Vegetative Index (IPV, 6th) and Neurological/Muscle Strain Index (INM, 7th). IPV is based on the previously outlined steps from the responses from sweating, salivation, nausea, burping, stomach awareness, and general discomfort conditions. Similarly, the INM is based on fatigue,

eye strain, difficulty focusing, headache, fullness of head, blurred vision, and again general discomfort conditions.

The last index is called Motion Sickness Index (IMS, 8th), and it is based on the weighted sum SumMS of all the MSSQ answers (Eq. 4.1) and steps 2 and 3.

$$SumMS = (0, 2.GenDisc + 0, 2.DizzVert$$
$$+0, 2. \sum(StomAwe, Nausea, Sweat, Saliv, Burp)+0, 2. \sum(Fatigue, EyeStr, DiffFocus)$$
$$+ 0, 2. \sum(Headache, FullHead, BlurrVis)) \quad (4.1)$$

Statistical analysis All the parameters extracted from EEG, EMG, and HR underwent a non-parametric statistical univariate explorative analysis in order to understand whether there was a statistically different grouping by IGenDis, IDizz, IStom, IHead, IFatig, IPV, INM, and IMs. All the indexes underwent univariate statistical analysis through the Mann–Whitney test.

Machine learning tools The ML analysis was performed by using KNIME Analytics Platform (v. 4.2.0). The following algorithms were implemented through the platform: Random Forests (RF), Gradient Boosting tree (GB), Ada-Boosting of decision tree (ADA-B), Support Vector Machine (SVM), K Nearest Neighbor (KNN), and Multilayer Perceptron (MLP).

The most employed evaluation metrics were used to assess the performance of the algorithms into the classifications tasks: accuracy, sensitivity, specificity, and Area Under the Curve Receiver Operating Characteristics (AUCROC). All these metrics were computed using the K-Fold Cross Validation with k = 10 using 10 different seeds. This means that the database is divided into 10 groups and each of them is used in turn as the test group while the other nine are used for the training of the model. Using 10 different seeds allows the creation of different 10-fold divisions, which allows a better exploration of the database and achieving the best results.

4.2.1.3 Results

Figure 4.5 shows the results of the statistical tests that assess the significance of the 19 parameters with the eight binary MSSQ indexes. Interestingly, only 4 out of 19 parameters never show a significance.

The EEG Beta and LG showed significance only for the individuals suffering from headache, fullness of head, and blurred vision (IHead), while no other significance were found for an EEG parameter.

The feature importance analysis (Figure 4.6) shows that parameters extracted from EMG were the most important ones by far for the classification of both indexes. The first EEG-based features can be found in the 5th place in the ranking while the first HR-based features can be found after the 10th place.

This feature importance analysis highlights low importance of all the features extracted from the EEG, they were below the seventh place in the final ranking (this also for the other indexes except EEG-Beta which is quite relevant for IPV and INM). This can be explained by the fact that a dry cap EEG was used for the acquisition. More noise was detected and led to a lower signal quality. Channels had to be rejected

	I_{GenDis}	I_{Stom}	I_{Fatig}	I_{Head}	I_{Dizz}	I_{PV}	I_{NM}	I_{MS}
EEG – Delta	0.734	0.903	0.790	0.383	0.841	0.529	0.993	0.667
EEG – Theta	0.934	0.880	0.388	0.613	0.400	0.927	0.184	0.181
EEG – Alpha	0.713	0.865	0.769	0.620	0.577	0.560	0.971	0.888
EEG – Beta	0.393	0.510	0.236	0.050*	0.194	0.105	0.130	0.335
EEG – LG	0.508	0.247	0.229	0.029*	0.070	0.087	0.081	0.217
EMG – L area	0.114	**0.001***	0.004**	**0.001***	**0.001***	**0.001***	**0.001***	**0.001***
EMG – R area	0.157	0.004**	**0.001***	**0.001***	**0.001***	0.004**	**0.001***	**0.001***
EMG – L 40–132	0.274	0.029*	0.006**	**0.001***	**0.001***	0.040*	0.004**	0.011**
EMG – L 132–224	0.941	0.492	0.274	0.079	0.165	0.444	0.285	0.449
EMG – L 224–316	0.247	0.031*	0.006**	**0.001***	**0.001***	0.090	0.010**	0.013**
EMG – L 316–408	0.236	0.025*	0.012**	0.003**	**0.001***	0.043*	0.003**	0.011**
EMG – L 408–500	0.286	0.023*	0.029*	0.003**	**0.001***	0.032*	0.002**	0.009**
EMG – R 40–132	0.040*	0.006**	0.003**	**0.001***	**0.001***	0.002**	**0.001***	0.008**
EMG – R 132–224	0.044*	0.027*	0.051*	0.035*	0.015**	0.005**	0.008**	0.100
EMG – R 224–316	0.079	0.026*	0.012**	0.007**	0.002**	0.037*	0.007**	0.040*
EMG – R 316–408	0.139	0.030*	0.006**	**0.001***	**0.001***	0.039*	0.003**	0.012**
EMG – R 408–500	0.118	0.020*	0.003**	**0.001***	**0.001***	0.018*	**0.001***	0.003**
HR average	**0.001***	0.219	0.082	0.314	0.012**	0.037*	0.010**	0.042*
HR std	0.040*	0.451	0.213	0.149	0.251	0.264	0.249	0.136

*Significant at 0.05. **Significant at 0.01. ***Significant at 0.001.

Figure 4.5: Significance of the 19 biometric parameters calculated with the univariate statistical analysis (Mann–Whitney test) for all the eight indexes.
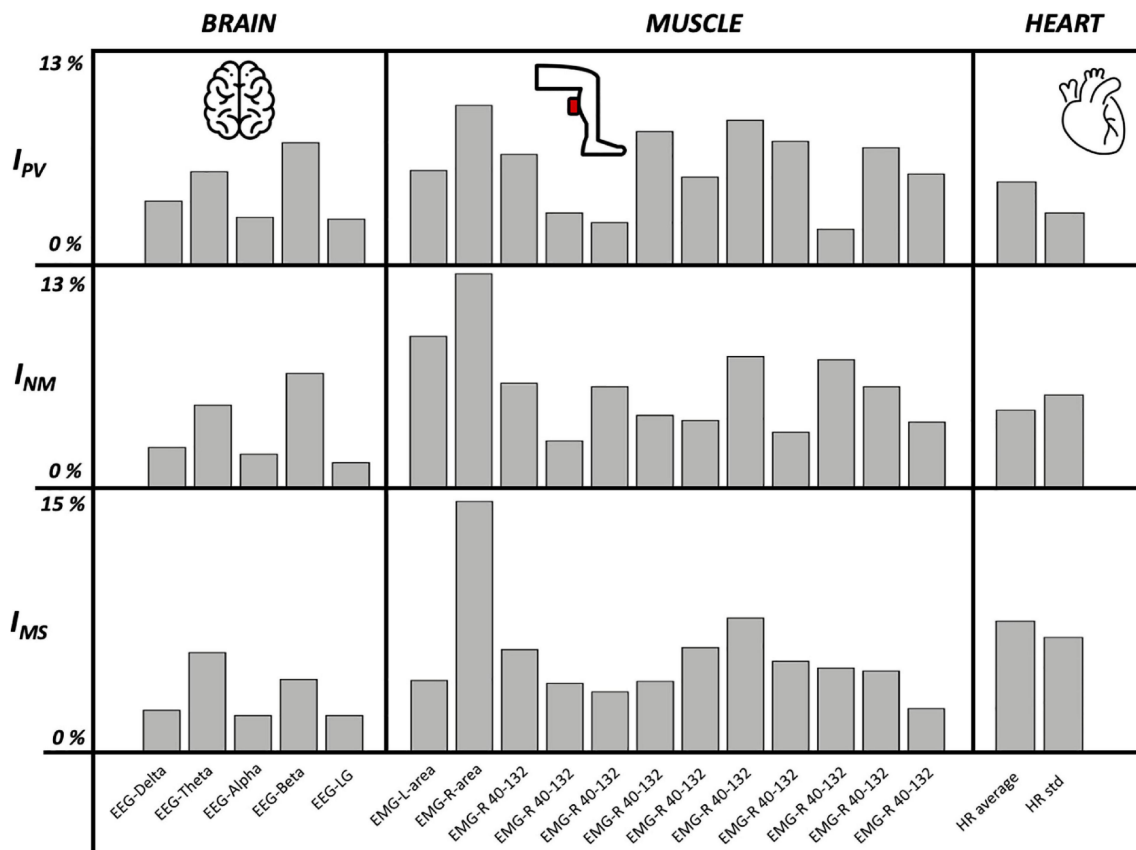
Figure 4.6: Brain, muscle, and heart feature importance for IPV, INM, and IMS using Random Forest algorithm.

and could not be interpolated, leading to an averaged PSD on less channels. This can be one of the reasons of the low significance related to EEG features.

4.2.1.4 Discussion

In this study, we use the BioVRSea research setup and focus on EEG, EMG, and HR bio-signals associated with subjective MS symptoms. Our EEG-coupled results show significant difference in brain neural networking in individuals indicating subjective symptoms of headache, fullness of the head, and blurred vision (IHead). In an earlier study, we showed that open eyes trials reflect a greater number of significant differences in EEG absolute spectral power across all bands during both adaptation and habituation. This suggests that following both acute and prolonged proprioceptive perturbation, cortical activity may be up-regulated with the availability of visual feedback [139]. These results generally support our prior hypothesis that the visual recognition of instability may play a critical role in governing cortical processes requisite for PC [140]. These results underline the importance of visual information in PC and simultaneously open up the VR afferent link in PC perturbations. Being able to couple these subjective symptoms, i.e., headache, fullness of the head, and blurred vision, to objective intracranial activity is crucial in clinical context and opens up ways for VR-coupled biosignal evaluation of PC pathologies [150]. This is in keeping with many other studies performed on motion and CNS triggers of head-related symptoms. Jang et al. [151] identified that the alpha band was linked to VR sickness, with a decrease of the absolute power during the experiment, followed by an increase during the recovery, highlighting a negative correlation with the MSSQ score. Kim et al. [152] detected that in the case of cybersickness, the severity of the symptoms was positively correlated with the delta wave, and negatively with the beta waves. It is interesting to see that, in our study, despite the low significance of EEG regarding the different indexes chosen, the power associated to the beta band is the parameter presenting the most importance in IPV and INM. This corroborates the fact that beta band is related to MS symptoms and is a feature that should be investigated in MS studies. Our results do not enable to drawing of hypotheses regarding the other power bands.

4.2.1.5 Limitations

This study has some limitations. The first is the small number of subjects that limits also the possibility of obtaining higher evaluation metrics in the ML analysis. The second is the type of population that has been analyzed in this research because it was limited regarding age and health status; all the subjects were young and healthy. Further studies could increase the number of subjects, which would allow improvements in the performance of ML and include in the population more diverse subjects. We use dry electrodes for the EEG acquisition resulting in high noise signal, which we believe has limited the value of the associated EEG parameters in both statistical significance and ML. The use of a wet cap EEG for further acquisitions is a potential improvement. Finally, the VR view that the investigated individual visualizes standing on a virtual small vessel is not a true scenario of working environment at sea but is nevertheless capable of creating MS sensation at least in experienced sailors (verbal statements after being on platform).

4.2.2   Exploratory study 2: Towards defining biomarkers to evaluate concussions using virtual reality and a moving platform (BioVRSea)

This work is adapted from a study published in *Scientific Reports* [153]. The aim of this study was to identify potential biomarkers of concussion, based on signals extracted from BioVRsea (EEG, EMG, heart rate, and CoP), and the gold-standard sport concussion assessment questionnaire, SCAT5.

4.2.2.1   Introduction

A concussion, or mild traumatic brain injury (mTBI), is a short-lived functional neurological impairment caused by a blow to the head or by a force transmitted to the head [154]. Participation in sports is a risk factor for sustaining multiple concussions[155]. Symptoms of concussion include headaches, loss of consciousness, amnesia, problems with balance. Although most cases of concussions resolve spontaneously, they can have persistent psychological, physical, and cognitive complications and protracted recovery times. There is currently no objective way to diagnose a concussion1, nor is there a precise, universal concussion definition [156]. When diagnosing concussions, medical professionals rely on clinical assessment, which can be problematic as symptoms are non-specific [157] and could relate to other illnesses, mental or physical. Medical records and clinical interviews are sometimes thought of as the gold standard in concussion research [158], inevitably resulting in a loss of accuracy as many who suffer from a concussion do not seek medical assistance[159]. In research, the Concussion Assessment Tool, fifth edition (SCAT5), has been useful when assessing symptoms after an incident and tracking recovery [157].

It is unclear how changes in neuronal function affect the development of concussion symptoms. Although not routine in clinical practice, neuroimaging might help us understand concussion symptoms and how they relate to functional changes in the brain. Electrophysiological assessments of concussions show promise. Electroencephalography (EEG) serves as a non-invasive method to measure electrical activity, providing insight into brain activity connected to concussion pathology[160] and has been used to identify functional changes in the brain following a concussion[161], [162]. Reduced brain network activation, measured by an EEG, has been related to post-traumatic migraine in concussion patients, possibly indicating symptom severity or persistency [163]. Concussion history has also been related to a change in theta and alpha activity[164]–[166]. However, because methodologies vary between studies, it is challenging to establish EEG markers as return-to-play guidelines[162], [167]. More research into the relationship between EEG and subjective concussion symptoms is needed, as it is important to include assessments using more than visual stimuli. More demanding actions, including physical movement, should be assessed in conjunction with EEG to be closer to real-world situations likely to induce concussion symptoms. Supporting this are findings that demonstrate a relationship between concussion and altered postural control [168]. When paired with a postural task, EEG signals have indicated that concussion sequelae could be found months after an injury [164]. These results indicate that EEG parameters are possible biomarkers for concussion.

Among the most common post-concussive symptoms are dizziness and balance problems. The objective assessment of postural control is, therefore, a natural candidate for investigation among those who have suffered a concussion. Centre of pressure (CoP) has been assessed in the maintenance of upright stance and is an important measure of postural stability [169] and as a possible indicator of a concussive injury [170]. Given this connection between concussion and postural control, electromyographic (EMG) recordings, could be used to assess possible biomarkers for concussion, as they can record muscular activity necessary to maintain postural stability[171]. Blood flow and heart rate (HR) present other objective measures and have been found helpful in clinical settings when assessing individual differences in outcome after a concussion[172]. As a part of a multi-faceted approach, virtual reality (VR) offers a novel way to evaluate and manipulate postural control and cortical activity[173]. Moreover, with such an approach, it is essential to carefully consider how the different data values should be processed to optimise the assessment. The use of Machine Learning (ML) can be found throughout various scientific fields, offering a way to classify large datasets by using learning algorithms[174]. ML is used in multiple biomedical areas, including concussion research, and its efficacy has been positively demonstrated in recent scientific literature.

This paper aimed to validate concussion/non-concussion classification and quantitatively assess different physiological responses during postural control tasks associated with concussion symptoms. The study was conducted on a homogenous cohort of female athletes with a background in sports with high impact contact. The athletes' self-reported concussion history was used to divide them in two groups: concussions and non-concussion. We first validated concussion history by asking them about concussion symptoms, using the SCAT5 questionnaire. Next, concussion groups were assessed in a novel measurement setup called BioVRSea (figure 4.7). Here, virtual reality and a synchronized moving platform were used to trigger a postural control reaction while measuring EEG, EMG, heart rate and center of pressure (CoP) parameters. This measurement allowed the assessment of physiological, neural and balance parameters during the simulation of a small boat at sea. We hypothesized that (1) The Icelandic versions of the SCAT5 symptoms checklist, although not a diagnosis tool, can be used to differentiate between concussed and non-concussed athletes (2) Changes of CoP, heart rate, EMG and EEG data can quantitatively measure concussion and concussion symptoms, (3) machine learning techniques using SCAT5 and neurophysiological parameters can improve assessment of concussion.

4.2.2.2 Material and methods

Participants Participants were all female athletes (N=54), competing at the highest level in Iceland. Mean age was 38.4 (SD=7.7). Almost half of the participants had a history of concussion/s, 48.1% (n=26), half had no concussion history, 51.9% (n=28). Mean years since retirement was 4.3 years (SD=4.9).

Experimental procedure All participants were provided written information about the study prior to signing an informed consent document. The study protocol was approved by the Icelandic National Bioethics Committee (no: 17–183-S1).
Participants were read a concussion definition and were asked if they had sustained a
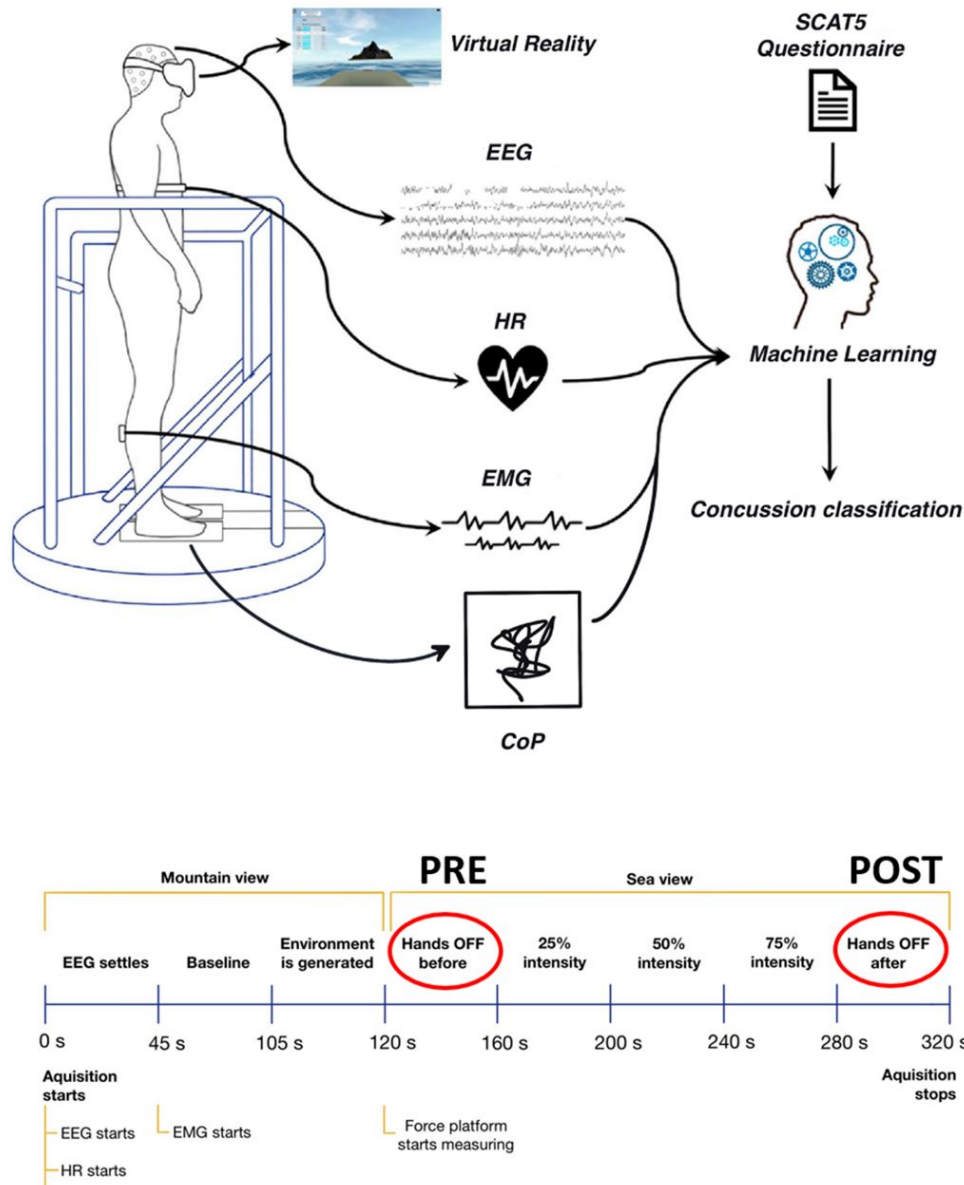
Figure 4.7: BioVRSea experimental Setup.

concussion. The definition was based on the Berlin Consensus statement on concussion in sport from 2016[157].

SCAT5 questionnaire   All participants completed the symptoms scale from The Sport Concussion Assessment Tool 5 (SCAT5)before the experiment. The overall score is calculated by the sum of each participant's responses. The scale has 22 items, each item scoring from 0 to 6, indicating the severity of the symptom26. In this study, it was hypothesized that the Icelandic versions of the SCAT5 symptoms checklist, could be used to differentiate between concussed and non-concussed athletes, it was used to validate the self-reported concussion status and assess for each group the changes of some physiological conditions associated with our experiment.

VR experiment   The participants were then prepared for the virtual reality and physiological measurement part of the experiment. This involved the placement of a

wet 64-electrode EEG cap (Sampling frequency 4096 Hz, ANTNeuro, Hengelo, The Netherlands), six wireless EMG sensors (Sampling frequency 1600 Hz Kiso ehf., Reykjavik, Iceland) on the tibialis anterior (TA), gastrocnemius lateral (GL), and soleus (S) muscles of each leg, and a heart rate sensor (sampling frequency 1 Hz, PolarBeat, Kempele, Finland) strapped around the chest. The EEG amplifier (ANTNEuro, Hengelo, The Netherlands) was connected to the cap and placed in a backpack with a tablet used for EEG signal acquisition. The participant put on the backpack and was instructed to step onto the force plates after removing their shoes. The position of the feet was in bipedal stance with feet hip width apart, while standing on the force sensors (Sampling frequency 90 Hz, Virtualis, Clapiers, France). Finally, the participant dons the VR goggles.

The experimental protocol was then explained to the participant. The explanation included that they should stand quietly on the platform with their hands by their side observing a mountain view for the first 2 min of the experiment. Then, the scene in the VR goggles would change, beginning the sea simulation. The participants were instructed to remain standing quietly with their hands by their side for the first 40s of the sea simulation. There was no platform movement in this part of the experiment, and it is called the PRE phase of the experiment. After 40s of quiet standing watching the sea simulation, the participant was instructed to hold onto the bars in front of them. The platform then began synchronized movement with the sea scene in the VR goggles, with 25%, 50% and 75% of maximal wave amplitude. In this central part, each segment lasted 40 s and the participant held the bars of the platform while continuing to observe the sea simulation. Finally, the platform stopped moving and the participant was asked to remove their hands from the bars and attempt to stand quietly with their hands by their side for the final 40s of the experiment. The sea scene was still observed by the participant for the final 40 s. This is called the POST phase of the experiment; it is performed identically to the PRE phase but after the participant has performed movement in the central part of the procedure. Figure 4.7 shows a schematic of the experimental setup. Each participant took part in a single trial according to the experimental protocol.

The operator can set the frequency of the waves between 0.5 Hz and 3 Hz and the amplitude of the waves between 0 and 2. During the simulation, we vary the amplitude of the platform movements from 0% up to 75% of the platform's maximal amplitude. Two different protocols were used at random throughout the study. The 'soft' protocol was defined as a wave frequency of 1 Hz with an amplitude of 0.6 while the 'hard' frequency was defined as a wave frequency of 3 Hz with an amplitude of 0.5. Each participant experienced either the hard or soft protocol once while taking part in the experiment.

Randomly selected amplitude of the experiment (soft or hard protocol) is made to mimic the variety of "sea behavior," to cover a wide possibility to trigger a postural control response.

Data acquisition During each protocol, muscle, brain, heart, and CoP data were acquired using the following technologies:
Brain electrical activity was measured using a 64-channel wet electrode cap (sampling frequency of 4096 Hz) from AntNeuro, Hengelo, the Netherlands.

Muscle electrical activities from the lower limbs was acquired using six wireless EMG sensors (sampling frequency of 1600 Hz) placed on the tibialis anterior (TA), gastrocnemius lateral (GL), and soleus (S) muscles of each leg (Kiso ehf, Reykjavik, Iceland).

Heart rate was measured using a chest heart sensor (Polar Electro, Kempele, Finland, sampling frequency 1000 Hz).

Force Plate measurements were made using 4 sensors located under each foot platform. The sensors give information about the center of mass in the Antero-posterior and Medio-Lateral axis (Virtualis, Clapiers, France, sampling frequency 90 Hz).

The data from each measurement were divided into 6 segments, corresponding to each stage of the protocol. Data for the EEG, EMG and CoP were analyzed by calculating POST–PRE (POST minus PRE) paradigm.

Division into subgroups by symptoms   Subjects from the concussion group were further divided into subgroups for quantification of some symptoms from the SCAT5 questionnaire. For instance, CoP measures may be different among the concussion participants that reported balance problems, compared to those that did not/non-concussion group. The following symptom-based subgroups were formed from the concussion participants for the following measurements:

For EEG: Pressure in the head symptom group (17 subjects), Fatigue/Low Energy symptom group (19 subjects), difficulty concentrating symptom group (16 subjects).

For HR: Nervous/Anxious group (20 subjects), Fatigue/Low Energy Group (19 subjects).

For EMG: Balance problem symptoms group (14 subjects).

For CoP: Balance problem symptom group (14 subjects).

EEG data processing   The EEG analysis was performed on the spectral domain. The focus was put on the difference between the PRE and POST segments. The considerable electrodes were identified between those two segments.

The EEG was recorded using a 64-electrode channel system. Data pre-processing and analysis were performed with Brainstorm[124] and Matlab 2020b, using the Automagic toolbox [175].

For each segment, we removed the 5 first and 5 last seconds, to ensure the data quality and to avoid artefacts. The data were resampled to 1024 Hz. Automagic was used to automatically pre-process every dataset, with a manual inspection at the end. The ICA MARA algorithm was used, with a variance of 20%. The data were notch filtered at 50 Hz. A high pass and low pass filter were set respectively to 1 Hz and 45 Hz. Finally, the bad electrodes were interpolated. Each segment was on average interpolated up to 10%.

The power spectral density (PSD) was computed for each epoch with 'Welch's method, with the following frequency bands: delta (1–4 Hz), theta (4–8 Hz), alpha (8–13 Hz), beta (13–30 Hz), low gamma (30–45 Hz). The relative power of each band was then computed obtaining a total of 5 EEG-related features.

Statistical tests The statistical significance for each electrode was computed (t-test, α=0.05) for the results from the difference Hands-off Post minus Hands-off Pre segments, for each frequency band, within each group (concussed and non-concussed). It was then corrected for multiple comparisons using the False Discovery Rate (FDR) (Benjamini-Hochberg) method [176].

4.2.2.3 Results

EEG analysis Figure 4.8 shows the results from the EEG analysis performed in the frequency domain. The figure shows the difference POST–PRE for the concussion group for the delta and theta band, the only bands that were significantly different. The 'x' represents the electrodes for which we found significant differences for each band.
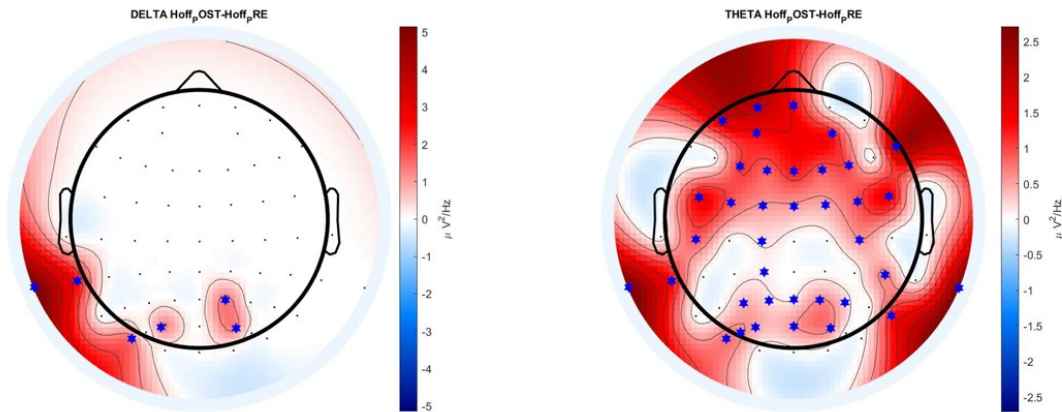
Figure 4.8: Topological plot for delta and theta frequency band of the concussion group. It displays the difference of power spectral density, between POST and PRE, only for the statistically significant electrodes ($0.032 \leq p \leq 0.047$, represented by a blue star in the figure). The delta band presented a few significant electrodes (6 out of 64) on the frontal and occipital cortex, whereas the theta band showed more distributed significant electrodes (36 out of 64) over the scalp

The difference was highlighted by an increase of power and significant evolution in the theta band mostly, and delta band for the concussion group (p=0.038), the theta band showing significantly higher POST power than PRE. The theta band displayed an important number (37 out of 64) of significant electrodes ($0.032 \leq p \leq 0.047$) (t-test, corrected with false discovery rate (FDR), Benjamini–Hochberg method), in the frontal (18 out of 64 electrodes) and occipital (11 out of 64) cortex. The non-concussion group did not display any significant results for this experiment.

We then divided the concussion group into subgroups based on symptoms identified from the SCAT5 questionnaire. We analyzed the Difficulty concentration symptoms

group (16 individuals), the Pressure in the head symptoms group (17 individuals), Fatigue and low energy group (19 individuals).

Figure 4.9 shows the results from the EEG analysis performed in the spectral domain. The figure shows the difference POST–PRE for the concussion subgroups, for the theta band, the only band that presented significance. Figure 4.9A shows the results for the Difficulty concentrating group, 4.9B for the Pressure in the head group, and 4.9C for the Fatigue and Low energy group.
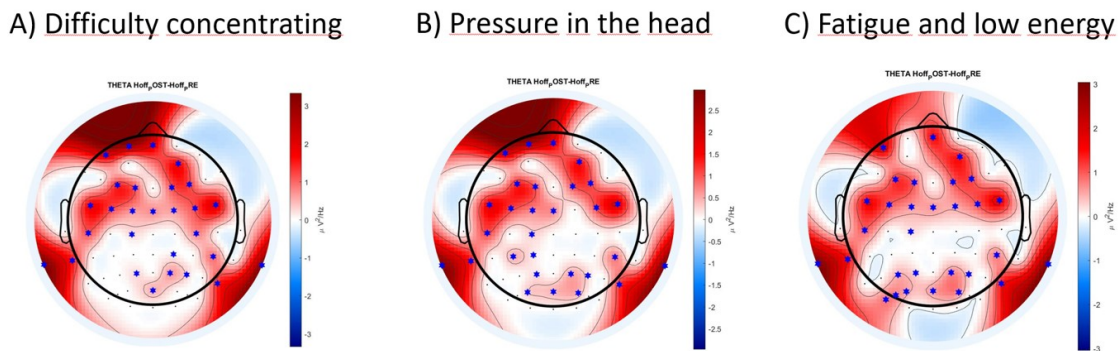
Figure 4.9: Topological plot for delta and theta frequency band of the concussion group. It displays the difference of power spectral density, between POST and PRE, only for the statistically significant electrodes ($0.032 \leq p \leq 0.047$, represented by a blue star in the figure). The delta band presented a few significant electrodes (6 out of 64) on the frontal and occipital cortex, whereas the theta band showed more distributed significant electrodes (36 out of 64) over the scalp

Figure 4.9 reveals that the subgroups present significant differences ($0.008 \leq p \leq 0.049$) for the theta band, with a global increase mostly in the frontocentral cortex (16 significant electrodes for difficulty concentrating, 15 for pressure in the head, and 14 for fatigue and low energy) for all of them, as well as an increase in the occipital lobe for the Pressure in the head (8 significant electrodes) and Fatigue and low energy (10 significant electrodes) subgroup.

Other symptoms groups were analyzed, such as headache (20 individuals), dizziness (14 individuals), balance problem (13 individuals) and more emotional group (11 individuals). These subgroups did not present any significant findings; therefore, their results will not be displayed.

Table 4.1 summarizes the significant electrodes ($0.008 \leq p \leq 0.049$) of Delta and Theta band, for the concussion group and the three subgroups detailed above.

4.2.2.4   Discussion

The EEG results indicated a significant difference (at some frequency bands) between those with a history of concussion and those with no history of concussion when participants had to maintain postural control and balance. Activity on the theta band was increased in those with a history of concussion. The theta wave activity has been associated with the ability to encode new information, and is correlated with cognitive performance, memory in particular[43], [177], and may appear normal during relaxed wakefulness[178]. Theta activity has been observed to increase during cognitive tasks compared to motor tasks, indicating an active role in problem solving[179] and has been associated with tasks that need more attention and cognitive demands[180]. An

Significant electrode Delta	Significant electrodes Theta	
Concussion group	M1 P2 PO3 PO4 TP7 PO7	Fp1 Fpz F3 Fz F4 F8 FC5 FC1 FC2 FC6 M1 C4 M2 CP1 CP6 P3 Pz P4 P8 Poz AF7 AF3 AF4 F1 F2 FC3 FCz FC4 C5 C1 P1 P2 PO5 PO3 PO4 TP7 PO7
Difficulty concentrating subgroup	–	Fp1 Fpz F3 F4 FC5 FC1 FC2 FC6 M1 C4 M2 CP2 CP6 P4 P8 Poz AF7 AF4 F1 F2 FC3 FCz FC4 C5 C1 P1 P2 TP7
Pressure in the head subgroup	–	Fp1 Fpz F3 F4 FC5 FC1 FC6 M1 M2 CP1 CP6 P4 P8 Poz AF7 AF4 F1 F2 FC3 FCz FC4 C5 C1 CP3 P1 P2 PO3 PO4 TP7
Fatigue and low energy subgroup	–	Fpz F3 F4 FC5 FC1 FC2 FC6 M1 M2 CP6 P3 P4 P8 Poz AF7 AF4 F1 F2 FC3 FCz FC4 C5 C1 P1 P2 PO3 PO4 TP7 PO7

Table 4.1: Significant electrodes of delta and theta band for the concussion group and subgroups.

increase in theta among those with a history of concussion when compared to those with no history of concussion may indicate a need for more attention and cognitive effort than those who do not have a history of concussion. The increase in theta was additionally present in concussion subgroups among participants that reported having difficulty concentrating, feeling pressure in the head, and feeling fatigue and low energy. Further supporting their reports of concussion symptoms and offering an objective way to assess post-concussive symptoms. Concussion history has been connected to cognitive impairment[181], [182], like attention and reaction[183], and cognitive fatigue has been suggested as a sub-type of concussion[184]. The increase in theta may support this type of cognitive impairment and indicates that the task was more demanding for those with a history of concussion. It is worth mentioning that theta increase has also been found in the frontal and central regions for postural control adaptation and habituation[139], highlighting its activation during balance and postural control disturbance[185].

4.2.2.5 Limitations

As participants were all actively or historically involved in contact sports and as such this is a group at elevated risk for receiving sub-concussive injuries throughout their careers. The comparison between the concussion and non-concussion groups is not a comparison between a concussion group and a normal population. Both groups will likely have received repeated head and body impacts, with possible sub-concussive blows. The limited number of participants limits the drawing of robust conclusion and reduces ML algorithm's predictive capabilities. Recruitment of more participants in the future could improve the results in terms of accuracy, and more complicated algorithmic models can be implemented.

4.2.2.6 Conclusion

In this study, a novel paradigm to measure postural control has been validated. We demonstrated that we can discriminate between concussion and non-concussion groups using the BioVRSea setup and particularly, symptoms associated with concussion, especially with balance problems, follow a pattern that can be quantified. This study shows the value of a subject-specific multi-faceted postural control assessment. More-

over, adapting the experiment to one protocol only, and changing the EEG device from dry to wet electrodes improved the signal quality and analysis, leading to more exploitable and reliable results regarding brain cortical activity.

4.2.3 Exploratory study 3: Predicting postural control adaptation measuring EEG, EMG, and center of pressure changes: BioVRSea paradigm

This work is adapted from a study accepted for publication in *Frontiers in Human Neuroscience* [186]. The aim of this study was, based on the data extracted from the biosignals, to classify the different phases of the experiment, that imply different type of stimulaiton.

4.2.3.1 Introduction

An upright posture is not only important when standing or walking, it is also crucial for successfully accomplishing everyday life tasks and therefore has a major impact on the quality of life. Falls are the worst consequences of postural control (PC) disorders [187], and for this reason, fall injuries are one of the most serious health care problems and one of the biggest threats to the independence of older adults. They are associated with an increased functional impairment, disability and decreased ability to independently manage activities of daily living [138], [188], [189]. PC can be defined as the ability to maintain the body's center of gravity within certain limits of stability during quiet stance or movement. The limits of stability are shaped like a cone and can be specified as the range in which the body's center of gravity can be shifted without requiring a change in the base of support [138], [187], [190]. PC involves two general skills of the human body: first, postural orientation, which describes the ability to maintain the body position in relation to the environment and ultimately provide an appropriate response to external perturbations; second, postural stability, which is the ability to maintain body position in equilibrium [138], [189], [190]. PC is a complex and dynamic central sensorimotor system that integrates information from the vestibular, visual and proprioceptive sensory systems. In daily activities, it relies on a multifaceted interplay of physiological mechanisms [169], [190]–[192]. External perturbations induce and trigger different adaptive PC strategies in the human body. Previous studies investigated these strategies, focusing on the task-dependent changes of strategies throughout the lifespan [193], the adaptive behavior of PC due to perturbations in the upright standing [194], [195] or the adaptive responses to virtual environments [196]. A person's CoP and its movement are indicators of stability and are considered particularly useful to study postural response. The CoP can be calculated using a force plate under the feet that determines the center of the vertical reaction force[138], [187]. In addition, an increasing number of studies are using brain electrical signals (EEG) as a viable measurement setup to investigate cortical activity and the neurophysiological behavior during PC tasks [197], [198]. Likewise, EMG has been used in several studies to investigate balance control as well as posture correction by lower leg muscles like tibialis anterior and gastrocnemius [198]. Due to the rising size and complexity of data sets the use of predictive analyses using machine learning analysis became common in biomedical engineering studies [199]. This results in the advantage of being able to use machine learning to examine large high-dimensional datasets for patterns in a brief period and derive quick and relevant conclusions. Regarding the classification models for machine learning, the goal is always to get generalizable models that can also predict other data sets that are not from the same data collection or environment [200]. The recent measurement setup BioVRSea has been used for various research purposes, including the prediction of motion sickness or the evaluation of biomarkers

for concussions [141], [153]. For this study, BioVRSea was used to explore brain activity, muscle activity, and center of mass to investigate changes in PC responses. With these biosignals recordings, features can be extracted and then used to classify the several segments of the experiment. In total, BioVRsea consists of 6 distinct phases with individual settings that have a unique influence on the subjects' responses in terms of PC. value. Firstly, from baseline to PRE, we have a visual onset with the beginning of the sea simulation. From PRE to 25%, we have a motion onset synchronized with the sea simulation. This movement progressively increases at 50% and 75%. Finally, the induced postural control response is measured while abruptly switching off the movement while the sea simulation remains on. Therefore, the feature extraction and analysis were performed for each phase with the aim to estimate and quantify these different physiological conditions and responses. Machine learning is of great impact as it helps to determine which biosignals are suitable to predict the different phases of the BioVRSea acquisition and which patterns can be found in the large amount of data collected.

4.2.3.2   Material and methods

Experimental protocol   BioVRSea is an innovative measurement setup for studying the physiology of PC. It mimics the sensation and gives the impression of being in a small boat on a rough sea. The goal of the experimental setup is to trigger a PC response and analyze the various biosignals during the acquisition. The setup consists of a virtual reality (VR) environment and a moving platform synchronized with the simulated environment. Subjects stand on the platform and wear VR goggles and various measurement devices to record the different biosignals. The participants were prepared for measurement with the placement of a wet 64-electrode EEG cap, six wireless EMG sensors on the tibialis anterior, gastrocnemius lateral, and soleus muscles of each leg, and the heart sensor strapped around the chest. The EEG amplifier was connected to the cap and placed in a backpack with a tablet used for EEG signal acquisition. The backpack is worn by the participant during the experiment. Finally, the participant enters the VR environment by climbing on a platform and donning VR goggles. The platform is equipped with a force plate to measure the sway movements of the participants during the experiment. The schematic experimental setup can be seen in Figure 4.10.

For the experiment and the following classification, 6 phases are considered, as depicted in Figure 4.11.

These segments will be the different classes to be predicted with the machine learning process. The first phase is the baseline segment, where the participant only sees a static mountain panorama through the VR goggles. During this time, the platform does not move, and the participant stands with their hands by their side while viewing the mountain view for a total of 2 minutes. For the signal processing part only the last 60 seconds were used. After the Baseline phase, the VR scene changes to the sea environment and the subject sees him/herself on a small boat at sea. The second phase lasts 40 seconds and is called the PRE phase. During this phase, the platform does not move, and the participant remains still with their hands by their side. In the third phase, the participant holds on to the safety bars and the platform moves in a synchronized manner with the waves seen in the VR scene. During these 40 seconds, the platform moves at 25% of the maximum amplitude. In the fourth and fifth phases, the platform increases the intensity to 50% and 75%, respectively
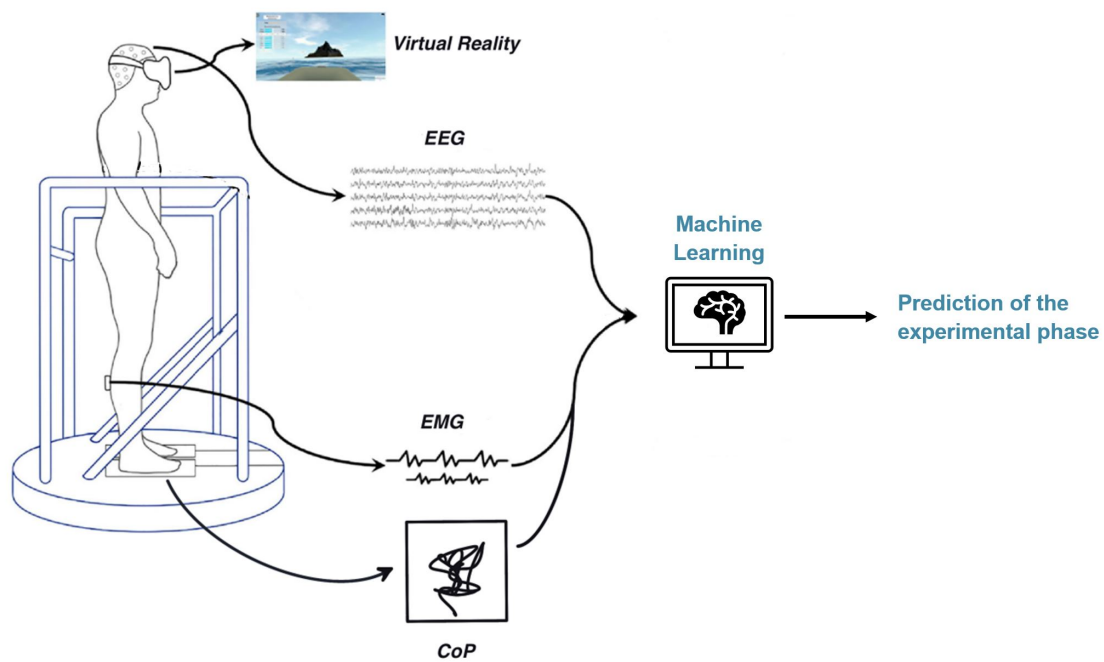
Figure 4.10: BioVRSea Measurement Setup
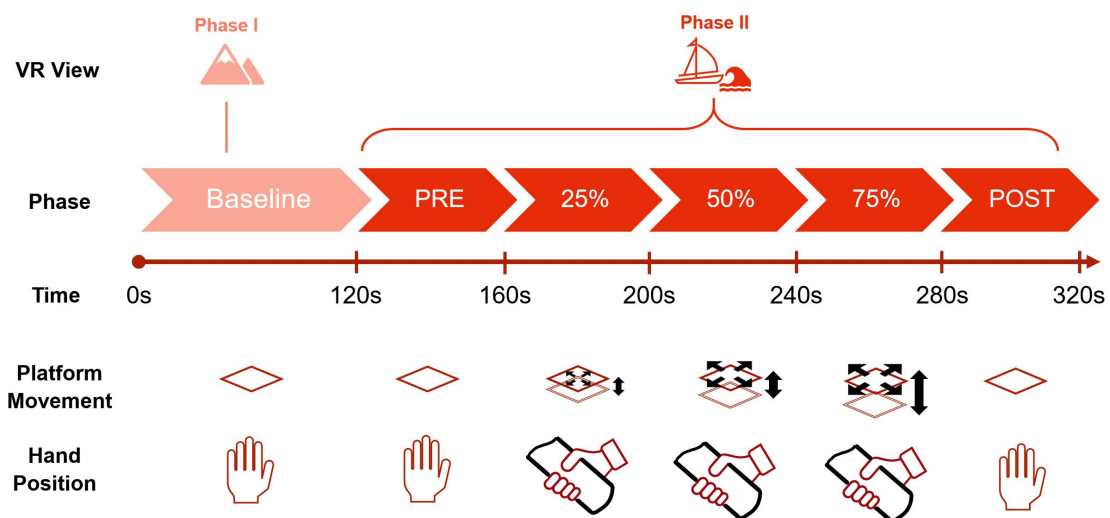
Figure 4.11: BioVRSea Measurement Setup

for 40 seconds each. In the last phase, the POST phase, the movement of the platform stops while the VR simulation continues. The participant takes their hands off the safety bar and stands quietly trying to maintain equilibrium watching the VR sea scene. After 40 seconds, this phase is over and so is the entire acquisition. The different materials used for the study include the VR software (Sampling frequency: 90Hz, Virtualis VR, Clapiers, France), the moving platform (Virtualis VR, Clapiers, France), the force platform (Virtualis VR, Clapiers, France), six wireless EMG sensors, attached to the soleus, tibialis anterioris, and gastrocnemius lateral on both the left and right legs (Sampling frequency: 1600Hz, Kiso ehf, Reykjavik, Iceland), and the 64-channel wet electrode cap (Sampling frequency: 4096 Hz ANTNeuro, Hengelo, The

Netherlands). The three integrated biosignals were recorded and synchronized using a software called MacroRecorder. This software enables to automatize all the consecutive computer tasks and to launch simultaneously the recording. The data processing and analysis procedure are described in the following sections.

Population   The study is based on 191 subjects (age: 34.1 ± 14.8), 79 male and 112 female subjects (ethic approval by the Icelandic Bioethics Commission – Number: VSN-20-101 – May 2020). Due to missing or inferior quality recordings, the CoP analysis was performed on only 172 subjects (age: 33.7 ± 14.7), 64 male and 108 female.

EEG   Brainstorm [124] and MATLAB 2022a (MathWorks, Inc., Natick, 158 Massachusetts, USA) with the Automagic Toolbox developed by Pedroni et al. [175] were used for preprocessing and analysis of the EEG data. In order to ensure data quality and to avoid artifacts, we removed the 5 first and 5 last seconds for each phase of the experiment. Afterwards, the data was resampled to 1024 Hz. Automagic was used for automatic preprocessing for each data set, with a manual check at the end. The ICA MARA algorithm was used with a variance of 20%. A high-pass and low-pass filter were set to 1 Hz and 45 Hz, respectively. The data were notch filtered at 50 Hz. Finally, the bad electrodes were interpolated. The 5 anatomic lobes of the cortex consisting of frontal, parietal, occipital and the two temporal lobes that are widely accepted in the scientific community [201], [202] are used as regions of interest. The power spectral density (PSD) was computed for each phase and each electrode using the Welch's method, with the following frequency bands: delta (1–4 Hz), theta (4–8 Hz), alpha (8–13 Hz), beta (13–30 Hz), low gamma (30–45 Hz). The relative power of each region of the cerebral cortex was then calculated by taking the mean of the electrodes located in that region to obtain a total of 5 EEG-related features per region and per experimental phase. All of this preprocessing was performed in a manner analogous to the study of Jacob et al. [153].

EMG   For the EMG features, preprocessing and feature extraction are required which were performed with MATLAB 2022a, using the built-in Signal Processing Toolbox. The muscle signal was analyzed for each segment. After the removing of the transition from one phase to another, each phase segment for 20 seconds. For further processing, we use a 4th order Butterworth bandpass, a cutoff frequency of 15 Hz and 500 Hz, and a sampling frequency of 1600 Hz. Time and frequency metrics were extracted from this final signal.

CoP   To calculate the anterior–posterior (AP) and medio-lateral (ML) displacement (in centimeters) of the CoP, the following formula was used:
$DisplacementAP = Y \text{x} 0.5 \text{x} StaticVRAP$ and $DisplacementML = X \text{x} 0.5 \text{x} StaticVRML$

The StaticVRAP (respectively StaticVRML) is the percentage of the vertical size (respectively horizontal size) of the platform sensors, with a value comprised between ˘1 and 1. In addition, X represents the dimension of the force platform in the ML direction and Y represents the dimension of the force platform in the AP direction. The processing of the CoP data was performed using MATLAB 2022a, and is the same as previously described in Jacob et al. [153]. During the experiment, the force platform

Signal	Modalities	Features	Total	
EEG	5 bands x 5 brain regions = 25 modalities	1	25	
EMG	3 muscles x 2 sides = 6 modalities	43	258	
CoP	1 modality	35	35	

Table 4.2: Total number of features

records the movement of the CoP, a projection of the center of mass of the subject on the plane of the machine, also called stabilogram. To filter the CoP data, we used a Savitsky-Golay filter with window size 7. Afterwards we used the stabilogram for feature extraction.

Machine Learning For the classification analysis, the interactive Classification Learner App was used: it is included in the Statistics and Machine Learning Toolbox 2022 in MATLAB 2022a. The data can be imported as a spreadsheet, which contains the different predictor and response variables. We used a training dataset containing 70% of the data and a test dataset with the remaining 30%. As is known from machine learning theory and literature, it is crucial that the model has never seen the test data set until finally the test accuracy gets computed to avoid overfitting and biased results [199], [200]. For the validation accuracy, we performed a 10-fold cross-validation and the validation error gets calculated by averaging over the 10 folds. Then, the model is trained using the entire training dataset (70% of the total data). Subsequently, we used the remaining 30% of the data to obtain test accuracy without bias. As predictors, we used the features extracted from the different bio-signals (Table 4.2). To obtain information about which biosignal is more suitable for predicting the phase of the experiment, we trained and tested prediction models separately for the EEG, EMG, and CoP data. Finally, we also trained classification models using both EMG and CoP features together.

Different configurations have been used for the classification. The first one was the prediction of the six different phases. For the CoP data, the recording starts only after the BL, so the second configuration was the prediction of five phases (PRE, 25%, 50%, 75% and POST). A third consideration was averaging the three movement phases (25%, 50%, 75%) in one unique phase, as the similarity of these phases made the classification more difficult. This leads to three (PRE, movement, POST) or four (BL, PRE, movement, POST) phases to classify. Finally, for the EEG signals, due to the low accuracy in the previous configurations, a binary classification was defined, to differentiate BL from the rest. The five phases that were not BL were averaged together in one single phase. This approach of merging was only possible because we had the same amount of data for each phase. This is also necessary for the classification to correctly assess and interpret the average overall accuracy [199]. The details of classification configuration and results are listed in table 4.3. For the feature selection, the ANOVA – analysis of variance - method was used. ANOVA provides the opportunity to determine the most relevant feature for classification. As a statistical test it's suitable to compare the differences between two or more means of the samples based on mean and variance. The ones with the lowest values show that they are independent of the target variable. The ones with a high value show a high relevance for the classification model. ANOVA is suitable for non-stationary data such as EEG for example and is used in various other studies in the field of

biomedical engineering and neuroscience [203]–[205]. Afterwards, the effect size has been computed, calculating η^2 for a confidence level of 95%.

4.2.3.3 Results

Table 4.3 sums up the classification results. The first column shows the biosignal used for the prediction. The second column shows the phases taken into account in the analyses. The "X" overlapping several cells, as on the first row of EEG, considers the merged phases. The next two columns represent the validation and test accuracy, followed by area under curve (AUC) for the validation and test. The seventh column shows which model has been used to obtain those results, and the last three columns show the top three features for the classification.

Bio-signal	Analyzed phases						Validation Accuracy [%]	Test Accuracy [%]	AUC Validation	AUC Test	Model	Feature Ranking		
	BL	PRE	25	50	75	POST						1.	2.	3.
EEG	X			X			76.1	74.6	0.82	0.82	Subspace Discriminant	LG – occipital	A – parietal	A – frontal
	X	X	X	X	X	X	24.3	27.1	0.57	0.61	Linear SVM	A – frontal	A – parietal	A – temporal – right
EMG	X	X	X	X	X	X	43.6	39..4	0.73	0.74	Linear Discriminant	LTKEO – TA – Right	LTKEO – TA – Left	LDASDV – TA – Right
		X	X	X	X	X	42.8	42.3	0.72	0.71	Linear Discriminant	LTKEO – TA – Right	LTKEO – GL– Right	LDASDV – TA – Right
	X	X		X		X	63	57.6	0.83	0.8	Linear Discriminant	LTKEO – TA – Right	LDASDV – TA – Right	MFL– TA – Right
CoP		X	X	X	X	X	72.1	71.7	0.92	0.92	Linear SVM	RDIST – ML	SD – ML	Direction Entropy
		X		X		X	80.1	85.1	0.93	0.93	Subspace Discriminant	Direction Entropy	RDIST – ML	SD – ML
EMG & CoP		X	X	X	X	X	64.5	74.4	0.91	0.92	Medium Gaussian SVM	RDIST – ML	SD - ML	Direction Entropy
		X		X		X	83.1	83.8	0.96	0.95	Subspace Discriminant	Direction Entropy	RDIST – ML	SD – ML

Table 4.3: Overview Classification Results and Performance Parameter

Phases classification The confusion matrices in Figure 4.12 visualize and summarize the performances of the models detailed in table 4.3, for each biosignal: EEG, EMG, COP, and EMG+COP. The table layout shows two dimensions, the true class in each row and the predicted class in each column and gives insights into the occurrence frequency in the corresponding field. Furthermore, the True Positive Rates (TPR) and the False Negative Rates (FNR) are shown next to that.

With the EEG features it's not possible to classify all the different phases of the experiment. But with a test accuracy of 74.6% it's possible to classify if the data is from Baseline or not. Regarding the use of EMG features with our test data, we could predict with an accuracy of 68.4% the Baseline. As it can be seen in Figure 4.12b, it is difficult for the models to classify the phases in between, resulting in high false negative rates for these phases. Using the CoP features we can classify 5 phases with a test accuracy of 71.7%. Striking is the True Positive Rate of 82.4% for predicting the PRE – Phase and 84.6% for the 25% phase as can be seen in Figure 4.12c. Due to the False Negative Rate of 36.5% for the Post phase it becomes clear that the model has more issues to predict the POST phase by only using the CoP data. Most of the mistakes in predicting the phase result in the fact that in 15.7% of the cases the predicted class is the PRE phase instead of the POST phase. Respectively this correlation can also be seen if the model tries to predict the PRE-Phase. By using both EMG and CoP features we get the best result for predicting the 5 different phases. For the trained model we achieved a test accuracy of 74.4% and an AUC value of 0.92. The single True Positive and the respective False Negative Rates can be seen in Figure 4.12d. The use of EEG, EMG and CoP features jointly did not bring an increase in the overall accuracy for predicting 5 phases of the experiment compared of the use of EMG and CoP features together.
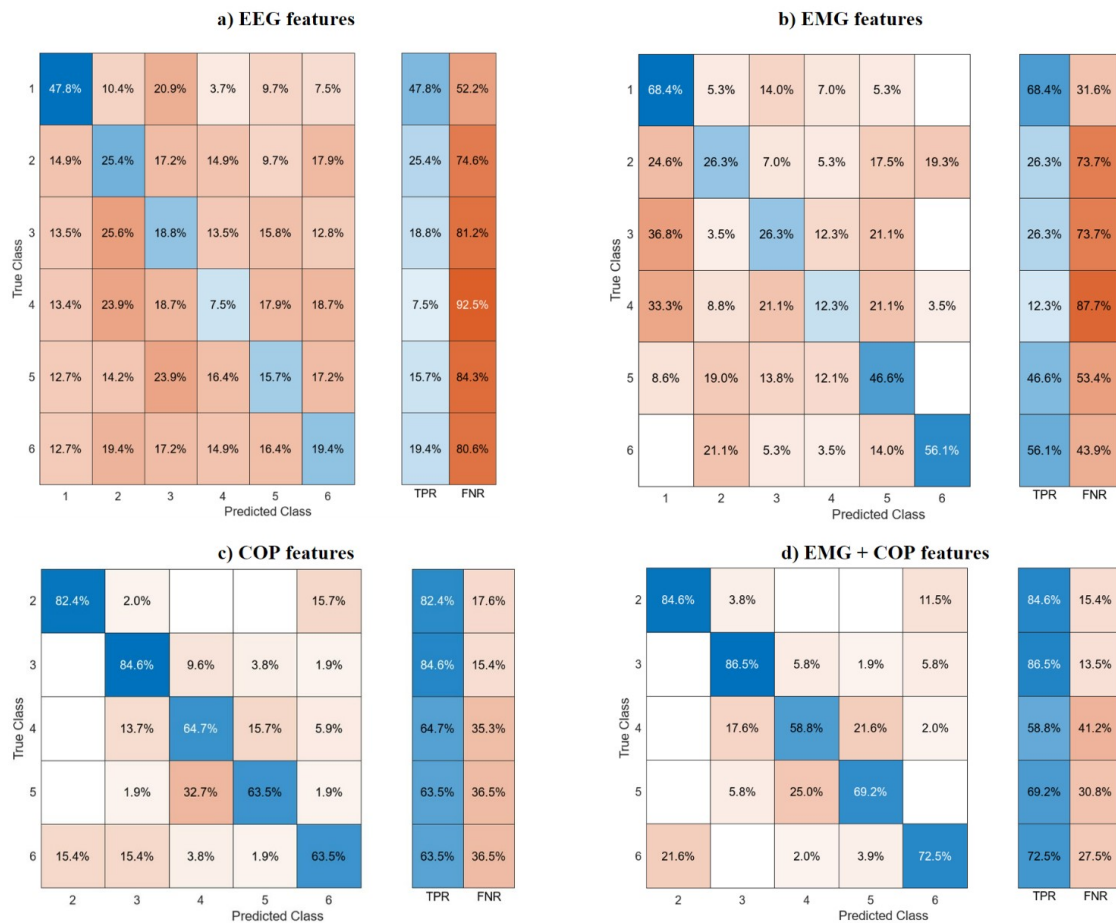
Figure 4.12: Confusion Matrices. a) EEG Features b) EMG Features c) CoP Features d) EMG & CoP Features

Feature ranking The 3 most relevant EEG features to classify the BL from the experiment are the power spectral density values for the low-gamma phase in the occipital region, the alpha phase in the frontal region and in the parietal region, represented in figure 4.13.
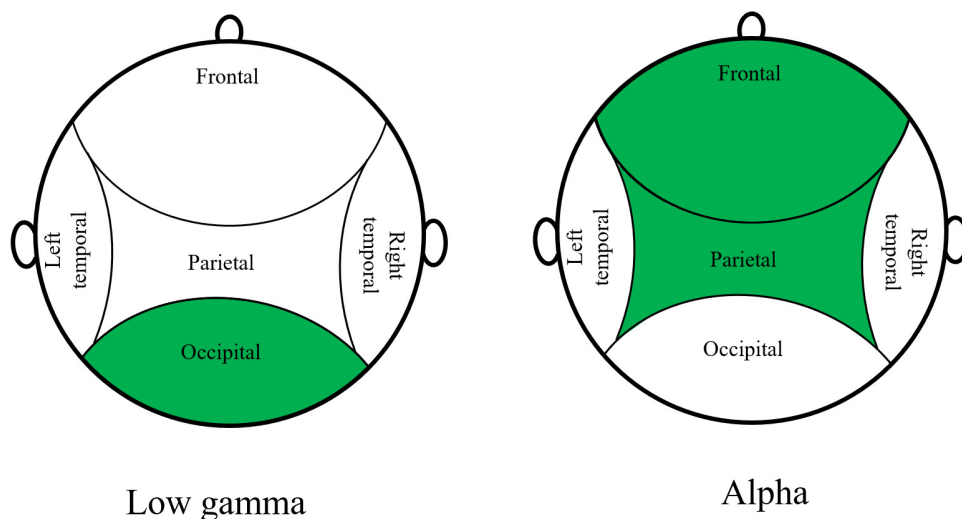
Figure 4.13: Top 3 EEG features to classify BL from the experiment

If only the EMG data is used, the most useful feature are the logarithmic Teager-Kaiser energy operator (LTKEO) of the Tibialis Anterioris Right, followed by LTKEO of the Tibialis Anterioris Left and the logarithmic difference absolute standard deviation value (LDASDV) of the Tibialis Anterioris Right. The LTKEO feature plotted for the Tibialis Anterior and for Baseline, PRE and POST can be seen in Figure 4.14.
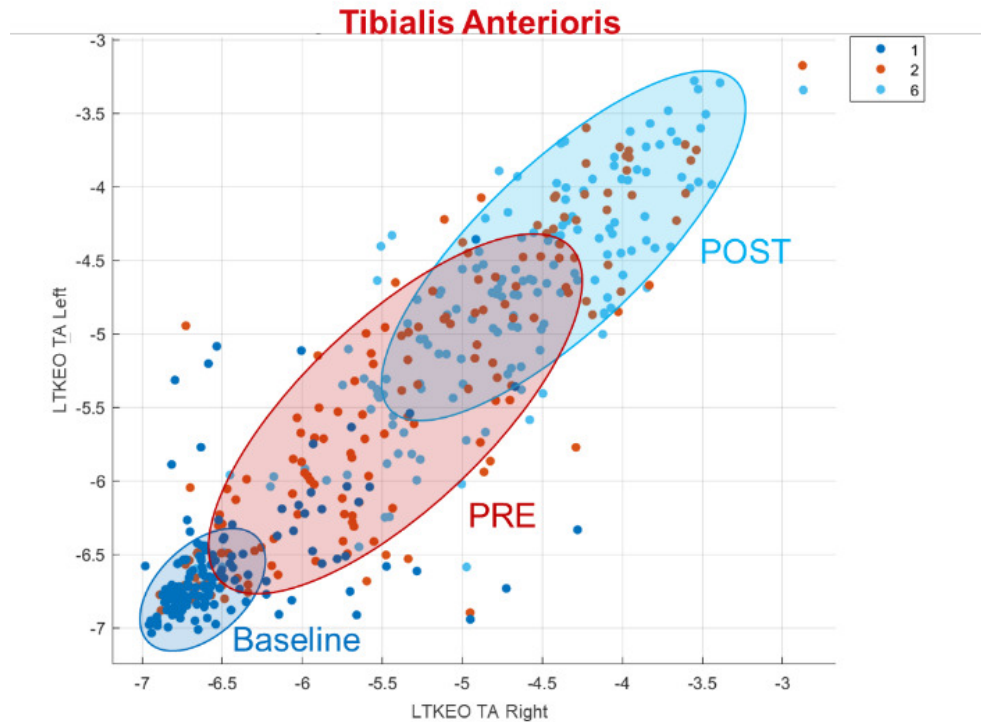
Figure 4.14: LTKEO Feature for Tibialis Anterioris

An increase is recognizable in the LTKEO feature with the ongoing experiment. Strikingly is also the concentrated clustering for Baseline and more widely distributed data dots for the PRE and POST phase. Regarding CoP, the 3 most relevant features for the classification algorithms are the squared root mean distance of the ML direction (RDISTML) as well as the standard deviation of points on the ML axis (SD ML) and the direction entropy. In general, it can be noticed that the ML features are more relevant to predict the phases than the AP features. The different phases of the experiment can be seen in figure 4.15, plotting the total CoP movement in AP Direction and ML Direction.

The PRE-Phase strikes out with the lowest values for the total movement regarding both directions. Furthermore, the data dots for the PRE-Phase are limited and concentrated in a small area. With the further progress of the experiment a stepwise increase is noticeable in the Medio-Lateral direction and also a slight increase in the Anterior-Posterior direction. The finishing POST-phase characterizes itself with increased values in the Anterior-Posterior direction as well as a widely distributed area. Table 4.4 describes the effect size for the top 3 features of each biosignal. EEG features have an effect size of around 0.05, highlighting a medium effect. However, EMG features have an effect size of 0.4, and COP features an effect size of 0.5, showing a high effect associated with those features.
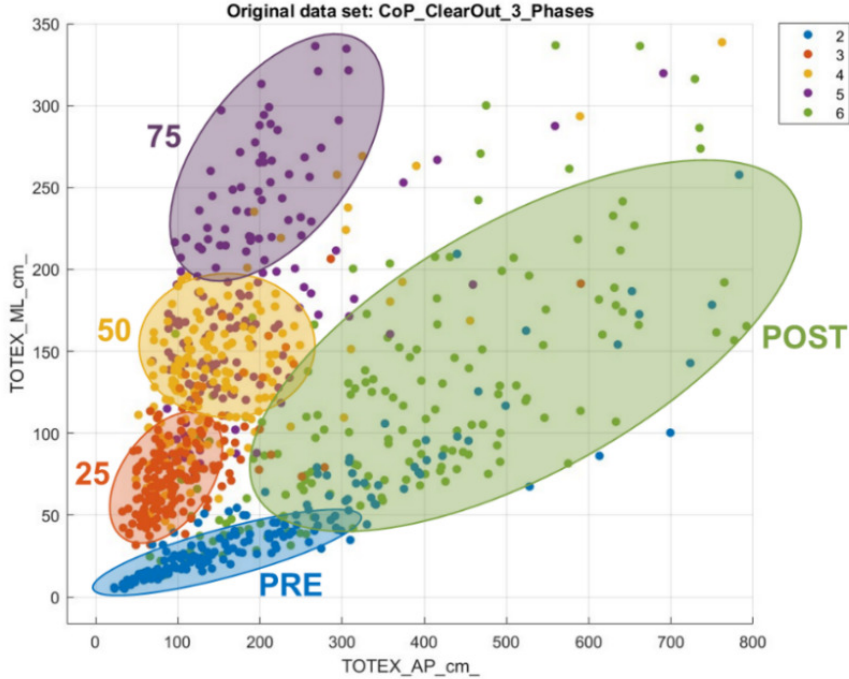
Figure 4.15: CoP movement in anterior-posterior and medio-lateral direction

Effect size			
EEG	**LG occipital**	**A parietal**	**A frontal**
η^2	0.04	0.05	0.07
EMG	**LTKEO − TA − Right**	**LTKEO − TA − Left**	**LDASDV − TA − Right**
η^2	0.41	0.39	0.41
COP	**RDIST − ML**	**SD − ML**	**Direction Entropy**
η^2	0.53	0.53	0.5

Table 4.4: Effect size description

4.2.3.4   Discussion

Postural control is a sensorimotor mechanism that can reveal neurophysiological disorder. The main goal in using the classification is to gain more insight into the dynamic changes in posture control and the different phases of the experiment. This is the reason behind the classification of the different phases of BioVRSea.

EEG features   With the EEG feature solely, we can only classify Baseline and not Baseline with an accuracy of 74.6%. This shows that there is a change in brain activity and a difference between those two stages is recognizable for the model. This difference can be deduced from the changing VR scene that also triggers the occipital region of the brain. This conclusion may fit together with the PSD value for the low gamma phase in the occipital region that is the most important feature for binary classification. The attempt to classify all the 6 phases was not successful. Considering the experimental setup this also seems reasonable as the phases of the moving platform (25%, 50% and 75%) will maybe trigger the same regions (such as the frontal and parietal regions) as they are needed for coordination and motion control [9], [66], [206]. This makes it

challenging for a classification model to predict a class. Another possible reason is the individual adaptive PC strategy to the sensory input with respect to the neural activity [169]. Other causes for the difficulties in predicting all the phases could be that in the study we took the average PSD value for the entire phase. A possible improvement could be to take epochs, so that averaging the different spikes on a per-wave basis could give a more appropriate feature extraction method. Including features derived from a dynamic analysis (not static as reported here) may also improve performance.

EMG interpretation   Regarding the EMG features, the high FNR for the phases 25%, 50% and 75% is expectable as they differ only in their intensity of the sensory input. As Baseline is the most different phase compared to the others (no sea simulation, no platform movements), it makes sense that it's also for the model one of the easiest phases to predict. The logarithmic Teager-Kaiser energy operator (LTKEO) of the Tibialis Anterioris is the most important feature for the classification with solely EMG features. It leads to a good classification result especially between Baseline and the other phases. Li et al. [207] discovered an improved detection of EMG onset using TKEO, especially at a low signal-to-noise ratio. Other studies were able to confirm this, reasoning that the calculated energy is derived from the instantaneous amplitude and instantaneous frequency of the signal [208], [209]. Laksono et al. [210] also performed EMG classification using the Matlab classification learning application and found an important role of TKEO for EMG classification and high accuracy. The overlapping clusters for the PRE and the POST phase in Figure 4.14 show that the LTKEO values are on average higher in the POST phase but it also shows that this feature on its own is not sufficient enough to distinguish these two Phases without mistakes. The reason why the LTKEO values are so low in the Baseline could be that it's the easiest phase to maintain PC as the VR environment with the static mountain view combined with the platform not moving is not a challenging task for subjects without PC disorders. In that phase the muscles are relaxed all the time, and the subjects rarely contract their muscles to keep balance. This leads to low instantaneous energy changes and therefore a low LTKEO value. A hypothesis for the widely distributed dots in PRE and POST visible in Figure 4.14 is that some of the people are using more balancing movements in those two segments, compared to others that just need less muscle activity to maintain PC. This quantitively underlines the fact that people are using individual adaptive PC strategies as identified in the literature [211].

CoP interpretation   Similar interpretation can be reached with the CoP data. Figure 4.15 shows how severe and individual the impact is on the subjects' PC. The increase in deviation from the neutral position indicates the substantial influence that the experiment had on most of the subjects. While observing the scattered plot, it can be observed that the post phase is more widely distributed, due to the fact that the severeness of the impact on the subjects is quite different. This result also has to be seen with the background that anatomical prerequisites also affect the adaptive strategies and are the reason why some people show a higher deviation from the neutral position than others [212]. The fact that more ML features are relevant for the classification leads to the conclusion that, for these features, the experiment results in patterns that differ among each phase, and help the classification model to predict. A clinical hypothesis for it could be that sways in AP direction are more individual and natural than sways in ML direction that are triggered by our acquisition [212]. In

addition to that the VR environment is mainly an AP visual oscillation that is active in all the phases besides Baseline. This could make it more difficult to predict the phase as differences between the phases are less significant. This result also matches with other findings from previous studies [213]–[215].

EMG and CoP interpretation By combining EMG and CoP measurements we obtain good classification results, with 73.3% of accuracy for 5 phases. The reason could be that with the EMG data it is difficult for the model to distinguish the phases of 25%, 50%, and 75%. For these phases, the model can use the CoP data to classify them. This leads to a high overall accuracy. Comparing the different biosignal features it becomes clear that EEG is not able to predict all the phases for the BioVRSea experiment. With EMG as well, the results are not sufficient. With CoP superior results can be achieved but really satisfying results for the classification of the distinct phases can only be achieved by using EMG and CoP features jointly. This leads to the result that those biosignals are needed to describe the dynamic behavior BioVRSea has on the subjects and to quantitatively assess the adaptive PC strategies.

Limitations The first limitation to mention is the amount of data. This is relatively large for a typical biomedical study with neurophysiological examinations, but the results, especially the learned classification models, could be even more reliable if the amount of data were larger. This is especially critical when subgroups are studied, as the number of subjects is then greatly reduced. In addition, the diversity of the subjects investigated should be increased in further studies. Also, relative to the average population, more women than men participated in the study. Another limitation was the subjects' behavior during the experiment. Even though we instructed them to stand still and look in front of them, some participants performed spontaneous movements that were not in reaction to the experiment. This could lead to artefacts or noise in the data collection. Also, it cannot be fully ensured that subjects remain fully focused on the experiment and do not pursue other conscious thoughts.

4.2.3.5 Conclusion

This work aimed to study the neurophysiological dynamics of PC, and how neurophysiological measures could help to quantify and predict PC adaptation, from a consequent healthy cohort. We demonstrated that for our paradigm, EEG could differentiate baseline from acquisition phases. Moreover, the combination of EMG and CoP parameters presented satisfactory results to characterize the 5 phases of the experiment involving the sea simulation. From those results, the best features of each signal were identified to classify the phases: alpha frontal and parietal PSD, lowgamma occipital PSD for the EEG, LTKEO for tibialis anterioris for the EMG, and RDIST and SD ML for the CoP. This work is a first step towards the definition of global healthy pattern, and will lead in the future to the development of tools to understand and quantify PC-related pathological conditions.

4.3   Postural control paradigm (BioVRSea) : Towards a neurophysiological signature

The work below is published in *Physiological measurement* [66]. The aim of this work was to establish a first neurophysiological reference of the BioVRSea paradigm, based on EEG data from 190 subjects.

4.3.1   Introduction

Maintenance of upright posture is a complex task, requiring the coordination of multiple muscles and joints while also integrating the feedback of different sensory systems, i.e. the vestibular, visual, and tactile systems. Evidence of the involvement of the cerebral cortex in the shaping of postural responses to external perturbations has been reported ([216]). Indeed, the importance of the cerebral cortex to bipedal stance has been shown in studies of those with pathologies affecting the cerebral cortex function such as stroke ([217]) and ([218]). Quantitative studies using functional magnetic resonance imaging (fMRI) in conjunction with caloric and galvanic stimulation studies ([219] and [220]) and also functional near-infra-red spectroscopy (fNIRS) have reported a network of cortical structures involved in the processing of integration of sensory information in the brain cortex ([221]). It is clear that the brain cortex has an important role to play in the maintenance of balance but has been under-explored in the literature, possibly due to the long-held belief that sub-cortical processes have a greater influence on upright posture control ([222]).

Electroencephalography (EEG) is a non-invasive and convenient tool for assessing brain response to an external stimulus. EEG is portable and much less expensive compared to MRI, and, therefore, it is more accessible for researchers and clinicians. Both fMRI and fNIRS measure changes in blood flow in the brain, which is a proxy of neuronal activation. In contrast, EEG directly measures the changes of electrical signals generated from the cortex that arrive over the scalp. Balance and postural control (PC) processes in the brain cortex can be evaluated using EEG while in an unperturbed stance or in challenging balance conditions. Event-related potentials (ERPs), which are stereotyped electrophysiological responses to a stimulus, have been used in many studies to distinguish the normal from the pathological response in many different population groups. The N1 response - a negative potential with a peak occurring approximately 100-150 ms after a perturbation is a prominent cortical potential related to loss of balance ([223] and [216]) and has been investigated to demonstrate the correlation between neurophysiological response and postural control perturbation ([224]). A comprehensive review of ERPs (also called perturbation evoked potentials or PEPs) is found in [225]. The review mostly reports work in the amplitude assessment of PEPs but also reviews research performed in the frequency domain, where the spectral characteristics can reveal modulations of EEG activity between baseline and task-related activity ([226]).

However little work has been carried out in exploring the spectral response from EEG data, despite it being a common method for EEG signal analysis. ([227]). The same paper reports frontal and parietal theta power in a cohort of 32 healthy male participants to be correlated with continuous balance performance for balance tasks of varying difficulty. [139] used HD-EEG (256-channel) to measure cortical activity

during vibratory proprioceptive stimulation, with significant changes in absolute power reported in the alpha and theta bands in adaptation to the stimulation.

The present study aims to capture a reference of EEG spectral response to BioVRSea, a dynamic postural control system mimicking the movement of a boat at sea, using a highly instrumented virtual reality (VR) measurement setup consisting of a moving platform, a VR simulation and several biosignals measurements (see Figure 4.16). A first study using this paradigm has been published analysing the behavior of people suffering from concussion ([153]). The present work aims to investigate neurophysiological behavior during dynamic postural control. We intend to identify potential neurophysiological biomarkers, investigating the evolution of power spectral density (PSD) from EEG signals, over several frequency bands.

4.3.2 Material and methods

4.3.2.1 Participants

The study was approved by the National Bioethics Committee of Iceland (Number: VSN-20-101). Participants were recruited through snowball sampling. Written information about the study was provided to every participant before signing an informed consent document. At the time of the study, 232 individuals participated in the experiment. Two of them interrupted the experiment due to an intense onset of symptoms related to motion sickness. Twenty-two individuals were rejected due to technical problems associated with the EEG setup (wrong configuration, software problems during the experiment, ...), and eighteen were rejected due to bad signal quality. This leads to a total of 190 individuals (76 men, 114 women, mean age : 32.9 years old, SD age : 13.8 years old, age range : 19 - 73 years old) presenting a complete EEG recording and good signal quality. No participants suffered from any clinical conditions or pathologies, and all considered themselves healthy.

4.3.2.2 Experiment

Acquisition procedure   The participants were prepared for the virtual reality and physiological measurement part of the experiment. This involved the placement of a wet 64-electrode EEG cap (Sampling frequency 4096 Hz, ANTNeuro, Hengelo, The Netherlands).

The EEG amplifier (ANTNeuro, Hengelo, The Netherlands) was connected to the cap and placed in a backpack with a tablet used for EEG signal acquisition. The participant put on the backpack and was instructed to step onto the force plates after removing their shoes. The position of the feet was in a bipedal stance with feet hip width apart while standing on the moveable platform (Virtualis, Clapiers, France). Finally, the participant donned the VR goggles. Figure 4.16 describes the setup of the experiment.

The experimental protocol was then explained to the participant. The subjects had to stand quietly on the platform with their hands by their side observing a mountain view for the first 2 minutes of the experiment (the last 60 seconds of this step were used as baseline (BL)). Then, the scene in the VR goggles would change, beginning the sea simulation. The participants were instructed to remain standing quietly with their hands by their sides for the first 40 seconds of the sea simulation. There was no platform movement in this part of the experiment, called task PRE. After 40 seconds
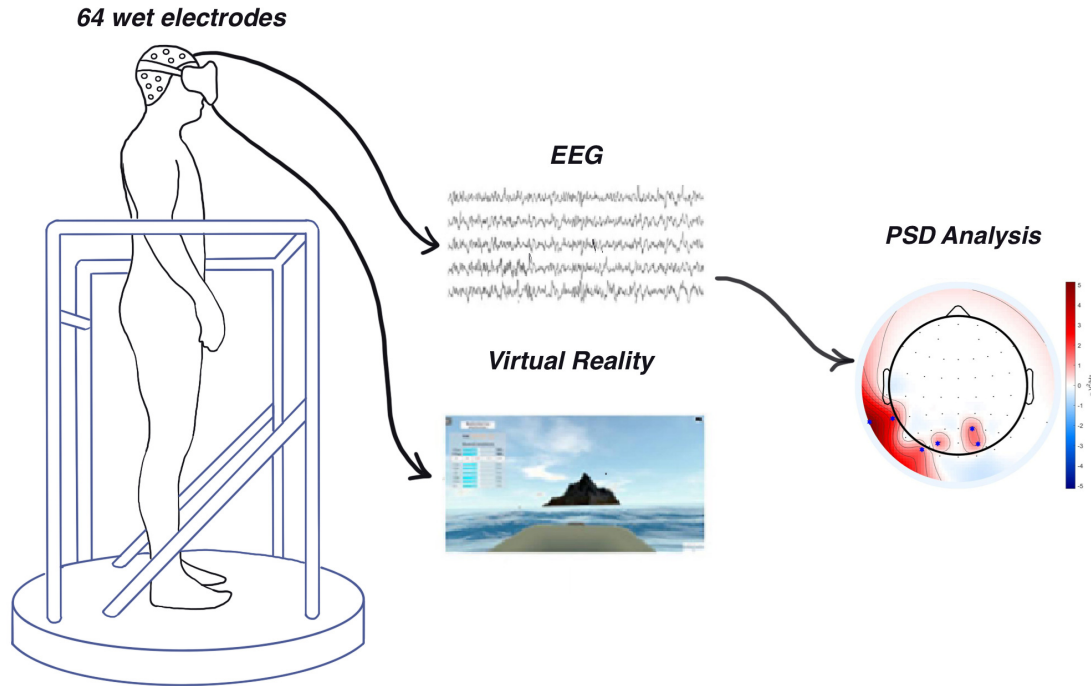
Figure 4.16: Acquisition setup

of quiet standing watching the sea simulation, the participant was instructed to hold onto the bars in front of them. The platform then began a synchronized movement with the sea scene in the VR goggles, with 25%, 50%, and 75% of maximal wave amplitude. In this central part, each segment lasted 40 seconds and the participant held the bars of the platform while continuing to observe the sea simulation. Finally, the platform stopped moving and the participant was asked to remove their hands from the bars and attempt to stand quietly with their hands by their side for the final 40 seconds of the experiment. The sea scene was still observed by the participant for the final 40 seconds. This is called the POST phase of the experiment; it is performed identically to the PRE phase but after the participant has performed movements in the central part of the procedure. We chose segments of 40s after improving and updating a protocol from a previous study ([141]). A segment of 40s enables to trigger postural control without creating a habituation phenomenon that could occur for a longer time for each phase of the experiment.

Figure 4.17 describes the phases of the experiment.
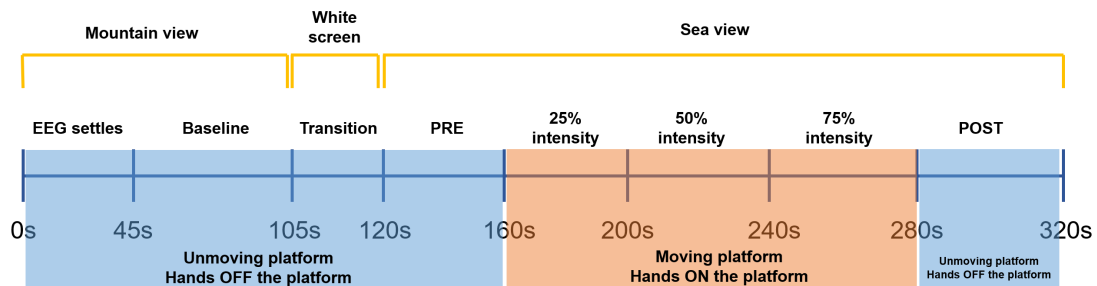
Figure 4.17: Platform workflow

Hereafter in the text, we will mention each task of the experiment as BL, PRE, 25%, 50%, 75%, and POST.

The operator could set the frequency of the waves between 0.5 Hz and 3 Hz and the amplitude of the waves between 0 to 2 (settings from the application internally designed by the manufacturer). During the simulation, we vary the amplitude of the platform movements from 0% up to 75%. (0-1.5). Two different protocols were used at random throughout the study. The 'light' protocol was defined as a wave frequency of 1 Hz with an amplitude of 0.6 while the 'hard' frequency was defined as a wave frequency of 3Hz with an amplitude of 0.5. Each participant experienced either the hard or light protocol once while taking part in the experiment. The randomly selected amplitude of the experiment (light or hard protocol) is made to mimic the variety of "sea behavior," to cover a wide possibility to trigger a postural control response.

4.3.2.3 EEG analysis

Data processing The EEG was recorded using a 64-electrode channel system. Data pre-processing and analysis were performed with Brainstorm ([124]) and Matlab2021b (MathWorks, Inc., Natick, 158 Massachusetts, USA), using the Automagic toolbox ([175]).

For each of the six tasks time segments, we removed the 5 first and 5 last seconds, to ensure the data quality and to avoid artefacts. The data were resampled to 1024 Hz. Automagic was used to automatically pre-process every dataset, with a manual inspection at the end. The data were notch filtered at 50 Hz. A high pass and low pass filter were set respectively to 1 Hz and 45 Hz. ICA MARA algorithm was used, with a variance of 20%. Finally, bad electrodes were interpolated. Each segment needing interpolation of more than 15% of the total amount of electrodes was rejected, and the associated individual was excluded from the experiment. Taking into account all the individuals comporting a complete EEG recording (208 individuals), rejected channels were 2.4±10.1 channels. After excluding subjects from the study, keeping only the 190 individuals with good signal quality, rejected channels were 0.5±1.3 channels.

From this complete EEG recording, the absolute and relative PSD were computed for each subject, using Welch's method ([64]), (1s Hamming window length, 50% overlap), for the following frequency bands: delta (1–4 Hz), theta (4–8 Hz), alpha (8–13 Hz), beta (13–30 Hz), low-gamma (30–45 Hz), known as the five main brain rhythms ([36], [37]). Welch's method is a PSD estimation method and is used to calculate the average periodogram of a time segment. Equation (4.2) defines the power spectral density, and (4.3) Welch's power spectrum, which is the mean average of the periodogram of each interval where it is computed.

$$S_l(\omega) = \frac{1}{M} | \sum_{n=0}^{M-1} w(n) x_i(n) e^{-j\omega n} |^2 \tag{4.2}$$

$$S(\omega) = \frac{1}{L} \sum_{l=0}^{L-1} S_l(\omega) \tag{4.3}$$

Then, the average power of the signal over each time segment is computed by integrating the PSD estimate, using the rectangle method. For each band, indices of relative power (RP) were obtained by expressing the absolute power (AP) in each frequency band as a percentage of the global absolute power obtained by summing the

five frequency bands. To investigate the robustness of the data, independently from the window length, the PSD was computed as well for the following window length: 2s, 4s, 8s, and 16s. Those results can be consulted in the supplementary material.

Statistical analysis The normality of the data was tested with a Kolgomorov-Smirnov test. As the data were not normal, a Wilcoxon signed-rank test was used, with a threshold of α=0.05. The statistical significance for each electrode was computed, comparing every single task (PRE, 25%, 50%, 75%, and POST) to the baseline. The comparisons were carried out, separately, for each frequency band, within each group (global population, male, female, under 30 years old, between 30 and 50 years old, over 50). Then the correction for multiple comparisons was performed using Bonferroni's method. The number of hypotheses tested was 64 channels for 5 frequency bands and 5 phases, leading to a final threshold of $\frac{0.05}{64 \cdot 5 \cdot 5}$=0.00003. To confirm this statistical power, another approach has been used, a permutation test, using 5000 permutations. The results from this last approach are displayed in the supplementary material.

4.3.3 Results

4.3.3.1 Global population results

Figure 4.18 shows the topological plots of PSD for each frequency band for the whole population. Figure 4.18a shows the absolute PSD and figure 4.18b the relative. Each column represents a frequency band, and each row represents the PSD difference of task (PRE, 25%, 50%, 75%, and POST) regarding BL. The "x" symbols represents significant electrodes (p<0.05). The "x" symbols highlighted in green represent significant electrodes after Bonferroni correction. The averaged PSD difference is plotted only for the significant electrodes after multiple comparisons correction.

For the absolute PSD, every band shows significant results for every task. The delta band has significant electrodes in the prefrontal and temporal scalp, with a PSD increase for each task regarding baseline. The theta band has significant electrodes mostly located in the parietal scalp, associated with a light PSD decrease. The alpha band has significant electrodes for the whole scalp, with a PSD decrease. The beta band shows significance in the whole scalp as well, with a PSD increase in the occipital area, and a PSD decrease everywhere else. Finally, the gamma band has significance mostly in the parietal, temporal, and occipital scalp areas, associated with a slight PSD decrease.

For the relative PSD, very little significance is shown in the theta band. A high PSD increase is observed on the whole scalp for the delta band, and a high PSD decrease is seen for the alpha band, for the whole scalp as well. The beta band shows a high significance in the PRE phase, on the fronto-parietal lobe, associated with a PSD increase. For the other tasks, there is a significant PSD decrease in the frontal scalp areas and a PSD increase in the occipital area. Finally, the low-gamma band shows a PSD increase in all the tasks, for all the scalp except the frontal one.

Figure 4.19 shows the number of significant electrodes in each task for all the bands, as well as the average PSD difference (phase - BL) evolution. Figures 4.19a and 4.19b present the number of significant electrodes for the absolute and relative PSD respectively, and the average PSD difference is presented in figure 4.19c for the absolute PSD and figure 4.19d for the relative PSD.
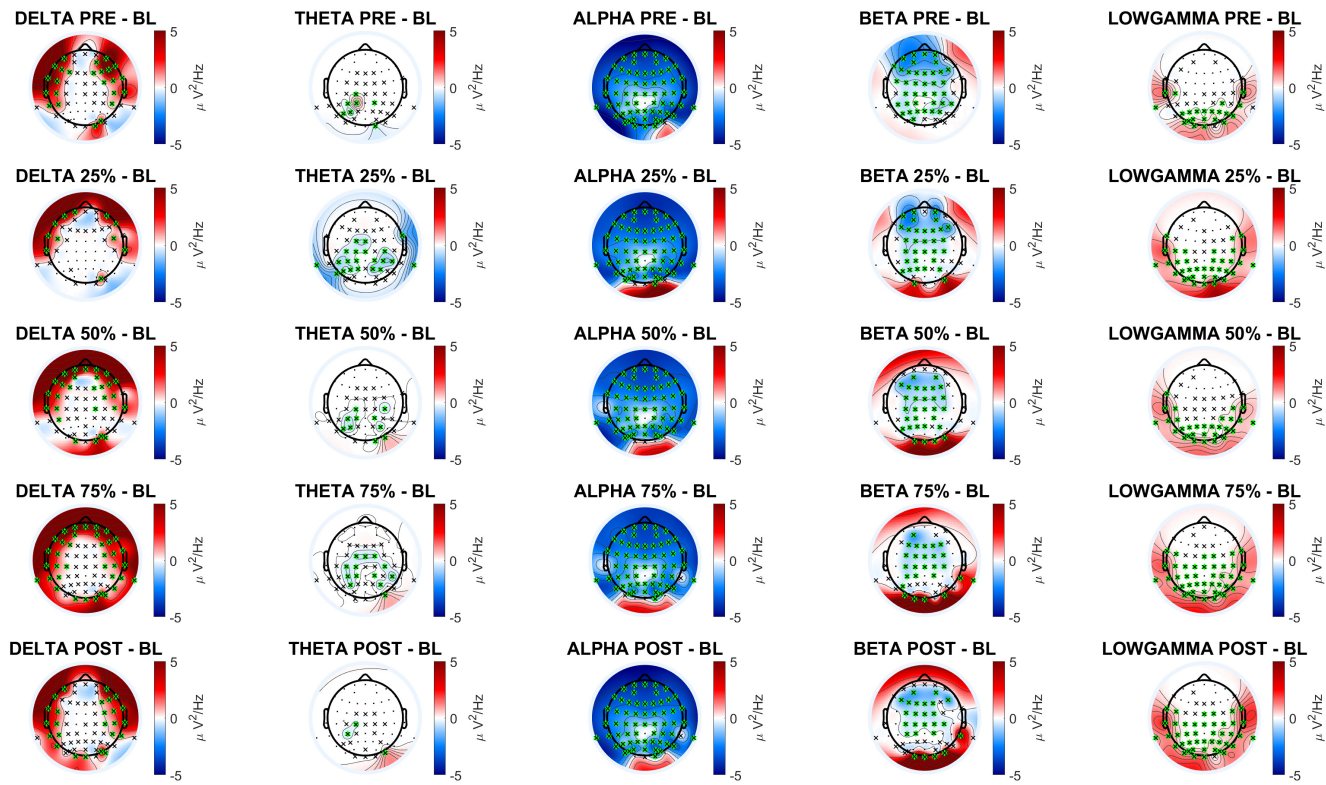
(a) Absolute PSD distribution of the whole population behaviour. The "x" highlighted in
green represents significant electrodes after Bonferroni correction.
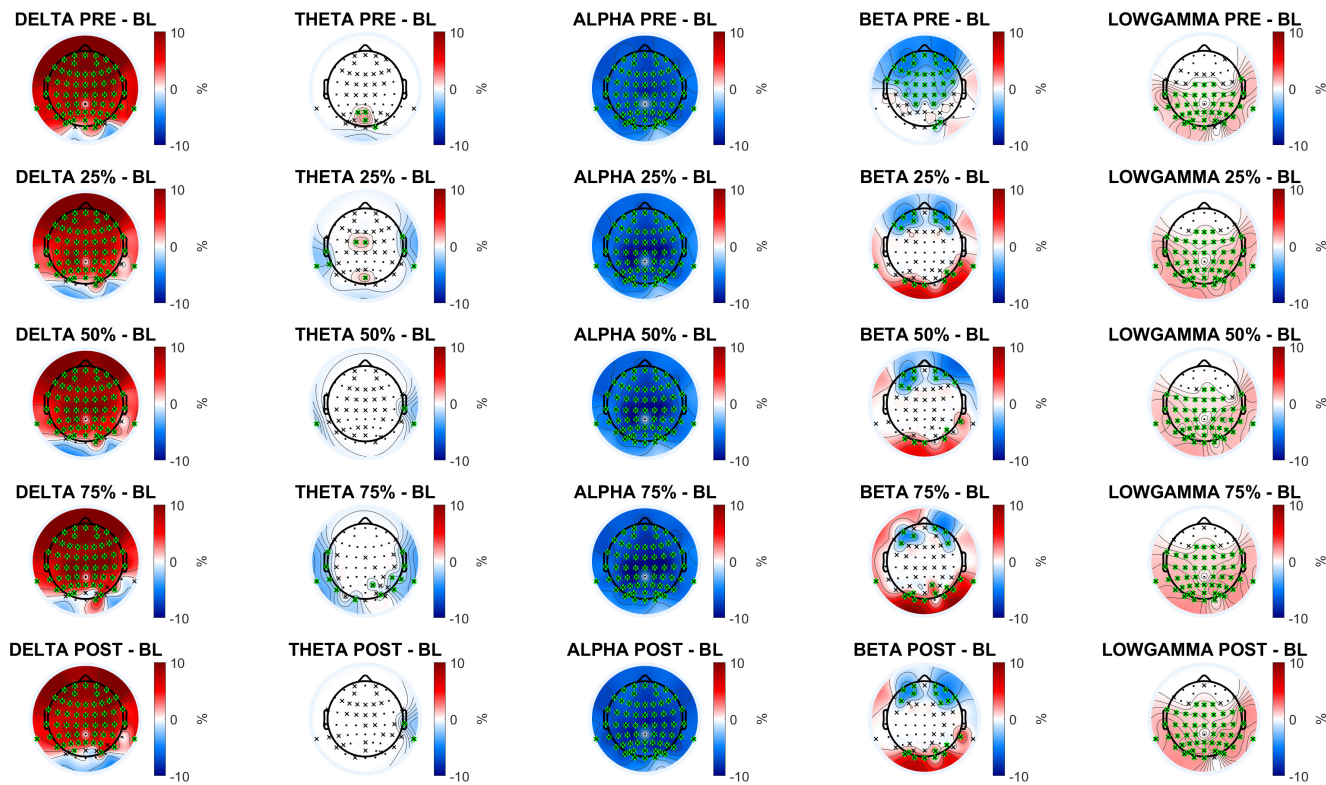
(b) Relative PSD distribution of the whole population behaviour. The "x" highlighted in
green represents significant electrodes after Bonferroni correction.

Figure 4.18: Global PSD distribution over the whole population.
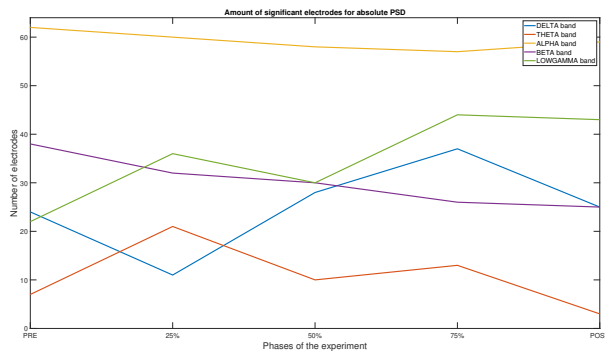
(a) Number of significant electrodes for every band, for each task, for the absolute PSD
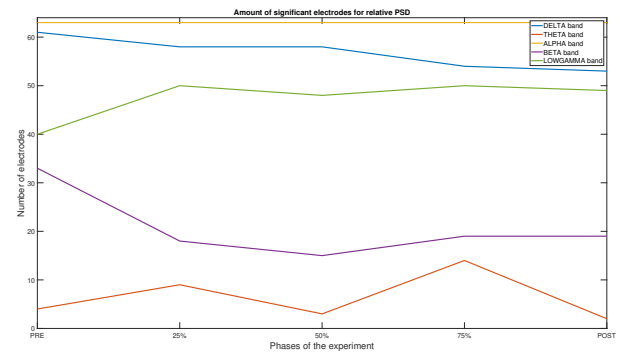
(b) Number of significant electrodes for every band, for each task, for the relative PSD
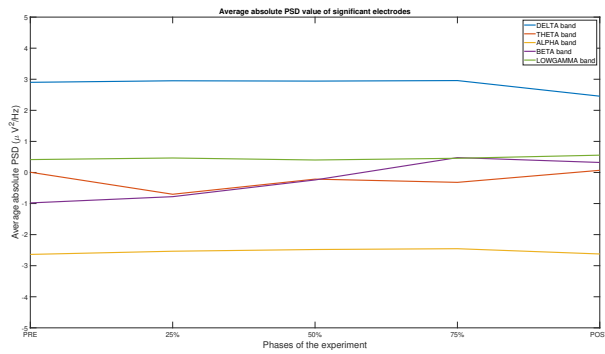
(c) Average absolute PSD (phase-BL) of significant electrodes for every band
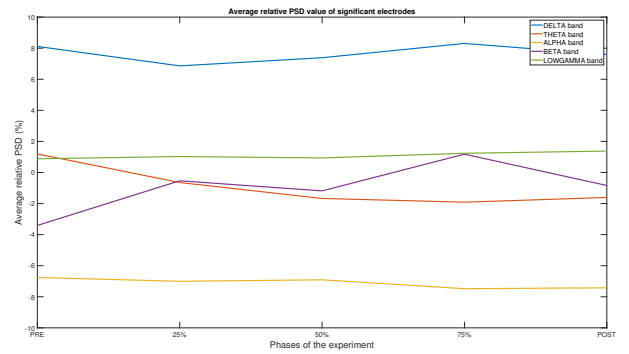
(d) Average relative PSD (phase-BL) of significant electrodes for every band

Figure 4.19: Amount of significant electrodes for every band, for each task

For the absolute PSD, the delta band (in blue) has 24 significant electrodes in the PRE phase, dropping to 10 in the 25% phase, then increasing constantly to 30 and 38 electrodes for 50% and 75% tasks. It is finally decreasing to 26 electrodes for POST. The associated PSD remains positive, staying constant at 3 μV^2/Hz, until the 75% phase, then slightly decreasing to 2.5 μV^2/Hz for the POST.

The theta band (in orange) has 8 significant electrodes in the PRE phase, increasing to 20 in the 25% phase, then decreasing to 10 for the 50% task. It slightly increases to 11 electrodes for the 75% task and then drops to 4 electrodes for the POST phase. The associated PSD starts at 0 μV^2/Hz for the PRE. It decreases to -1 μV^2/Hz in the 25% task, then increases slightly to -0.2 μV^2/Hz in the 50% task, remaining stable around -0.4 μV^2/Hz for the 75% task, to being very little above 0 μV^2/Hz for the POST task.

The alpha band (in yellow) presents more than 55 significant electrodes during the whole experiment, slightly decreasing from 62 to 57 from PRE to 75% task, then increasing to 61 electrodes for the POST. The associated PSD is always negative, slightly increasing from -2.7 to -2.5 μV^2/Hz until the 75% task, then decreasing to -2.7 μV^2/Hz for the POST.

The beta band (in purple) has 38 significant electrodes in the PRE task, constantly decreasing until 25 electrodes for the POST task. The associated PSD constantly increases from -1 μV^2/Hz in the PRE task to 0.5 μV^2/Hz for the 75% task, then slightly decreases to 0.4 μV^2/Hz for POST.

The low-gamma band (in green) has 22 significant electrodes in the PRE task, increasing to 37 electrodes for the 25% task, decreasing to 30 electrodes in the 50% task, increasing to 43 electrodes in the 75% task, and then remaining stable to 42 electrodes for the POST. The associated PSD is remaining constant for the all experiment duration, around 0.5 μV^2/Hz.

For the relative PSD, the delta band (in blue) has 61 significant electrodes in the PRE phase, and constantly decreases until 54 electrodes in the POST. The associated PSD remains positive, keeping a value between 7 and 9%.

The theta band (in orange) has 5 significant electrodes in the PRE phase, increasing to 10 in the 25% phase, then decreasing to 4 for the 50% task. It increases to 15 electrodes for the 75% task and then drops to 3 electrodes for the POST phase. The associated PSD starts at 1% for the PRE. It steadily decreases until around -2% in the 75% task, remaining stable at around -1.8% for the POST task.

The alpha band (in yellow) presents 63 significant electrodes during the whole experiment. The associated PSD is always negative, remaining around 7%.

The beta band (in purple) has 34 significant electrodes in the PRE task, decreasing to 19 electrodes in the 25% task, and 16 electrodes in the 50% task. It then increases constantly until 19 electrodes for the POST task. The associated PSD increases from -3.5% in the PRE task to -0.5% for the 25% task. It remains around -1% in the 50% task, then increases to 1% in the 75% phase. It finally decreases to -1% for POST.

The low-gamma band (in green) has 40 significant electrodes in the PRE task, increasing to 50 electrodes for the 25% task, decreasing to 47 electrodes in the 50% task, increasing to 50 electrodes in the 75% task, and then remaining stable to 49 electrodes for the POST. The associated PSD is remaining constant for the all experiment duration, around 1%.

Figure 4.20 are showing violin plots of the PSD distribution of the significant electrodes for all the bands, for each phase regarding BL. Figure 4.20a shows the absolute PSD, and figure 4.20b the relative. The average and standard deviation for each electrode across subjects are summed up in the supplementary material.
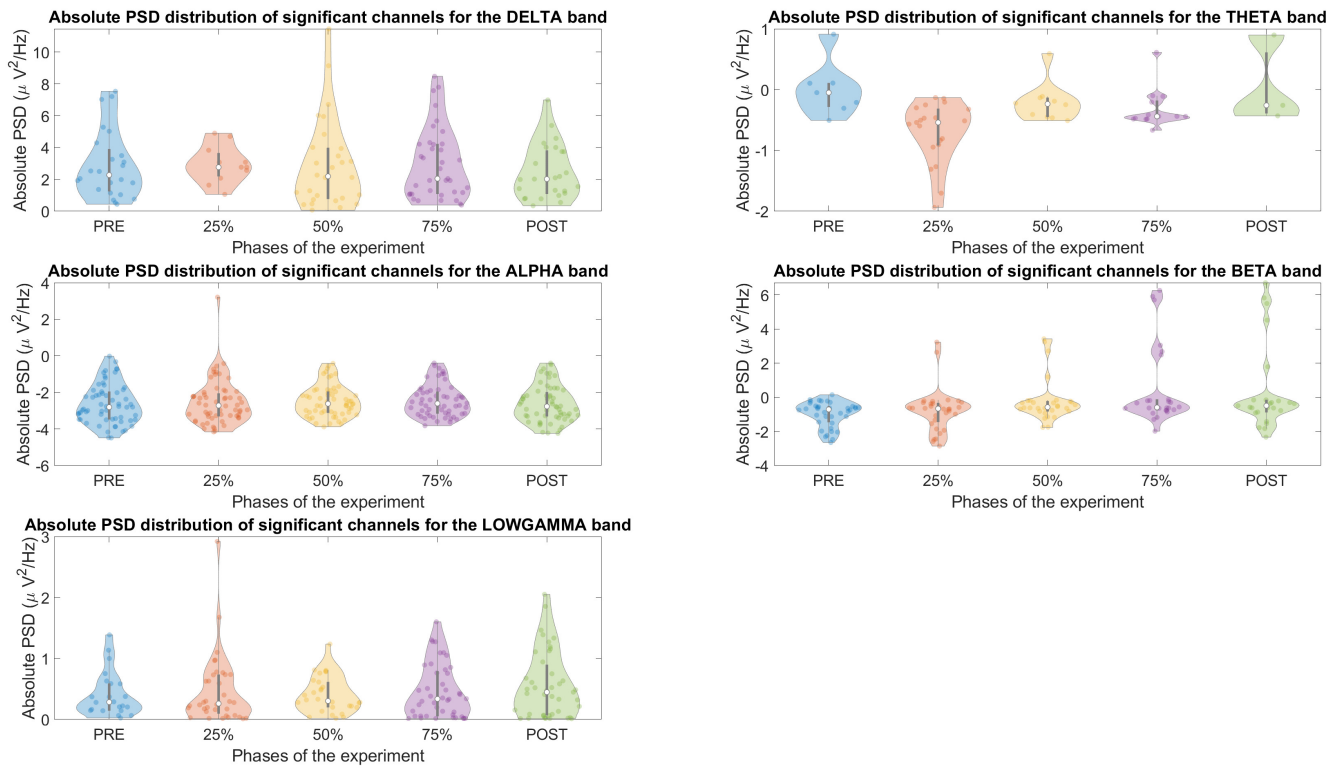
(a) Absolute PSD distribution of significant channels
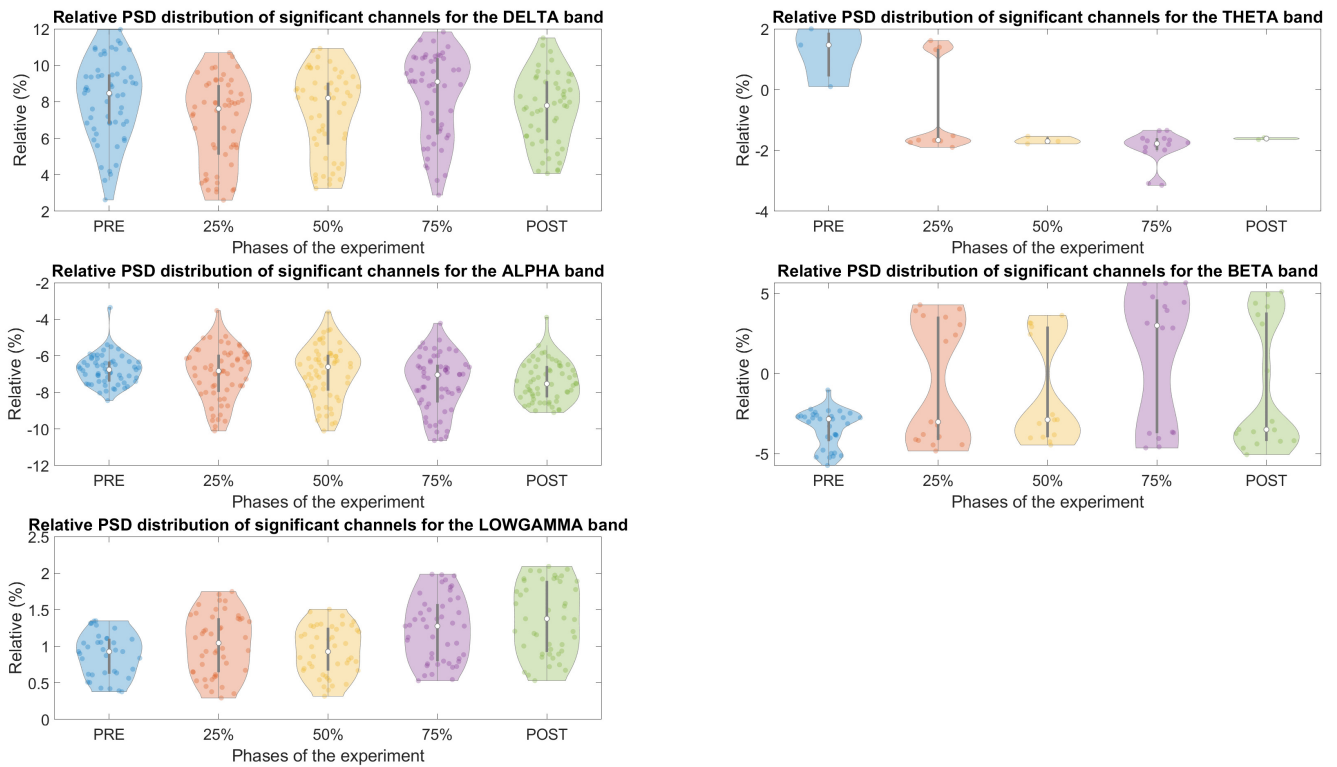
(b) Relative PSD distribution of significant channels

Figure 4.20: PSD distribution of significant channels

For the absolute PSD, alpha, beta, and low-gamma bands have similar distributions for all the tasks, with a high concentration of electrodes distributed around the median. For delta, and theta bands, most of the electrodes are located around the median as well, however, the distribution is more spread.

For the relative PSD, alpha, and low-gamma bands have similar distributions for all the tasks, with a high concentration of electrodes distributed around the median. For delta, theta, and beta bands, most of the electrodes are located around the median as well, however, the distribution is more spread.

4.3.3.2 Subgroups results

The results from subgroups have also been computed.

Men and women results   Figures 4.21 and 4.22 show the topological PSD plots of averaged male and female individuals for the alpha and beta band, the other bands showing no significance. Figures 4.21a and 4.21b show the absolute PSD for males and females, respectively, and figures 4.22a and 4.22b show the relative PSD for males and females, respectively.

For the absolute PSD, the behaviour looks close to the one of the global population, especially for females, with significant changes on the whole scalp for every task of every band, with the same areas involved. A global lower significance is observed in delta and theta. Male individuals present a similar trend, however, less significance is observed globally, with almost no significance in the theta band, and less significance in beta, and low-gamma.

For the relative PSD, for both males and females, the behavior is completely similar to the global one, with the high significance in delta associated with a power increase, and a high significance in alpha associated with a power decrease. The beta band shows a significant PSD decrease in the frontal scalp and a PSD increase in the occipital area. The low-gamma band shows a PSD increase in all the tasks, for all the scalp areas except the frontal one.

Results of age groups   Figure 4.23 shows the topological absolute PSD plots of the different age categories. Figure 4.23a shows the value for the under 30 years old, figure 4.23b for the 30 to 50 years old, and figure 4.23c for the over 50 years old.

For the absolute PSD, the behaviour of the under 30 years old is similar to the global population, with significant differences on the whole scalp for every task of every band. However, the two other age groups present way less significance. If some significance can still be observed in alpha and beta bands, the number of significant electrodes is very low (less than 15) compared to those under 30 years old.

Figure 4.24 shows the topological relative PSD plots of the different age categories. Figure 4.24a shows the value for the under 30 years old, figure 4.24b for the 30 to 50 years old, and figure 4.24c for the over 50 years old.

For the relative PSD, the behaviour of all age groups is similar to the global one. Less significance is observed in the 30 to 50 and over 50 years old age groups, but the amount of significant electrodes is still consistent, and it can be still noticed a strong significance in alpha and delta. For the low-gamma bands, there is a gradual decrease of significant electrodes through the age groups. Theta band shows no significance. The beta band shows a significance in the occipital area for the under 30 years old, for
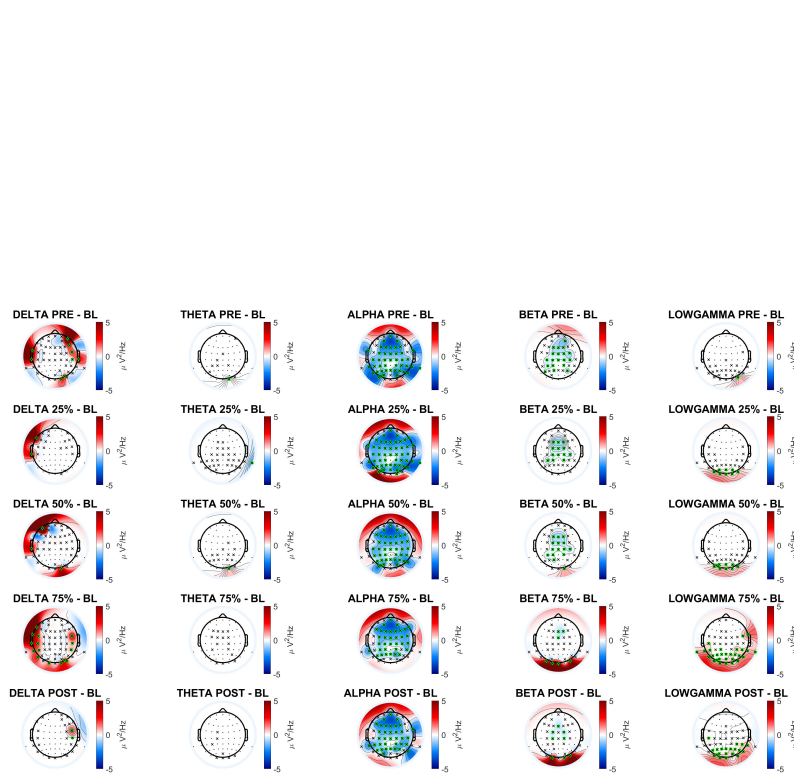
(a) Absolute PSD distribution of the male individuals. The "x" highlighted in green represents significant electrodes after Bonferroni correction.
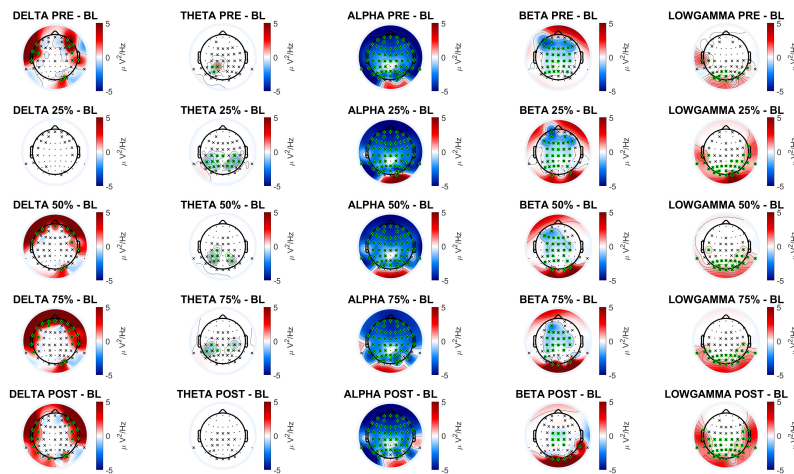
(b) Absolute PSD distribution of the female individuals. The "x" highlighted in green represents significant electrodes after Bonferroni correction.

Figure 4.21: Absolute PSD distribution of the male and female individuals
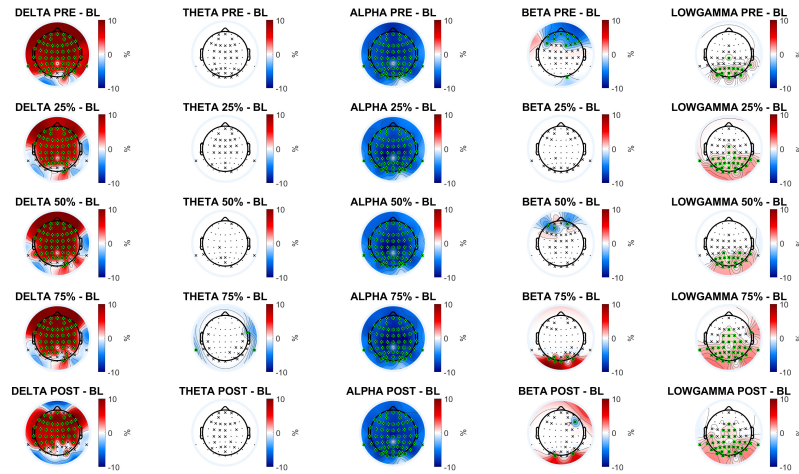
(a) Relative PSD distribution of the male individuals. The "x" highlighted in green represents significant electrodes after Bonferroni correction.
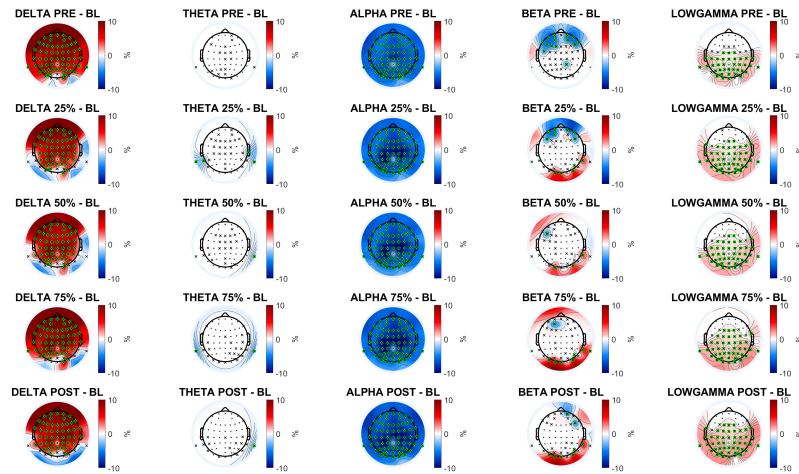
(b) Relative PSD distribution of the female individuals. The "x" highlighted in green represents significant electrodes after Bonferroni correction.

Figure 4.22: Relative PSD distribution of the male and female individuals
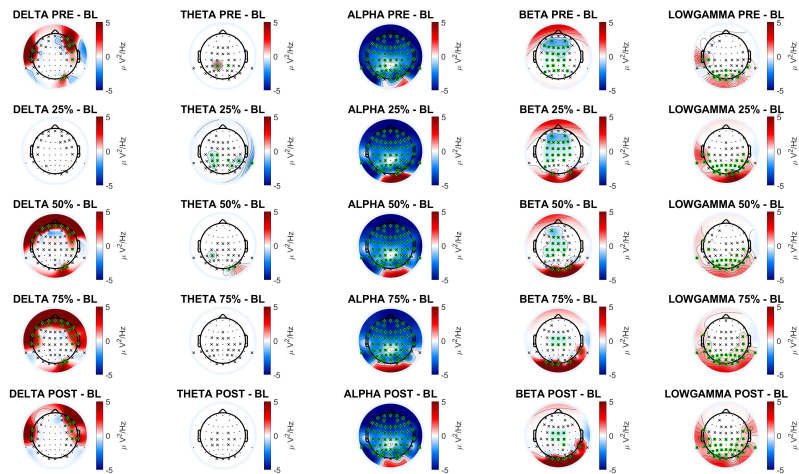
(a) Absolute PSD distribution of the under 30 years old individuals. The "x" highlighted in green represents significant electrodes after Bonferroni correction.
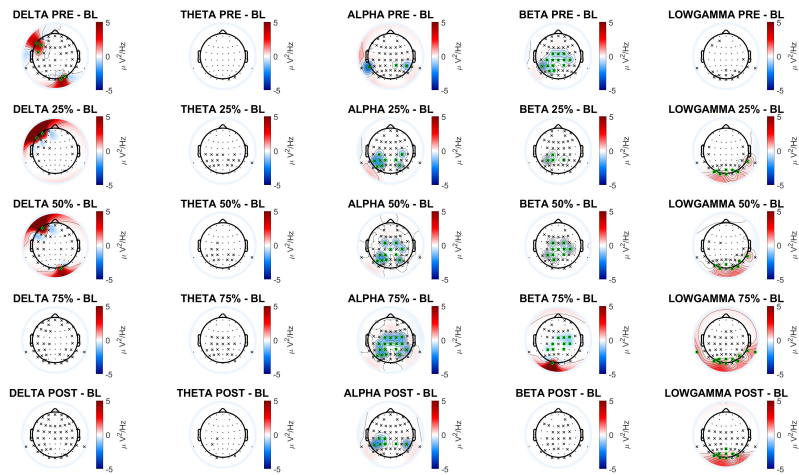
(b) Absolute PSD distribution of the 30 to 50 years old individuals. The "x" highlighted in green represents significant electrodes after Bonferroni correction.
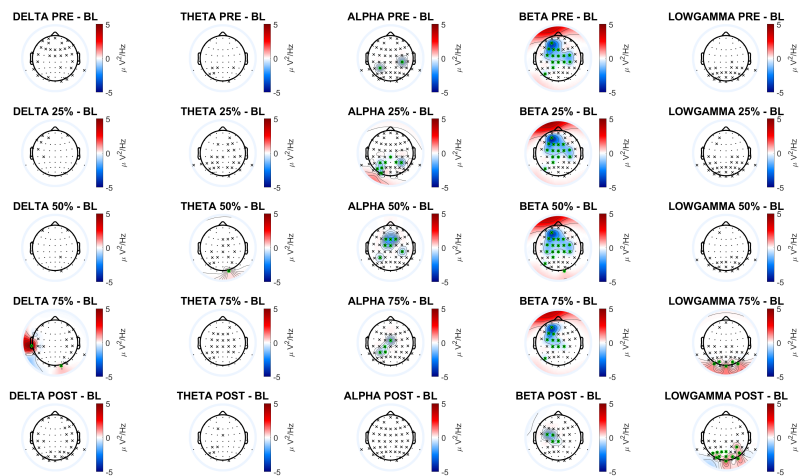
(c) Absolute PSD distribution of the over 50 years old individuals. The "x" highlighted in green represents significant electrodes after Bonferroni correction.

Figure 4.23: Absolute PSD distribution of the different age categories
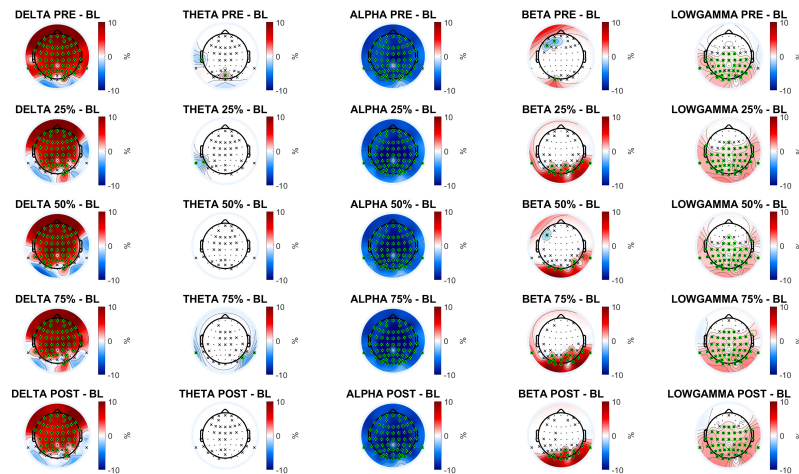
(a) Relative PSD distribution of the under 30 years old individuals. The "x" highlighted in green represents significant electrodes after Bonferroni correction.
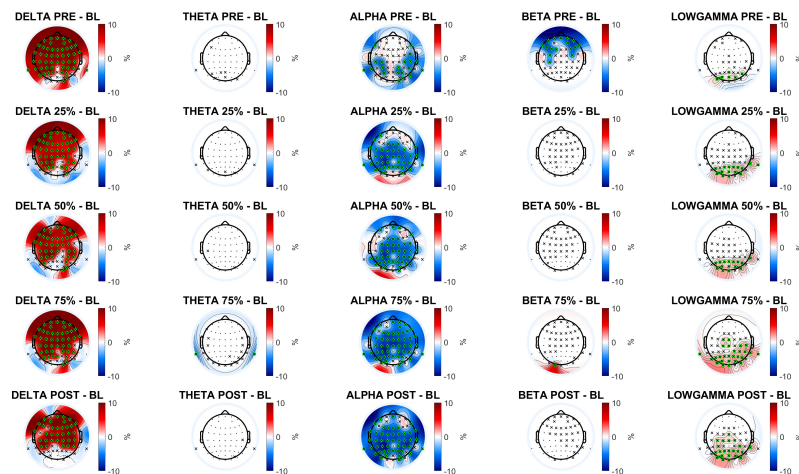
(b) Relative PSD distribution of the 30 to 50 years old individuals. The "x" highlighted in green represents significant electrodes after Bonferroni correction.
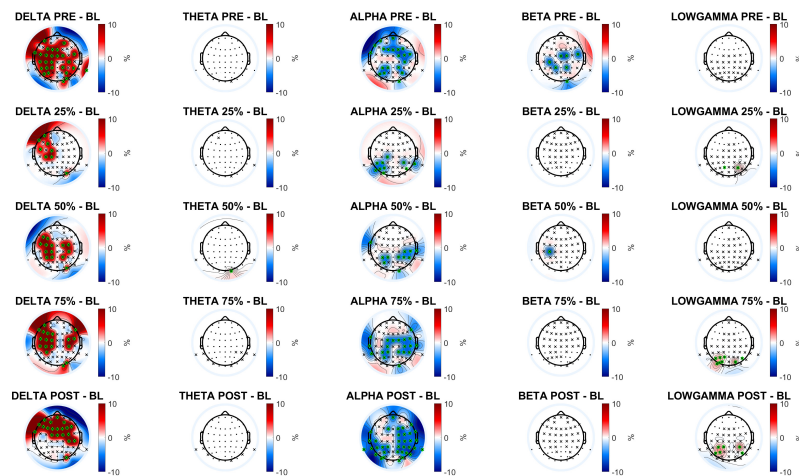
(c) Relative PSD distribution of the over 50 years old individuals. The "x" highlighted in green represents significant electrodes after Bonferroni correction.

Figure 4.24: relative PSD distribution of the different age categories

all the tasks, but a frontal significance only, for the PRE phase, for the 30 to 50 years old group, and for the PRE phase, parietal scalp, for the over 50 years old.

4.3.4   Discussion

The study aims to define a signature for the neurophysiological assessment of human behaviour during a complex postural control task. 190 individuals have been measured in a moving platform triggering MS to evaluate the brain response. This work suggests that quantifying neurophysiology associated with postural control tasks is possible. The results show a pattern of general behaviour: at the whole population level, all the bands are showing significant differences compared to the BL.

4.3.4.1   PSD modulations in delta band

The delta band shows a power increase for every task, in the frontal and temporal areas. [228] reported that an increased delta frontal activity is associated with an inhibition of sensory afferences that can disturb concentration. The frontal power increase during our experiment could reveal the presence of inhibitory oscillations to avoid spontaneous motor movement or to modulate peripheric activity. Other studies presented that the presence of delta oscillations could be related to motivation, attention, and subliminal perception ([229]). In terms of postural control, delta increased activation has been found over frontal and parietal scalp areas as the experiment became more sensory challenging, independently of the age range ([230]). A recent study highlighted that a higher delta power is linked with instability ([231]). Our experiment is directly linked with visual and/or movement stimuli and requires staying focused to maintain the posture and deal with balance perturbation. The high power increase in the frontal and temporal delta during our experiment reveals a standard response to this sensory stimulation and testifies to constant instability. These results are confirmed with significance over the whole scalp for the relative power, associated with a power increase as well. Even though results on the delta band have to be affirmed with caution, as it is highly sensitive to motion and ocular artifacts ([232]), the large cohort investigated in this study, as well as the thorough pre-processing pipeline before the power computation, make us believe that those results are robust. Delta power increase in frontal and temporal scalp areas should be considered in postural control studies to investigate sensory perturbation and instability.

4.3.4.2   PSD modulations in theta band

The theta band is the band showing less significance, mostly located in the parietal scalp during the platform movement, and has a quite small power decrease compared to BL. Theta activity is associated with cognitive tasks and memory in particular ([43]) and is increasing with a task requiring a lot of attention and cognitive demands ([233]). A previous work highlighted a lack of interaction between postural control task difficulty and theta power ([197]), but observe a similar theta power decrease. This is in accordance with what we observe, as the participant is asked to hold a bar during the platform movement. However, [234] observed a higher theta power for a task implying visual perturbation, assuming that the higher theta power is linked with a higher cognitive involvement as maintaining the balance is more difficult ([227]). All these

studies agree on the fact the fronto-parietal activity in theta is linked with error detection and processing, as well as planning and execution of movements related to balance ([235]). Regarding our experiment, the low power decrease and the little number of significant electrodes, only located in the parietal scalp, during the platform activation, compared to BL, could imply that the subjects did not provide a high cognitive effort for the activity proposed by the experiment and that a healthy population did not suffer much from a balance or postural control disturbance throughout the acquisition.

4.3.4.3 PSD modulations in alpha band

The alpha band shows significant changes over the whole scalp for all the tasks. Moreover, the alpha power for each task is lower than the baseline. Studies have shown that alpha suppression is a signature of mental and body engagement tasks, implying focused attention during a challenging task ([236], [237]). This suppression testifies to brain activity that involves information gathering, coordination, and concentration on the task ([238]). The parieto-occipital scalp remains significantly involved during the whole experiment for that band. The occipital area is activated during visual processing and perception tasks ([239]), and the parietal scalp is implicated in tasks implying body coordination and sensory perception of the environment ([240]), and these scalp areas are both correlated with alpha power suppression ([241], [242]). The BioVRSea setup used during this experiment combines postural control challenges with visually induced motion sickness. The fact that healthy participants presented a consistent significance in those areas and a power suppression in the alpha band can define a new marker of standard reaction to our experiment. This is strengthened by the fact that more than 90% of the electrodes remain significant for this band. The same behaviour is seen for both absolute and relative power, with a strong significance over the whole scalp and a high power decrease. Those results are in line with the literature regarding postural control, alpha power decrease in several scalp areas has been observed as well ([197], [234], [235], [243]). Alpha power suppression is one of the main neurophysiological markers of postural control, such as in our study.

4.3.4.4 PSD modulations in beta band

The beta band shows significant differences in several areas. The occipital scalp area shows a power increase compared to the baseline, except for the PRE phase, and the fronto-parietal areas of the scalp have a global power decrease. The occipital scalp areas are involved in visual processing, related for instance to spatial orientation ([244]). Research stated that beta power is associated with motor tasks, involving movement planning or execution ([245]). The beta power is constantly increasing during the experiment, especially from PRE to 25% and 50 to 75% tasks (with 75% and POST tasks having positive values regarding baseline). There is a peak of significant electrodes during the 75% task. This behaviour shows a higher commitment of the brain when responding to motor tasks, which are the activation of the platform and the maximum amplitude. This is confirmed by the power peak for the maximum amplitude task. The natural behaviour to this task would be a high beta power activity, testifying of movement execution, especially after a precise task such as grabbing a bar, requiring attention and anticipation ([246]), as well as resistance to a stimulus ([247]). Moreover, a high beta power is revealing the cue onset followed by a decrease

during movement planning and execution ([248]). Regarding postural control studies, [243] observed a beta suppression in the bilateral sensorimotor cortices, that was associated with stabilization support, but however an overall larger broadband power over the supplementary motor area. The power increase in occipital beta is associated with motor tasks, and the global power decrease in fronto-parietal scalp areas is observed as well in terms of relative PSD. This should be investigated as it could be the marker of the interaction between visual stimulation and motor movements during our experiment.

4.3.4.5   PSD modulations in low-gamma band

The low-gamma band shows significant electrodes in the whole parietal, occipital and temporal scalps. The average power remains positive compared to BL throughout the whole experiment. Low-gamma augmentation is linked with cognitive tasks, especially in the posterior cortex when associated with visual processing ([48]), but also related to instability ([249]). From our experiment, the higher low-gamma power in the posterior cortex can testify to the higher commitment to the task related to a visual stimulus. Regarding postural control, occipital low-gamma power has been found to increase during visual-related tasks, especially in the occipital area ([234]). A low-gamma increase in the whole fronto-parietal area has also been observed related to task difficulty ([235]). This is in line with our results, where the low-gamma significance is quite high in the parietal and occipital areas, especially in the POST task, for both absolute and relative PSD. These power increases testify to a high cognitive involvement associated with visual processing, but also a gradual instability feeling.

4.3.4.6   PSD modulations in subgroups

The same work has been done regarding subgroups, based on sex and age. Between men and women, the behaviour is quite similar in all bands. The main difference is the absence of significance in theta for men compared to women, and a generally lower significance in all the bands. The relative PSD on the other hand presents the same behaviour for both groups. For the age groups, people under 30 years old presented more significance than the others regarding the absolute PSD: all the bands are significant for every task. On the other hand, the two other age groups present few significant differences in the bands. However, the relative power presents similar results for all the groups, with slightly less significant electrodes for those over 50 years old. Despite being limited, differences between sex and age groups, on one hand, may be explained by the differences in samples size (particularly for age groups, there was a lower number of subjects (n=33) in those over 50 years old, compared to the others) but, on the other hand, they are not easily addressable for the presence of several subjective psychological factors (such as some anxious personality traits strictly linked to higher neurovegetative reactions) that may influence the neurophysiological responses during the execution of the postural control paradigm and that were not investigated.

4.3.4.7   Absolute vs relative PSD

In the current manuscript, we implemented one of the most classical methods to explore EEG signal, the analysis of the spectral power (using PSD), which is a linear method

for the frequency-domain representation of the variance of the signal. The spectral power of the EEG was expressed as AP (energy/power in a chosen frequency band) and RP (energy/power in a chosen frequency band divided by the total energy/power of five frequency bands). On one hand, RP may lose some quantity of frequency information because of its own nature of being a "power standardization" measure ([250]): power is standardized for total power, the summation of the different five frequency bands is constantly one and, subsequently, the values of RP may decrease when the values of AP increases. On the other hand, RP is not susceptible to any power distortion, caused by frequency mismatch ([251]) or volume conduction, which may largely affect AP. The main differences in significance we observed in the current manuscript between AP and RP may be due to the changes in the variance in the whole EEG signal / in the power of the five frequency bands since, as discussed above, RP is adjusted for the EEG total power. Thus, we cannot exclude that those differences in scalp maps and frequency bands between AP and RP may be generated by the "power standardization" expressing in a standardized way changes and shifts among frequency bands. Additionally, we may speculate that AP and RP are sensitive to different brain processes or different expressions of the same process in different brain areas. In particular, RP can be susceptible to distinct processes because this measure is the result of a mixture of several frequency band powers. However, in our study the differences observed between AP and RP are only visible regarding significance; for each band and each task with enough significance for both powers, the same power variation is observed in AP and RP. The higher significance of RP compared to RP in the two extreme frequency bands of our study (delta and low-gamma) confirms first, the interest in considering those two bands in postural control studies, and second, that RP is a measure of interest in EEG studies, and should be investigated alongside AP. Moreover, RP showed a better significance in subgroups, highlighting its importance to differentiate smaller cohorts of different characteristics. All those reasons lead us to believe that RP provides valuable information that should be investigated in further studies.

4.3.4.8 Limitations

Because of the originality of the paradigm of postural control we implemented, we recognize that our results are generally not comparable with other studies on postural control. Furthermore, this work has some limitations, mainly related to the compositin of the enrolled smaple. First of all, the people measured in this study are all healthy. The results can not be compared yet with a cohort presenting pathologies, related to central postural control disturbance, like Parkinson's disease or stroke for instance, or related to peripheral postural control disturbance, like those people affected by chronic low back pain or osteoarticular disorders of the hips or knees for instance. It would also be interesting to compare those results with subjects suffering from known pathologies presenting a different brain response, such as epilepsy or schizophrenia, or those mental illnesses with a high arousal activation such as anxiety or stress-/trauma-related disorders. Also, the population is heterogeneous in gender and age distribution: there is a majority of women and subjects under 30 years old, even if the number of men and people over 30 years old remains adequate to draw conclusions. Harmonizing the demographic characteristics of the cohort will help to strengthen our results.

4.3.5 Conclusion

This work proposes a new perspective towards the identification of a neurophysiological signature during a dynamic postural control paradigm. Our study uses an innovative setup, BioVRSea, that already showed promising results regarding postural control. A large number of individuals (190) participated in this study. This experiment is based on a dynamic task triggering postural control, where the analysis of the different phases can give us a strong indication of behavioral patterns in healthy individuals. The frequency band analysis of our experiment's global cohort presented valuable results. The confirmation of important results of the literature, such as alpha suppression and low-gamma increase, proves that the methodology used during this study is robust and viable. Moreover, it highlights the impact of this experiment on postural control, and leads to the identification of potential neurophysiological markers:

- for the delta band, an absolute power increase in the frontal area, and a relative power increase over the whole scalp;

- for the theta band, no strong significance is seen, but the absolute power inhibition in the parietal scalp areas, related to motion and visual stimulation, should be investigated more in detail;

- for the alpha band, a global power inhibition in the whole scalp;

- for the beta band, a power inhibition in the fronto-parietal area and a power activation in the occipital area;

- for the low-gamma band, a power activation in the parieto-occipital scalp.

The identification of neurophysiological markers of postural control, as well as the identification of a reference assessment and later signature of a healthy response towards dynamic postural control task, would be of help towards a deeper understanding of brain cortical activity during postural control. Moreover, it could lead to the development of potential diagnostics of neurodegenerative conditions and assessment methods for rehabilitation. This work will be pursued with more advanced analysis, such as the study of brain connectivity, through the analysis of the dynamics of brain networks throughout the experiment. Besides, balancing the subjects' population by gender and age as well as implementing this approach with individuals suffering from pathologies such as Parkinson's disease will help to validate these results as a new reference for the neurophysiological assessment of PC. This work is the first step towards a neurophysiological signature to evaluate complex postural control tasks.

4.4 Brain network dynamics

The work below is currently under review in *Journal of Neural Engineering*. The aim of this study was to decipher brain network dynamics during a complex postural control task, computing functional networks from EEG time-series, and using clustering algorithm to segment brain network states, over 158 individuals.

4.4.1 Introduction

The role of postural control (PC) is crucial in daily life. Maintaining upright balance during postural tasks, gait and orientation are demanding and rely on PC [135]. PC is a complex mechanism, based on the interaction of dynamic sensorimotor processes [190]. It is a central nervous system feedback control system, where neural activity is essential to communicate with muscle activity and physiological as well as visceral autonomic control systems, to anticipate and react to gravity, movements, and constant changing posture[169], [252]. Thus, any events provoking a dysfunction of neural activity will disturb PC. This implies that studying PC could help to diagnose, or at least differentiate healthy behavior from a pathological one, such as neurodegenerative disease for instance [253]. This is a reason why the identification of quantitative metrics regarding PC, on the neurophysiological level, is of high interest. However, even though neural circuitry is prominent to ensure steady PC, the underlying neural mechanism is still largely unknown. Using neuroimaging techniques such as fMRI or functional near-infrared spectroscopy (fNIRS) several studies highlighted the role of brain activity in PC studies [254], [255], to study the impact of brain traumatic injury on balance performance for instance [256]. The same approach has been used to study these injuries with electroencephalography (EEG) [257]. EEG proved to be of high interest in PC studies, during the control of balance to specific motor stimulation [243], or to decipher adaptation and habituation phenomena [139], [140]. Compared to other imaging techniques, EEG is more flexible: it does not require a licensed training, it's inexpensive, but above all, it enables mobile experiment setups, and provides a very high temporal accuracy [33], enabling to track fast changes of brain cortical activity. For those reasons, EEG is very convenient to use in PC experiments, where brain activity can be easily recorded while a subject is undergoing different stimulations challenging its balance.

Based on EEG analysis, it has been shown that spectral power extracted from the different frequency bands of the brain is an indicator of cerebral cortex involvement during PC tasks [227], or to differentiate a healthy behavior from a pathological one [164]. Other studies used evoked potentials to highlight the correlation between brain cortical activation and balance related tasks [224], [258]. Yet, more advanced techniques, using mathematical tools, are built up to deepen the analysis and identify more accurate metrics.

An innovative methodology, based on graph theory, has been emerging recently and has shown encouraging results so far. Brain functional connectivity is using the EEG time series at the scalp level to reconstruct brain sources and compute brain networks. It, therefore, studies the interplay between brain regions as well as the strength of the connections. Its robustness and usefulness have been observed in many studies [68], [126] and already showed promising results in terms of PC analysis [257], [259]. Brain network analysis helps to identify the functional regions involved during a task, thus the cognitive processes involved. Previous works [24] observed specific networks

patterns during common tasks (e.g., resting state, visual, auditory tasks). The identification of these patterns and the associated hubs involved during those tasks set the foundation of resting state networks (RSN). Computing brain networks from EEG, and comparing their metrics to the known RSN, is a concrete application of brain functional connectivity to decipher brain functional response to dynamic tasks. However, for now, the functional connectivity associated with EEG in PC did not fully exploit the high temporal resolution of this measuring technique.

Based on previous studies [57], [260], the analysis of EEG time series showed voltage topographies remain stable for a period of around 80-120ms. Those stable periods have been mentioned as functional microstates. The study of microstates helped to comprehend brain states and to characterize brain functions in several studies [261], [262]. More and more tools are available to process and analyze microstates [262], [263]. During dynamic tasks, the review of microstates is a promising tool to decode brain cortical remodeling. From this aspect, we are interested to study the dynamicity of brain networks (that are now mostly limited in time), based on the method developed to compute EEG microstates.

The current work will introduce an innovative workflow, combining the two approaches mentioned above. From the EEG time series, sequences of brain connectivity matrices and dynamic brain networks will be computed. Then, we will identify states, by clustering network distributions, mainly due to stable network configurations over time. These resulting states will be called brain network states (BNS). The study of BNS evolution and characteristics will help to validate this new methodology and open new perspectives on the appreciation of brain function during dynamic tasks. This approach has already been used with a few subjects at rest [264], [265], or more recently developed in the study of Parkinson's disease [266]. Yet, the spatiotemporal dynamics of functional brain networks during complex PC tasks are still unclear.

As a model PC, we have recently developed the 'BioVRSea' (figure 4.25), a novel measurement setup that consists of a moving platform and a virtual reality (VR) simulation mimicking the behavior of a boat in the sea, and several biosignals measurements. BioVRSea paradigm is a dynamic PC task, where the stimulation is modulated through time. It already showed promising results in terms of deciphering PC responses, for instance with concussion [153], and has been used as a first step towards the identification of markers of motion sickness [141]. Here, our objective is to decipher the spatiotemporal dynamics of brain networks during the BioVRSea paradigm. We believe that this approach will allow us to observe the dynamic remodeling of the brain during a complex PC task, by watching the dynamic network evolution through the experiment. To do so, we use advanced EEG analysis consisting of constructing the time-varying functional brain networks at the source-level. The k-means clustering algorithm was then used to segment these time-varying connectivity matrices into a set of BNS. Applied to a relatively large sample size (N=158) of healthy participants, our results showed that this data-driven segmentation matches very well with different transitions during the task. The work presented in this study would be the first to show spatiotemporal brain network dynamics in 158 individuals.
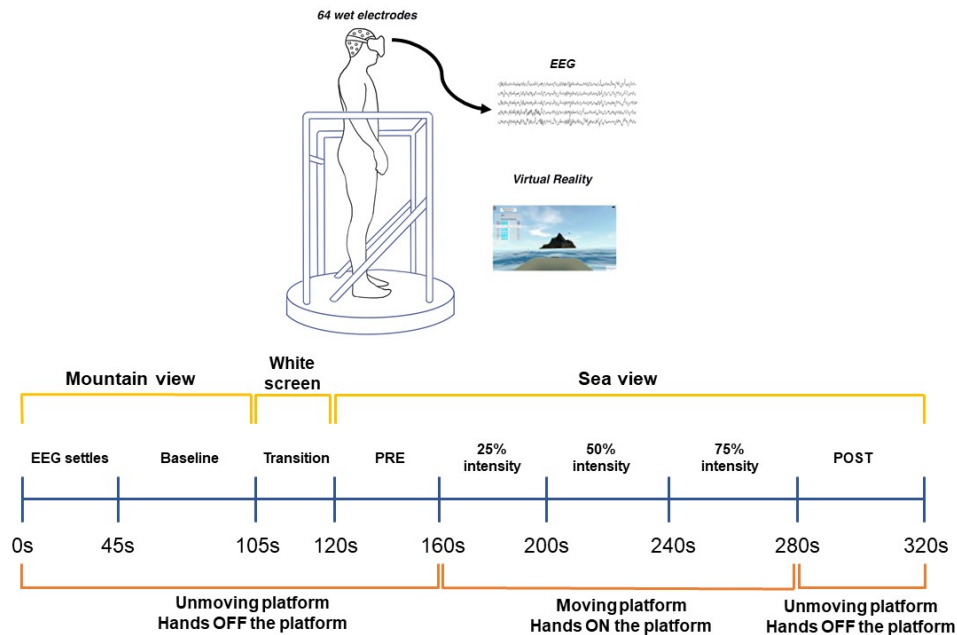
Figure 4.25: Experimental setup, acquisition workflow

4.4.2 Material and methods

4.4.2.1 Participants

Participants were recruited through snowball sampling. Written information about the study was provided, and all the participants had to sign a written informed consent before starting the acquisition procedure. At the time of the study, 158 individuals (93 women, 65 men, age range= 19-72 years old, mean age=32.9 years old, std age=13.2 years old) completed the experiment.

4.4.2.2 Questionnaire

Before the acquisition, the participants were asked to answer a Motion Sickness Susceptibility Questionnaire (MSSQ) based on the adult questionnaire proposed by Golding[143]. Subsequently, the participants also had to fill out a motion sickness symptoms questionnaire right before and right after the experiment. This questionnaire evaluates 10 motion sickness symptoms on a score from 0 to 3: General discomfort, Fatigue, Headache, Eye strain, Difficulty focusing or concentrating, Increased salivation, Sweating, Nausea, Blurred vision, Dizziness, or vertigo. From that information, two scores were calculated, the MSSQ score and the symptoms score. The MSSQ score is calculated by using the same formula explicated in Golding. This MSSQ is composed of 9 items (scores from 0 to 3), with a maximum score of 27. The symptoms questionnaire score is calculated by subtracting the average of the symptoms before the experiment from the average of the symptoms after the experiment, to obtain a final score between 0 and 3.

4.4.2.3 Acquisition

The acquisition procedure is the same one that has been described in Jacob et al [153]. Before the acquisition started, the subject was equipped with a wet 64-electrode EEG cap (Sampling frequency 4096 Hz, ANTNeuro, Hengelo, The Netherlands). The

participant was then asked to step onto the platform. The subjects had to stand
quietly on the platform with their hands by their side observing a mountain view for
1min45s (the last 60 seconds of this step were used as a baseline). Then, the scene
in the VR goggles would change, with a white screen preparing for the sea simulation
(15s). The participants were instructed to remain standing quietly with their hands
by their sides for the first 40 seconds of the sea simulation. There was no platform
movement in this part of the experiment, called task PRE. After 40 seconds of quiet
standing watching the sea simulation, the participant was instructed to hold onto the
bars in front of them. The platform then began a synchronized movement with the
sea scene in the VR goggles, with 25%, 50%, and 75% of maximal wave amplitude.
In this central part, each segment lasted 40 seconds and the participant held the bars
of the platform while continuing to observe the sea simulation. Finally, the platform
stopped moving and the participant was asked to remove their hands from the bars
and attempt to stand quietly with their hands by their side for the final 40 seconds
of the experiment. The sea scene was still observed by the participant for the final 40
seconds. This is called the POST phase of the experiment; it is performed identically
to the PRE phase but after the participant has performed movements in the central
part of the procedure. Figure 4.26 sums up the data processing workflow.
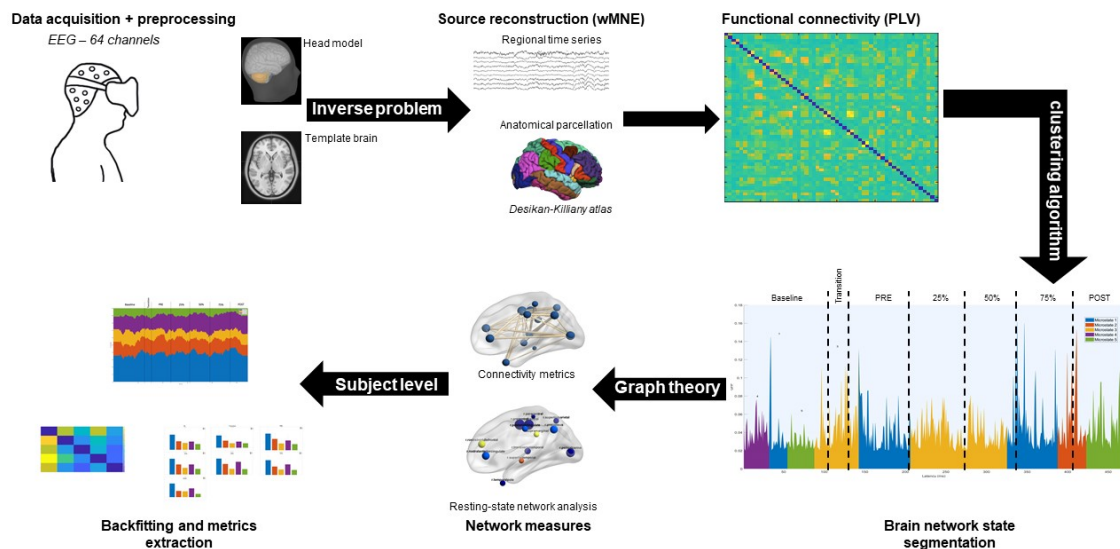
Figure 4.26: Data processing workflow. From the EEG time-series, ROIs are recon-
structed. The functional connectivity between those ROIs is computed. Then, using
clustering algorithm, BNS are segmented at the group level. Using graph theory, met-
rics are extracted from the network to quantify and analyze their functions. Then, the
segmentation is studied at the subject level to study the prevalence of each BNS.

4.4.2.4 Data preprocessing

The EEG was recorded using a 64-electrode channel system. Data pre-processing and
analysis were performed with Brainstorm [124] and Matlab2021b (MathWorks, Inc.,
Natick, 158 Massachusetts, USA), using the Automagic toolbox [175]. The data were
resampled to 1024 Hz. The data were notch filtered at 50 Hz. A high pass and low pass

Variable	Description	Value
N	Number of dynamic connectivity matrices	478
n	Dimension of dynamic connectivity matrices	56
Ai,j	Element of one connectivity matrix	-

Table 4.5: Summary of variables describing matrices information

filter were set respectively to 1 Hz and 45 Hz. Automagic was used to automatically pre-process every dataset, with a manual inspection at the end. The ICA MARA algorithm was used, with a variance of 20%. Finally, bad electrodes were interpolated. Each file needing interpolation of more than 15% of the total amount of electrodes was rejected, and the associated individual was excluded from the experiment, leading to 158 complete EEG recordings lasting around 5min18s.

4.4.2.5 Data processing – Dynamic network computation

In the two following sections, several variables are expressed to describe the matrices information. Table 4.5 sums up the listed variables and their description.

Brain networks were constructed from the pre-processed EEG signals, using an approach called 'dense-EEG source connectivity', which was developed and used in previous studies [68], [126], [266], [267]. This method aims to solve the inverse problem and reconstruct brain sources from EEG time-series. The 45 first seconds of the acquisition have been used to constitute the noise covariance matrix. Then, the weighted minimum-norm estimation (wMNE) method was used to obtain the source distribution [126]. Of the 64 electrodes, 56 regions of interest (ROI) were estimated, based on the Desikan-Killiany atlas [4]. The list of the ROI is provided in the supplementary material. Finally, the connectivity matrices between these 56 ROIs were computed, for the alpha band (8-13Hz), using the phase-locking value (PLV), a sliding window approach, with a window size of 6 cycles [268], resulting in a window of 571ms. It leads to N = 478 matrices per subject, of dimensions 56 × 56, where each element Ai,j of a matrix represents the weight of the connection from the node i to the node j. This element is called edge.

4.4.2.6 Data processing – Brain network state identification

These dynamic matrices have been averaged over 158 subjects, to have a final structure of 478 matrices. From this final dataset, brain network states segmentation was performed, using clustering to identify stable periods over time. This analysis was done based on some functions developed in the EEGLab Microstate toolbox [263]. This toolbox is designed for EEG voltage topography, but we adapted the pipeline to use it with functional brain network as an input. Since the n n matrix (n=56) is symmetric, we vectorized it in a (n*(n-1)/2) =1540 elements vector. Then, the modified k-means algorithm [269] was used as a clustering algorithm, and the BNS were sorted according to global explained variance (GEV)[263]. To identify the right number of BNS, we tested the segmentation from 2 to 20 BNS. The number of random initializations was set at 100, and the max number of iterations was set at 1000, with a default convergence threshold of 10^{-6}. To ensure an optimal segmentation, the process has been rerun several times (in our case four times), and has been compared qualitatively to select the most suited. After the segmentation, a smoothing has been performed

to remove the small peaks or unstable states. All states being present in less than 20 consecutive matrices were changed to the next most likely brain network state.

4.4.2.7 Data processing – Brain network states and Resting-states network correspondence

Each segmented state was then computed from a vector to a 56×56 symmetric matrix. This represents the functional network associated with the BNS. Based on the studies published by Kabbara et al.[267], and Shirer et al.[24], we associated each of the 56 nodes with 7 RSN: DMN, DAN, SAN, MOT, AUD, VIS, and Other. The affiliation of each node and RSN is summed up in the supplementary material. Then, using Brain Connectivity Toolbox [129], the strength (sum of weights of each link connected to the node) of each node has been computed. We then computed the strength of each RSN by summing the values of each node associated with this RSN and dividing it by the number of nodes belonging to the RSN. To identify the dominant RSN for each BNS, we elicited those with a value superior to the sum of the average and standard deviation of the 7 RSN strengths. For visualization purposes, only the nodes with a strength > 0.1 were displayed, using BrainNetViewer [270]. Each region of interest (ROI) defined from the Desikan-Killiany atlas is affiliated with the corresponding RSN.

4.4.2.8 Data processing – Quantification

After the BNS segmentation was performed on the averaged matrix, we returned to the subject level by performing a backfitting. Each sample is associated with the most similar BNS, based on global map dissimilarity [61], [263]. As a result, we have a BNS distribution for each subject. To analyze it, the percentage of BNS repartition per subject is computed for each of the 478 matrices. Moreover, two metrics are computed: first, the transition probabilities matrix, revealing the transition probabilities from one state to another, and the occurrence, which indicates the average number of times per second a BNS is dominant [263].

4.4.2.9 Data processing – Relation with questionnaire

As mentioned in the results section, the relationship between metrics (global transition matrix, transition matrix per phase of the experiment, global occurrence, occurrence per phase) has been investigated with age groups and questionnaire results groups, dividing them with the following criteria:
• Age: 30 youngest (age range= 19-22 years old, mean age=21.2 years old, std age=0.7 years old) compared to the 30 oldest individuals (age range= 48-72 years old, mean age=56.1 years old, std age=6 years old)
• Motion sickness susceptibility questionnaire (MSSQ): 15 highest scores against 15 lowest
• Motion sickness symptoms (MSS): 15 highest scores against 15 lowest
For the age, we chose the 20% top and 20% lowest to observe the age difference impact and have enough subjects in each group to draw a relevant statistical analysis. For the MSSQ and MSS, we chose 10% of the top and lowest scores, to remain coherent in the groups, and not include people that were not feeling sick or prone. Even though the number of individuals is not high, it is enough to perform preliminary statistical analysis, and therefore observe a trend in the results.

4.4.2.10 Statistics

For the relationship between age or MS related questionnaire, a Wilcoxon rank sum test (α=0.05) has been performed. If a parameter was observed as statistically significant, it was then corrected for multiple comparisons using a false discovery rate [176].

4.4.3 Results

4.4.3.1 EEG reveals five brain network states during PC

The functional brain networks were computed over the entire experiment, at the alpha band– due to its significance in previous connectivity and PC studies [259] – using the EEG source connectivity method [126]. Briefly, we estimated the dynamics of brain sources, then we computed the statistical coupling between brain regional time series (N=56). This was done using a sliding-window approach (window size of 6 cycles according to Lachaux et al [268]. This yields 478 connectivity matrices for the entire task. Then, we wanted to cluster those matrices into brain network states (BNS), using the k-means algorithm, which is a set of networks that dominate over time. The BNS segmentation was performed on the averaged dynamic networks from all the subjects (see Materials and Methods for details about EEG signals processing, network construction, and BNS segmentation). As detailed in the Material and Methods section, the BNS segmentation has been repeated four times, and a qualitative inspection has been done in each of them, to result in an optimal number of clusters k=5.
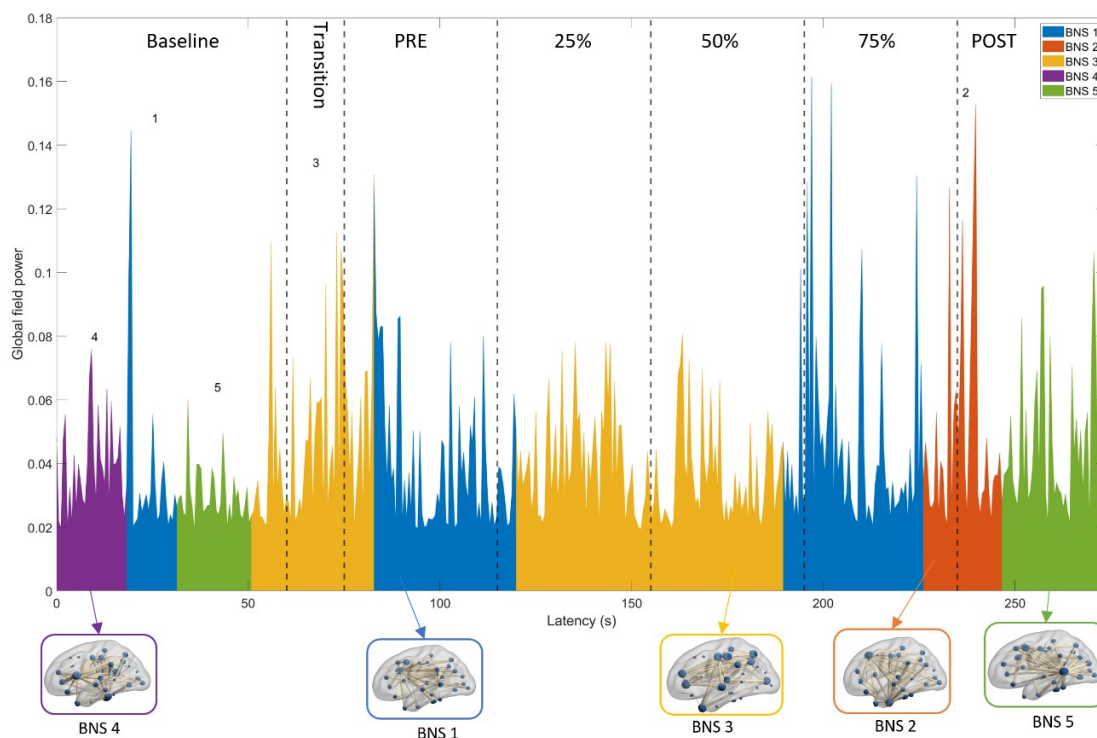
Figure 4.27: Dynamic BNS segmentation over the fulltime experiment. This figure shows the results of the BNS segmentation on the experiment, displaying their distribution over the time. 5 BNS have been identified, and their respective networks are shown below the distribution.

The segmentation leads to five BNS during this PC paradigm (figure 4.27). The correspondence of each BNS to a functional network (according to previous studies(Kabbara et al., 2017; Shirer et al., 2012)) is illustrated in figure 4.28. The baseline is composed of BNS 4 (default mode network –DMN-), BNS 1 (salience network -SAN-), and BNS 5 (SAN). BNS 3 (auditory and motor networks) appears slightly before the transition phase, until slightly after the PRE phase. Then BNS 1 appears again until the end of the PRE phase. BNS 3 is present for the whole 25 and 50% tasks, and switches to BNS 1 right before the 75% task. A bit before the POST phase, BNS 1 switches to BNS 2 (Visual network -VIS-), until a third of the POST phase, where it switches to BNS 5.
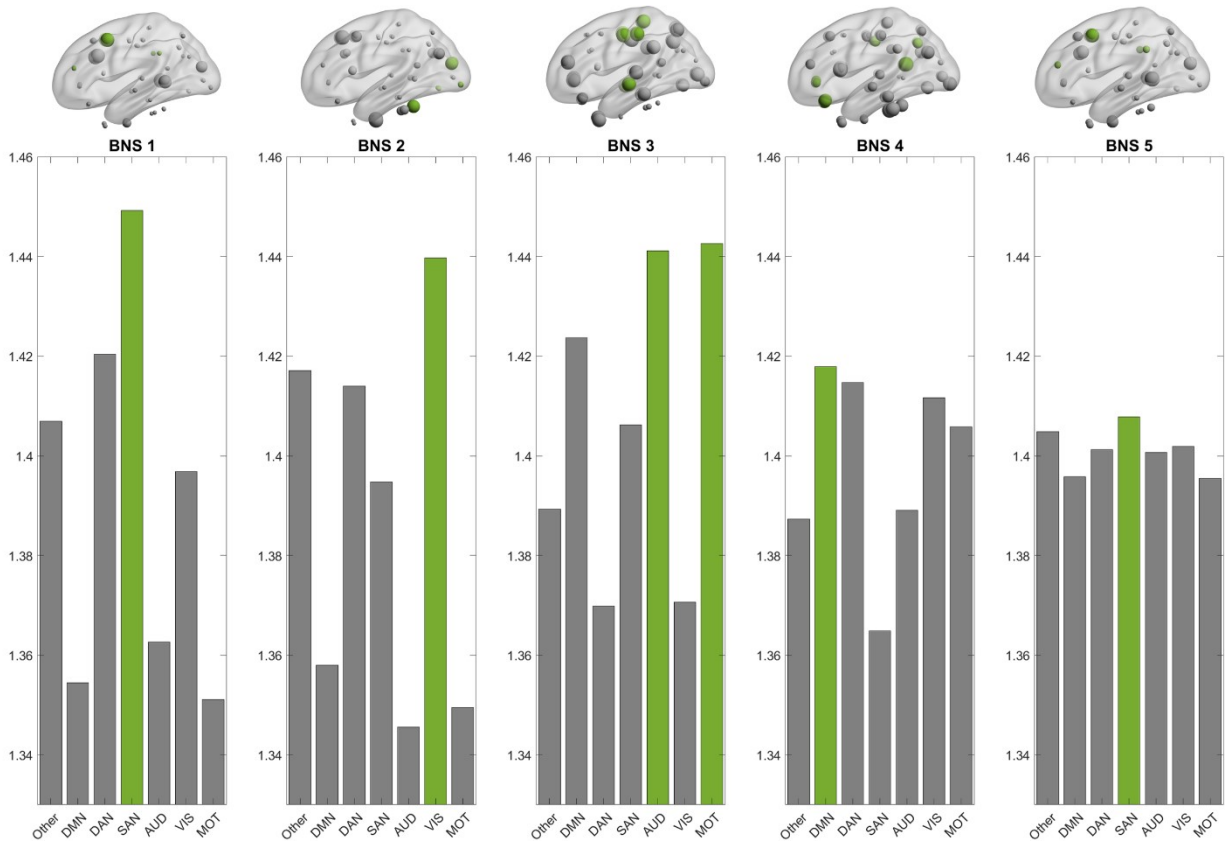
Figure 4.28: Affiliation of each BNS to the closest RSN. This figure shows the affiliation each BNS to the closest RSN, based on the RSN strength. A histogram for each BNS is presenting the strength of the seven different RSN. To identify the dominant RSN for each BNS, we elicited those with a value superior to the sum of the average and standard deviation of the 7 RSN strengths. BNS 1 highest strength is for the SAN network (1.45). BNS 2 highest strength is for the VIS network (1.44). BNS 3 highest strength is for the MOT and AUD network (1.44). BNS 4 highest strength is for the DMN network (1.42). BNS 5 highest strength is for the SAN network (1.41).

4.4.3.2   Quantification

Following this global average segmentation, we then investigated the presence of each state at the level of the individual subject. This process is called backfitting and consists of associating with each EEG sample the state it is the most similar with. The backfitting allows us to compute several metrics to quantify, for instance, the

transition probability between one state to another, and the occurrence of each state per phase of the experiment. Figure 4.29A shows the BNS repartition (in %) after the backfitting. It is completed by the mentioned metrics, e.g., in 4.29B, transition matrix probability from one state to another (where the element Ai,j represents the probability to switch from state i to state j), and in 4.29C, the global occurrence of each BNS which indicates the average number of times per second a BNS is dominant.
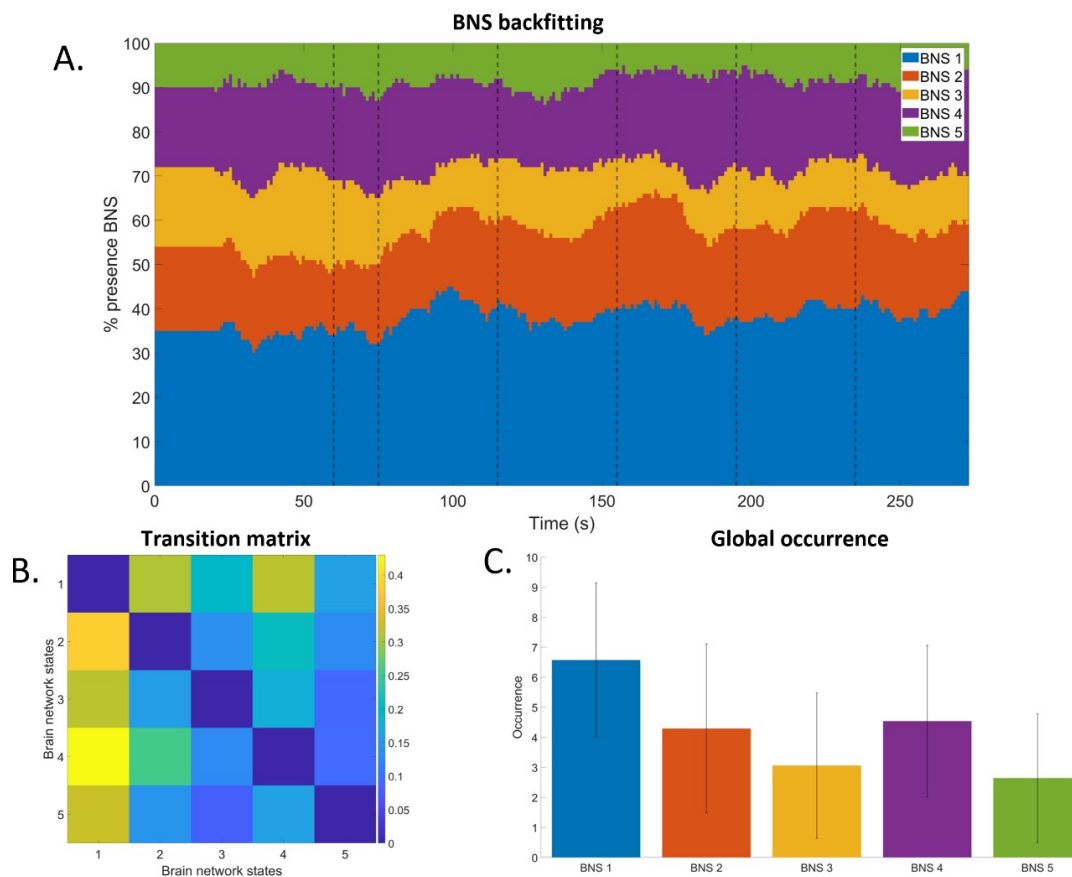
Figure 4.29: BNS backfitting distribution, and their associated transition matrix and occurrence. Panel A) shows the backfitting distribution, the x-axis represents the time of the experiment, and the y-axis the percentage of the subjects where the BNS is present. Panel B) shows the transition matrix probability from one state to another (where the element Ai,j represents the probability to switch from state i to state j). Panel C) shows the global occurrence of each BNS.

The BNS 1 (salience network) is the most present state, being there in around 35% of the individuals during the whole experiment. The second most present states are BNS 4 (default mode network) and BNS 2 with around 15-20% presence, then BNS 3 and BNS 5, around 10%. The highest transitions (figure 4.29B) are from all states to BNS1, the state with the highest occurrence in every phase, followed by BNS 4.

4.4.3.3 Quantification

Here, we investigate the possible correlation between the brain network dynamics as described above and some of the participants' information such as age and motion sickness assessments. Statistical analysis has been performed for each component of the transition matrix, as well as BNS occurrence, for the global metrics and the metrics

by phase. Figure 4.30A shows the global metrics presenting statistical relevance, which is the transition matrix from BNS 5 to BNS 1 for age. No significance was shown on the global for other groups or metrics. Figure 4.30B shows the correlation between the 2 groups with the transition probability, as well as a boxplot displaying the significant transition probability value for each group.
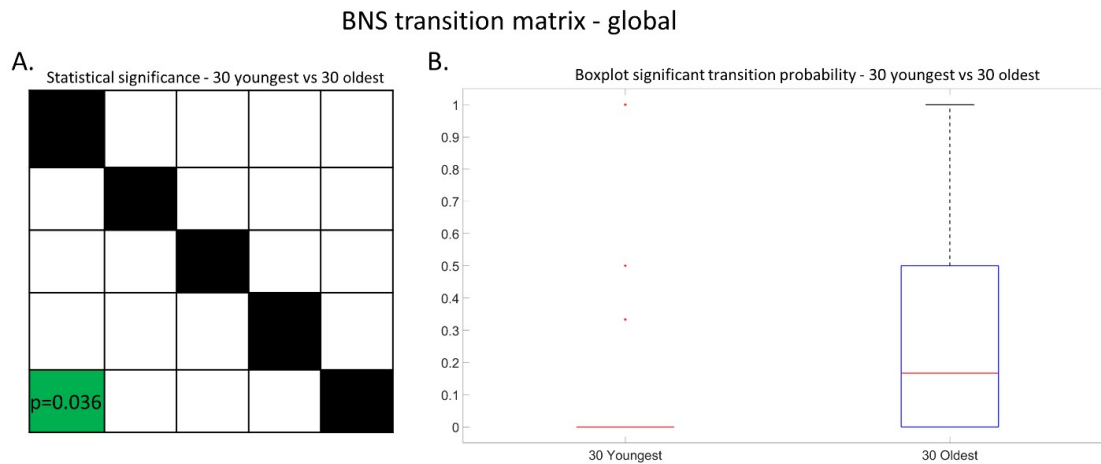
Figure 4.30: Correlation results between BNS metrics and age. Panel A) shows the significant transition with the associated p-value. Panel B) shows the boxplot of the significant transition probability value for each group.

For the global transition matrix, the transition from state 5 to state 1 was significantly different (p=0.036) between the 30 youngest and 30 oldest. It can be seen that most of the young cohort has no transition from state 5 to 1, whereas the transition is more present for the old group.

4.4.4 Discussion

The results from this study highlight a dynamic remodeling of the brain during a complex PC task. A novel methodology has been developed using microstate segmentation at the brain network level.
From the average dynamic functional brain network, a BNS segmentation has been performed. The first observation is the fact the BNS distribution is representative of the experimental phases. Indeed, for each phase change, a state transition happens slightly before or after. The only exception is for the transition between 25% and 50% phases, which can be easily explained by the fact that there is no difference in stimulation between the tasks, only a higher amplitude of movement. Going deeper into the analysis, we break down each phase and observe the repartition of the BNS. It can be noted that only two states appear only one time in the distribution: BNS 4, at the beginning of the baseline, and BNS 2, between 75% and POST. From the results displayed in figure 4.28, BNS 4 main function is linked with DMN. It is coherent as the baseline starts when the subject is already standing on the platform with the same view for around a minute. DMN is a state that is activated when the subject is in the

resting-state mode and focus is in internal mental state process [271], [272], or mind wandering [273] and is deactivated when a cognitive task starts.

BNS 2 main function is linked with VIS. This state occurs at the end of 75% and the beginning of POST, so when the platform is moving at the maximal amplitude and then stops moving, while the subject is always seeing the sea simulation inside the VR headset. The subject must maintain its balance during this phase, but its PC is not challenged by any motion stimulus, only visual. The presence of a visual network state at this period testifies to the cognitive involvement into this task, as its prominence during visual stimulations experiments has been highlighted in previous works [274], [275].

BNS5 appears two times, at the end of baseline and the end of POST. Its main function is linked with SAN. BNS 1 appears in the middle of the baseline, in the whole PRE phase, and in the whole 75% phase. Its main function is linked with SAN. Studies showed that SAN interacts with DMN and other executive networks [276]. This explains the transition from state 4, which is DMN, to state 1 from state 1 to state 5 in the baseline, as during baseline, the brain is at rest and is preparing for what comes next. Moreover, SAN is also more presents when the brain needs to be aware of what it should focus on to move, quickly between information gathering, decision planning, and execution [277]. State 1 is present shortly after the PRE starts, which is the first actual PC disturbance: the subject needs to maintain equilibrium even though the platform is not moving, due to the visual stimulation. It needs to adapt and understand from where the mismatch between what is seen and what is felt comes from. This occurs as well with BNS 5 in the POST phase, which is like the PRE. Then, BNS 1 is present for the whole 75%, while the platform is still in motion, but after already moving for more than a minute. We can hypothesize that the motor cortex is less activated due to the habituation of the phenomenon and that the SAN is dominant in that case to anticipate the upcoming task. To differentiate the 2 BNS, we can look at their second most dominant RSN. For BNS 1, the second RSN is the DAN, which is involved during passive viewing tasks [278], and in general during a focus on a particular task, selective attention [279]. This is experimented during the 75% task, where the subject responds to the platform movements and focuses on a specific point of reference in the VR environment. For BNS 5, the second BNS is Other, which corresponds to the 7 other RSN identified by Shirer et al. [24], but not explicated in this study. However, the strength of the other RSNs is in the same range. This BNS does not have a second dominant RSN. This would explain that it is following BNS1 in the baseline, as they are both salience and prepared to switch to another state. Moreover, this BNS is also at the end of the experiment, in the second half of the POST phase, showing that the subject is focused on information gathering, and decision making to maintain the balance, but also knowing that experiment is coming to its term, then the salient network is helping with the anticipation of the end of the task.

BNS 3 is present during the whole Transition phase, and the whole 25% and 50% phases. Its main function is linked to AUD and MOT. During the Transition phase, the screen turns white and the sound of the waves and environment appears, while it is completely silent during the baseline. Since there is no motion or visual stimulation, the presence of a dominant auditory network is coherent, as previous studies identified this network to be more activated during audio stimulation [280]. Secondly, state 3 is also present during the whole 25% and 50% tasks, so when the platform activates and starts moving at different intensities. It is during this period that we ask the subject to put his hands on the bar. Those phases of the experiment are based on

motion stimulation, and the dominance of the motor network is perfectly illustrating this point, as the motor network is mostly solicited during tasks requiring movements [281].

The global BNS segmentation based on the alpha band network shows a clear dynamic brain remodeling during the experimental protocol. Thus, it is interesting to observe the results at a patient-level, and figure out if a similar trend can be observed. The backfitting results reveal an explicit dominance of BNS 1 during the whole experiment. This BNS is associated with a salience network, which is known to interact between cognition of DMN and cognition of the executive network [276]. Since our experiment is dynamically composed of different stimulations (visual, motor), the salience network is playing a key role to catch the attention on where the brain should focus, and facilitate the transition between information gathering, decision planning, and internal focus [277]. This is supported by the average transition matrix. It can indeed be seen that the highest transitions occur from state 1 towards every state, and from states 2 and 4 to state 1, confirming the role of BNS 1 to regulate and orientate brain cortical activity depending on the stimulation.

According to the occurrence metrics, after BNS 1, BNS 2 and 4 have a similar presence during the whole experiment. As the visual stimulation is constant during the experiment, through the VR headset, it is then expected to see an average occurrence of state 2. Regarding state 4, since the DMN testifies to internal focus and cognition [271], [272], it can be hypothesized that a good part of the participants was not challenged a lot during the simulation, and therefore did not need to be involved a big part of their cognition during the experiment.

The analysis of the whole cohort gives promising results. The BNS segmentation reveals an explicit remodeling of the brain during this dynamic PC task. The prevalence of RSN depending on the phase shows the pertinence of this approach. This study also aimed to study the potential differences in the cognitive behavior between two groups based on different criteria: motion sickness susceptibility and age.

On the age aspect, significance is observed in the transition probabilities. The transition from BNS 5 to BNS 1 is significantly higher in the 30 oldest people than in the 30 youngest. The two states have a salience network as the most dominant RSN, so they principally have the same main function. However, the second most dominant RSN is DAN for BNS 1 and Other for BNS 5. Thus, since DAN is activated when there is a particular focus on the task, we can speculate that the oldest people, while their salience network is activated, have increased activation of the attentional network, as they need more attention to the task and might suffer more from the experiment, due to the age-related decline in PC, and a need of increasing attention to maintain balance [137].

4.4.5 Limitations

This work presents some limitations. First, the algorithm used to cluster the BNSs is stochastic, meaning that it will give different results every time it is run. However, it should converge to an optimal solution, thanks to the settings used. In our study, we are setting the algorithm to 100 restarts and 1000 iterations, which is sufficient to obtain a reliable segmentation.

Secondly, we chose to focus on the alpha band, due to its significance in previous studies associated with PC [259]. It could be interesting to observe how the brain network segmentation is performing on the other frequency bands, or even on the

global frequency spectrum. Thirdly, no significance has been found in global metrics related to motion sickness parameters. This aspect should be pursued to adapt the group definition, as well as the characterization of motion sickness in people.

Lastly, this work has been done on healthy people only. It would be interesting to compare this work with groups suffering from pathologies affecting their neural activity or PC. We can also compare this distribution with new data from a healthy cohort to confirm that the results obtained in this study are consistent.

4.4.6 Conclusion

This study aimed to decipher brain network dynamics during a complex PC task. 158 individuals underwent the BioVRSea experiment. We demonstrated that, on the alpha band, the brain network state segmentation was illustrated appropriately in the evolution of the different phases of the experiment. Each BNS was studied to determine its dominant RSNs, giving a better insight into functional connectivity and how it translates brain behavior in PC. The BNS distribution has then been monitored on the subject level, showing the prevalence of one state, which comports a dominant salient network. Finally, a proof of concept has been done to study differences between groups, based on age, and motion sickness susceptibility. The results showed statistical differences in some metrics and transition probabilities for the age difference. This work validates an innovative approach, based on a robust methodology and a consequent cohort, to quantify the brain networks dynamics in the BioVRSea paradigm. Further studies will confirm those results by comparing new data to this distribution, and by observing the distribution of people presenting pathologies. This is the first step towards the definition of a reference of brain network behavior in dynamic PC.

Chapter 5

Tools and paradigms to assess brain electrical activity: discussion

The reported investigations from this dissertation developed new tools for brain cortical activity assessment. Under two research scopes, schizophrenia and postural control, several approaches of EEG time-series analyses have been implemented, with an aim to identify neurophysiological markers of brain response to different stimulation, and to bring quantitative metrics that can be used for further assessment.

5.1 Summary

The work detailed in this dissertation has a two-fold impact: first, it confirmed findings identified in previous literature, with the use of different and innovative paradigms. Second, it uncovered novel findings, that could be crucial for a better understanding of brain cortical activity and its associated cognitive process. Above all, this essay validate the use of EEG, and the need to find robust, reliable and original methodology, in order to go further in our knowledge regarding brain mechanisms. Table 5.1 sums up the principal findings of the work.

Findings	Paradigms	Spectral analysis	Functional connectivity
rTMS and schizophrenia	**High variance** between subjects regarding **rTMS impact**	**Correspondence** between increasing **psychometrics** score and **higher alpha and beta** power	**Correspondence** between increasing **psychometrics** score and **higher beta participation coefficient**
BioVRSea and concussion	**Differentiation** between **concussion and non-concussion** group	**Significant increase in theta band** through the experiment for **concussion**	
BioVRSea neurophysiological signature	**First reference** of BioVRSea postural control paradigm	**Significant differences** in **prefrontal delta, occipital gamma, whole alpha and beta bands** for postural control challenging tasks compared to resting-state	
BioVRSea and brain network dynamics	**Validation of brain network state approach**, combining microstates clustering and functional connectivity algorithm		**Identification of 5 brain network states** and their **dominant function** describing adequately the experiment

Table 5.1: Summary of the main findings

The findings obtained throughout this work can be divided in two categories: methodological and neurophysiological.

Methodological findings

Confirmed findings   The first confirmed methodological findings concerns study design. Chapter 3 corroborates the use of ERP in the study of schizophrenia, and more precisely the P300 paradigm regarding schizophrenia with AVH. Regarding the number of electrodes, both research studies showed interesting results spatially, through connectivity or topological power map. It justifies the use of at least 64 electrodes to perform these types of analysis. The use of more electrodes (128, or 256 as related in chapter 3) can be necessary for more accuracy, and is sometimes crucial to identify neuropathological behaviour. The setup and placement of an HD-EEG cap on a subject is however more laborious, which highligths the importance of finding the good compromise when designing a protocol.

Regarding the sampling frequency, the results from both chapters back the use of 1024Hz as a sampling frequency. It is enough to track fast response and to observe the dynamicity of brain mechanism. Regarding our studies, the use of a higher sampling frequency would not be much benefitial and would lead to larger datasets, thus longer processing time and more storage requirement.

The second confirmed methodological findings that we can list concerns data analysis: chapter 3 illustrates well the different approaches defined in chapter 2. First, the temporal and Fourier-based spectral analysis, that are already a standard way of analysis in this field, provided valuable information, based on signal latency and amplitude for the temporal analysis, and on power variation for the spectral analysis. The latter is confirmed in chapter 4, where the Fourier-based spectral analysis has been used in different studies, to observe the effects of concussion on postural control, but also to build a foundation of a neurophysiological reference in a new postural control paradigm. In both cases, this approach has been successful, with robust and reliable results. On top of those two approaches, chapter 3 supports as well the use of metrics extracted from network analysis, based on brain connectivity. This methodology is quite recent, but is increasingly used in the last 10 years, especially based on EEG time-series data. Some metrics were also used in chapter 4, to help the quantification and interpretation of brain networks.

Novel findings   The first novel methodological findings is the use of a BioVRSea as an experimental setup. This complex paradigm combines VR and a moving platform to replicate the behaviour of a boat at sea. It triggers postural control during the different phases of the experiment, based on visual and/or motor stimulation. The different studies and results presented in chapter 4 validate the use of this setup combined with EEG measurement. It showed promising results for postural control assessment and related pathologies.

The second novel methodological finding is the combination of more complex and innovative methods to understand dynamic brain remodeling during complex tasks. Microstates segmentation algorithms, usually based on EEG voltage topography, have been used on reconstructed brain networks to compute dynamic network distribution during BioVRSea experiments. The resulting states, called brain network states, have been analyzed and quantified using network analysis. This approach is new and recent,

and has been developed for the first time, in postural control studies and for that many subjects (158), during this PhD work. The outcome of this study validated the use of this methodology, and should therefore be pursued in different areas.

All of those findings confirm the importance of designing a coherent study, from the equipment, the experimental setup, to the data analysis pipeline. This thesis presents several tools that are, on one hand, favorable to study longitudinal impact of neuropathological treatment, such as rTMS on schizophrenia, and on the other hand, to quantitatively assess neurophysiological dynamics on complex brain mechanisms, such as postural control.

Neurophysiological findings

Confirmed findings The confirmed neurophysiological findings are, first, the latency and changes in amplitude in P300 paradigm for patients with schizophrenia and AVH detailed in chapter 3.
Regarding chapter 4, a significant power variation in specific bands, mainly theta, was observed for people who suffered from concussion, compared to people who did not. This confirm the neurophysiological impact of concussion regarding cognitive impairment, and the way it can affect balance.

Novel findings The first novel neurophysiological findings is the impact of rTMS as treatment for schizophrenia with AVH. Chapter 3 details a case study where some preliminary results encourage a further use of this technique. A power variation in alpha and beta and changes in network metrics reveal a trend of positive changes one week after the treatment. Of course, the sample size is very low, and only short-term effects are presented. However, the innovative use of rTMS, that is usually employed in other diseases, and the associated cortical remodeling are results of interest to base further studies on.
Chapter 4 presented strong results to find a first neurophysiological reference of postural control related to BioVRSea paradigm. Its strength relies on the high number of subjects measured (190 in one study, 158 in another). It shows a localised power variation in every frequency band during the different phases of the experiment, highlighting the constant cortical activation or deactivation during postural control. On a more dynamic aspect, this thesis identified brain network states segmentation, during BioVRSea, illustrating adequately the evolution during the different phases of the experiment. Moreover, each state was analyzed to determine its dominant resting-state network, giving more insight about their function. This results underline the constant neurophysiological changes, activating the most suitable brain areas to anticipate and respond to a stimulus.
Those findings validate the use of EEG with adapted paradigms to study brain cortical activity associated with cognitive processes. It is very helpful to assess the efficacy of a treatment, and to identify biomarkers that are essential in the clinical assessment. Moreover, the study of a healthy cohort as a point of reference is crucial, first to establish a standard behaviour regarding the developed paradigm, and second, to analyze and interpret the associated activity. The results can later be used as a comparison with other patients, suffering from neurodegenerative diseases. The significant differences between the groups will help to identify clear markers of those diseases, that can

help first, for a clinical assessment, but also in terms of rehabilitation, to identify the potential causes and consequences, how to treat it, and how to monitor the efficiency of the chosen solution. All of this can be investigated with the use of EEG.

5.2   Discussion of the findings

Neurophysiology is an essential tool for clinical applications. The use of continuous EEG in intensive clinical units has proven itself vital for seizure detection, treatment follow-up, and most generally neurological monitoring [282]. To deal with the risk of data corruption or poor signal analysis from several sources of artefacts, guidelines have been proposed [283], and the use of quantitative EEG have made it more readable and reliable for clinicians [284]. Thus, it is without doubt that EEG is a reliable tool for clinical use. However, the use of EEG on a more restricted duration, for diagnostics or assessment purpose, is more limited in the clinical field. To date, it did not fulfill the expectations of eliciting biological markers, but can be useful to provide insight regarding pathologies by documenting functional remodeling of the brain during specific conditions, such as sleep in the frame of dementia research [285]. More and more studies in the recent years identified metrics that could be used in a clinical evaluation, regarding Parkinson's disease [286], Fragile X syndrome [287], or delirium [288]. However, those metrics need to be investigated and validated more thoroughly, with the support of psychometric scales for instance, to be accepted as biomarkers of a condition, and some EEG analysis approaches, such as functional connectivity, or longitudinal studies, have not been sufficiently used for now, despite their promising potential. The work related in this thesis aimed to address this aspects, by proposing new tools and approaches, that could lead to the development of quantitative data to be used in future clinical application.

Methodological findings   This dissertation emphasizes the importance of adequate methodology for a correct assessment of brain cortical activity. ERP remain a key aspect of EEG analysis, and their numerous paradigms (visual, auditory,...) enabled to identify clear patterns of a normal response, and therefore the characterisation of an abnormal one. Moreover, this process being time-locked, it is very convenient to analyze, and allows a great variety of approaches, from the temporal, spectral, to connectivity domain. Each approach can give a specific insight about brain cortical activity, and therefore help the interpretation of the underlying mechanism. This diversity of analysis leads to a huge potential of biomarker identification, of a neurodegenerative condition, of a treatment impact. Thus, due to its ease to design and setup, ERP is a crucial tool to assist clinical evaluation.

The design of more advanced measurements setup to target complex mechanisms is also necessary. Taking the example of postural control, a great number of researches studying this process involve simple setups such as a vibratory platform. It contributed to set the fundamentals of our understanding regarding postural control. However, the use of more advanced and dynamic setup, with different stimulation, helps to combine different concepts and to deepen the analysis. The first results from BioVRSea paradigm are in line with the current knowledge of postural control and motion sickness. This point is crucial. On one hand, it ascertains the use of this setup to study postural control. On the other hand, it opens a door towards new methodologies, new

ideas, and further analysis. Spectral analysis remains a solid and basic technique to study EEG time-series, as developed throughout this thesis. Yet, this work also insists on the pertinence to investigate functional connectivity from EEG. It relies on robust mathematical concepts, and provide supplementary information on brain function during cognitive process. The advantage of using it on EEG is to benefit from the high temporal resolution. It becomes very easy to track precise brain dynamics, which gives an important insight regarding brain remodeling. This approach has been more and more used, and the combination of brain connectivity and microstates is promising as it gives a concrete description of brain status, and can be easily quantified. Alike ERP, it can in the future become an essential tool for clinical assessment.

Neurophysiological findings This work presents promising neurophysiological findings, that are not robust enough yet to be considered as biomarkers, but are basis on which to pursue the analysis. Regarding schizophrenia with AVH, our results suggest that rTMS has at least a short term impact into brain remodeling. Of course, the sample size was very low, so the significance of the study is far from sufficient. However, this study should be considered as a proof of concept, and propose a new way to assess treatment techniques based on neurophysiological results, and not only relying on scales. The EEG based features confirmed the psychometrics scales, and helped to have better idea of rTMS impact on brain response. More precisely, the spectral based features and the connectivity coefficients could be potential biomarkers of rTMS impact in the frame of schizophrenia with AVH. Thus, this analyses should be pursued on larger scale and longer term researches. If those preliminary results are later confirmed, it would be a great asset for the clinical field. First, it would open the way to new treatment assessment, and second, it would enable to follow and evaluate the long term progression of patients with schizophrenia, and eventual positive evolution. Postural control is a complex mechanism, relying on the central nervous system. It is widely studied, but it lacks of clear quantification, due to the numerous different ways to measure it, based on different sensors: stabilogram, muscle activity, brain activity. Yet, many disorders are known to affect postural control, due to neurodegeneration for instance. BioVRSea paradigm offered a new glance at the induced cortical activity. It emphasized the fact that every band is involved in this mechanism, and gave new knowledge about their cognitive implication. Those results corroborated the ones from previous postural control studies, with a higher number of subjects. Therefore, the changes of power in every frequency bands during the different tasks are a way to quantify healthy postural control response. Further studies will use BioVRSea to study postural control for patients with balance-related disorders, such as Parkinson's disease. It will enable to track signal differences for patients suffering from pathologies, and underline those differences a biomarkers that can be used later for clinical assessment. It has been confirmed with a proof of concept, studying the impact of brain traumatic injuries, showing a first trend between questionnaire assessment tools and brain signals, and a difference of behaviour in brain activity between people who underwent concussion and people who did not, which is promising for the clinical assessment.

Perhaps the most noteworthy finding of the reported studies is presented in the final work, the brain network state segmentation. Each brain network state function was analyzed, and it is intriguing to observe how quickly and efficiently the brain reacts and adapts to the stimulation it is exposed to. Those results confirm the importance

of salience network, to analyze and facilitate the transition from one state to another. The global network distribution presented a real coherence regarding the different phases of our experiment, providing a lot of information regarding brain behaviour. Indeed, thanks to graph theory and microstates based algorithms, it is very convenient to extract reliable and descriptive quantities to measure postural control response, and interpret the associated neurophysiological behaviour. This metrics will be compared in the future with different cohorts, to have a deeper understanding of brain function associated with PC, and ultimately become a milestone for further clinical assessment.

5.3   Conclusion

This thesis dissertation relates several research studies with the aim of developing new tools and paradigms for brain cortical activity assessment. It studied the impact of rTMS on patients with schizophrenia on one hand, and brain activity related to postural control on the other hand, based on EEG time-series. The first conclusion we can draw from this work is the great potential of EEG signals to describe brain behaviour, and the different analysis domains all provide valuable information. In both research scopes, significant differences were observed on the spectral domain, and, in the case of ERP paradigms, in time domain. It enables to study the longitudinal effect of a treatment, or to differentiate groups according to previous traumas or pathologies. However, the main outcome from this thesis would be the remarkable benefit of using functional connectivity. This approach gives numerous new measures that provide concrete information of the brain remodeling. Moreover, it can be used in a static or dynamic experiment. Thanks to the high temporal resolution of EEG, dynamic network segmentation can be performed, revealing precisely the causes of changes in brain activity, as well as how it is translated in a functional aspect. This methodology can provide a better understanding of brain mechanisms under various situations, as concrete metrics can be extracted from brain network and their clustering through time. Future works should incorporate this technique, as it would lead to reliable biomarkers of a condition, and therefore be of critical use in clinical evaluation.

Chapter 6

New methodology to assess cartilage condition: EU project RESTORE

A parallel project performed during this thesis was the contribution to a EU project: RESTORE (`http://restoreproject.eu/`).

6.1 Context

Restore project aimed to develop nanoenabled solution for personalised cartilage regeneration. In the frame of the EU project Restore, Reykjavik University developed the 1st European database of chondral lesions morphometric and associated 3D models (`https://restore-project.ru.is/`). Thanks to its partnership with the University Hospital Landspitali, 47 knees have been scanned since March 2019. Three different types of subjects have been recruited : 25 degenerative (D), 14 traumatic (T), and 8 healthy acting as control (C). This database contains information regarding the different type of chondral lesions and the behaviour of the cartilage, based on Computed Tomography (CT) and Magnetic Resonance (MRI) images. Exhaustive measurements, regarding the thickness, the grading of the cartilage, as well as the presence of medical pathologies such as cysts, bone attrition, were performed on those medical images, for each patients, based on a robust radiological approach. It provides a complete overview of the patient's condition from those 2D images.

On the 3D aspect, using high performing medical imaging software (Materialise, MIMICS), these images were processed in order to segment and dissociate the different part of the knee : femur, tibia and patella. CT and MRI acquisitions were taken positioning the patient knee in the same way therefore an accurate registration between the datasets was possible, in order to have in the same dataset bone and cartilage. The geometry is studied from this processed images.

From this final dataset, we extract information about density and volume : the mean value of Hounsfield Unit (HU), a scale to quantify the radiodensity, is computed for each bone and cartilage part. This enables us to conduct preliminary analyses that will be displayed in the database.

This section will relates two studies (one published, one under peer-review) analysing the data extracted from the different image modalities, in order to find new metrics for cartilage assessment.

6.2 CT and MRI based 3D reconstruction of knee joint to assess cartilage and bone

The work below has been published in *Diagnostics* ([289]).

6.2.1 Introduction

Osteoarthritis (OA) is among the most common forms of arthritis [290], occurring when protective hyaline cartilage between bones breaks down through injury or disease. Hyaline cartilage in the knee is an important tissue which, due to avascularity, does not heal spontaneously after injury and often requires surgical intervention. OA of the knee is a major cause of disability worldwide [291], causing significant burden on healthcare systems [292]. The lifetime risk of developing symptomatic knee OA is approximately 45%, with a higher risk being associated with obesity (60.5%) and advancing age [293]. The incidence of OA is predicted to increase in the decades to come due to older populations and obesity [294], [295].

OA is a polysymptomatic disease but is generally characterized by thinning and loss of cartilage. Assessment of cartilage condition and thickness is therefore crucial for both detection and monitoring the progression of OA. Diagnosis is usually based on a clinical assessment and a radiographic examination. Planar X-rays of the knee are used routinely in radiographic evaluation, however, soft tissue is not adequately visualized, nor is this modality sensitive to changes in the joint over time [296]. Magnetic Resonance Imaging (MRI) is the state-of-the-art imaging modality for the assessment of hyaline cartilage and has seen rapid developments in hardware, sequences and image analysis in the last decade [296]–[299]. MRI provides a visual assessment of the cartilage and presents a means for quantitative evaluation of the volume and dimensions of the cartilage, and its chemical composition. Comprehensive overviews of MRI sequences for assessing morphological and compositional aspects of knee cartilage are described in [296], [297], [300]. MRI is capable of accurately assessing the size and thickness of articular cartilage [298], [301], [302]. In addition to visualizing the cartilage, MRI also images other tissues involved in OA, such as subchondral bone, meniscus and soft tissue. Computed Tomography (CT) imaging also provides an excellent 3D representation of cortical bone [303]–[305], osteophytes and soft tissue calcification and has been used to investigate changes in the joint, including trabecular bone remodeling, subchondral cysts and bone sclerosis, all of which can be OA-related changes in the joint [306]. As the understanding of OA develops due to advances in medicine and imaging, it is important that OA is viewed as a disease of the whole organ, involving multiple joint tissues [296].

The severity of OA can be assessed by the degree of joint space narrowing and damage to cartilage and underlying bone. Several scales that exist assess the extent of OA. Kellgren-Lawrence (KL) grading is used for the rating of OA on planar x-rays, where the definite presence of an osteophyte (Kellgren-Lawrence grade 2) confirms a structural diagnosis of OA [307]. Kellgren-Lawrence combines an overall grade for OA from joint space narrowing and osteophyte presence, which incorrectly assumes that these structural changes appear continuously [296]. Other grading systems such as the OA Research Society International (OARSI) Atlas system separate a joint space narrowing grade from the presence of osteophytes. Both however only assess the tibiofemoral joint, underestimating the patellofemoral contribution to the disease [296]. Other com-

monly used scales include that developed by Ahlbäck in 1968 [308] which is based on the measurement of joint space narrowing. A 2003 study measuring the inter and intraobserver reliability of the Ahlbäck scale reported low to medium agreement coefficients, especially when reporting on radiographs of earlier stage OA [309]. Comparisons of knee OA scales have shown moderate correlation with arthroscopic findings and also have moderate to high reliability between individual observers [310]. In a study on severe OA, five radiological grading systems demonstrated medium correlation with intraoperative findings of full-thickness cartilage loss, and moderate interobserver reliability for all systems [311]. In both studies, Kellgren-Lawrence and Ahlbäck showed the highest correlation with cartilage loss, although still in the moderate range. Semiquantitative MRI based grading systems such as Whole Organ Magnetic Resonance Imaging Score (WORMS) and Knee OA Scoring System (KOSS) are based on a variety of features of the MR image from the whole knee joint, including cartilage size and depth, bone marrow lesions, subchondral cysts to name but a few. Some of these semiquantitative scoring systems have demonstrated 'within grade' changes over time, thus exhibiting increased sensitivity compared to traditional grading systems [296]. Quantitative measures using MRI include the cartilage volume and thickness calculated as a continuous variable, requiring segmentation of the cartilage in the MR image. This type of analysis requires high resolution 3D imaging to facilitate accurate measurements and delineation of defined subregions of the cartilage [296]. Comparison of several clinical, radiographic, and biochemical measures revealed that the relatively strongest predictor of longitudinal MRI-defined cartilage thinning was reduced baseline cartilage thickness in the medial femur [312].3D cartilage surface mapping (3D-CaSM) has also shown promise for tracking changes in cartilage thickness, where 6-month changes were observable using the semi-automatic 3D-CaSM algorithm. [313]. Recent work in healthy knees has also shown the utility of 3D ultrasound in quantifying cartilage volume when registered with MRI scans [314].

Injury to the knee joint presents a substantial risk of development of OA. Planar X-ray imaging, CT arthrography, and MRI have all been used in the assessment of knee trauma following injury [315]. An MRI-based score incorporating traumatic and subsequent degenerative changes was introduced in 2014 by [316]. The Anterior Cruciate Ligament OsteoArthritis Score (ACLOAS) evaluates structural joint damage, features of OA (including cartilage loss) and acute signs of inflammation in traumatic injury to the knee. The ACLOAS aims to be used for longitudinal assessment of injury and subsequent OA in the knee joint.

6.2.1.1   Cartilage new assessment methods/gold standard

There are two main volumetric analyses used in the cartilage assessment of this research. The first is a wall-thickness analysis, where the cartilage mesh is taken and the thickness of each element is calculated from surface to surface. The hypothesis for this analysis is that degenerative and traumatic patients' cartilages will be thinner in specific places based on the patient category than the control group. The second is the curvature analysis, which measures the Gaussian curvature of an element based on its surrounding elements. The hypothesis here is that around areas of higher cartilage degradation there will be higher curvature as holes and depressions form around these areas.

6.2.1.2   Use of 3D modelling Tools

In this project, the medical 3D modelling software Materialise MIMICS (Materialise Interactive Medical Image Control System, Materialise, Belgium) and 3-Matic were used to analyze the cartilage. The application of the MIMICS software is to segment and isolate the specific cartilages from a CT scan and export the generated 3D mesh for further analysis. MIMICS allows the user to directly extract geometric measurements and densities in Hounsfield unit (HU) values for each element. The exported cartilage parts are subsequently imported into 3-Matic, where components' meshes are analyzed and features extracted.

6.2.1.3   Machine Learning and Artificial Intelligence

In the scientific literature, it is possible to find multiple applications of Machine Learning (ML) and Deep Learning (DL) starting from MRI or other medical images of the knee related to OA. The progression of OA over time can be predicted with the use of ML algorithms using principal component analysis (PCA) [317], x-ray images and general clinical data [318]. DL was used by Liu et al. [319] to detect acute cartilage injuries within the knee joint, while Bien et al. [320] utilized DL efficiently to detect general abnormalities on knee MRI exams. Moreover, DL was used for OA diagnosis [321] and the prevention of total knee replacement using MRI and non-image features [322]. The KL grade system described above was predicted with DL by Kwon et al. [323], having as initial features gait data and radio-graphic images. Moreover, gene expression signature and ML technologies were used to identify OA through liquid biopsy [324], [325]. In this research, ML was used, more specifically by using tree-based algorithms for a three-classes classification using the novel 3D features introduced here as initial features: these are employed to classify traumatic, degenerative and control (healthy) subjects.

This study presents a novel workflow developed in the frame of the EU project RESTORE. It is based on the segmentation and processing of medical images to 3D reconstruct a model of the knee joint. The analysis of these models provides an extensive set of metrics that can be used to assess cartilage and bone condition.

6.2.2   Materials and Methods

Figure 6.1 represents a graphical abstract of the study workflow.
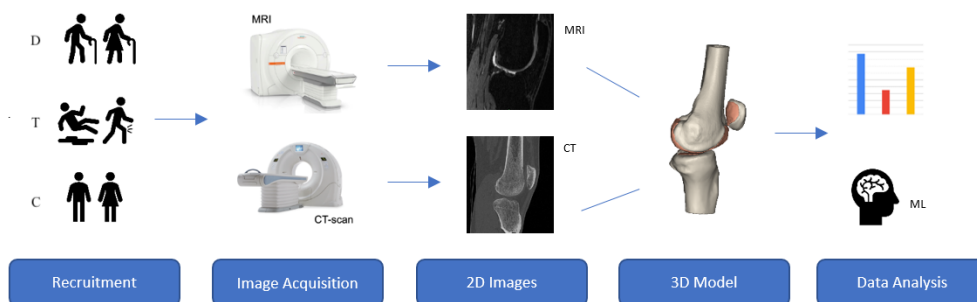
Figure 6.1: Graphical abstract

6.2.2.1 Participants

Participants were recruited as part of the European project RESTORE (`https://restoreproject.eu/`) (CORDIS grant agreement ID: 814558). The aim of RESTORE is to implement patient-specific solutions for cartilage regeneration. This study has been approved by the Icelandic Bioethics Commission (approval number: VSN-19-050).

Recruitment After completing an informed consent, 47 subjects (24 females, 23 males, mean age = 50 years, std age = 19 years, min age = 20 years, max age = 81 years) underwent X-Ray, CT scan and MRI of one knee at Landspitali University Hospital in Reykjavik, Iceland, using standardized acquisition protocols and patient positioning. From the total of patients, 24 subjects (12 females, 12 males, mean age = 64 years, std age = 12 years, min age = 35 years, max age = 81 years) were suffering from degenerative (D) cartilage. They were on a waiting list for prosthetic replacement. 15 subjects (9 females, 6 males, mean age = 35 years, std age = 11 years, min age = 20 years, max age = 50 years) suffered from a knee trauma (T) with possible cartilage injury, and 8 participants (3 females, 5 males, mean age = 34 years, std age = 14 years, min age = 24 years, max age = 67 years) were involved in the study as control (C) subjects (no knee symptoms or history of trauma).

Scanning process

    CT scanner The CT scanner was a Toshiba Aquillion One, 320 slice, that covered a 16 cm area of interest in a single gantry rotation. Slice thickness was 0.5mm with an increment of 0.25mm. Tube voltage was 120kV, tube current was 250mA and effective mAs was 125. The protocol covered about 15cm of area (axial plane) centered at the knee joint with small variations according to patient size. No intravenous contrast was administered. The initial CT dose index was set to 12.1mGy. The preliminary dose-length product was 193.2mGy*cm. These values have been individually recalculated by the CT scanner for each patient according to size/thickness of the examined area.

    MRI The MRI was a 3T Siemens Healthcare Prisma scanner. Volumetric 3D sequences with isotropic voxels of 0.6mm were acquired in the axial plane with a surface coil without intravenous contrast. This allowed for reconstructions in various planes along regions of interest. A 3D fast spin echo, intermediate weighted and fat-suppressed sequence which allowed for morphologic evaluation of cartilage and for better assessment of subchondral bone marrow was used. The maximum field of view was 16cm, with a minimum matrix size of 256x256. The area of interest was cartilage-covered areas around the knee. The protocol covered 14cm centered at the knee joint.

6.2.2.2 Data processing and analysis

Segmentation All acquired images were processed using a medical imaging software, MIMICS, as shown in Figure 6.2. Knee bones of femur, tibia and patella and their corresponding cartilages (femoral, lateral tibia, medial tibia and patellar) have been considered. The segmentation process was done following the same protocols both for bones and cartilages, respectively taken from CT scan and MRI.
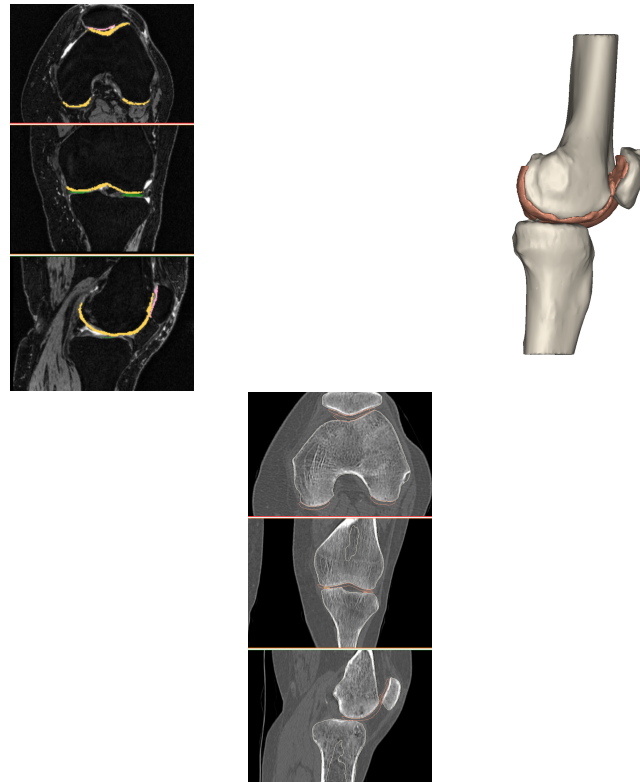
Figure 6.2: (**a**) Segmentation of femur cartilage from MRI file. (**b**) Model 3D of bones and cartilages. (**c**) Registration on CT file.

The first step was to create a mask for each entity by setting a density threshold interval. If necessary, editing operations were performed to refine the masks and improve their fitting accuracy. These masks were then converted into 3D objects. Next, a new image was created with Image Registration: MRI and CT images were registered, and bones and cartilage objects were combined. This was done by choosing at least four landmarks. The most suitable points are: highest and lowest points on the patella bone in the sagittal view, the upper point of tibial tubercules and the lateral side of the tibia in the coronal view (in any case, also other points can be chosen as landmarks). On the newly created image, a realignment process was manually made in order to place bones and cartilages on the correspondent anatomy, aligning the cartilage around the correspondent bone and trying to avoid their overlapping. Once this operation was completed, bones and cartilages masks were created from 3D objects. A manual inspection was done to remove any overlap of cartilage over bone. A final visual proof was made on 3D models of cartilages. Contact between bones is clearly visible from X-ray images and it justifies damages in cartilage tissue. We verified the presence of holes in related objects. Scanned bone segments resulted in different sizes due to the acquisition process. Moreover, our interest is to consider only the part of bone near the cartilages. For these two reasons, we decided to crop femur and tibia bones, selecting a region of interest (Figure 6.3). The patella is not subject to these issues because it is a small bone, always acquired in its entirety.

MIMICS allows calculation of the radio density in HU directly from a region of interest on CT scans. Human tissues absorb or attenuate X-rays beam according to their density. The HU is a radio density measurement for CT images based on a linear transformation of the X-ray beam attenuation coefficient. Water corresponds to zero
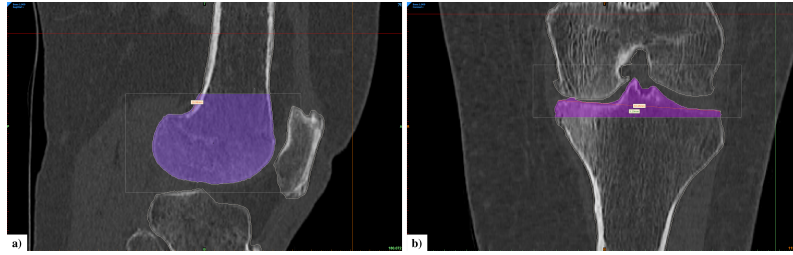
Figure 6.3: (**a**) Cropped mask of femur bone in sagittal view. (**b**) Cropped mask of tibia bone in coronal view.
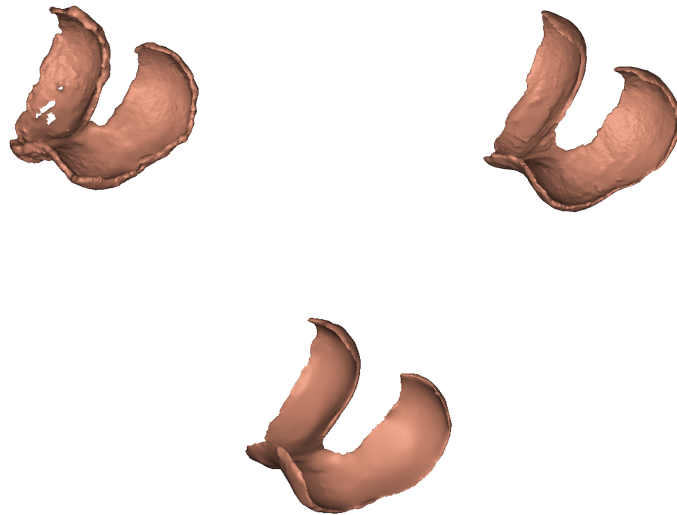
Figure 6.4: (**a**) Degenerative Femoral Cartilage (**b**) Traumatic Femoral Cartilage. (**c**) Control Femoral Cartilage.

in the HU scale, while bones have values higher than 400 [326]. Therefore, cartilages masks were filtered between 0-300 HU, which provides a good range for visualization of soft tissue pixel intensities (cartilage being soft tissue). The cartilage radiodensity was then extracted from the final mask. At the same time, bone mineral density (BMD) was computed from the radiodensity (in HU) using a linear formula that was determined empirically based on a phantom [327]. Volume and surface data were extracted from masks and 3D objects respectively. Regarding those cartilages that presented holes, we evaluated the size of damage using the best fit of an ellipse. We subdivided them into three main categories: grade zero in the absence of holes, grade one when the area is equal to or lower than 20mm^2, grade two when the area is higher than 20mm^2.

Figure 6.4 shows the 3D computed models of femoral cartilage for each group.

Wall thickness and curvature analysis After the four cartilages were segmented, a Python script was used to export the parts as STL (Standard Tessellation Language) files to 3-Matic and automatically perform the two analyses for each patient on each cartilage. This results in eight analyses per patient which can be further processed for parameter extraction. The analyses give a result for each element in the STL part file and the parameters extracted are standard deviation (STD), variance (VAR), the

mean, root mean square (RMS). Other parameters can also be extracted based on the hypothesis, such as the normalized number of elements below one STD of the mean for the wall thickness analysis and normalized number of elements above one STD of the mean for the curvature analysis. This results in 48 parameters per patient. It is important to understand how the results of the analyses are obtained. Each analysis is a text file where each line contains a data point containing the coordinates that make up each triangular element of the STL cartilage file along with a value of thickness or curvature of that element. Since the results are obtained element-wise, one cannot simply take the raw numbers, as the size of each element differs. First, a normalized data set must be calculated, and this can be done by applying weights to each result to give them an importance factor. The thickness of a larger element weighs more than the thickness of a smaller one, and the same for curvature. As the units for ML methods are somewhat arbitrary, one way of normalisation can be to multiply the analyses values by the area of each element. In this manner, it is possible to obtain normalized statistics of the data set. Although the units are different, we still create a standardized form of statistical variance between the patients.

$$Y_i = A_i X_i \tag{6.1}$$

where Y_i is the normalized area result of data point i and X_i is the ith value of the data point e.g. the curvature of the ith element and A_i is the area of the ith datapoint. The next step is to extract statistical features from the normalized data set. Since it is hypothesized that there will be a higher degree of thinner elements in degenerative and traumatic patient cases, it may be interesting to look at the percentage of elements below a certain degree of the mean for the wall-thickness analysis following the equation

$$W_{percent} = \frac{(N_E < \mu_w - \alpha\sigma)}{N_E} \tag{6.2}$$

where μ_w is obtained for each individual analysis, and is the mean of the standardized data set of the wall-thickness analyses. The parameter σ is the standard deviation of each individual analysis. The parameter α being the weight attached to it, α is also constant for each type of analyses and cartilage, e.g. curvature analyses of the femoral cartilage should all have the same α, it is obtained through a guess and check method to create the highest possible separation of the patient groups. N_E is the total number of elements in each individual analysis. Therefore $W_{percent}$ is the ratio of number of elements below a certain degree of the standard deviation of the mean divided by the total number of elements in each individual analysis. A similar equation can represent the curvature analysis, but instead, it should be interesting to look at the percentage of elements above a certain degree of the mean, as a rougher surface should have more curvature

$$C_{percent} = \frac{(N_E > \mu_c + \alpha\sigma)}{N_E} \tag{6.3}$$

where $C_{percent}$ is the ratio of elements, μ_c is the average curvature of the normalized data set and the rest of the parameters the same as in equation 6.2.

6.2.2.3 Statistical Analysis

A Shapiro-Wilk test has been performed to verify the normality of the distribution of the extracted data. Since the data tested were mostly not normally distributed,

a Kruskal-Wallis test was conducted on each extracted feature. In cases where the results showed significant differences, a Dunn's test was used as post-hoc to analyze the specific sample pairs (C-D, D-T, T-C). The significance level (alpha) was set at 0.05, and the statistical results that present a p-value lower than alpha are considered significant. For each comparison, the elements in the sets are the number of patients present in the groups considered (24 in D, 15 in T, 8 in C). Data comes from a half-normal distribution, due to the small sample size and the thresholding applied during the segmentation process.

6.2.2.4   Machine Learning Classification

The aim of the use of MLis to prove the potential ability of these novel 3D features to classify degenerative, traumatic, and control subjects. Knime analytics platform was used: it is widely known and gives good performance in biomedical and health engineering applications [328]–[330]. Three tree-based algorithms were selected for the present ML analysis: decision tree (DT), random forest (RF) and gradient boosting (GB) [331], [332]. DT simply builds a basic tree while the other two use the DT to improve the power of their predictions. RF combines randomization and bagging while GB applies both bagging and randomization, adding the boosting technique which assigns weights to the classified subjects. Both are known to perform efficiently in multiple health engineering fields [333], [334]. K-fold cross-validation was performed during the train and test division with k=5 folds [335]. Accuracy, specificity and sensitivity for all three classes were used as classification metrics to evaluate the performances of the algorithms.
Different feature selections were given as input to the three tree-based algorithms for a total of 5 with respective numbers between parenthesis:

1. Bone (#8): All the features extracted from the Knee Bones

2. Cartilage (#16): All the features extracted from the Knee Cartilages

3. Bone and Cartilage (B-C) (#24): All the features extracted from the Knee Bones and Cartilages

4. Wall Thickness and Curvature (WT-C) (#27): All the features explained in the previous paragraph 2.2.2. Initially, there were a total of 48 of these features, but 13 of them were not considered because their standard deviation was too high compared to the average values, and these data could affect the classification process.The other 8 are the curvature standard deviation weight and the wall standard deviation weight, which are the same for every subject.

5. Total features (TOT) (#51): B-C and WT-C features together

Hole-related features have not been considered because most of them are zero, so they do not add any useful information for the classification.
A feature importance calculation was performed after the classification process for the RF algorithm model.

6.2.3   Results

6.2.3.1   3D measurements

The main damage from injury or disease in the cartilage tissue are highlighted by alterations in the composition of the synovial joint and surface degeneration, remodeling of subchondral bone, formation of osteophytes and appearance of holes in cartilage [336]. The data shown in Table 6.1 display the average bone mineral density, as well as radiodensity, volume and surface from each cartilage after tissue segmentation. The results were calculated for each group (Degenerative, Traumatic and Control) and compared.

Table 6.1: 3D Results. Mean is reported for each group. Standard deviation is reported in brackets and median in the row below in bold.

	D	T	C
Bone Mineral Density (g/cm^3)			
Femur	1.25 (0.03)	1.29 (0.03)	1.27 (0.03)
	1.25	**1.30**	**1.27**
Tibia	1.28 (0.02)	1.32 (0.03)	1.30 (0.03)
	1.29	**1.32**	**1.30**
Patella	1.34 (0.05)	1.41 (0.04)	1.41 (0.05)
	1.35	**1.42**	**1.40**
Patella Volume (mm^3)	20368.41 (4486.86)	17747.93 (4389.93)	19375.79 (5009.31)
	19315.82	**16575.77**	**20508.23**
Patella Surface (mm^2)	4867.88 (1614.10)	5648.82 (3180.33)	4105.83 (725.54)
	4402.45	**4516.32**	**4234.59**
Radiodensity (HU)			
Femur Cartilage	88.55 (5.74)	88.64 (12.34)	94.06 (7.45)
	89.51	**86.56**	**97.17**
Lateral Tibia Cartilage	88.45 (8.30)	91.78 (19.85)	91.76 (3.10)
	88.20	**89.53**	**92.21**
Medial Tibia Cartilage	104.20 (19.94)	101.32 (16.70)	104.93 (7.65)
	98.90	**97.33**	**103.74**
Patella Cartilage	78.98 (17.53)	79.19 (18.27)	95.10 (16.47)
	74.94	**77.16**	**88.36**
Cartilage Volume (mm^3)			
Femur Cartilage	20265.18 (6856.78)	13429.59 (2725.04)	11764.49 (4479.56)
	19618.83	**12956.89**	**9654.09**
Lateral Tibia Cartilage	2075.11 (1515.56)	1110.60 (409.59)	757.59 (380.87)
	1371.79	**1160.67**	**725.18**
Medial Tibia Cartilage	1526.14 (1226.54)	981.93 (610.23)	555.76 (368.51)
	1067.28	**868.62**	**440.17**
Patella Cartilage	3241.89 (1164.37)	2778.97 (656.93)	2866.61 (715.97)
	3199.50	**2734.05**	**2854.35**
Cartilage Surface (mm^2)			
Femur Cartilage	14737.79 (2866.13)	12270.98 (1378.72)	11968.50 (2663.58)
	14076.96	**12319.56**	**11541.29**
Lateral Tibia Cartilage	1809.96 (922.87)	1299.96 (437.06)	1082.64 (371.60)
	1458.98	**1238.18**	**1038.20**
Medial Tibia Cartilage	1702.80 (997.76)	1233.47 (469.07)	949.80 (400.35)
	1288.59	**1172.29**	**1001.64**
Patella Cartilage	2546.89 (469.92)	2443.72 (480.52)	2517.28 (409.93)
	2588.05	**2371.60**	**2530.24**
Presence of holes (%)	3.76	0.47	0

The D group presents lower BMD values compared to the others. The T and C groups have same values of density for patella bones, while for femur and tibia, the T group has higher values. Significant statistical results are between T-D groups both for femur (p-value=0.000352) and for tibia (p-value=0.00294); for patella between C-D groups (p-value=0.0236) and T-D groups (p-value=0.00044). The T group has the lowest volume and the highest surface in the patella. The D and C groups show similar trends in the volume and surface for the patella. However, no significant evidence come
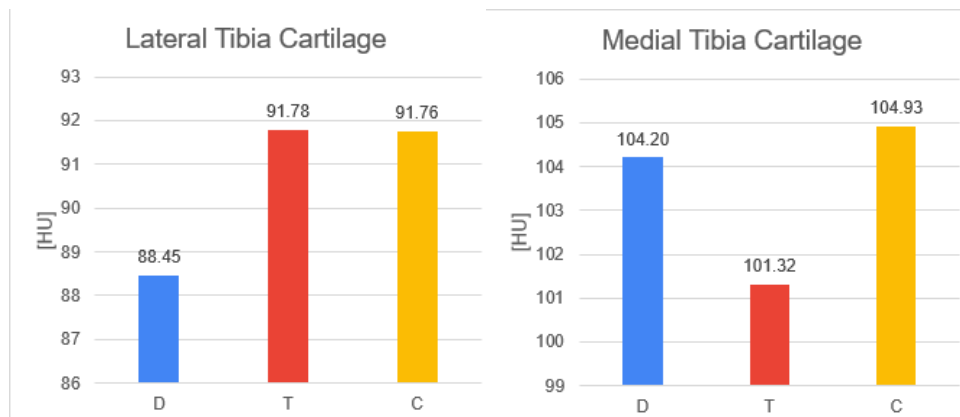
Figure 6.5: Differences in HU values for the two parts of tibia cartilage for D, T, C groups. The results are the same than in table 1.

from patella volume and surface. The C group present higher HU values for all cartilage segments. The T and D groups differ from case to case for every cartilage. The D and T have inferior values in the femoral cartilage and lower in the patella cartilage. However, the only significant difference in density is on the patella cartilage among C-D groups (p-value=0.0144). Medial and lateral tibial cartilage have opposite HU behaviors in T and D conditions (Figure 6.5), while these values remain constant in the C group. For all cartilages, volumes are higher in the D group compared to the other groups. The T group has higher volume than the C group for the femoral and tibia cartilage. In patella cartilage, volume is higher in the C group. Surface results are also higher in all cartilage parts for the D group. Moreover, the volume and surface of femoral cartilage demonstrate significant differences: significant differences in the volume are present among C-D (p-value=0.00212) and T-D groups (p-value=0.0055) and on the surface only between T-D (p-value=0.0143). For all other features no significant results appear.

Holes are detected in 8 patients of D group with the damage mainly in the femoral cartilage, followed by tibia and patella cartilage, as shown in Tables 6.2 and 6.3. Only one traumatic patient presents several holes.

Table 6.2: Number of holes.

Patients	Femoral Cartilage	Lateral Tibia Cartilage	Medial Tibia Cartilage	Patella Cartilage
1 (D)	3	1	7	0
2 (D)	2	0	0	0
3 (D)	1	0	1	0
4 (D)	1	0	0	1
5 (D)	1	0	0	3
6 (D)	4	0	0	0
7 (D)	1	0	0	0
8 (D)	1	0	0	0
9 (T)	5	0	0	2

Table 6.3: Total holes surface.

Patients	Femoral Cartilage (mm^2)	Lateral Tibia Cartilage (mm^2)	Medial Tibia Cartilage (mm^2)	Patella Cartilage (mm^2)
1 (D)	50.11	1.18	53.79	0.00
2 (D)	186.83	0.00	0.00	0.00
3 (D)	29.57	0.00	22.91	0.00
4 (D)	3.06	0.00	0.00	2.97
5 (D)	10.52	0.00	0.00	4.03
6 (D)	19.80	0.00	0.00	0.00
7 (D)	0.78	0.00	0.00	0.00
8 (D)	4.60	0.00	0.00	0.00
9 (T)	488.81	0.00	0.00	1.87

6.2.3.2   Wall Thickness and Curvature Analyses

The two analyses were run on each patient's femoral, patellar, medial and lateral tibial cartilages, resulting in eight data files for each patient. Each row of the data file contains three (x, y, z) coordinates in millimeters defining the element and the analyses value for that element. After the element values were normalized according to equation 6.1 the variables described in the section 6.2.2.2 were extracted.
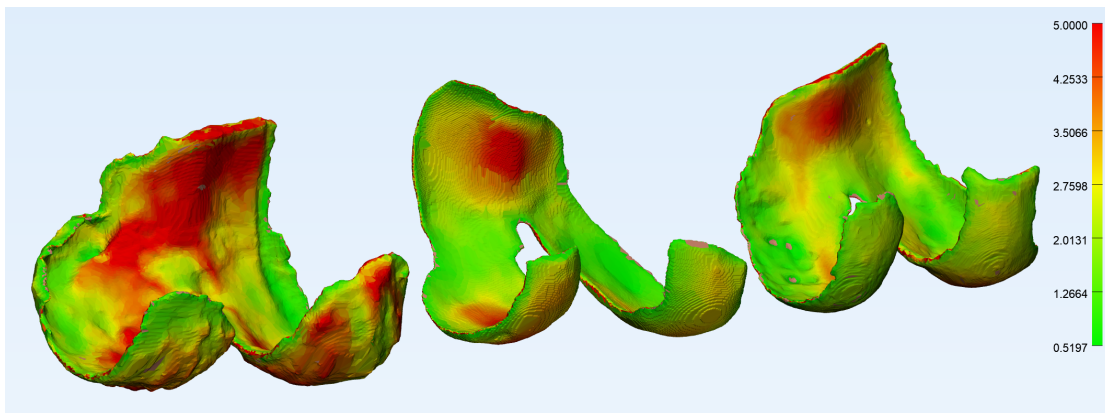
Figure 6.6: The wall-thickness analysis of a femoral cartilage in 3-matic, degenerative group (left), traumatic group (center) and control group (right)

Figures 6.6 and 6.7 show the wall-thickness and curvature analyses of a femoral cartilage, respectively. The wall-thickness analysis shows the distribution of thickness and one can see the very thin areas, especially around the holes in the cartilage. The curvature analysis shows the distribution of curvature about the cartilage, most of the regions of high curvature are around the edges. There are a few elements in the regions around the holes with high curvature, but they are badly represented as the edges around the holes are very thin and therefore contain very few elements.

Figure 6.8 shows the number of elements below 0.5 STD of the mean wall thickness for the femoral, patellar and medial cartilages and 0.3 for the lateral. These weights on the standard deviation gave a consistent separation of the traumatic and degenerative patients from the control patients.
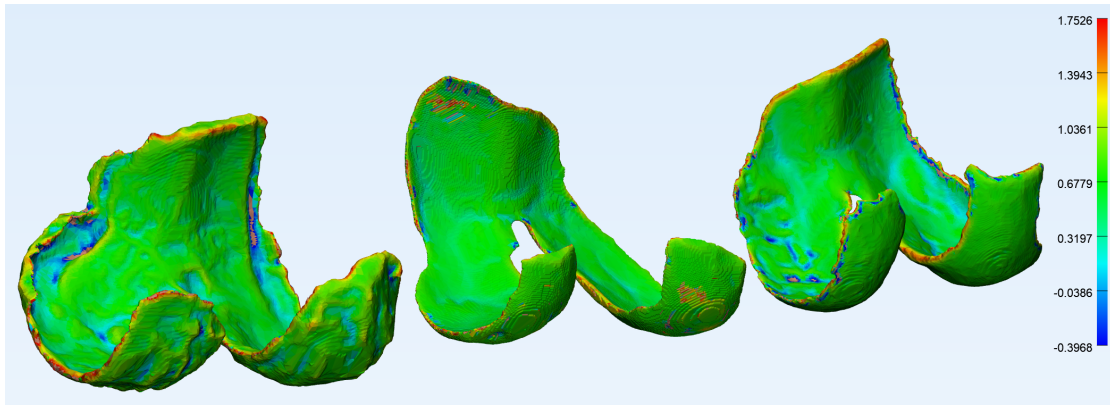
Figure 6.7: The curvature analysis of a femoral cartilage in 3-matic, degenerative group (left), traumatic group (center) and control group (right)

Figure 6.9 shows elements above 5 STD of the mean curvature for all cartilages. It was a bit more difficult to find a weight on the STD for the curvature to create a separation of the groups, but one can see that there is some separation, at least for the degenerative patient group.
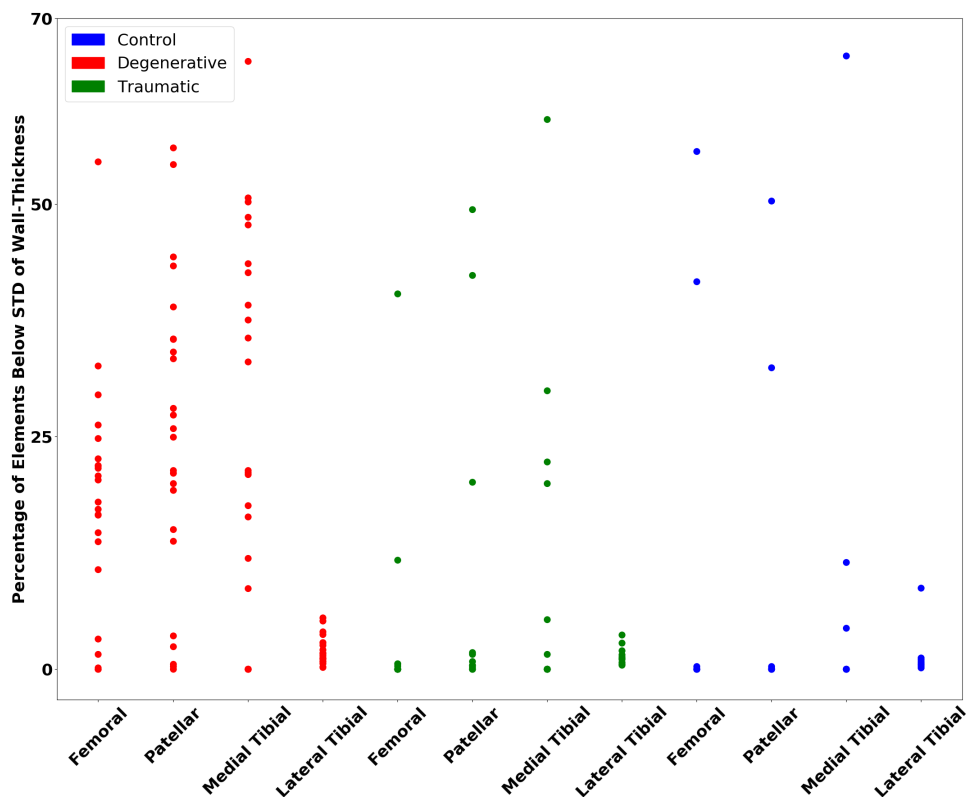
Figure 6.8: Percentage of elements below a certain standard deviation of the mean, using an STD weight of 0.5 for femoral, patellar, and medial tibia cartilages and 0.3 for the lateral tibia cartilage as per equation 6.2
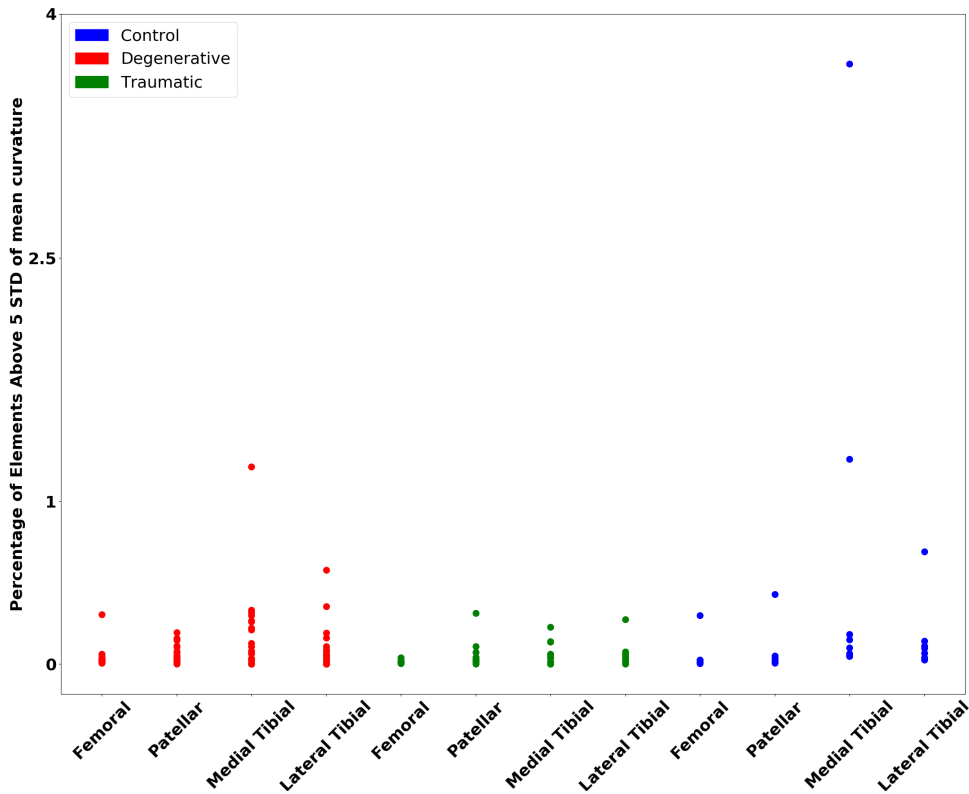
Figure 6.9: Percentage of elements above a certain standard deviation of the mean, using an STD weight of 5 for all cartilages as per equation 6.3

6.2.3.3 Machine Learning

Table 6.4 shows the evaluation metrics for the three-classes classification of degenerative, traumatic and control subjects using the five different feature selections described in the previous section. The best accuracy is 76.1 obtained with the B-C and Bone selection performing the RF algorithms, which gives the best accuracy in all the models. The TOT selection gives an accuracy higher than 70, while Cartilage and WT-C can reach a maximum of 69.6 and 63.0, respectively. The highest sensitivity is always obtained for the degenerative subjects, while the lowest is for the control subjects having a maximum of 50. Traumatic subject sensitivity is between the other two having a maximum of 87.5 with the RF algorithm and Bone selection. Specificity is generally high, having a value of around 90 for all the control patients.

The feature importance obtained with the RF algorithm can be seen in Table 6.5: it is clear that the volume of the Femoral Cartilage (FemCartVOL) has high influence for all the selection in which is present. Patella density (PatellaDENS) is also important in the multi-class classification with the TOT and B-C feature selection. The WT-C selection was not considered in this analysis because of the low accuracy obtained (maximum of 63.0) (Table 6.4), but it can be noticed that some of its features have quite a good importance in the TOT model (Table 6.5).

Table 6.4: Classification metrics for the three classes classification (Degenerative (D), Traumatic (T), Control (C)) using the five different features selections.

Feat. Selection	Alg.	Acc.	Sens D	Spec D	Sens T	Spec T	Sens C	Spec C
TOT	RF	71.7	87.5	63.6	57.1	93.8	50.0	92.1
	GB	67.4	87.5	68.2	64.3	84.4	12.5	92.1
	DT	63.0	79.2	59.1	71.4	78.1	0.00	97.4
B-C	RF	**76.1**	87.5	68.2	85.7	90.6	25.0	97.4
	GB	69.9	79.2	72.7	71.4	90.6	37.5	86.8
	DT	58.7	66.7	77.3	78.6	65.6	0.00	92.2
Bone	RF	**76.1**	91.7	72.7	87.5	87.5	12.5	91.4
	GB	67.4	83.3	68.2	78.6	78.1	0.00	97.4
	DT	60.9	79.2	63.6	50.0	81.2	25.0	89.5
Cartilage	RF	69.6	87.5	59.1	50.0	90.6	50.0	94.7
	GB	63.0	75.0	77.3	57.1	81.2	37.5	84.2
	DT	63.0	75.0	86.4	57.1	71.9	37.5	86.6
WT-C	RF	63.0	83.3	77.3	57.1	75.0	12.5	89.5
	GB	60.9	75.0	77.3	57.1	75.0	28.6	86.8
	DT	60.9	75.0	72.7	57.1	81.2	25.0	84.2

6.2.4 Discussion

This work aims to develop a new workflow to assess cartilage condition. Based on CT and MRI scans, a complete segmentation of the knee is performed. A 3D model is reconstructed from this segmentation, from which a unique set of data is extracted. The relationship between systemic bone mineral density (BMD) and cartilage properties has been enhanced in recent years. Previous reviews indicate the positive correlation between BMD and cartilage defects, particularly related to the knee joint [337], [338]. The results of this study show the degenerative group presenting lower BMD values for healthy and traumatic individuals. Although several studies have demonstrated that higher systemic BMD is associated with increased progression of cartilage defects, this relationship is still under investigation [339]. A recent study demonstrated that BMD was the highest when the knee OA was mild, and was significantly lower in moderate and severe OA. Generally, it is considered that the severity of OA increases and the level of BMD decreases with increasing age [340]. The different correlations between data could be due to the restricted number of participants, their characteristics, outcome measures, or the status of the knee joint (as it is in the early stage). However, BMD could be an index of the cartilage condition because it is now validated that bone condition affects the course of the most common joint disease. In summary, the indexes based on the bone could show a way to differentiate the groups. This is proved by the conducted statistical analysis: on the patella bone, the D group can be discernible from C and T groups and on the femur and tibia bones, it differentiates from the T group. Moreover, the T group shows lower patella volume than the other groups. Some trauma may have involved the patella and caused its dislocation and subsequent cartilage lesion leading to early OA [341]. Thus, the examination of the patella volume can be of interest to investigate the presence of traumas.

Still, regarding the patella, its cartilage density results a good discriminator between C and D groups. In general, control patients present higher HU values for all

Table 6.5: Feature Importance: The most important features for all the feature selections (excluding WT-C) for the RF algorithm classification model (12 features for the TOT and B-C selections, respectively out of 51 and 24). It is shown the percentage of importance for each parameter in the correspondent feature selection. All eight features are presented for the Bone selection and eight out of sixteen for the Cartilage selection. "DENS" stands for Density and when "Cart" is not mentioned in the name of the feature it means that the bone value is considered. STD refers to the DENS values.

Impo	TOT	%	B-C	%
1	FemCartVOL	6.69	PatellaDENS	8.54
2	PatellaDENS	5.69	FemCartVOL	7.91
3	FemWallBelowSTDWeight	4.22	FemCartSURF	7.28
4	FemCartDENS	3.77	TibiaDENS	6.16
5	PatWallVar	3.65	PatCartDENS	5.91
6	LatWallMean	3.45	TibCartLatVOL	5.41
7	PatCartDENS	3.41	PatellaSTD	5.35
8	FemWallRMS	3.16	PatellaSURF	4.72
9	PatWallBelowSTDweight	3.13	FemCartDENS	4.51
10	TibiaDENS	3.06	TibCartLatSURF	4.37
11	FemCartSTD	3.01	PatellaVOL	4.35
12	FemWallMean	2.82	TibCartMedSURF	4.30

Impo	Bone	%	Cart	%
1	FemurDENS	17.74	FemCartVOL	14.21
2	FemurSTD	16.87	FemCartDENS	11.07
3	TibiaDENS	15.20	PatCartDENS	9.31
4	TibiaSTD	12.57	FemCartSURF	8.14
5	PatellaDENS	12.21	TibCartLatVOL	6.84
6	PatellaSTD	10.24	TibCartMedSTD	6.51
7	PatellaVOL	7.69	TibCartLatDENS	5.96
8	PatellaSURF	7.48	FemCartSTD	5.85

cartilage segments, while traumatic and degenerative change case to case. This could be because of the fact that cartilages in the early stages of OA generally present a greater amount of water with respect to physiologically normal cartilages [342]. Therefore, the density calculated on the entire cartilage volume can discriminate between pathological and healthy conditions. Since traumatic and degenerative patients have opposite HU behaviors on lateral and medial tibial cartilages, while control ones remain constant on both parts, this result could represent proof of control regarding tissue density and pathologies.

The measurements of cartilages show a characteristic trend: volume increases for all the cartilages in degenerative patients. This is also strongly confirmed by the significant difference between the degenerative and the other two groups for the femoral cartilage. Greater volume may indicate cartilage swelling in the early stage of degeneration due to an increased water content [343], [344]. It is in agreement with biomechanical evidence, which suggests that the volume of degenerative cartilages and surrounding tissues would be greater than healthy and traumatic circumstances. Moreover, all degenerative surfaces cartilage results were higher and we found a correspondending

statistical difference between traumatic ones regarding the femoral cartilage. It is
particularly interesting how the patella bone and cartilage play a fundamental role
in the diagnosis. Until now, the evaluation of cartilage was conducted mainly on the
tibiofemoral joint, and the predominant scales for cartilage diseases do not take into
account patellofemoral compartment [345]. Our study reveals that this patellar joint
should be considered with more interest in knee assessment.

The visual inspection of the 3D models reveals that holes are present only in the
degenerative cartilage. A third of the patients in the degenerative group present holes
in their cartilage, mainly in the femur. Despite the limited amount of data analyzed in
this paper, the fact that holes are only present in the degenerative group establishes a
ground for future research with aim of demonstrating that the detection of holes can
be an indicator of degenerative cartilage.

The wall thickness analysis presented results of interest. A clear separation of the
degenerative and traumatic patients is visible from the control group. Although a
more significant separation was expected for the traumatic group, the wall thickness
analysis did not take into account the holes that have formed in the cartilages, which
should be considered, as it is a form of degeneration. This is supported by Vincent and
Wann [346], as they have found a link between trauma to cartilage and a decreased
wall thickness, as seen much more clearly in the degenerative case. The curvature
analysis shows less clear results, although a separation for the degenerative group can
be observed. Studies such as Folkesson et al. [347] have found that the curvature for
patients suffering from OA is significantly higher when compared to control patients,
which is shown in the results here, as OA is a degenerative disease. Although it might
be expected to find similar trends in the traumatic patients, the analysis results do
not show as noteworthy of a difference.

Most of the ML results can be considered highly satisfactory: it is clear that the
models, especially using RF, can predict with good sensitivity the degenerative and
traumatic subjects, and all the 3D novel features extracted to have a good predictive
power (excluding the WT-C selection, which results are lower). This can also be seen
from the feature importance results (Table 6.5), where cartilage and bone features
assume a dominant role in the classification. To our knowledge, these features extracted
manually from bones and cartilage images of the knee were never used to distinguish
the type of injury that provoked OA. A similar accuracy was obtained by Kwon et al.
[323] using the gait and x-ray data (75,5%) predicting KL grade, while Du et al. [317]
using a PCA approach had a similar sensitivity with RF in the KL grade classification,
reaching better results with other algorithms in respect to RF, like simple artificial
neural networks or support vector machines. A future improvement of the study can
be to extend the classification to existing evaluation grades like KL, which, knowing
the current results, can give us interesting results in terms of accuracy and sensitivity
and eventually use other algorithms like simple or advanced artificial neural networks.
A new index can also be developed, starting from these results, integrating to the 3D
ones, other features extracted from the 2D images manual elaboration of the CT-scans
and MRI knee exams, like for example bone osteonecrosis, sclerosis, osteophytes and
others.

6.2.4.1 Limitations

This work presents some limitations. The number of patients is limited. Moreover,
the three categories are unbalanced: there are currently a lot of degenerative and few

control subjects. This affects the specificity results in the ML classification for the control subjects: in the future the application of algorithms that can balance more the number of subjects of the different classes (i.e. SMOTE [348]) can be considered and, generally speaking, the results would be more accurate with an increased number of samples. More samples will eventually allow the use of more advanced artificial intelligence technologies like DL and advanced neural networks. In addition, to improve the accuracy, the control patients could be excluded, and a binary classification can be performed on degenerative and traumatic patients.

The segmentation was manually done, leading to possible inaccuracies in the elements' conformation. Although a standard protocol was defined, the overall procedure was performed by different people, and occasionally, decisions have been taken based on visual interpretations. Therefore, some inaccuracies can be present in the final data.

Image quality also affects the initial steps of the segmentation process and the subsequent data extraction.

The wall-thickness analysis also did not take into account any holes in the cartilage; this leaves out valuable information that could be extracted from the cartilage models as the traumatic patient group often times have gaps in their cartilage. This could explain the relatively low percentage of elements below the standard deviation of the mean in figure 6.8 compared to the degenerative patients.

6.2.5 Conclusion

The research focuses on the realization of a new methodology to assess cartilage condition, based on density and geometric features from 3D reconstructed knee joint. Both bone and cartilage metrics revealed interesting indicators to evaluate cartilage status. For the bones, it is shown that bone mineral density is related to cartilage integrity. Also, patellar bone volume can help to differentiate healthy knees from traumatic ones. On the cartilage aspect, the radiodensity of cartilage can be a robust index to distinguish pathological and healthy conditions. Similarly, cartilage volume can testify to cartilage degeneration. An in-depth analysis of cartilage geometries showed that thickness and curvature analysis are powerful tools to discriminate healthy patients from patients suffering from a pathological condition. The patellofemoral compartment should be investigated in more depth to evaluate the knee joint condition. Those individual results combined have shown the potential to be reliable indicators of knee condition. Advanced statistics and machine learning demonstrated that it is possible to classify the knee cartilage status based on the previously extracted features.This study is a step towards defining of solid indicators of knee joint quality. Pursuing this research by adding new parameters such as age, gender, and also longitudinally observing the evolution of the presented knee joints through time, would be interesting to confirm and identify more accurate markers of cartilage health.

6.3 Towards new assessment of knee cartilage degeneration

The work below has been published in *CARTILAGE* ([349]).

6.3.1 Introduction

This study compares different cartilage assessment metrics, developing a novel work-flow to 3D model bone and cartilage and, moreover, analyzing new features for a more sensitive cartilage assessment, currently required as a support element towards more patient-specific treatment development.

6.3.2 Material and methods

Figure 6.10 shows the work done in this manuscript starting from the recruitment to the data acquisition, analysis, and computation of the feature importance.
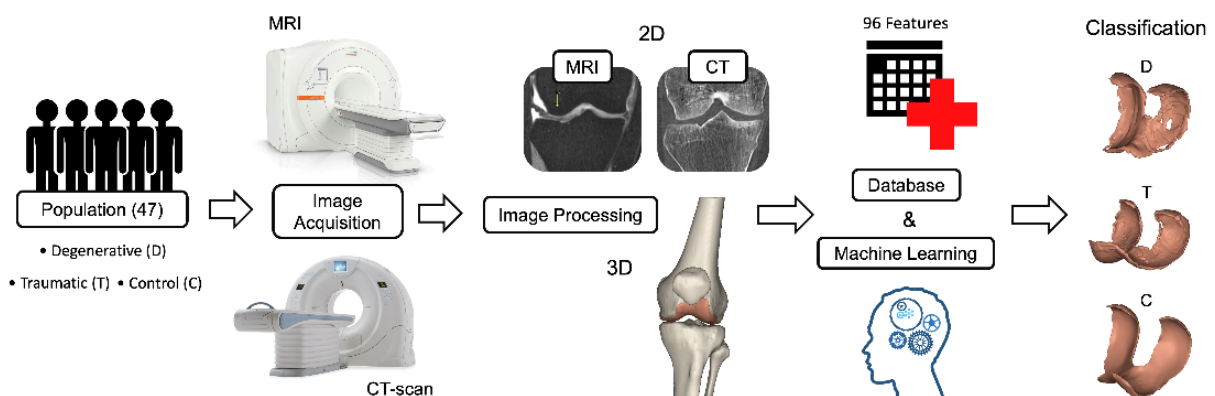
Figure 6.10: Graphical abstract

6.3.2.1 Participants

Recruitment: After completing a written informed consent, 47 subjects (24 females, 23 males, age = 50±19 years) underwent CT and MRI scans of a single knee at Landspitali University Hospital in Reykjavik, Iceland, using standardized acquisition protocols and patient positioning. From the total of patients, 23 subjects (12 females, 11 males, age = 64±12 years) were suffering from degenerative (D) cartilage. They were examined by an orthopaedic doctor due to pain from osteoarthrosis and were placed on the waiting list for treatment with TKA (Total Knee Arthroplasty).16 (9 females, 7 males, age = 35±11 years) suffered from a knee trauma (T) with possible cartilage injury. The emergency clinic provided an alert when there is a patient with suspected ligament injury and patella dislocation. They underwent plain x-ray to exclude fracture. Then, they were called to exclude any history of knee injuries or problems. The alert was received within a week, and the patients underwent CT and MRI during the second week from the day of the trauma. Finally, 8 subjects (3 females, 5 males, age = 34±14

years) were involved in the study as control (C) subjects (no symptoms of history of knee trauma/degeneration). For D and T group, in addition to the CT and MRI data that were acquired for this study, X-ray data was also available, as a part of the routine clinical evaluation detailed above. The X-rays were not performed for the C group.

6.3.2.2 2D measurements

An exhaustive radiological examination was performed on the bones and articular cartilages of the knee joint to assess their condition. These observations were based on three types of 2D medical imaging: X-ray, CT and MRI. The assessment was done on femur and tibia from both the medial (MC) and lateral (LC) compartments as well as on the patella and femoral trochlea within the femoropatellar compartment (FPC) of the scanned knee.

Bone Figure 6.11 sums up examples and brief definitions of the pathologies observed on the femur, tibia, and patella. The subfigures on the left (a, c, e, g and i) correspond to CT scans while the right subfigures (b, d, f, h, and j) correspond to MRI scans. As observed in figure 2, some pathologies could be found in both CT and MRI, while others (i, j) had a particular 2D image.

Cartilage Figure 6.12 contains examples and brief definitions of the gold standard observations made on the cartilage and the joint space. Except for the Ahlbäck grading, which was observed on an X-ray, the rest of the observations were made on MRI scans.

Articular cartilage thickness To manually measure the articular cartilage thickness (ACT) from an MRI scan of the knee, a single investigator followed the methods previously proposed by Koo et al. [350] to segment both femoral condyles into three regions of interest. These regions, called anterior, medial, and posterior were estimated as the main weight bearing regions of the articular cartilage in a sagittal view plane. The method to define these regions consisted of locating a central axis perpendicular to the sagittal plane by fitting a cylinder that best represented the articular cartilage geometries[298]. Then, tibiofemoral contact points were identified, and lines were drawn from that central axis to these contact points to define the three regions. In the LC, the 0° is defined as the most inferior point of the condyle, while for the MC this point occurs about 20° anterior to that of the LC. The anterior region in both compartments extends 30° anterior to the 0°, the middle region from 0° to 30° posterior to the 0° line and the posterior region from 30° to 60° posterior to the 0° line. Finally, the points where the measurements were taken were located at the center of each of the three regions in each compartment, as shown below in Figure 6.13. The values of the ACT shown in the Results section are an average of the three contact points (anterior, medial and posterior) for both medial and lateral compartments.

From the same slices used to measure the femoral ACT in the medial and lateral compartments, the tibial ACT was measured. In both cases and as shown in figure 6.14, an anteroposterior line representing the length of the tibial cartilage was drawn and divided into three regions of equal length. The center of each region (anterior, middle, and posterior) was determined as the point where the cartilage thickness was measured. The values for the tibial cartilage thickness in each compartment are later displayed as the average of these three points.
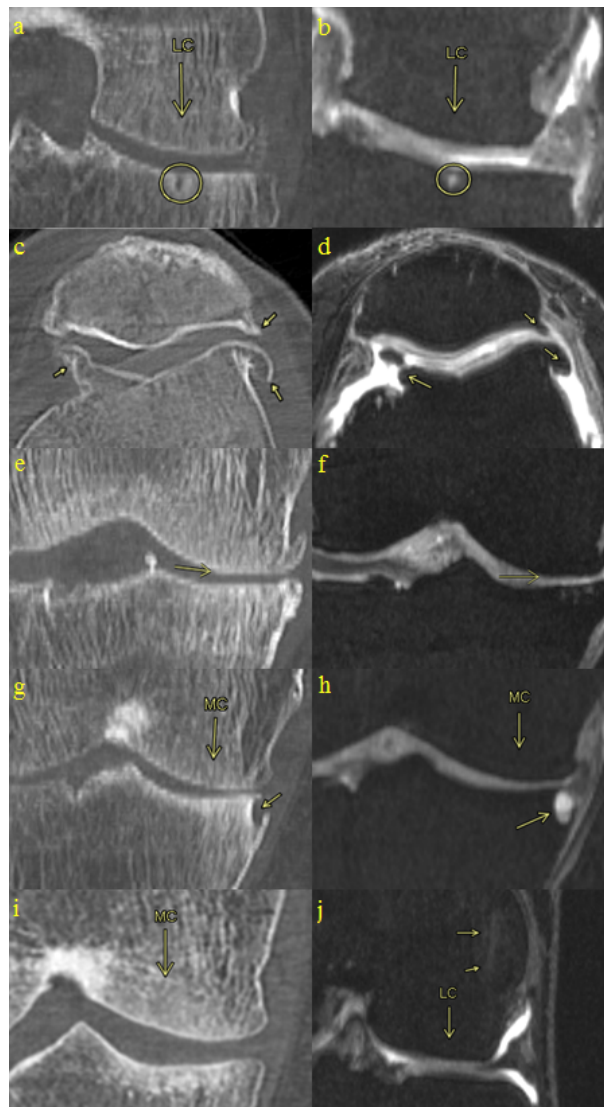
Figure 6.11: **Bone observations**. (a, b) Subchondral bone cysts are typically spherical or ellipsoidal fluid-filled cavities within the subchondral bone region. (c, d) Osteophytes are cartilage-capped bony proliferations (spurs) that most commonly develop at the margins of a synovial joint as a response to articular cartilage damage. (e, f) Bone attrition is the result of flattening or depression of the articular surfaces, probably because of bone remodeling. (g, h) Osteonecrosis is a generic term referring to the ischemic death of the constituents of the bone and is observed as if the bone is missing a piece. (i) Subchondral bone sclerosis is a thickening of the bone seen in joints affected by OA. It is observed as a 'whitening' of the bone only in CT. (j) Subchondral bone edema is a build-up of fluid in the bone marrow as a response to an injury or OA condition visible on MRI but not on CT.

As for the FPC, the measurements were taken from an axial plane view, where both articular cartilages from the femoral trochlea and the patella were the thickest in the same slice. This means that the chosen slice depended on both cartilages and was not the same for all patients. On the patella, three points were used to measure the cartilage thickness, the center one as the most inferior point of the patella, then a medial point as the center point of the medial part of the patella cartilage and a lateral one as the center of the lateral part of the cartilage. Lastly, on the femoral
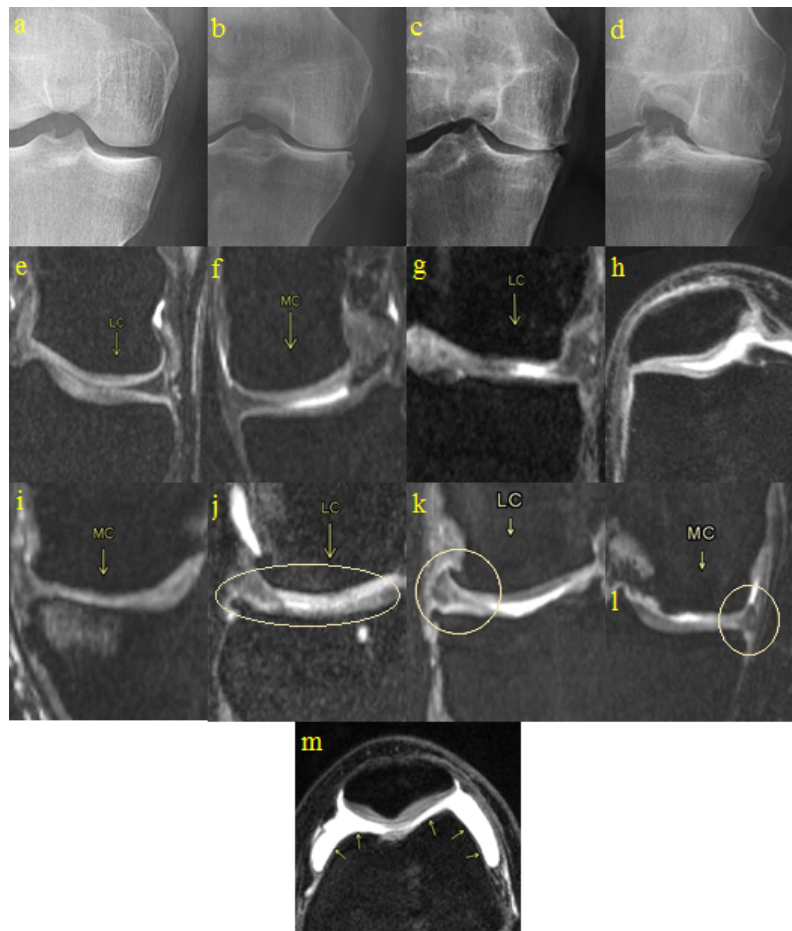
Figure 6.12: **Cartilage and joint space observations**. (a, b, c, d) Ahlbäck grading is a classification system that focuses on the reduction of the joint space as an indirect sign of cartilage loss. (a) grade 0: normal. (b) grade 1: joint space narrowing (less than 3 mm). (c) grade 2: joint space obliteration (elimination). (d) grade 3: minor bone attrition (0-5 mm). (e, f, g, h, i) ICRS (International Cartilage Repair Society) grading is the most used score system for quantification of existing cartilage defects at the knee. (e) grade 0: normal cartilage. (f) grade 1: nearly normal cartilage. Superficial lesions; soft indentation and/or superficial fissures and cracks. (g) grade 2: abnormal cartilage. Lesions extending down to <50% of cartilage depth. (h) grade 3: severely abnormal cartilage. Defects extending down to >50% of cartilage depth; down to calcified layer but not through the subchondral bone. Blisters. Defects more visible towards the medial area of the patella. (i) grade 4: severely abnormal. Lesions extending down through the subchondral bone. (j, k, l) Meniscal pathology is associated with an elevated prevalence of MRI-detected cartilage damage. There are three types of pathology; (j) degeneration: not acute as a tear, this injury is a more gradual onset and tends to occur as we get older. (k) rupture: is a tear in the lateral or medial meniscus due to rotational forces directed to a flexed knee. (l) protrusion: when the location of the outer edge of a meniscus is beyond the tibial articular surface. (m) Synovitis – Effusion. While synovitis is the inflammation of the synovium; effusion is when excess synovial fluid accumulates in or around the knee joint. It is observed generally in the FPC as a white stain.

trochlea, two points were used to assess the cartilage thickness, one at the center of
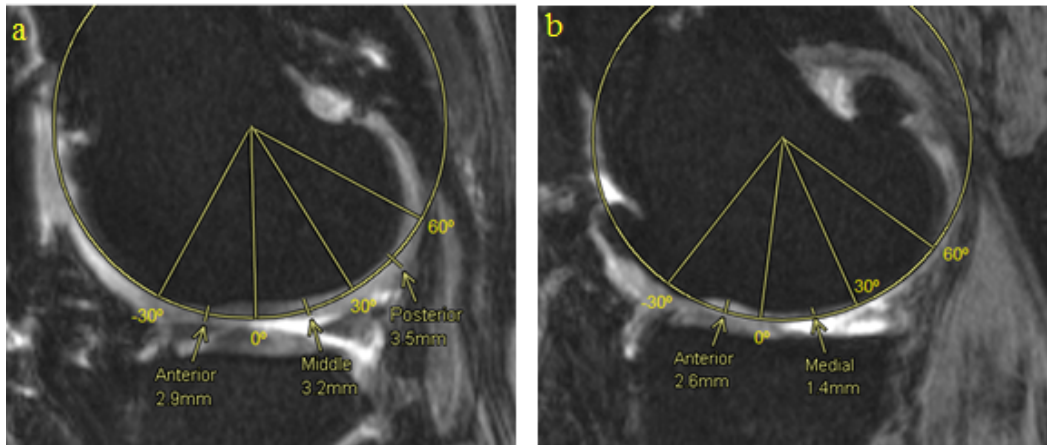
Figure 6.13: **Femoral cartilage thickness measurements, medial and lateral compartments**. Fitting cylinder method to obtain three regions of interest, anterior (-30º-0º), medial (0º-30º) and posterior (30º-60º) in the lateral compartment (a) and the medial compartment (b).
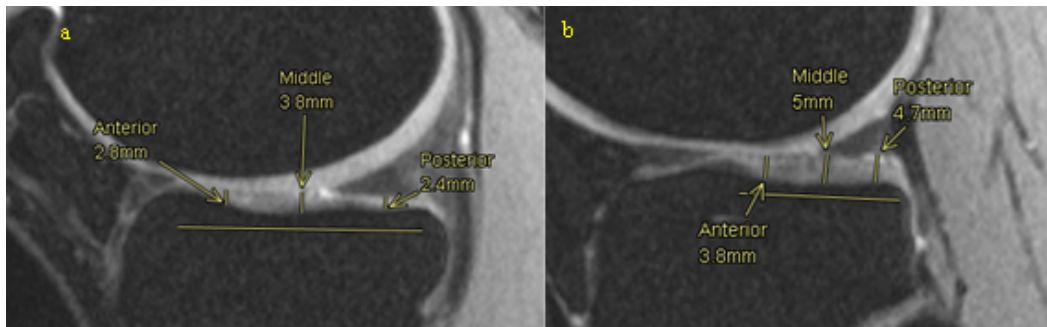
Figure 6.14: **Tibial cartilage thickness measurements**. Anterior, middle and posterior points are measured along the tibial cartilage in medial (a) and lateral (b) compartments.

the medial condyle cartilage and another at the center of the lateral condyle cartilage (Figure 6.15).
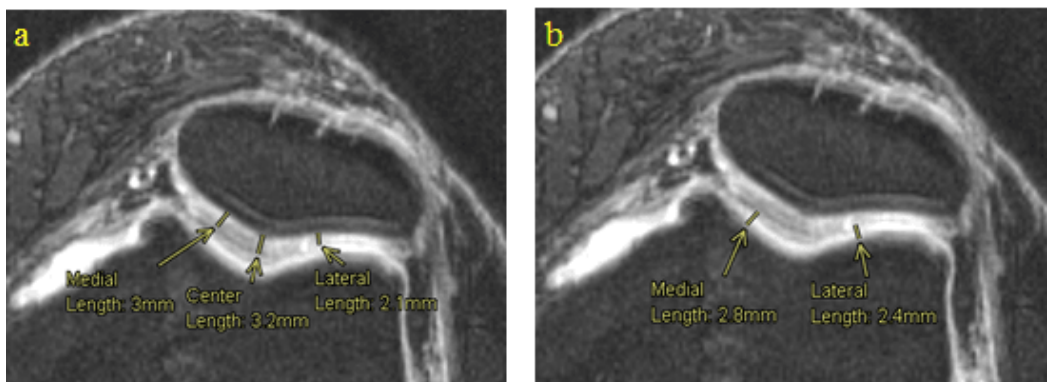
Figure 6.15: **Cartilage thickness measurements, femoropatellar compartment**. Measurement of the articular cartilage thickness at three points on the patella (a) and articular cartilage thickness of the femoral trochlea on two different points (b).

Cumulative index based on bone conditions A cumulative index (CI) from 0 to 6, was used to quantify the bone anomalies present in each bone, i.e., subchondral cysts, subchondral sclerosis, osteophytes, bone attrition, osteonecrosis and/or subchondral edema, regardless of the compartment for each patient. Hence, for an observed pathology (either in CT or MRI) a 1 was assigned and consequently, the index was the sum of pathologies present in a certain bone of a certain patient. Sometimes, when the CI is compared against observations made within a compartment such as the AG or the ICRS score, the index is then considered for the bone in question within a compartment.

6.3.2.3 3D measurements

The DICOM images were imported into a medical device software (MIMICS, Materialise, Belgium). Figure 6.16 describes the processing workflow. This workflow was repeated and evaluated 3 times by 3 biomedical engineers, under the supervision of a project manager, to obtain the most accurate segmentation. The bones (femur, tibia, patella, and fibula) were segmented from the CT scan. From the MRI datasets, the cartilage of femur, tibia and patella were segmented using the same pipeline: first, a mask was created by setting a density threshold interval, to delimit the part of interest. Then, a manual adjustment was performed to define as precisely as possible the mask for each entity. A visual inspection was done to check that no mask was overlapping with another. Each mask was then calculated in 3D and was smoothed and wrapped to ensure a better model quality. From the CT scans, 4 objects were 3D calculated: the femur, the tibia, the patella, and the fibula (all bones). From the MRI, 4 objects were also 3D calculated: the femoral cartilage, the medial tibia cartilage, the lateral tibia cartilage, and the patellar cartilage.
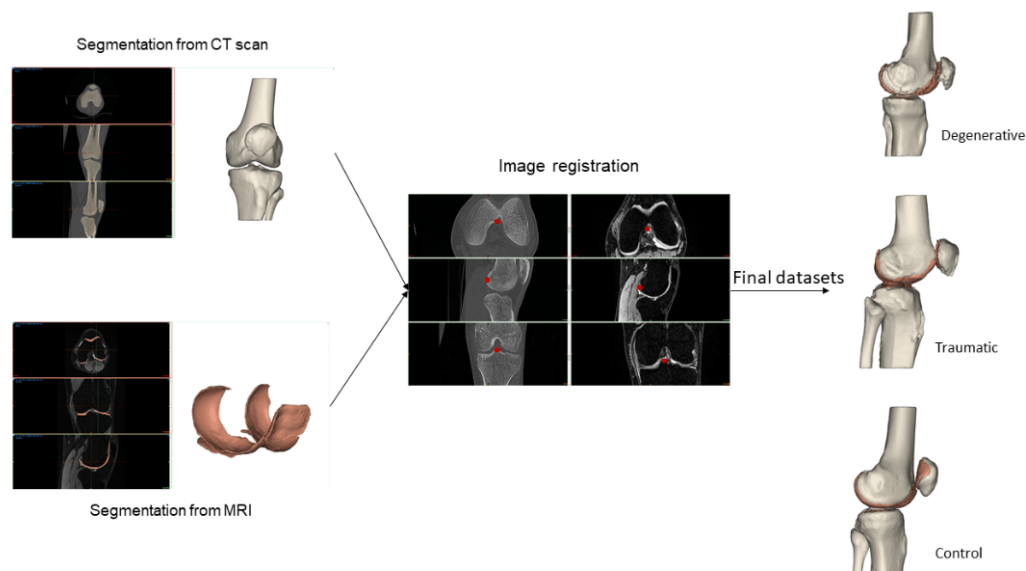
Figure 6.16: Segmentation workflow

The next step was the image registration, done from the CT scan. The MRI objects were combined with the CT objects. Bone anatomical landmarks were identified from the two scans. The two sets can be aligned, by superimposing these points into the two separate scans (Figure 6.17). From the combined dataset, 3D models of femoral,
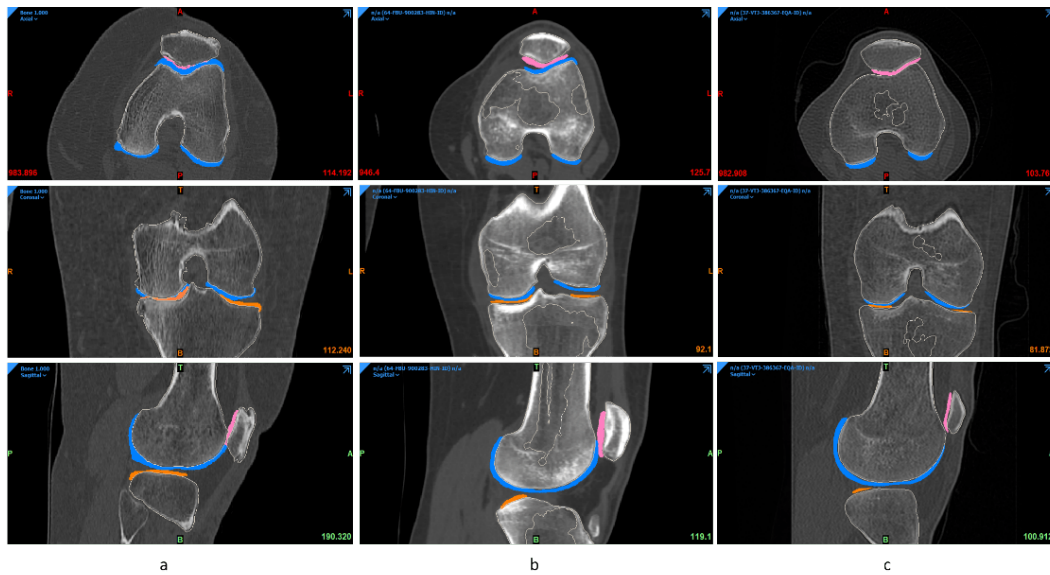
Figure 6.17: Final registration for the three groups of patients (a) Degenerative (b) Traumatic (c) Control.
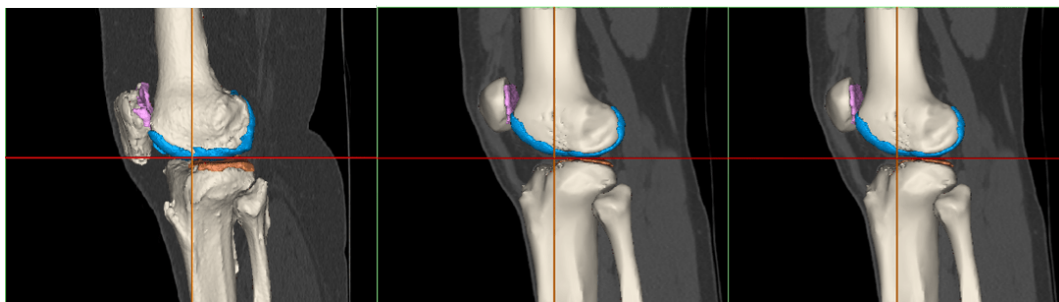
Figure 6.18: 3D model from the registration for the three groups of patients (a) Degenerative (b) Traumatic (c) Control.

tibial, patella, and fibula bones and cartilages were created and displayed (Figure 6.18). A visual inspection was done to check that no parts were overlapping, and that the anatomy was respected. If not, manual adjustments or a new image registration were performed. From this final file, the radiodensity of each part (bone and cartilage), was extracted in Hounsfield Units (HU). The Hounsfield scale is a quantitative scale to define radiodensity. Water is arbitrarily assigned as 0 HU, meaning that materials denser than water have positive values and materials less dense have negative values. The bone mineral density (BMD) (in g/cm3) was computed from the radiodensity using a linear formula that was determined empirically based on phantoms. To avoid partial volume effect between two shades of gray, an erosion of 1 pixel was performed for each cartilage segment. Next, the cartilage mask was filtered between 0-300 HU to eliminate pixels with intensities outside the soft tissues range. The cartilage radiodensity was extracted from this final mask. The volume (in mm3) and the surface (in mm2) were also computed from each 3D object.

6.3.2.4 Data analysis

Statistics To determine whether there were significant differences between the three groups (D, T, C) an ANOVA test was performed, and differences were considered

Feature Selection	Number of Features	Source
Tot Feat	96	All the available features from MRI, CT, and 3D elaboration
2D Feat	78	Features from MRI (52) and CT (26)
3D Feat	18	Features of cartilage volume and density (and its standard deviation) from 3D elaboration
Ct - Scan Feat	26	Features from CT – part of the 2D group
MRI Feat	52	Features from MRI – part of the 2D group
Bone Feat	50	Features of Bone from CT and MRI (subchondral bone cysts, sclerosis and edema, osteophytes, osteonecrosis, and bone attrition)
Cartilage Feat	26	Features of Cartilage from MRI (ICRS grades, meniscal pathology, synovitis-effusion, and measurements of thickness)

Table 6.6: Feature Selection Sets used as inputs for the ML analysis

significant at p<0.05. If differences were encountered, a post-hoc test with Bonferroni correction was used to determine which group or groups were significantly different.

Machine learning   Knime analytics platform (v. 4.3.1) [328] was adopted to develop the steps of the ML analysis: this software was previously employed in multiple biomedical studies that confirm its efficiency [329], [334]. In the present ML analysis, two tree-based algorithms were applied to the multi-classification of the degenerative, traumatic, and healthy (control) patients: Random Forest (RF) and Gradient Boosting (GB) [331], [332]. Both RF and GB rely on the use of the decision tree creating an ensemble of trees which drastically increases the prediction performance and addresses the instability of a single tree. RF works by combining randomization and bagging: it builds a set of basic decision trees during the training and the predicted class is the mode of the classes of the individual tree. GB applies boosting and randomization in a similar way to RF, adding bagging techniques that assign a higher weight to wrongly classified. RF was performed using the same random seed for every model and the same hyper-parameters (number of trees=100, split criterion= Information Gain Ratio, maximum three depth=10, and minimum node size=1). The same was done with GB (number of trees=100, maximum three depth=4, and learning rate=0,1). A 10-fold cross validation was performed for the train and test division of the dataset to have a complete and reliable view of all the dataset during the ML analysis. Accuracy, precision, recall, and F1 have been considered as classification metrics. To better understand the prediction ability of the different features extracted from the medical image analysis, seven subsets are chosen as input to the tree-based algorithms: details can be seen in Table 6.6. Based on the ML models with the best results for each subset, a feature importance analysis is performed using the software tools included in Knime analytics platform (v. 4.3.1).

6.3.3 Results

6.3.3.1 2D measurements

Bone Of the six pathologies observed in bone, figure 6.19 only shows the percentages of three of them that best indicate differences between the groups.
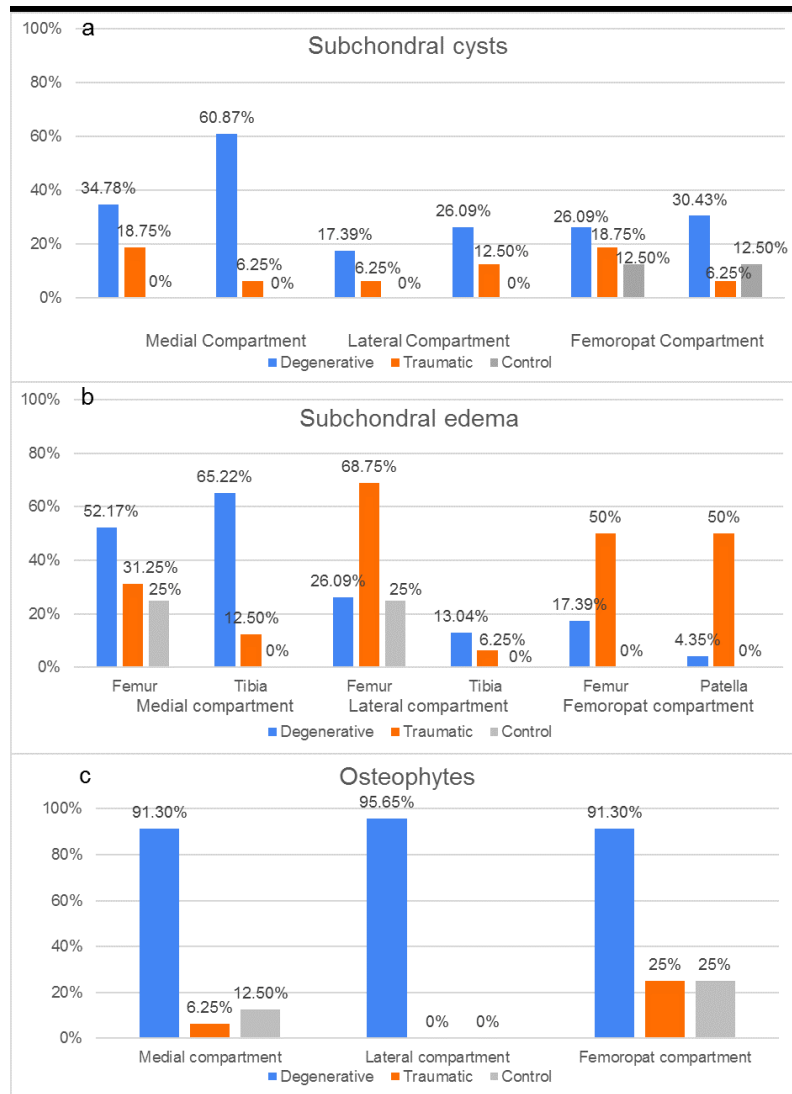
Figure 6.19: **Bone pathologies distribution**. Percentages of patient groups (D, T, C) with (a) Subchondral cysts. (b) Subchondral edema, and (c) Osteophytes. according to the respective compartment.

Cartilage Figure 6.20 shows the percentage of patients in each group which presented meniscal pathology and synovitis-effusion.

As the ICRS grading is not a binomial result, their average values and standard deviation (SD) for each group are shown instead (Figure 6.21). The results indicate that in the MC, both femur and tibia had a significant higher grading in the D group compared to T and C (p<0.01). Meanwhile, there were no significant differences of the ICRS grading in the LC bones between the groups. Finally, in the FPC the femoral trochlea of the D group had a significant higher grading (p<0.05) than the T and C
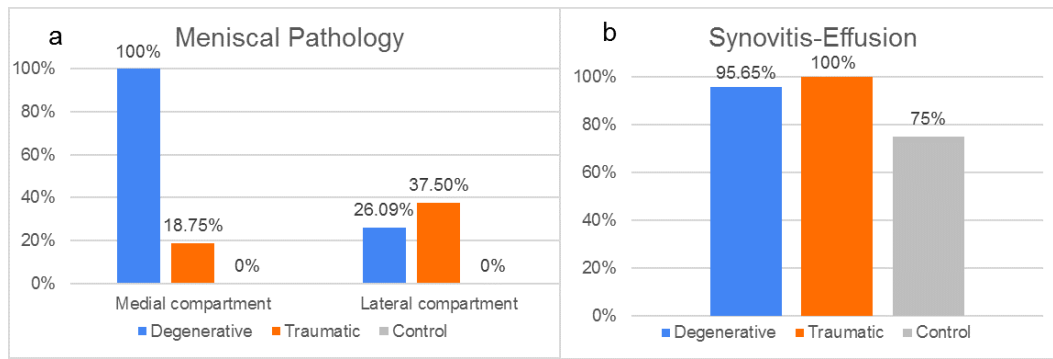
Figure 6.20: **Cartilage and joint space pathology distribution**. Percentage of patient groups (D, T, C) with (a) meniscal pathology (b) synovitis-effusion, according to the respective compartment.

groups while in the patella the ICRS values was higher (p<0.05) in D and T when compared to the C group.
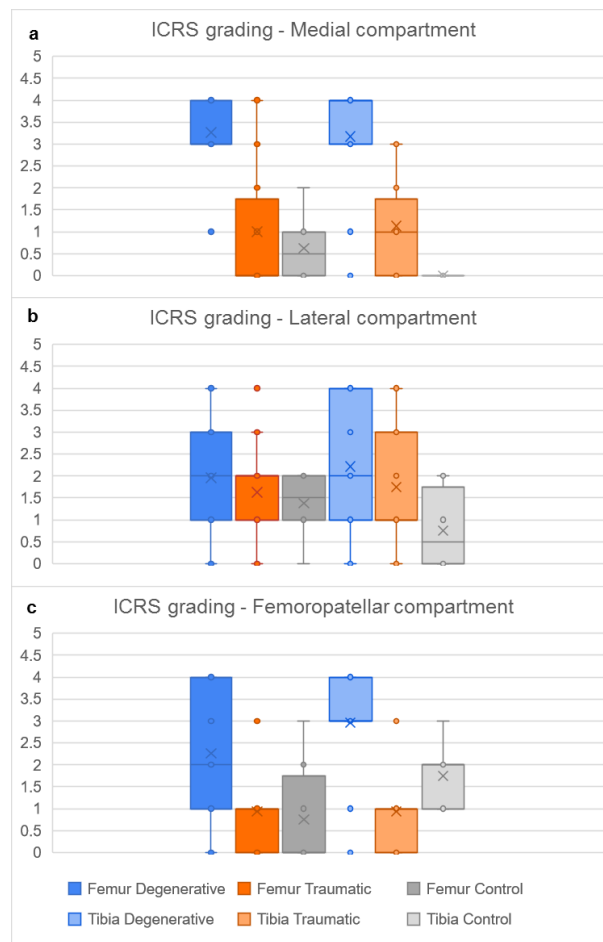
Figure 6.21: Distribution of the ICRS grading according to bones in each compartment, (a) medial, (b) lateral and (c) femoropatellar, for the three groups (degenerative, traumatic and control).

Cumulative index based on bone conditions For the femur, the cumulative index displayed in Figure 6.22 was higher in the degenerative group when compared with

the traumatic (p< 0.05) and control (p< 0.01) groups, while the CI of the traumatic group was higher than the CI in the control one (p<0.05). Then, for the tibia the degenerative group presented a higher index than the traumatic and control groups (p<0.01).
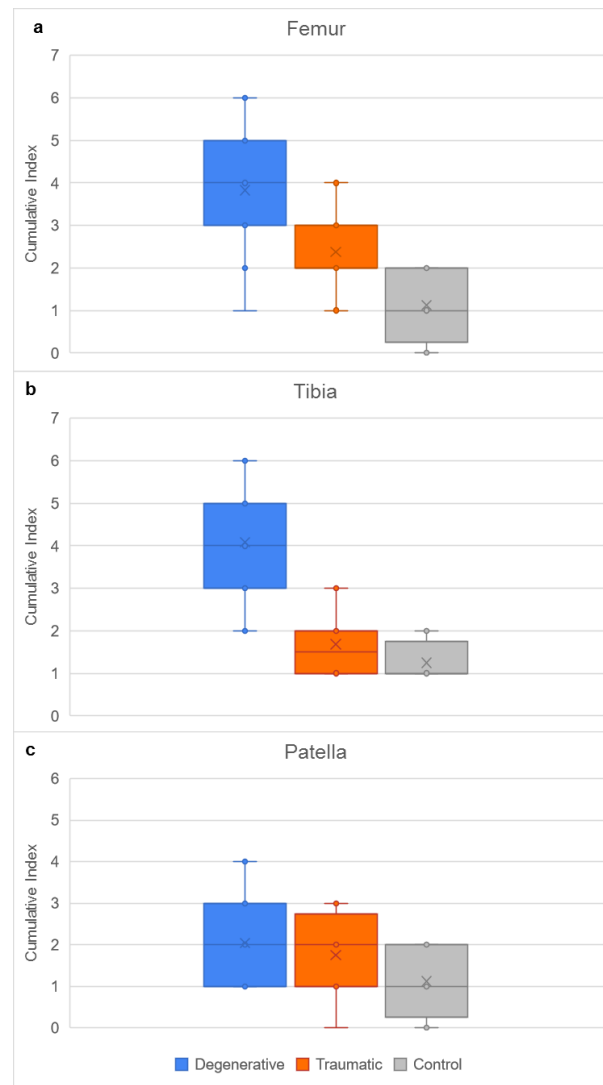
Figure 6.22: Distribution of cumulative index of pathologies in (a) femur, (b) tibia, and (c) patella for the three groups.

The cumulative index has then been investigated more precisely in the D group, to observe the results in the frame of sex and age. Figure 6.23 below compares the cumulative index in the three different compartments (MC, LC and FPC), for males and females. No significant differences have been observed between the two cohorts. The results according to age will be detailed in the following section.

Comparison of different metrics to assess cartilage degeneration

CI, Ahlbäck and ICRS grading vs age in the D group   Figure 6.24 shows age dependency in degenerative group (D) for the different grading system: Ahlbäck grading (AG), ICRS and CI. While the CI and AG were positively correlated in all cases, the ICRS grading was positively correlated with age for both femur and tibia in
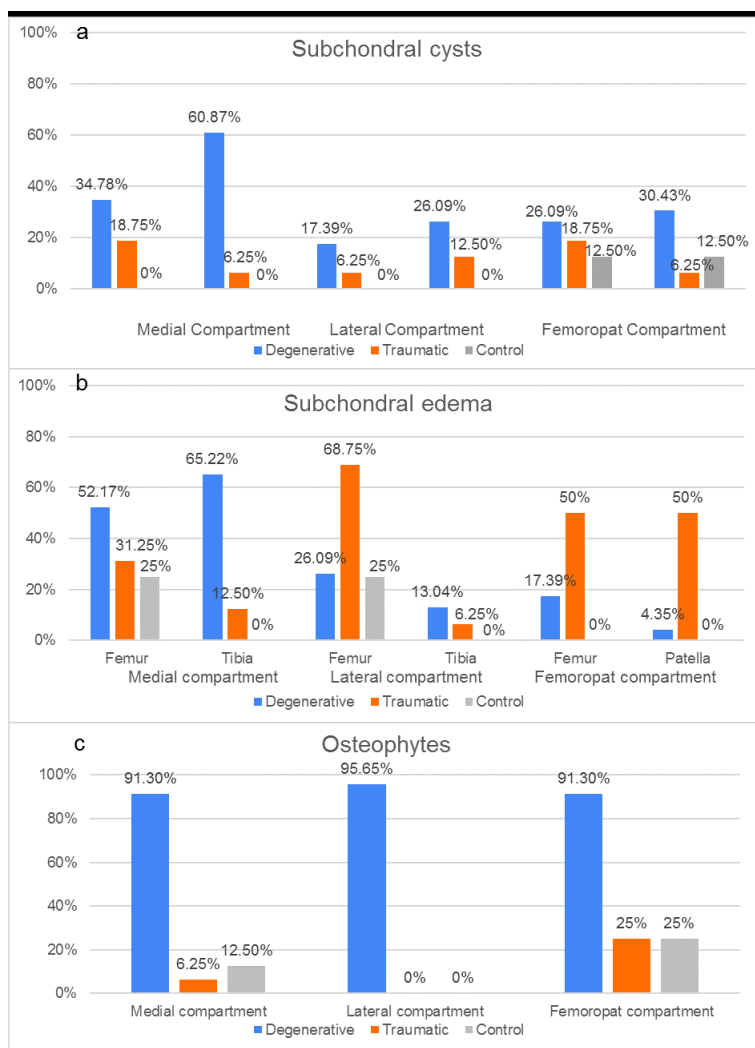
Figure 6.23: Comparison of cumulative index of pathologies between males (blue) and females (orange) in D group, for the three compartments.

the lateral compartment and for the patella in the FPC. In the rest of the cases, the ICRS was not correlated (a, e) or negatively correlated with age (b).

CI and cartilage thickness vs age   For the next comparison (Figure 6.25), the articular cartilage thickness of femur and tibia was considered as the average thickness of the three contact points (anterior, middle, posterior) measured in the medial as well as in the lateral compartment. Meanwhile, for the femoropatellar compartment the ACT was considered as the average of the two contact points (medial and lateral) in the femoral trochlea and of three contact points (medial, center and lateral) in the patella. The results show that the cumulative index was positively correlated with age, while the average thickness of the cartilage was negatively correlated with age in all cases.

Summary of statistics   Table 6.7 shows a summary of the statistical analysis made for the CI, ICRS grading and the ACT between the groups.

The cumulative index in Femur and Tibia shows a high significance to differentiate D group from the two other groups. Similarly, the ICRS shows significant differences

Hypothesis	Variable	Statistical Test	*p-value*
Difference between D&T	CI (Femur)	ANOVA-Bonferroni correction	**0.002**
	CI (Tibia)		**<0.001**
	CI (Patella)		0.99
Difference between D&C	CI (Femur)	ANOVA-Bonferroni correction	**<0.001**
	CI (Tibia)		**<0.001**
	CI (Patella)		0.06
Difference between T&C	CI (Femur)	ANOVA-Bonferroni correction	**0.033**
	CI (Tibia)		0.98
	CI (Patella)		0.36
Difference between D&T	ICRS MC (Femur)	ANOVA-Bonferroni correction	**0.001**
	ICRS MC (Tibia)		**0.001**
	ICRS LC (Femur)		1
	ICRS LC (Tibia)		0.85
	ICRS FPC (Femur)		**0.004**
	ICRS FPC (Patella)		0.3
Difference between D&C groups	ICRS MC (Femur)	ANOVA-Bonferroni correction	**0.001**
	ICRS MC (Tibia)		**0.001**
	ICRS LC (Femur)		0.77
	ICRS LC (Tibia)		**0.03**
	ICRS FPC (Femur)		**0.001**
	ICRS FPC (Patella)		**0.001**
Difference between T&C	ICRS MC (Femur)	ANOVA-Bonferroni correction	1
	ICRS MC (Tibia)		0.08
	ICRS LC (Femur)		1
	ICRS LC (Tibia)		0.26
	ICRS FPC (Femur)		1
	ICRS FPC (Patella)		**0.014**
Difference between D&T	ACT MC (Femur)	ANOVA-Bonferroni correction	***<0.001***
	ACT MC (Tibia)		**0.006**
	ACT LC (Femur)		0.51
	ACT LC (Tibia)		0.15
	ACT FPC (Femur)		**0.049**
	ACT FPC (Patella)		0.41
Difference between D&C	ACT MC (Femur)	ANOVA-Bonferroni correction	***<0.001***
	ACT MC (Tibia)		**0.005**
	ACT LC (Femur)		0.16
	ACT LC (Tibia)		0.12
	ACT FPC (Femur)		0.28
	ACT FPC (Patella)		1
Difference between T&C	ACT MC (Femur)	ANOVA-Bonferroni correction	1
	ACT MC (Tibia)		1
	ACT LC (Femur)		1
	ACT LC (Tibia)		1
	ACT FPC (Femur)		1
	ACT FPC (Patella)		0.68

Table 6.7: Summary of 2D measurements statistics. Hypothesis, variable, statistical test and p-value are displayed
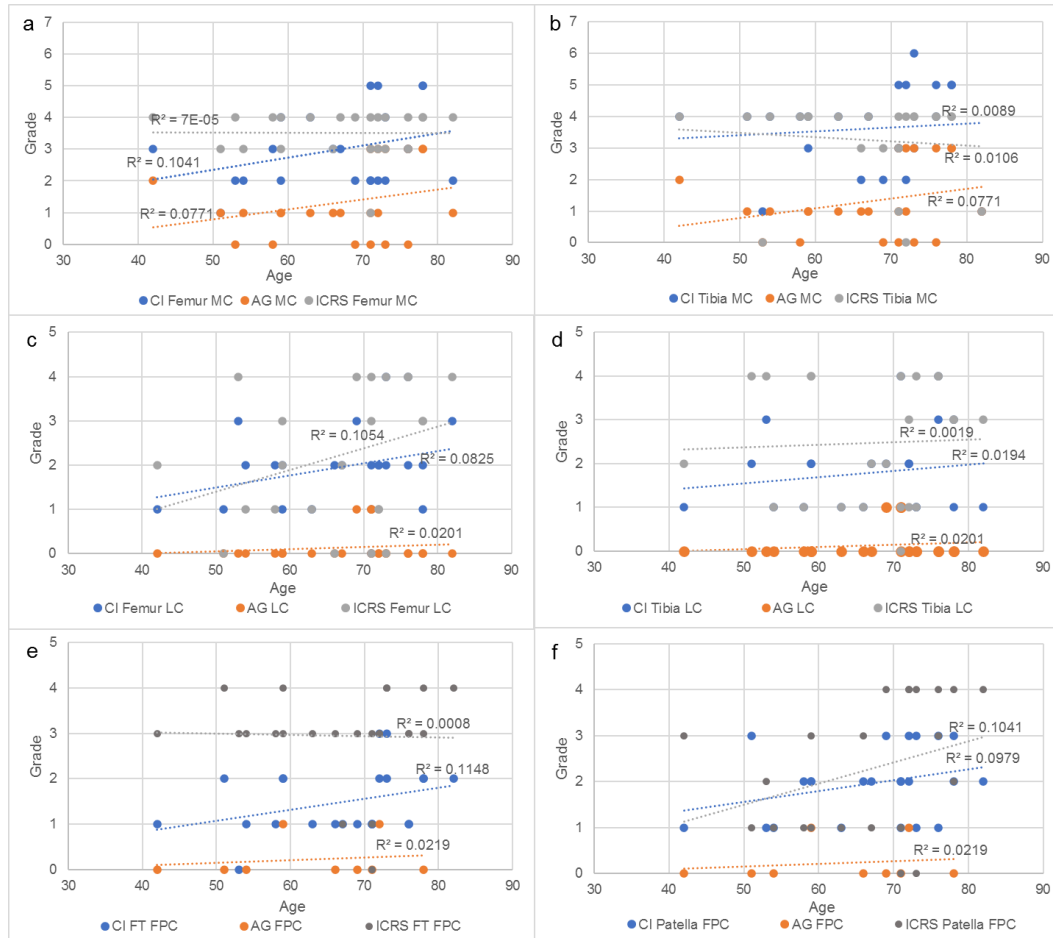
Figure 6.24: Trendlines and the r2 coefficient of the CI, AG and ICRS vs age in a) femur and b) tibia in the MC; c) femur and d) tibia in the LC; e) femoral trochlea and f) patella in the FPC.

between D and C groups for all the compartments of each bone, except for the femoral lateral compartment. Finally, the average cartilage thickness in the medial compartment for femur and tibia shows significant differences between D and the two other groups.

6.3.3.2   3D measurements

The results shown in table 6.8 display the average bone mineral density, as well as radiodensity, volume and surface from each cartilage after tissue segmentation. The results were calculated for each group (D, T and C).

T group has the highest density of all the bones. D group and C group have similar values for the femur density, while D group has higher density in tibia, and lower in patella. D group has the lowest density in the femoral cartilage, the highest in the patella, and a slightly lower but similar values than C group in both lateral and medial tibia cartilage. D group has the highest cartilage volume for every part. C group has a higher volume than T group for the patella and the lateral tibia. D group has the highest cartilage surface for every part. T group has a higher surface than the C group for the patella and the medial tibia. It can be noted that for the patella, D group has the lowest bone density, the lowest cartilage density, the highest volume, and the highest surface. In general this table does not show a significant trend among patient
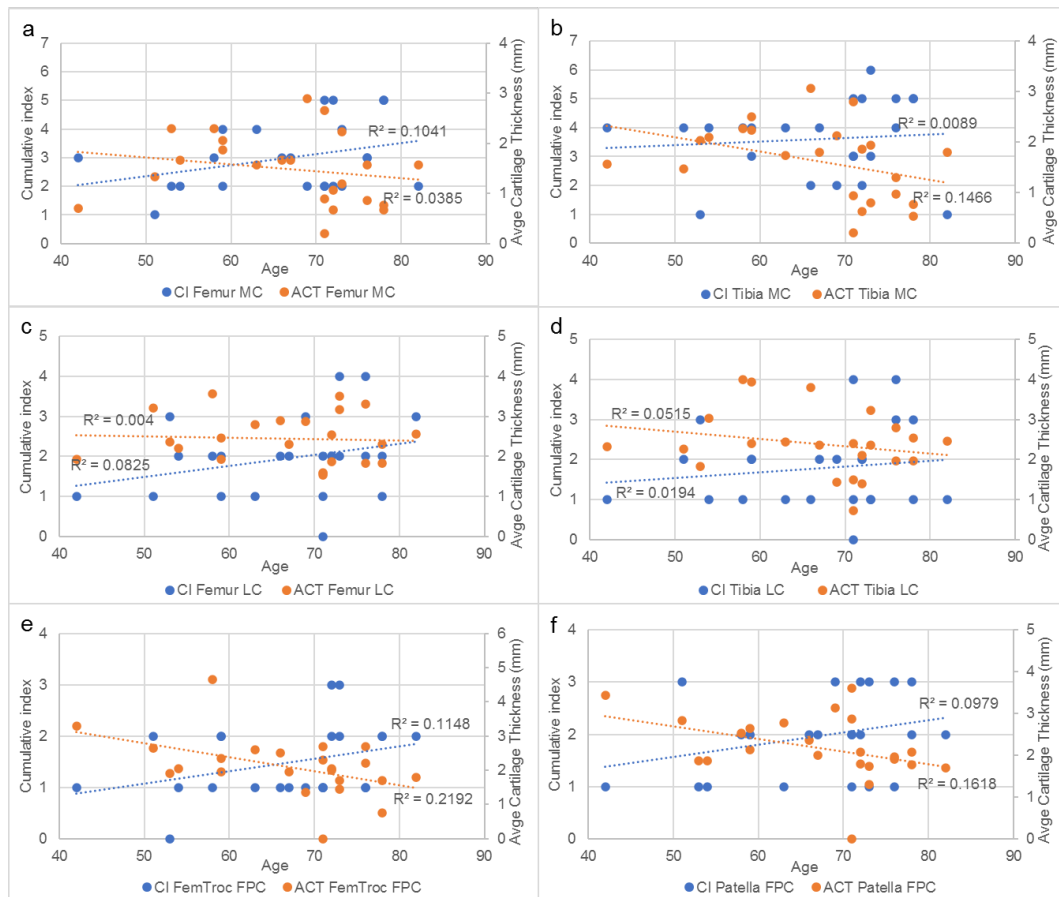
Figure 6.25: Trendlines and the r2 coefficient of CI and average cartilage thickness vs age in a) femur and b) tibia in the MC; c) femur and d) tibia in the LC and e) femoral trochlea and f) patella in the FPC.

	Degenerative	Traumatic	Control
Bone Mineral Density (g/cm3)			
Femur bone	1,32 (1,13)	1,33 (1,14)	1,32 (1,12)
Tibia bone	1,32 (1,13)	1,35 (1,15)	1,29 (1,16)
Patella bone	1,36 (1,12)	1,40 (1,14)	1,41 (1,11)
Radiodensity (HU)			
Femur cartilage	85,19 (57,47)	88,67 (49,90)	93,53 (54,37)
Lateral Tibia cartilage	87,84 (51,10)	88,69 (44,97)	91,19 (49,21)
Medial Tibia cartilage	98,49 (55,92)	93,63 (44,14)	103,79 (52,82)
Patella cartilage	78,36 (50,68)	81,56 (44,97)	99,09 (55,45)
Volume (mm3)			
Femur cartilage	17303 (5530)	12460 (2710)	11276 (4505)
Lateral Tibia cartilage	2851 (2336)	1100 (439)	1501 (1927)
Medial Tibia cartilage	1915 (1638)	907 (566)	552 (362)
Patella cartilage	2761 (830)	2589 (781)	2703 (705)
Surface (mm2)			
Femur cartilage	14381 (2636)	12610 (1496)	11809 (2791)
Lateral Tibia cartilage	2435 (1503)	1415 (499)	2073 (2530)
Medial Tibia cartilage	2016 (1367)	1301 (550)	967 (407)
Patella cartilage	2602 (760)	2574 (488)	2495 (390)

Table 6.8: 3D measurements results. The results show the average variable for each group (with standard deviation between parentheses)

groups due to high interpatient variability, however patient specific 3D measurements

Hypothesis	Variable	Statistical test	*p-value*
Difference between D&T	BMD (Femur)	ANOVA-Bonferroni correction	**0.014**
	BMD (Tibia)		**<0.001**
	BMD (Patella)		**<0.001**
Difference between D&C	BMD (Femur)	ANOVA-Bonferroni correction	0.82
	BMD (Tibia)		1
	BMD (Patella)		**0.002**
Difference between T&C	BMD (Femur)	ANOVA-Bonferroni correction	0.72
	BMD (Tibia)		0.078
	BMD (Patella)		1
Difference between D&T	CD (Femur)	ANOVA-Bonferroni correction	1
	CD (Tibia)		1
	CD (Patella)		1
Difference between D&C	CD (Femur)	ANOVA-Bonferroni correction	0.43
	CD (Tibia)		1
	CD (Patella)		0.1
Difference between T&C	CD (Femur)	ANOVA-Bonferroni correction	0.38
	CD (Tibia)		1
	CD (Patella)		0.11
Difference between D&T	CV (Femur)	ANOVA-Bonferroni correction	**<0.001**
	CV (Tibia)		0.13
	CV (Patella)		0.73
Difference between D&C	CV (Femur)	ANOVA-Bonferroni correction	**<0.001**
	CV (Tibia)		**0.027**
	CV (Patella)		1
Difference between T&C	CV (Femur)	ANOVA-Bonferroni correction	1
	CV (Tibia)		0.93
	CV (Patella)		1

Table 6.9: Summary of 3D measurements statistics. Hypothesis, variable, statistical test and p-value are displayed.

are used in the machine learning part to enlarge the set of features predicting the patient status.

CI and radiodensity vs age   Table 8 shows a summary of the statistical analysis made for the BMD, cartilage radiodensity and cartilage volume between the groups.

Summary of statistics   After comparison with other 2D metrics, the cumulative index was compared with the cartilage radiodensity (Figure 6.26A) and the cartilage volume (Figure 6.26B) and plotted against the age of those patients who belonged to the D group.

The results show a higher correlation of the cumulative index in very case compared to the cartilage radiodensity and the cartilage volume

6.3.3.3   Machine learning

Table 6.10 shows all the results of the ML analysis. The best accuracy results are 89.4, which is obtained with RF using the whole feature set and the 2D measurements feature set. F1 score is high for the Degenerative patients (always around 90%), while it is slightly lower for the other two groups. These F1 scores are due to the higher number of degenerative patients but also demonstrate that with the selected features, it is efficient to classify patients with degenerative cartilage using RF and GB. The best metrics for the classification of control subjects are obtained with the 2D feature set, while all 96 features give the best F1 score for classifying traumatic patients using RF. In terms of accuracy, good results are obtained with MRI, Bone and Cartilage feature selections, especially with the RF algorithm, while 3D selection is the worst, with a maximum of 76.6 accuracy with GB. With RF, the bone features give better results in
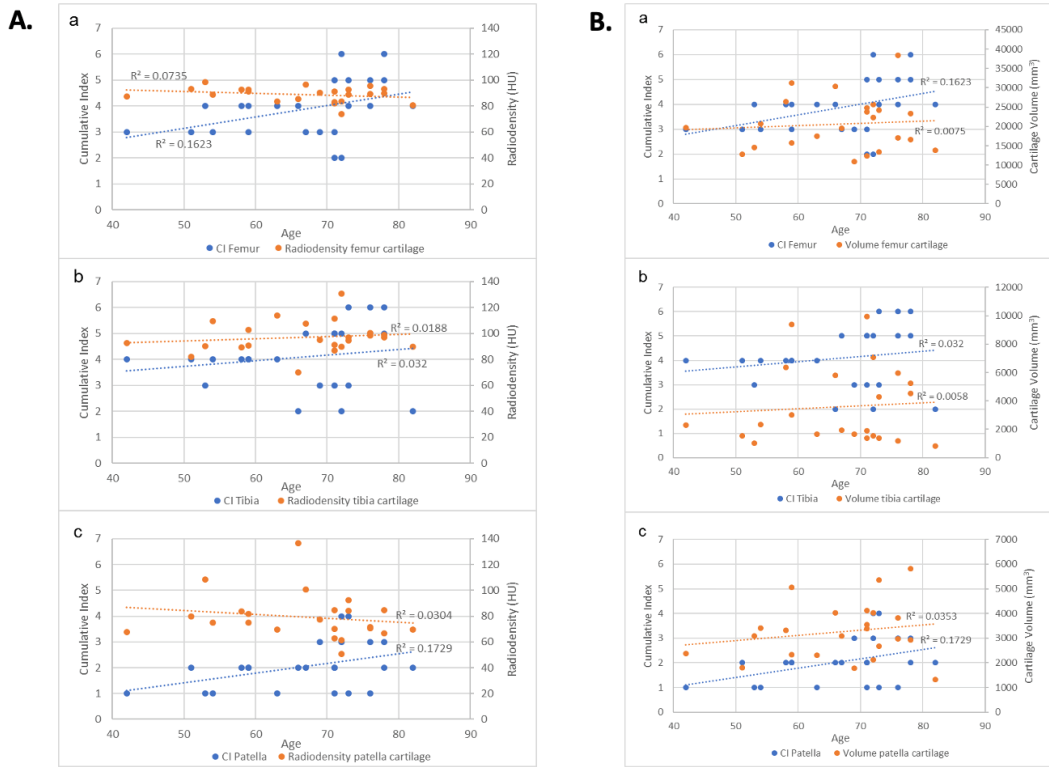
Figure 6.26: A) Trendlines and the r2 coefficient of the CI and the cartilage radiodensity of the a) femur; b) tibia and c) patella. B) Trendlines and the r2 coefficient of the CI and the cartilage volume of the a) femur; b) tibia and c) patella.

Features Selection	Alg.	Acc.	Re [D]	Pr [D]	F1 [D]	Re [T]	Pr [T]	F1 [T]	Re [C]	Pr [C]	F1 [C]
Tot Feat [96]	RF	89.4	95.9	92	93.9	93.3	82.4	87.5	62.5	100	76.9
	GB	87.2	91.7	95.7	93.6	93.3	73.7	82.4	62.5	100	76.9
2D Feat [78]	RF	89.4	91.7	91.7	91.7	86.7	86.7	86.7	87.5	87.5	87.5
	GB	87.2	91.7	91.7	91.7	80	80	80	87.5	87.5	87.5
3D Feat [18]	RF	74.5	83.3	83.3	83.3	66.7	66.7	66.7	62.5	62.5	62.5
	GB	76.6	87.5	84	85.7	66.7	76.9	58.8	62.5	55.6	58.8
CT-Scat Feat [26]	RF	80.9	91.7	95.7	93.6	66.7	71.4	69	75	60	66.7
	GB	74.5	87.5	84	85.7	60	75	66.7	62.5	50	55.6
MRI Feat [52]	RF	87.2	95.8	95.8	95.8	87.6	76.5	81.2	62.5	83.3	71.4
	GB	87.2	91.7	88	89.8	80	85.7	82.8	87.5	87.5	87.5
Bone Feat [50]	RF	85.1	91.7	91.7	91.7	86.7	76.5	81.2	62.5	83.3	71.4
	GB	76.6	87.5	95.5	91.3	73.3	64.7	68.8	50	50	50
Cartilage Feat [26]	RF	83	91.7	88	89.8	73.3	73.3	73.3	75	85.7	80
	GB	83	91.7	88	89.8	67.7	76.9	71.4	87.5	77.8	82.4

Table 6.10: classification metrics (Recall (Re) Precision (Pr) and F1 [%]) for the 2 different tree-based ML algorithms and the seven different features selections (Degenerative [D] - Traumatic [T] - Control [C]).

all three classes compared to the cartilage feature set. Using GB and cartilage feature set, only control subjects are classified with higher metrics. We can state that RF is the most efficient of the two tree-based algorithms.

Tables 6.11 and 6.12 show the 12 most important features and the percentage of importance of all the different feature groups for the RF classification ML model using the 96 total features as input. This model was selected for the feature importance analysis because it can be considered the most significant in terms of accuracy (89.4 is the highest). It allows for a complete overview of the full set of features and their respective importance in the classification process. The highest importance is attributed to two features from the 3D collection (the volume of the tibialis cartilage lateralis and

TibCartLatVOL [mm3]	4,804
TibCartMedVOL [mm3]	4,631
CT Lat Osteophytes	4,594
MRI Med Cart Thick FEM [mm] - Med	4,262
MRI Med Menisc Pathol	3,909
MRI Lat Osteophytes	3,805
FemCartVOL [mm3]	3,644
TibCartLatSTD	2,543
MRI Lat Cart Thick FEM [mm] - Ant	2,491
MRI Med Cart Thick FEM [mm] - Post	2,402
MRI Lat Cart Thick TIB [mm] - Med	2,352
CT Med Osteophytes	2,343

Table 6.11: 12 most important features [%] for the RF classification model with 96 Tot Features

2D	66,08%
MRI (part of 2D features)	51,69%
CT (part of 2D features)	14,39%
3D	33,12%
BONE (from CT and MRI)	28,29%
CARTILAGE (from MRI)	37,79%

Table 6.12: Importance of the groups of features [%] for the RF classification model with 96 Tot Features

medialis). The 3D features set contribute 33% of importance despite being only 18 compared to the 78 2D features. The cartilage set of features has higher importance compared to the bones. In contrast, the CT scan features contribute to only 14,39% of the importance having only two of them in the first 12 most important features (lateral and medium osteophytes).

6.3.4   Discussion

This work developed a methodology to evaluate cartilage degeneration. It uses a multimodal image approach to segment and 3D model bones and cartilages from the knee area. Indeed, the MRI provides information about pathologies, morphology of the cartilages, as well as a geometric representation of the tissue damage, while CT data presents a good overview of bone pathologies, especially in boundary regions. The combination of both imaging techniques gives a 3D representation of the knee, and additional information about bone and cartilage. This data overview makes the definition of 96 features possible, which demonstrated various levels of significance with regards to contribution towards the cartilage quality evaluation. From the 2D measurements, the first parameters shown in the results are those which better testify to degeneration on the D group such as the presence of cysts, osteophytes, and meniscal pathology in the MC when compared to the T and C groups. This agrees with other biomechanical evidence [351], which suggests that the medial tibiofemoral joint reaction forces are greater than the lateral ones during gait and therefore the degeneration of the cartilage and the surrounding tissue would be more evidently seen on the medial side.

Meanwhile, the T group demonstrated greater incidence of subchondral edema within the femoropatellar compartment when compared to the other two groups, becoming this an interesting and useful indicator for example in the development of protective elements to avoid injury. The cumulative index, which is based on the bone condition, indicates statistically that the degenerative patients present more pathologies in femur and tibia than the other patients. These results were expected, as the degeneration of the knee is known to affect the condition of both bones and cartilage, as confirmed by the ICRS values, which showed a significantly worse cartilage condition for the D group within the medial and femoropatellar compartments. Consequently, to assess the accuracy/utility of the cumulative index as an indicator of cartilage degeneration, the CI was subject to comparison with other 2D metrics only within the D group in the frame of age, since males and females did not show significant differences in any of the three compartments. Therefore, when compared to the AG and the ICRS for the different compartments the CI showed a regular trendline suggesting a higher index with ageing of the degenerative patients. In some cases, the r2 indicated a better fit for the CI than the other metrics as in the femur in the medial and FPC. Later, when compared with the average cartilage thickness, the cumulative index presented a regular trend as well as the thickness, where the older the patient, the thinner the cartilage and the higher the index. In summary, the cumulative index based only on the bone condition shows a way to differentiate the groups, and it is strengthened by the statistical power analysis.Then, when compared against other metrics, the general low R2 values of the index are an indication of the high interpatient variability, which (despite the small sample size) was expected based on our hypothesis of needing higher sensitivity in the assessment of cartilage degeneration towards improving patient-specific profile and subsequently, treatment.

The fact that degeneration is mainly located in the same areas explain why the D group is easier to discriminate. The T group shows less homogeneous results, where only subchondral edemas helped to differentiate them. Trauma affects a specific region that varies for each patient; therefore, it is harder to find any similar trends according to which bone or cartilage is studied. The BMD calculated for the femur, and tibia bones do not discriminate the cartilage condition, probably because we calculated the overall BMD over the entire scanned bone segment without focusing on the boundary Bone/Cartilage. Moreover, the results on the patella bone show higher BMD in healthy and traumatic individuals. The likeliest reason is that in this case, we have a complete and small bone volume, and a limited HU variability [289]. The density calculated on the entire cartilage volume is also not a significant discriminator between degenerative, traumatic, and healthy conditions. However, a trend of decreased density in degenerative cartilage can be seen after eroding the cartilage mask and filtering the HU distribution. After this process, the differences between healthy and pathological conditions were more evident. This is in line with a known behavior regarding tissue density and pathologies. It has been shown that people suffering from rheumatoid arthritis present lower muscle density associated with joint destruction[352]. Thus, people suffering from degenerative cartilage can present similarly a lower cartilage density associated to this damaged joint. For these reasons, we wanted to examine the cartilage density and cartilage volume alongside the bone CI, on the D group. The study of CI and cartilage density regarding age reveals that for each cartilage, the cartilage density remains similar through age, whereas the CI shows an increasing trend. The same behavior is observed regarding the volume, which does not change much with age compared to CI. The low R2 (R2<0.04) in both volumes and

radiodensity metrics, lead us to believe that even though those parameters should be considered for group classification, they do not provide sensitive enough information to thoroughly assess cartilage degeneration. One reason for that is the lack of objective automatic methods for segmentation [353], leading to a bias or a lack of accuracy for 3D segmentation, that influences the data results. Future studies with more advanced segmentation techniques should confirm this outcome. For now, the best indicator identified in our study to quantify cartilage degeneration is the bone cumulative index. ML results underline significant recall and precision, as well as F1, especially on the classification of degenerative patients, reaching a maximum recall value of 95.9 using the total and MRI feature selections, having almost 90% accuracy. The use of all the 96 features gives the best classification metrics and allows a complete feature importance analysis which gives new significant hints for studying the degeneration condition of the knee cartilage. Noteworthy are the results obtained with the single Bone and Cartilage feature selections. While a good accuracy value is expected for the latter as we are classifying subjects relative to their cartilage status, the classification metrics obtained with the Bone selection are of high impact. Cartilage status is highly dependent on the bone's condition, as has been demonstrated by Cai et al. [354], which observed changes in the subchondral bone with OA progression. Moreover, Bonakdari et al. [355] recently used bone features to predict cartilage volume loss obtaining a correlation coefficient of more than 0.78. Similarly, we demonstrated that bone has high importance in the classification process. Still, if combined with cartilage and 3D features, the metrics significantly increase, indicating that with the contribution of all these sets of features, a more in-depth view of the knee cartilage status can be given. If we consider 3D features or cartilage feature sets alone for the classification process, the metrics are not significant due also to the limited number. But, looking at the results, they assume a significant relevance if we consider the whole complete set (the two most relevant features, volume of the tibialis cartilage lateralis and medialis, are from the novel 3D group). 3D features contribute one-third of the importance despite the limited number. At the same time, they give the lowest accuracy of 74.5 if considered the only input to the tree-based algorithms. The 26 cartilage features alone can give a decent 83% accuracy but, if taken together with the other 70, contribute to the classification for almost 40% of total importance. We can conclude that the complete set of features gives the best input for future developments of this study: all the 96 bone, cartilage, and 3D features together could be used to develop new clinical solutions like the design of a patient-specific cartilage status profile which will help the clinicians and the researchers in an easier and objective classification of the cartilage status and an evaluation of the degeneration level. This novel methodology, combining 2D and 3D measurements, is of interest to assess cartilage quality. By designing indexes of pathology and combining it with other parameters such as radiodensity, it is possible to categorize cartilage into a group condition. This preliminary study should be pursued with a larger range of subjects to ensure its efficiency.

6.3.4.1   Limitations

The 2D assessment through CT and MRI is normally performed by one person and can be sometimes difficult to assess some pathology because of the image quality or the subjectivity of the researcher and this situation might affect the evaluation of the bone and cartilage. Likewise, the 3D segmentation process is quite long and mostly manual. Despite multiple adjustments and cross-verification, some inaccuracies can

remain, which can affect the 3D pipeline, therefore the density, volume, and surface values. An improvement of the segmentation workflow, using a semi-automatic or fully automatic method, would help to get more accurate values. The number of subjects in each group, especially in the C group, remains small. Therefore, the statistical results must be observed with caution, and the preliminary trend observed to differentiate the groups has to be confirmed with a larger sample of participants. The bone 3D measurements suffered from a high variability because we are studying the whole bone instead of regions of interest (boundaries around the cartilage). It has been done this way to avoid partial volume effect and image artefacts. However, it also results in a less precise way to evaluate bones. ML analysis also presents some limitations. The number of subjects is not particularly high,: this could affect the classification performances and a partial overfitting may occur in some models . Moreover, the multi-class approach can significantly decrease the classification metrics: for future work, a binary classification option can be performed to study the prediction potential of the features to distinguish degenerative patients from all the others. A higher number of control subjects could also potentially be the starting point for a binary classification between degenerative vs healthy or traumatic vs healthy subjects.

6.3.5 Conclusion

We developed a cartilage segmentation and 3D modelling procedure that can be used as benchmark for 3D bioprinting design and to advance cartilage assessment. Based on a cumulative index of bone properties (CI), we demonstrate the importance of bone condition and the sensitivity of these measurements on medial and femoropatellar compartments. Moreover, we show that a combination of 2D radiological measurements and 3D measurements revealed potential biomarkers of cartilage degeneration, especially from medial femur. This work is a first step toward a patient-specific cartilage profile based on the combination of CT and MRI datasets. This could be crucial for improving cartilage assessment. Indeed, when evaluating patients with knee pain either following trauma or with acute or chronic illness, the patient's symptoms are always the cornerstone in the treatment decision, whether medical or surgical. Following plain x-ray, a CT scan and most often also MR scan are the best tools in elucidating the interior of the knee joint. The CT scan is both easy to get and fast to execute but uses ionising radiation. It reveals, however, best all the bony structures and injuries. It may also give some clues about the bone marrow and surrounding soft tissues. The MR, however, is the best examination to evaluate the status of both the cartilage and the ligaments. The drawback is both the long time until it can be executed and long running time which can sometimes be impossible in patients with severe pain. When merged, these two examinations give the most superior evaluation ever for the knee joint and should always be chosen prior to invasive arthroscopy. Our study shows the feasibility of extending the cartilage assessment using existing and new parameters from both image modalities.

6.4 Discussion of the findings

This chapter reports two studies that developed a new image segmentation workflow in order to improve knee cartilage assessment, and more especially to find biomarkers of knee cartilage degeneration. Table 6.13 sums up the main findings of this section.

Findings	Paradigms	2D measurements	3D measurements
CT- and MRI-Based 3D Reconstruction	New image segmentation pipeline		**Differentiation of healthy and degenerative** cartilage based on patellofemoral joint
Assessment of knee cartilage degeneration	New workflow for cartilage assessment	**Development of a new index** based on **bone** radiological inspection	

Table 6.13: Main findings

Assessment of cartilage condition is critical to diagnose and follow the evolution of OA. The current assessment techniques are however quite limited, as it requires radiological inspection and lacks quantitative measurements. Most of the existing scales evaluate the severity of OA by measuring the joint space narrowing and observing cartilage and associated bones damage. Those methods are therefore subjective, and can suffer from interoperator variability. The identification of objective and robust metrics are necessary. The two studies detailed in this chapter propose new features, combining recognized image modalities (CT and MRI), to, on one hand, provide an exhaustive radiological inspection of bone and cartilage conditions based on 2D images, and on the other hand, to reconstruct a 3D model of the knee joint, throught an innovative workflow, to extract 3D based features. The low number of individuals does not enable to ensure the role of those features as biomarkers of cartilage degeneration, however it opens the door to further studies based on these workflow and features to deepen our understanding of cartilage assessment. Those preliminary results proposed a new index based on bone condition, presenting a better sensitivity to detect cartilage degeneration compared to other well known scales. Moreover, the different set of features based on 2D and 3D features enabled to differentiate healthy and degenerative cartilage. Those results are of interest, as they could be essential for the recognition of biomarkers of cartilage degeneration, leading to a more reliable and objective clinical evaluation.

Chapter 7

Conclusion

The emergence of more and more advanced technologies enables the discovery of new methodologies and applications. These tools rely on solid and well-studied foundation, but their novelty might be a pivot point for the clinical field. It will help for more robust and objective assessment, based on personalised evaluation and solution. This dissertation reports methodologies leaning towards this direction, studying two different parts of the body: the brain on one side, and the knee joint and on the other side. Despite their totally different mechanisms and research questions, the global problem and approach remains the same. These systems have been widely studied, but the current knowledge to assess their condition remains limited, or should at least be improved by the use of quantitative approaches, and limit the effects of subjective evaluation. In this dissertation, reported research studies regarding those two distinct body parts are then quite similar in the approach. After setting the study goal, adapted measurement setup and experimental paradigms are designed and applied. From this datasets, pre-processing and processing are performed, to then proceed to the data analysis and feature extraction.

Concerning the brain, the work is based on EEG times-series analysis, measuring brain electrical activity in the outer cortex. Two general research studies have been proposed, one analyzing the effect of rTMS as a treatment solution for patients with schizophrenia and AVH, and the other to provide a quantitative evaluation of postural control. For each research study, the global pipeline is analogous; the nuance is the use of the adequate and optimal paradigm, and the proposal of novel methodologies to offer new perspectives and strengthen the analysis.

In the case of schizophrenia, the approach was based on ERP, using the P300 paradigm, which has been widely used to study this condition. The novelty concerned first, the use of new metrics, extracted from functional connectivity, an emerging approach built on solid mathematical concepts; and second, the evaluation of a treatment that showed efficacy in other diseases, but is still under investigation for schizophrenia. Encouraging results were observed regarding the pertinence of using functional connectivity, providing a new and complementary insight regarding brain cortical remodeling, and can be used in the frame of longitudinal study to evaluate the progression of a condition or the impact of a therapeutical solution.

In the case of postural control, the different research studies were based on a novel and complex postural control paradigm, BioVRSea, challenging postural control with motor and/or visual stimulation. Several exploratories studies were performed, to validate the experimental protocol and justify the use of this device. It first relied on well-known EEG based analysis, computing Fourier-based spectral analysis over the

different frequency bands of the brain. It showed promising results for a future clinical outcome; differentiating people who suffered from concussion from people who did not, and setting a first neurophysiological reference of healthy response for this paradigm, setting the basis for future researches concerning balance-related disorders. However, the most innovative approach of this dissertation was also elicited in this research scope, combining two robust approaches based on EEG-times series to study dynamic remodeling: microstates segmentation and functional connectivity. The outcome of this work revealed a strong brain network state segmentation, describing adequately our experiment, and giving more and more insight regarding brain function and its fast behaviour during cognitive tasks. This global works shows the interest and impact of using novel methodological approaches to obtain new and more robust quantities. Functional connectivity is a methodology that, when possible, should be implemented frequently to study brain cortical activity. It will be of great help for clinical application.

Concerning knee joint, the work was performed in the frame of EU project RESTORE, with the general objective of developing personalised solution for cartilage degeneration. This thesis detail two research studies proposing a new methodology to observe and assess cartilage condition, and more precisely to evaluate degeneration. The data imaging modalities were based on two renowned techniques, CT and MRI, to provide a unique dataset that present an exhaustive number of radiological features, and can be combined into an accurate 3D model. From those 2D and 3D measurements, features were extracted an analysed to identify the most suitable for cartilage degeneration. This work identified a first trend of important features, highlighting the role of bone characteristics to assess cartilage condition, and the interest of using a more complete imaging workflow, to gain more objective information that could be used for future clinical evaluation.

This dissertation illustrates the necessity and interest to look for, design and propose innovative paradigms in the frame of biomedical research studies. On one hand, it confirms or provides additional knowledge regarding our body systems, their mechanisms, their function. On the other hand, it identifies markers and quantities to assess more objectively this behaviour, with a final aim to improve and facilitate clinical application. Future works should pursue the path designed in this thesis to finalise the identification of biomarkers.

Bibliography

[1] L. Thau, V. Reddy, and P. Singh, "Anatomy, central nervous system", en, in *StatPearls*, Treasure Island (FL): StatPearls Publishing, Jan. 2022.

[2] A. Parent and M. B. Carpenter, *Carpenter's human neuroanatomy*. Williams & Wilkins, 1996.

[3] H. Gray, "Antomy of the human body", *Annals of surgery*, vol. 68, no. 5, pp. 564–566, 1918.

[4] R. S. Desikan, F. Segonne, B. Fischl, *et al.*, "An automated labeling system for subdividing the human cerebral cortex on MRI scans into gyral based regions of interest", en, *NeuroImage*, vol. 31, no. 3, pp. 968–980, Jul. 2006, Number: 3, ISSN: 10538119. DOI: `10.1016/j.neuroimage.2006.01.021`. [Online]. Available: `https://linkinghub.elsevier.com/retrieve/pii/S1053811906000437` (visited on 07/22/2022).

[5] C. Chayer and M. Freedman, "Frontal lobe functions", *Current Neurology and Neuroscience Reports*, vol. 1, no. 6, pp. 547–552, Nov. 2001, ISSN: 1534-6293. DOI: `10.1007/s11910-001-0060-4`. [Online]. Available: `https://doi.org/10.1007/s11910-001-0060-4`.

[6] D. T. Stuss and R. T. Knight, *Principles of frontal lobe function*. Oxford University Press, 2013.

[7] W. Penfield and T. Rasmussen, "The cerebral cortex of man; a clinical study of localization of function.", 1950.

[8] D. Baldauf, H. Cui, and R. A. Andersen, "The posterior parietal cortex encodes in parallel both goals for double-reach sequences", *Journal of Neuroscience*, vol. 28, no. 40, pp. 10 081–10 089, 2008.

[9] L. Fogassi and G. Luppino, "Motor functions of the parietal lobe", *Current opinion in neurobiology*, vol. 15, no. 6, pp. 626–631, 2005.

[10] K. Grill-Spector, T. Kushnir, T. Hendler, S. Edelman, Y. Itzchak, and R. Malach, "A sequence of object-processing stages revealed by fmri in the human occipital lobe", *Human Brain Mapping*, vol. 6, no. 4, pp. 316–328, 1998. DOI: `https://doi.org/10.1002/(SICI)1097-0193(1998)6:4<316::AID-HBM9>3.0.CO;2-6`.

[11] A. Rehman and Y. Al Khalili, *Neuroanatomy, Occipital Lobe*. StatPearls Publishing, Treasure Island (FL), 2022. [Online]. Available: `http://europepmc.org/books/NBK544320`.

[12] H. Eichenbaum, A. Yonelinas, and C. Ranganath, "The medial temporal lobe and recognition memory", *Annual review of neuroscience*, vol. 30, p. 123, 2007.

[13] M. Tervaniemi and K. Hugdahl, "Lateralization of auditory-cortex functions", *Brain research reviews*, vol. 43, no. 3, pp. 231–246, 2003.

[14] G. Spitsyna, J. E. Warren, S. K. Scott, F. E. Turkheimer, and R. J. Wise, "Converging language streams in the human temporal lobe", *Journal of Neuroscience*, vol. 26, no. 28, pp. 7328–7336, 2006.

[15] R. L. Buckner, "The cerebellum and cognitive function: 25 years of insight from anatomy and neuroimaging", *Neuron*, vol. 80, no. 3, pp. 807–815, 2013.

[16] G. Paxinos and X.-F. Huang, *Atlas of the human brainstem*. Elsevier, 2013.

[17] J. Parvizi and A. Damasio, "Consciousness and the brainstem", *Cognition*, vol. 79, no. 1-2, pp. 135–160, 2001.

[18] F. A. Azevedo, L. R. Carvalho, L. T. Grinberg, *et al.*, "Equal numbers of neuronal and nonneuronal cells make the human brain an isometrically scaled-up primate brain", *Journal of Comparative Neurology*, vol. 513, no. 5, pp. 532–541, 2009.

[19] K. R. Jessen and R. Mirsky, "Glial cells in the enteric nervous system contain glial fibrillary acidic protein", *Nature*, vol. 286, no. 5774, pp. 736–737, 1980.

[20] T. Kirschstein and R. Köhling, "What is the source of the eeg?", *Clinical EEG and neuroscience*, vol. 40, no. 3, pp. 146–149, 2009.

[21] E. M. Hillman, "Coupling mechanism and significance of the bold signal: A status report", *Annual review of neuroscience*, vol. 37, p. 161, 2014.

[22] N. K. Logothetis, "What we can do and what we cannot do with fmri", *Nature*, vol. 453, no. 7197, pp. 869–878, Jun. 2008, ISSN: 1476-4687. DOI: `10.1038/nature06976`. [Online]. Available: `https://doi.org/10.1038/nature06976`.

[23] M. P. van den Heuvel and H. E. Hulshoff Pol, "Exploring the brain network: A review on resting-state fmri functional connectivity", *European Neuropsychopharmacology*, vol. 20, no. 8, pp. 519–534, 2010, ISSN: 0924-977X. DOI: `https://doi.org/10.1016/j.euroneuro.2010.03.008`. [Online]. Available: `https://www.sciencedirect.com/science/article/pii/S0924977X10000684`.

[24] W. R. Shirer, S. Ryali, E. Rykhlevskaia, V. Menon, and M. D. Greicius, "Decoding Subject-Driven Cognitive States with Whole-Brain Connectivity Patterns", en, *Cerebral Cortex*, vol. 22, no. 1, pp. 158–165, Jan. 2012, Number: 1, ISSN: 1460-2199, 1047-3211. DOI: `10.1093/cercor/bhr099`. [Online]. Available: `https://academic.oup.com/cercor/article-lookup/doi/10.1093/cercor/bhr099` (visited on 07/20/2022).

[25] D. J. Heeger and D. Ress, "What does fmri tell us about neuronal activity?", *Nature Reviews Neuroscience*, vol. 3, no. 2, pp. 142–151, Feb. 2002, ISSN: 1471-0048. DOI: `10.1038/nrn730`. [Online]. Available: `https://doi.org/10.1038/nrn730`.

[26] J. D. Power, B. L. Schlaggar, and S. E. Petersen, "Recent progress and outstanding issues in motion correction in resting state fmri", *NeuroImage*, vol. 105, pp. 536–551, 2015, ISSN: 1053-8119. DOI: `https://doi.org/10.1016/j.neuroimage.2014.10.044`. [Online]. Available: `https://www.sciencedirect.com/science/article/pii/S1053811914008702`.

[27] J. D. Power, M. Plitt, T. O. Laumann, and A. Martin, "Sources and implications of whole-brain fmri signals in humans", *NeuroImage*, vol. 146, pp. 609–625, 2017, ISSN: 1053-8119. DOI: `https://doi.org/10.1016/j.neuroimage.2016.09.038`. [Online]. Available: `https://www.sciencedirect.com/science/article/pii/S1053811916305158`.

[28] D. Cohen, "Magnetoencephalography: Detection of the brain's electrical activity with a superconducting magnetometer", *Science*, vol. 175, no. 4022, pp. 664–666, 1972.

[29] J. Gross, S. Baillet, G. R. Barnes, *et al.*, "Good practice for conducting and reporting meg research", *NeuroImage*, vol. 65, pp. 349–363, 2013, ISSN: 1053-8119. DOI: `https://doi.org/10.1016/j.neuroimage.2012.10.001`. [Online]. Available: `https://www.sciencedirect.com/science/article/pii/S1053811912009895`.

[30] F. De Pasquale, S. Della Penna, A. Z. Snyder, *et al.*, "Temporal dynamics of spontaneous meg activity in brain networks", *Proceedings of the National Academy of Sciences*, vol. 107, no. 13, pp. 6040–6045, 2010.

[31] J. Liu, A. Harris, and N. Kanwisher, "Stages of processing in face perception: An meg study", in *Social Neuroscience*, Psychology Press, 2013, pp. 75–85.

[32] H. Berger, "Über das elektroenkephalogramm des menschen", *Archiv für psychiatrie und nervenkrankheiten*, vol. 87, no. 1, pp. 527–570, 1929.

[33] M. X. Cohen, "It's about Time", *Frontiers in Human Neuroscience*, vol. 5, 2011, ISSN: 1662-5161. DOI: `10.3389/fnhum.2011.00002`. [Online]. Available: `http://journal.frontiersin.org/article/10.3389/fnhum.2011.00002/abstract` (visited on 10/05/2022).

[34] M. X. Cohen, *Analyzing neural time series data: theory and practice*. MIT press, 2014.

[35] M. Teplan *et al.*, "Fundamentals of eeg measurement", *Measurement science review*, vol. 2, no. 2, pp. 1–11, 2002.

[36] X.-J. Wang, "Neurophysiological and computational principles of cortical rhythms in cognition", *Physiological Reviews*, vol. 90, no. 3, pp. 1195–1268, 2010, PMID: 20664082. DOI: `10.1152/physrev.00035.2008`. eprint: `https://doi.org/10.1152/physrev.00035.2008`. [Online]. Available: `https://doi.org/10.1152/physrev.00035.2008`.

[37] G. Buzsaki and A. Draguhn, "Neuronal oscillations in cortical networks", *Science*, vol. 304, no. 5679, pp. 1926–1929, 2004. DOI: `10.1126/science.1099745`. eprint: `https://www.science.org/doi/pdf/10.1126/science.1099745`. [Online]. Available: `https://www.science.org/doi/abs/10.1126/science.1099745`.

[38] J. Cannon, M. M. McCarthy, S. Lee, *et al.*, "Neurosystems: Brain rhythms and cognitive processing", *European Journal of Neuroscience*, vol. 39, no. 5, pp. 705–719, 2014.

[39] S. R. Jones, "When brain rhythms aren't 'rhythmic': Implication for their mechanisms and meaning", *Current Opinion in Neurobiology*, vol. 40, pp. 72–80, 2016.

[40] C. S. Herrmann, D. Strüber, R. F. Helfrich, and A. K. Engel, "Eeg oscillations: From correlation to causality", *International Journal of Psychophysiology*, vol. 103, pp. 12–21, 2016.

[41] T. Harmony, T. Fernandez, J. Silva, *et al.*, "Eeg delta activity: An indicator of attention to internal processing during performance of mental tasks", *International journal of psychophysiology*, vol. 24, no. 1-2, pp. 161–171, 1996.

[42] G. G. Knyazev, "Eeg delta oscillations as a correlate of basic homeostatic and motivational processes", *Neuroscience & Biobehavioral Reviews*, vol. 36, no. 1, pp. 677–695, 2012.

[43] W. Klimesch, "Eeg alpha and theta oscillations reflect cognitive and memory performance: A review and analysis", *Brain Research Reviews*, vol. 29, no. 2, pp. 169–195, 1999, ISSN: 0165-0173. DOI: `https://doi.org/10.1016/S0165-0173(98)00056-3`. [Online]. Available: `https://www.sciencedirect.com/science/article/pii/S0165017398000563`.

[44] P. Sauseng, B. Griesmayr, R. Freunberger, and W. h, "Control mechanisms in working memory: A possible function of eeg theta oscillations", *Neuroscience & Biobehavioral Reviews*, vol. 34, no. 7, pp. 1015–1022, 2010.

[45] E. Niedermeyer, "Alpha rhythms as physiological and abnormal phenomena", *International journal of psychophysiology*, vol. 26, no. 1-3, pp. 31–49, 1997.

[46] G. Pfurtscheller, "Central beta rhythm during sensorimotor activities in man", *Electroencephalography and clinical neurophysiology*, vol. 51, no. 3, pp. 253–264, 1981.

[47] X. Jia and A. Kohn, "Gamma rhythms in the brain", *PLoS biology*, vol. 9, no. 4, e1001045, 2011.

[48] S. Fitzgibbon, K. Pope, L. Mackenzie, C. Clark, and J. Willoughby, "Cognitive tasks augment gamma eeg power", *Clinical Neurophysiology*, vol. 115, no. 8, pp. 1802–1809, 2004, ISSN: 1388-2457. DOI: `https://doi.org/10.1016/j.clinph.2004.03.009`. [Online]. Available: `https://www.sciencedirect.com/science/article/pii/S1388245704000938`.

[49] S. Sutton, M. Braren, J. Zubin, and E. R. John, "Evoked-potential correlates of stimulus uncertainty", *Science*, vol. 150, no. 3700, pp. 1187–1188, 1965, ISSN: 0036-8075. DOI: `10.1126/science.150.3700.1187`. eprint: `https://science.sciencemag.org/content/150/3700/1187.full.pdf`. [Online]. Available: `https://science.sciencemag.org/content/150/3700/1187`.

[50] A. Dietrich and R. Kanso, "A review of eeg, erp, and neuroimaging studies of creativity and insight.", *Psychological bulletin*, vol. 136, no. 5, p. 822, 2010.

[51] R. Oostenveld and P. Praamstra, "The five percent electrode system for high-resolution eeg and erp measurements", *Clinical neurophysiology*, vol. 112, no. 4, pp. 713–719, 2001.

[52] J. V. Odom, M. Bach, C. Barber, *et al.*, "Visual evoked potentials standard (2004)", *Documenta ophthalmologica*, vol. 108, no. 2, pp. 115–123, 2004.

[53] P. Walsh, N. Kane, and S. Butler, "The clinical role of evoked potentials", *Journal of neurology, neurosurgery & psychiatry*, vol. 76, no. suppl 2, pp. ii16–ii22, 2005.

[54] G. Hajcak, J. Klawohn, A. Meyer, *et al.*, "The utility of event-related potentials in clinical psychology", *Annual Review of Clinical Psychology*, vol. 15, no. 1, pp. 71–95, 2019.

[55] A. Pfefferbaum, J. M. Ford, B. G. Wenegrat, W. T. Roth, and B. S. Kopell, "Clinical application of the p3 component of event-related potentials. i. normal aging", *Electroencephalography and Clinical Neurophysiology/Evoked Potentials Section*, vol. 59, no. 2, pp. 85–103, 1984.

[56] R. W. McCarley, S. F. Faux, M. E. Shenton, P. G. Nestor, and J. Adams, "Event-related potentials in schizophrenia: Their biological and clinical correlates and new model of schizophrenic pathophysiology", *Schizophrenia research*, vol. 4, no. 2, pp. 209–231, 1991.

[57] D. Lehmann, "Multichannel topography of human alpha EEG fields", en, *Electroencephalography and Clinical Neurophysiology*, vol. 31, no. 5, pp. 439–449, Nov. 1971, Number: 5, ISSN: 00134694. DOI: `10.1016/0013-4694(71)90165-9`. [Online]. Available: `https://linkinghub.elsevier.com/retrieve/pii/0013469471901659` (visited on 07/20/2022).

[58] D. Van de Ville, J. Britz, and C. M. Michel, "Eeg microstate sequences in healthy humans at rest reveal scale-free dynamics", *Proceedings of the National Academy of Sciences*, vol. 107, no. 42, pp. 18179–18184, 2010.

[59] T. Koenig, L. Prichep, D. Lehmann, *et al.*, "Millisecond by millisecond, year by year: Normative eeg microstates and developmental stages", *Neuroimage*, vol. 16, no. 1, pp. 41–48, 2002.

[60] S. J. Luck, "Ten simple rules for designing and interpreting erp experiments", *Event-related potentials: A methods handbook*, vol. 4, 2005.

[61] M. M. Murray, D. Brunet, and C. M. Michel, "Topographic ERP Analyses: A Step-by-Step Tutorial Review", en, *Brain Topography*, vol. 20, no. 4, pp. 249–264, Jun. 2008, ISSN: 0896-0267, 1573-6792. DOI: `10.1007/s10548-008-0054-5`. [Online]. Available: `http://link.springer.com/10.1007/s10548-008-0054-5` (visited on 07/22/2022).

[62] F. F. Gonen and G. V. Tcheslavski, "Techniques to assess stationarity and gaussianity of eeg: An overview", *International Journal Bioautomation*, vol. 16, no. 2, p. 135, 2012.

[63] H. J. Nussbaumer, "The fast fourier transform", in *Fast Fourier Transform and Convolution Algorithms*, Springer, 1981, pp. 80–111.

[64] P. Welch, "The use of fast fourier transform for the estimation of power spectra: A method based on time averaging over short, modified periodograms", *IEEE Transactions on Audio and Electroacoustics*, vol. 15, no. 2, pp. 70–73, 1967. DOI: `10.1109/TAU.1967.1161901`.

[65] G. M. Saletu-Zyhlarz, O. Arnold, P. Anderer, *et al.*, "Differences in brain function between relapsing and abstaining alcohol-dependent patients, evaluated by eeg mapping", *Alcohol and Alcoholism*, vol. 39, no. 3, pp. 233–240, 2004.

[66] R. Aubonnet, A. Shoykhet, D. Jacob, G. Di Lorenzo, H. Petersen, and P. Gargiulo, "Postural control paradigm (biovrsea): Towards a neurophysiological signature", *Physiological Measurement*, 2022.

[67] O. Sporns, "Structure and function of complex brain networks", *Dialogues in clinical neuroscience*, 2022.

[68] M. Hassan and F. Wendling, "Electroencephalography source connectivity: Aiming for high resolution of brain networks in time and space", *IEEE Signal Processing Magazine*, vol. 35, no. 3, pp. 81–96, 2018.

[69] R. Grech, T. Cassar, J. Muscat, *et al.*, "Review on solving the inverse problem in eeg source analysis", *Journal of neuroengineering and rehabilitation*, vol. 5, no. 1, pp. 1–33, 2008.

[70] H. Hallez, B. Vanrumste, R. Grech, *et al.*, "Review on solving the forward problem in eeg source analysis", *Journal of neuroengineering and rehabilitation*, vol. 4, no. 1, pp. 1–29, 2007.

[71] L. Douw, D. Nieboer, C. J. Stam, P. Tewarie, and A. Hillebrand, "Consistency of magnetoencephalographic functional connectivity and network reconstruction using a template versus native m ri for co-registration", *Human brain mapping*, vol. 39, no. 1, pp. 104–119, 2018.

[72] S. Iwaki and S. Ueno, "Weighted minimum-norm source estimation of magnetoencephalography utilizing the temporal information of the measured data", *Journal of Applied physics*, vol. 83, no. 11, pp. 6441–6443, 1998.

[73] S. Aydore, D. Pantazis, and R. M. Leahy, "A note on the phase locking value and its properties", *Neuroimage*, vol. 74, pp. 231–244, 2013.

[74] M. Hassan, I. Merlet, A. Mheich, *et al.*, "Identification of interictal epileptic networks from dense-eeg", *Brain Topography*, vol. 30, no. 1, pp. 60–76, 2017. DOI: `10.1007/s10548-016-0517-z`. [Online]. Available: `https://doi.org/10.1007/s10548-016-0517-z`.

[75] A. Fornito, A. Zalesky, and E. Bullmore, *Fundamentals of brain network analysis*. Academic Press, 2016.

[76] S. Saha, D. Chant, J. Welham, and J. McGrath, "A systematic review of the prevalence of schizophrenia", *PLoS medicine*, vol. 2, no. 5, e141, 2005.

[77] N. C. Andreasen, "The lifetime trajectory of schizophrenia and the concept of neurodevelopment", *Dialogues in clinical neuroscience*, 2022.

[78] R. A. McCutcheon, T. R. Marques, and O. D. Howes, "Schizophrenia—an overview", *JAMA psychiatry*, vol. 77, no. 2, pp. 201–210, 2020.

[79] R. Valle, "Schizophrenia in icd-11: Comparison of icd-10 and dsm-5", *Revista de Psiquiatría y Salud Mental (English Edition)*, vol. 13, no. 2, pp. 95–104, 2020.

[80] D. P. Eisenberg and K. F. Berman, "Executive function, neural circuitry, and genetic mechanisms in schizophrenia", *Neuropsychopharmacology*, vol. 35, no. 1, pp. 258–277, 2010.

[81] N. Sartorius, A. Jablensky, A. Korten, *et al.*, "Early manifestations and first-contact incidence of schizophrenia in different cultures: A preliminary report on the initial evaluation phase of the who collaborative study on determinants of outcome of severe mental disorders", *Psychological Medicine*, vol. 16, no. 4, pp. 909–928, 1986. DOI: `10.1017/S0033291700011910`.

[82] A. T. Barker, R. Jalinous, and I. L. Freeston, "Non-invasive magnetic stimulation of human motor cortex", *The Lancet*, vol. 325, no. 8437, pp. 1106–1107, 1985.

[83] M. S. George, J. J. Taylor, and E. B. Short, "The expanding evidence base for rtms treatment of depression", *Current opinion in psychiatry*, vol. 26, no. 1, p. 13, 2013.

[84] Y.-h. Chou, V. T. That, and M. Sundman, "A systematic review and meta-analysis of rtms effects on cognitive enhancement in mild cognitive impairment and alzheimer's disease", *Neurobiology of aging*, vol. 86, pp. 1–10, 2020.

[85] C. W. Slotema, J. D. Blom, R. [Lutterveld], H. W. Hoek, and I. E. Sommer, "Review of the efficacy of transcranial magnetic stimulation for auditory verbal hallucinations", *Biological Psychiatry*, vol. 76, no. 2, pp. 101–110, 2014, Schizophrenia and Bipolar Disorder: New Insights into Novel Mechanisms, ISSN: 0006-3223. DOI: `https://doi.org/10.1016/j.biopsych.2013.09.038`. [Online]. Available: `http://www.sciencedirect.com/science/article/pii/S0006322313009499`.

[86] N. N. Boutros, C. Arfken, S. Galderisi, J. Warrick, G. Pratt, and W. Iacono, "The status of spectral eeg abnormality as a diagnostic test for schizophrenia", *Schizophrenia research*, vol. 99, no. 1-3, pp. 225–237, 2008.

[87] Y. Li, S. Tong, D. Liu, *et al.*, "Abnormal eeg complexity in patients with schizophrenia and depression", *Clinical Neurophysiology*, vol. 119, no. 6, pp. 1232–1241, 2008.

[88] S. Sur and V. Sinha, "Event-related potential: An overview", *Industrial Psychiatry Journal*, vol. 18, no. 1, pp. 70–73, 2009. DOI: `10.4103/0972-6748.57865`. [Online]. Available: `http://www.industrialpsychiatry.org/article.asp?issn=0972-6748;year=2009;volume=18;issue=1;spage=70;epage=73;aulast=Sur;t=6`.

[89] E. Olejarczyk and W. Jernajczyk, "Graph-based analysis of brain connectivity in schizophrenia", *PloS one*, vol. 12, no. 11, e0188629, 2017.

[90] S. Kähkönen, S. Komssi, J. Wilenius, and R. J. Ilmoniemi, "Prefrontal tms produces smaller eeg responses than motor-cortex tms: Implications for rtms treatment in depression", *Psychopharmacology*, vol. 181, no. 1, pp. 16–20, 2005.

[91] R. Aubonnet, O. C. Banea, R. Sirica, *et al.*, "P300 analysis using high-density eeg to decipher neural response to rtms in patients with schizophrenia and auditory verbal hallucinations", *Frontiers in Neuroscience*, vol. 14, 2020, ISSN: 1662-453X. DOI: `10.3389/fnins.2020.575538`. [Online]. Available: `https://www.frontiersin.org/articles/10.3389/fnins.2020.575538`.

[92] B. curcic-Blake, J. M. Ford, D. Hubl, *et al.*, "Interaction of language, auditory and memory brain networks in auditory verbal hallucinations", *Progress in Neurobiology*, vol. 148, pp. 1–20, 2017, ISSN: 0301-0082. DOI: `https://doi.org/10.1016/j.pneurobio.2016.11.002`. [Online]. Available: `http://www.sciencedirect.com/science/article/pii/S0301008216300880`.

[93] K. Kasai, M. E. Shenton, D. F. Salisbury, *et al.*, "Progressive decrease of left superior temporal gyrus gray matter volume in patients with first-episode schizophrenia", *American Journal of Psychiatry*, vol. 160, no. 1, pp. 156–164, 2003, PMID: 12505815. DOI: `10.1176/appi.ajp.160.1.156`. [Online]. Available: `https://doi.org/10.1176/appi.ajp.160.1.156`.

[94] P. Homan, *On the Neurobiology of Hallucinations*. 2013. [Online]. Available: `https://books.google.is/books?id=Bt2YoAEACAAJ`.

[95] C. D. Frith and D. J. Done, "Towards a neuropsychology of schizophrenia", *British Journal of Psychiatry*, vol. 153, no. 4, pp. 437–443, 1988. DOI: `10.1192/bjp.153.4.437`.

[96] T. Dierks, D. E. Linden, M. Jandl, *et al.*, "Activation of heschl's gyrus during auditory hallucinations", *Neuron*, vol. 22, no. 3, pp. 615–621, 1999, ISSN: 0896-6273. DOI: `https://doi.org/10.1016/S0896-6273(00)80715-1`. [Online]. Available: `http://www.sciencedirect.com/science/article/pii/S0896627300807151`.

[97] O. Howes, A. Egerton, V. Allan, P. McGuire, P. Stokes, and S. Kapur, "Mechanisms underlying psychosis and antipsychotic treatment response in schizophrenia: Insights from pet and spect imaging", English, *Current Pharmaceutical Design 18*, vol. 15, no. 22, pp. 2550–2559, Aug. 2009, ISSN: 1381-6128. DOI: `10.2174/138161209788957528`.

[98] A. D. Stanford, Z. Sharif, C. Corcoran, N. Urban, D. Malaspina, and S. H. Lisanby, "Rtms strategies for the study and treatment of schizophrenia: A review", *International Journal of Neuropsychopharmacology*, vol. 11, no. 4, pp. 563–576, 2008. DOI: `10.1017/S1461145707008309`. [Online]. Available: `https://doi.org/10.1017/S1461145707008309`.

[99] E. M. Wassermann, J. Grafman, C. Berry, *et al.*, "Use and safety of a new repetitive transcranial magnetic stimulator", *Electroencephalography and Clinical Neurophysiology/Electromyography and Motor Control*, vol. 101, no. 5, pp. 412–417, 1996, ISSN: 0924-980X. DOI: `https://doi.org/10.1016/0924-980X(96)96004-X`. [Online]. Available: `http://www.sciencedirect.com/science/article/pii/0924980X9696004X`.

[100] R. Chen, J. Classen, C. Gerloff, *et al.*, "Depression of motor cortex excitability by low-frequency transcranial magnetic stimulation", *Neurology*, vol. 48, no. 5, pp. 1398–1403, 1997, ISSN: 0028-3878. DOI: `10.1212/WNL.48.5.1398`. eprint: `https://n.neurology.org/content/48/5/1398.full.pdf`. [Online]. Available: `https://n.neurology.org/content/48/5/1398`.

[101] R. E. Hoffman, N. N. Boutros, R. M. Berman, *et al.*, "Transcranial magnetic stimulation of left temporoparietal cortex in three patients reporting hallucinated "voices"", *Biological Psychiatry*, vol. 46, no. 1, pp. 130–132, 1999, ISSN: 0006-3223. DOI: `https://doi.org/10.1016/S0006-3223(98)00358-8`. [Online]. Available: `http://www.sciencedirect.com/science/article/pii/S0006322398003588`.

[102] K. Kompus, R. Westerhausen, and K. Hugdahl, "The "paradoxical" engagement of the primary auditory cortex in patients with auditory verbal hallucinations: A meta-analysis of functional neuroimaging studies", *Neuropsychologia*, vol. 49, no. 12, pp. 3361–3369, 2011, ISSN: 0028-3932. DOI: `https://doi.org/10.1016/j.neuropsychologia.2011.08.010`. [Online]. Available: `http://www.sciencedirect.com/science/article/pii/S0028393211003897`.

[103] J.-P. Lefaucheur, N. Andre-Obadia, A. Antal, *et al.*, "Evidence-based guidelines on the therapeutic use of repetitive transcranial magnetic stimulation (rtms)", *Clinical Neurophysiology*, vol. 125, no. 11, pp. 2150–2206, 2014, ISSN: 1388-2457. DOI: `https://doi.org/10.1016/j.clinph.2014.05.021`. [On-

line]. Available: http://www.sciencedirect.com/science/article/pii/S138824571400296X.

[104]   W. Klimesch, M. Doppelmayr, H. Russegger, T. Pachinger, and J. Schwaiger, "Induced alpha band power changes in the human eeg and attention", *Neuroscience Letters*, vol. 244, no. 2, pp. 73–76, 1998. DOI: https://doi.org/10.1016/S0304-3940(98)00122-0. [Online]. Available: http://www.sciencedirect.com/science/article/pii/S0304394098001220.

[105]   M. S. Barr, F. Farzan, T. Arenovich, R. Chen, P. B. Fitzgerald, and Z. J. Daskalakis, "The effect of repetitive transcranial magnetic stimulation on gamma oscillatory activity in schizophrenia", *PLOS ONE*, vol. 6, no. 7, pp. 1–11, Jul. 2011. DOI: 10.1371/journal.pone.0022627. [Online]. Available: https://doi.org/10.1371/journal.pone.0022627.

[106]   X.-D. Lin, X.-S. Chen, C. Chen, *et al.*, "Effects of repetitive transcranial magnetic stimulation treatment on event-related potentials in schizophrenia", *Chinese Medical Journal*, vol. 131, p. 301, Feb. 2018. DOI: 10.4103/0366-6999.223846.

[107]   A. Mazaheri and T. W. Picton, "Eeg spectral dynamics during discrimination of auditory and visual targets", *Cognitive Brain Research*, vol. 24, no. 1, pp. 81–96, 2005. DOI: https://doi.org/10.1016/j.cogbrainres.2004.12.013. [Online]. Available: http://www.sciencedirect.com/science/article/pii/S0926641004003519.

[108]   Y.-W. Jeon and J. Polich, "Meta-analysis of p300 and schizophrenia: Patients, paradigms, and practical implications", *Psychophysiology*, vol. 40, no. 5, pp. 684–701, 2003. DOI: 10.1111/1469-8986.00070. eprint: https://onlinelibrary.wiley.com/doi/pdf/10.1111/1469-8986.00070. [Online]. Available: https://onlinelibrary.wiley.com/doi/abs/10.1111/1469-8986.00070.

[109]   D. J. Fisher, D. M. Smith, A. Labelle, and V. J. Knott, "Attenuation of mismatch negativity (mmn) and novelty p300 in schizophrenia patients with auditory hallucinations experiencing acute exacerbation of illness", *Biological Psychology*, vol. 100, pp. 43–49, 2014, ISSN: 0301-0511. DOI: https://doi.org/10.1016/j.biopsycho.2014.05.005. [Online]. Available: http://www.sciencedirect.com/science/article/pii/S0301051114001045.

[110]   E. Bramon, S. Rabe-Hesketh, P. Sham, R. M. Murray, and S. Frangou, "Meta-analysis of the p300 and p50 waveforms in schizophrenia", *Schizophrenia Research*, vol. 70, no. 2, pp. 315–329, 2004, ISSN: 0920-9964. DOI: https://doi.org/10.1016/j.schres.2004.01.004. [Online]. Available: http://www.sciencedirect.com/science/article/pii/S0920996404000349.

[111]   M. Lijffijt, S. D. Lane, S. L. Meier, *et al.*, "P50, n100, and p200 sensory gating: Relationships with behavioral inhibition, attention, and working memory", *Psychophysiology*, vol. 46, no. 5, pp. 1059–1068, 2009. DOI: 10.1111/j.1469-8986.2009.00845.x. eprint: https://onlinelibrary.wiley.com/doi/pdf/10.1111/j.1469-8986.2009.00845.x. [Online]. Available: https://onlinelibrary.wiley.com/doi/abs/10.1111/j.1469-8986.2009.00845.x.

[112] J. M. Ford, D. H. Mathalon, S. Kalba, L. Marsh, and A. Pfefferbaum, "N1 and p300 abnormalities in patients with schizophrenia, epilepsy, and epilepsy with schizophrenialike features", *Biological Psychiatry*, vol. 49, no. 10, pp. 848–860, 2001, ISSN: 0006-3223. DOI: `https://doi.org/10.1016/S0006-3223(00)01051-9`. [Online]. Available: `http://www.sciencedirect.com/science/article/pii/S0006322300010519`.

[113] H. A. Earls, T. Curran, and V. Mittal, "A Meta-analytic Review of Auditory Event-Related Potential Components as Endophenotypes for Schizophrenia: Perspectives From First-Degree Relatives", *Schizophrenia Bulletin*, vol. 42, no. 6, pp. 1504–1516, May 2016, ISSN: 0586-7614. DOI: `10.1093/schbul/sbw047`. eprint: `https://academic.oup.com/schizophreniabulletin/article-pdf/42/6/1504/16976249/sbw047.pdf`. [Online]. Available: `https://doi.org/10.1093/schbul/sbw047`.

[114] C. Ogura, Y. Nageishi, M. Matsubayashi, F. Omura, A. Kishimoto, and M. Shimokochi, "Abnormalities in event-related potentials, n100, p200, p300 and slow wave in schizophrenia", *Psychiatry and Clinical Neurosciences*, vol. 45, no. 1, pp. 57–65, 1991. DOI: `10.1111/j.1440-1819.1991.tb00506.x`. eprint: `https://onlinelibrary.wiley.com/doi/pdf/10.1111/j.1440-1819.1991.tb00506.x`. [Online]. Available: `https://onlinelibrary.wiley.com/doi/abs/10.1111/j.1440-1819.1991.tb00506.x`.

[115] D. A. Nowak, C. Grefkes, M. Dafotakis, *et al.*, "Effects of Low-Frequency Repetitive Transcranial Magnetic Stimulation of the Contralesional Primary Motor Cortex on Movement Kinematics and Neural Activity in Subcortical Stroke", *Archives of Neurology*, vol. 65, no. 6, pp. 741–747, Jun. 2008, ISSN: 0003-9942. DOI: `10.1001/archneur.65.6.741`. eprint: `https://jamanetwork.com/journals/jamaneurology/articlepdf/795742/noc80003\_741\_747.pdf`. [Online]. Available: `https://doi.org/10.1001/archneur.65.6.741`.

[116] T. Nyffeler, P. Wurtz, H.-R. Lüscher, *et al.*, "Repetitive tms over the human oculomotor cortex: Comparison of 1-hz and theta burst stimulation", *Neuroscience Letters*, vol. 409, no. 1, pp. 57–60, 2006, ISSN: 0304-3940. DOI: `https://doi.org/10.1016/j.neulet.2006.09.011`. [Online]. Available: `http://www.sciencedirect.com/science/article/pii/S0304394006009414`.

[117] C. K. Loo, K. Sainsbury, P. Mitchell, D. Hadzi-Pavlovic, and P. S. Sachdev, "A sham-controlled trial of left and right temporal rtms for the treatment of auditory hallucinations", *Psychological Medicine*, vol. 40, no. 4, pp. 541–546, 2010. DOI: `10.1017/S0033291709990900`.

[118] S. Rossi, M. Hallett, P. M. Rossini, and A. Pascual-Leone, "Screening questionnaire before tms: An update", *Clinical Neurophysiology*, vol. 122, no. 8, p. 1686, 2011, ISSN: 1388-2457. DOI: `https://doi.org/10.1016/j.clinph.2010.12.037`. [Online]. Available: `http://www.sciencedirect.com/science/article/pii/S1388245710008692`.

[119] R. Drake, G. Haddock, N. Tarrier, R. Bentall, and S. Lewis, "The psychotic symptom rating scales (psyrats): Their usefulness and properties in first episode psychosis", *Schizophrenia Research*, vol. 89, no. 1, pp. 119–122, 2007, ISSN: 0920-9964. DOI: `https://doi.org/10.1016/j.schres.2006.04.024`. [Online]. Available: `http://www.sciencedirect.com/science/article/pii/S0920996406002131`.

[120] G. Haddock, J. McCarron, N. TARRIER, and E. B. Faragher, "Scales to measure dimensions of hallucinations and delusions: The psychotic symptom rating scales (psyrats)", *Psychological Medicine*, vol. 29, no. 4, pp. 879–889, 1999. DOI: `10.1017/S0033291799008661`.

[121] J. C. Flanagan, "A research approach to improving our quality of life.", 1978.

[122] T. A. Brown, B. F. Chorpita, W. Korotitsch, and D. H. Barlow, "Psychometric properties of the depression anxiety stress scales (dass) in clinical samples", *Behaviour Research and Therapy*, vol. 35, no. 1, pp. 79–89, 1997, ISSN: 0005-7967. DOI: `https://doi.org/10.1016/S0005-7967(96)00068-X`. [Online]. Available: `http://www.sciencedirect.com/science/article/pii/S000579679600068X`.

[123] S. Marcu, E. Pegolo, E. ivarsson, *et al.*, "Using high density eeg to assess tms treatment in patients with schizophrenia", *European Journal of Translational Myology*, vol. 30, no. 1, pp. 134–138, 2020. DOI: `10.4081/ejtm.2019.8903`. [Online]. Available: `https://www.pagepressjournals.org/index.php/bam/article/view/8903`.

[124] F. Tadel, S. Baillet, J. C. Mosher, D. Pantazis, and R. M. Leahy, "Brainstorm: A user-friendly application for meg/eeg analysis", *Computational Intelligence and Neuroscience*, vol. 2011, p. 879 716, 2011. DOI: `10.1155/2011/879716`. [Online]. Available: `https://doi.org/10.1155/2011/879716`.

[125] M. Schartner, A. Seth, Q. Noirhomme, *et al.*, "Complexity of multi-dimensional spontaneous eeg decreases during propofol induced general anaesthesia", *PLOS ONE*, vol. 10, no. 8, pp. 1–21, Aug. 2015. DOI: `10.1371/journal.pone.0133532`. [Online]. Available: `https://doi.org/10.1371/journal.pone.0133532`.

[126] M. Hassan, O. Dufor, I. Merlet, C. Berrou, and F. Wendling, "Eeg source connectivity analysis: From dense array recordings to brain networks", *PLOS ONE*, vol. 9, no. 8, pp. 1–15, Aug. 2014. DOI: `10.1371/journal.pone.0105041`. [Online]. Available: `https://doi.org/10.1371/journal.pone.0105041`.

[127] J. Modolo, M. Hassan, G. Ruffini, and A. Legros, "Probing the circuits of conscious perception with magnetophosphenes", *Journal of Neural Engineering*, vol. 17, no. 3, p. 036 034, 2020. DOI: `10.1088/1741-2552/ab97f7`.

[128] C. J. Stam, "Modern network science of neurological disorders", *Nature Reviews Neuroscience*, vol. 15, no. 10, pp. 683–695, 2014. DOI: `10.1038/nrn3801`. [Online]. Available: `https://doi.org/10.1038/nrn3801`.

[129] M. Rubinov and O. Sporns, "Complex network measures of brain connectivity: Uses and interpretations", *NeuroImage*, vol. 52, no. 3, pp. 1059–1069, 2010, Computational Models of the Brain, ISSN: 1053-8119. DOI: `https://doi.org/10.1016/j.neuroimage.2009.10.003`. [Online]. Available: `http://www.sciencedirect.com/science/article/pii/S105381190901074X`.

[130] D. C. Javitt, K. M. Spencer, G. K. Thaker, G. Winterer, and M. Hajos, "Neurophysiological biomarkers for drug development in schizophrenia", *Nature Reviews Drug Discovery*, vol. 7, no. 1, pp. 68–83, 2008. DOI: `10.1038/nrd2463`. [Online]. Available: `https://doi.org/10.1038/nrd2463`.

[131] J. Polich, "On the relationship between eeg and p300: Individual differences, aging, and ultradian rhythms", *International Journal of Psychophysiology*, vol. 26, no. 1, pp. 299–317, 1997, ISSN: 0167-8760. DOI: `https://doi.org/10.1016/S0167-8760(97)00772-1`. [Online]. Available: `http://www.sciencedirect.com/science/article/pii/S0167876097007721`.

[132] S. H. Patel and P. N. Azzam, "Characterization of n200 and p300: Selected studies of the event-related potential", *Int J Med Sci*, vol. 2, pp. 147–154, 2005. DOI: `10.7150/ijms.2.147`. [Online]. Available: `http://www.medsci.org/v02p0147.htm`.

[133] W. Ray and H. Cole, "Eeg alpha activity reflects attentional demands, and beta activity reflects emotional and cognitive processes", *Science*, vol. 228, no. 4700, pp. 750–752, 1985, ISSN: 0036-8075. DOI: `10.1126/science.3992243`. eprint: `https://science.sciencemag.org/content/228/4700/750.full.pdf`. [Online]. Available: `https://science.sciencemag.org/content/228/4700/750`.

[134] A. Fornito, A. Zalesky, and M. Breakspear, "The connectomics of brain disorders", *Nature Reviews Neuroscience*, vol. 16, no. 3, pp. 159–172, 2015. DOI: `10.1038/nrn3901`. [Online]. Available: `https://doi.org/10.1038/nrn3901`.

[135] J. Massion, "Postural control system", *Current Opinion in Neurobiology*, vol. 4, no. 6, pp. 877–887, 1994, ISSN: 0959-4388. DOI: `https://doi.org/10.1016/0959-4388(94)90137-6`. [Online]. Available: `https://www.sciencedirect.com/science/article/pii/0959438894901376`.

[136] A. Paillard, G. Quarck, F. Paolino, *et al.*, "Motion sickness susceptibility in healthy subjects and vestibular patients: Effects of gender, age and trait-anxiety", *Journal of Vestibular Research*, vol. 23, no. 4-5, pp. 203–209, Nov. 2013, ISSN: 18786464, 09574271. DOI: `10.3233/VES-130501`. [Online]. Available: `https://www.medra.org/servlet/aliasResolver?alias=iospress&doi=10.3233/VES-130501` (visited on 07/26/2022).

[137] B. E. Maki and W. E. McIlroy, "Postural Control in the Older Adult", en, *Clinics in Geriatric Medicine*, vol. 12, no. 4, pp. 635–658, Nov. 1996, ISSN: 07490690. DOI: `10.1016/S0749-0690(18)30193-9`. [Online]. Available: `https://linkinghub.elsevier.com/retrieve/pii/S0749069018301939` (visited on 07/26/2022).

[138] P. A. Hageman, J. M. Leibowitz, and D. Blanke, "Age and gender effects on postural control measures", *Archives of physical medicine and rehabilitation*, vol. 76, no. 10, pp. 961–965, 1995.

[139] F. Barollo, R. Frioriksdottir, K. J. Edmunds, *et al.*, "Postural Control Adaptation and Habituation During Vibratory Proprioceptive Stimulation: An HD-EEG Investigation of Cortical Recruitment and Kinematics", en, *IEEE Trans. Neural Syst. Rehabil. Eng.*, vol. 28, no. 6, pp. 1381–1388, Jun. 2020, ISSN: 1534-4320, 1558-0210. DOI: `10.1109/TNSRE.2020.2988585`. [Online]. Available: `https://ieeexplore.ieee.org/document/9069925/` (visited on 04/27/2022).

[140] K. J. Edmunds, H. Petersen, M. Hassan, *et al.*, "Cortical recruitment and functional dynamics in postural control adaptation and habituation during vibratory proprioceptive stimulation", *Journal of neural engineering*, vol. 16, no. 2, p. 026 037, 2019.

[141] M. Recenti, C. Ricciardi, R. Aubonnet, *et al.*, "Toward predicting motion sickness using virtual reality and a moving platform assessing brain, muscles, and heart signals", *Frontiers in Bioengineering and Biotechnology*, vol. 9, 2021, ISSN: 2296-4185. DOI: `10.3389/fbioe.2021.635661`. [Online]. Available: `https://www.frontiersin.org/article/10.3389/fbioe.2021.635661`.

[142] H. Petersen, "[seasickness]", *Laeknabladid*, vol. 98, no. 12, pp. 653–659, 2012, ISSN: 0023-7213. DOI: `10.17992/lbl.2012.12.468`. [Online]. Available: `https://doi.org/10.17992/lbl.2012.12.468`.

[143] J. F. Golding, "Predicting individual differences in motion sickness susceptibility by questionnaire", *Personality and Individual Differences*, vol. 41, no. 2, pp. 237–248, 2006, ISSN: 0191-8869. DOI: `https://doi.org/10.1016/j.paid.2006.01.012`. [Online]. Available: `https://www.sciencedirect.com/science/article/pii/S0191886906000602`.

[144] J. T. Reason, "Motion sickness adaptation: A neural mismatch model", *Journal of the Royal Society of Medicine*, vol. 71, no. 11, pp. 819–829, 1978.

[145] G. E. Riccio and T. A. Stoffregen, "An ecological theory of motion sickness and postural instability", *Ecological psychology*, vol. 3, no. 3, pp. 195–240, 1991.

[146] A. Koohestani, D. Nahavandi, H. Asadi, *et al.*, "A knowledge discovery in motion sickness: A comprehensive literature review", *IEEE access*, vol. 7, pp. 85 755–85 770, 2019.

[147] R. Laboissiere, J.-C. Letievant, E. Ionescu, P.-A. Barraud, M. Mazzuca, and C. Cian, "Relationship between spectral characteristics of spontaneous postural sway and motion sickness susceptibility", *PLoS One*, vol. 10, no. 12, e0144466, 2015.

[148] R. S. Kennedy, N. E. Lane, K. S. Berbaum, and M. G. Lilienthal, "Simulator sickness questionnaire: An enhanced method for quantifying simulator sickness", *The international journal of aviation psychology*, vol. 3, no. 3, pp. 203–220, 1993.

[149] J. F. Golding, "Motion sickness", *Handbook of clinical neurology*, vol. 137, pp. 371–390, 2016.

[150] R. Maire, A. Mallinson, H. Ceyte, *et al.*, "Discussion about visual dependence in balance control: European society for clinical evaluation of balance disorders", 2017.

[151] K.-M. Jang, Y. Shin Woo, and H. Kyoon Lim, "Electrophysiological changes in the virtual reality sickness: Eeg in the vr sickness", in *The 25th International Conference on 3D Web Technology*, 2020, pp. 1–4.

[152] Y. Y. Kim, H. J. Kim, E. N. Kim, H. D. Ko, and H. T. Kim, "Characteristic changes in the physiological components of cybersickness", *Psychophysiology*, vol. 42, no. 5, pp. 616–625, 2005.

[153] D. Jacob, I. S. Unnsteinsdóttir Kristensen, R. Aubonnet, *et al.*, "Towards defining biomarkers to evaluate concussions using virtual reality and a moving platform (biovrsea)", *Scientific Reports*, vol. 12, no. 1, p. 8996, 2022, ISSN: 2045-2322. DOI: `10.1038/s41598-022-12822-0`. [Online]. Available: `https://doi.org/10.1038/s41598-022-12822-0`.

[154] P. McCrory, N. Feddermann-Demont, J. Dvořák, *et al.*, "What is the definition of sports-related concussion: A systematic review", *British journal of sports medicine*, vol. 51, no. 11, pp. 877–887, 2017.

[155] J. A. Langlois, W. Rutland-Brown, and M. M. Wald, "The epidemiology and impact of traumatic brain injury: A brief overview", *The Journal of head trauma rehabilitation*, vol. 21, no. 5, pp. 375–378, 2006.

[156] S. E. Chancellor, E. S. Franz, O. V. Minaeva, and L. E. Goldstein, "Pathophysiology of concussion", in *Seminars in Pediatric Neurology*, Elsevier, vol. 30, 2019, pp. 14–25.

[157] P. McCrory, W. Meeuwisse, J. Dvorak, *et al.*, "Consensus statement on concussion in sport—the 5th international conference on concussion in sport held in berlin, october 2016", *British journal of sports medicine*, vol. 51, no. 11, pp. 838–847, 2017.

[158] S. P. Broglio and T. W. Puetz, "The effect of sport concussion on neurocognitive function, self-report symptoms and postural control", *Sports Medicine*, vol. 38, no. 1, pp. 53–67, 2008.

[159] K. Dams-O'Connor, J. B. Cantor, M. Brown, M. P. Dijkers, L. A. Spielman, and W. A. Gordon, "Screening for traumatic brain injury: Findings and public health implications", *The Journal of head trauma rehabilitation*, vol. 29, no. 6, p. 479, 2014.

[160] N. A. Shaw, "The neurophysiology of concussion", *Progress in neurobiology*, vol. 67, no. 4, pp. 281–344, 2002.

[161] A. C. Conley, P. S. Cooper, F. Karayanidis, *et al.*, "Resting state electroencephalography and sports-related concussion: A systematic review", *Journal of neurotrauma*, vol. 36, no. 1, pp. 1–13, 2019.

[162] J. N. Ianof and R. Anghinah, "Traumatic brain injury: An eeg point of view", *Dementia & neuropsychologia*, vol. 11, pp. 3–5, 2017.

[163] A. P. Kontos, A. Reches, R. Elbin, *et al.*, "Preliminary evidence of reduced brain network activation in patients with post-traumatic migraine following concussion", *Brain imaging and behavior*, vol. 10, no. 2, pp. 594–603, 2016.

[164] J. Thompson, W. Sebastianelli, and S. Slobounov, "Eeg and postural correlates of mild traumatic brain injury in athletes", *Neuroscience letters*, vol. 377, no. 3, pp. 158–163, 2005.

[165] S. Guay, L. De Beaumont, B. L. Drisdelle, J.-M. Lina, and P. Jolicoeur, "Electrophysiological impact of multiple concussions in asymptomatic athletes: A re-analysis based on alpha activity during a visual-spatial attention task", *Neuropsychologia*, vol. 108, pp. 42–49, 2018.

[166] C. Cao, R. L. Tutwiler, and S. Slobounov, "Automatic classification of athletes with residual functional deficits following concussion by means of eeg signal using support vector machine", *IEEE transactions on neural systems and rehabilitation engineering*, vol. 16, no. 4, pp. 327–335, 2008.

[167] E. S. Papathanasiou, T. Cronin, B. Seemungal, and J. Sandhu, "Electrophysiological testing in concussion: A guide to clinical applications", *Journal of Concussion*, vol. 2, p. 2 059 700 218 812 634, 2018.

[168] J. T. Cavanaugh, K. M. Guskiewicz, C. Giuliani, S. Marshall, V. Mercer, and N. Stergiou, "Detecting altered postural control after cerebral concussion in athletes with normal postural stability", *British journal of sports medicine*, vol. 39, no. 11, pp. 805–811, 2005.

[169] Y. Ivanenko and V. S. Gurfinkel, "Human postural control", *Frontiers in Neuroscience*, vol. 12, 2018, ISSN: 1662-453X. DOI: `10.3389/fnins.2018.00171`.

[170] S. Patejak, J. Forrest, E. Harting, M. Sisk, and E. Schussler, "A systematic review of center of mass as a measure of dynamic postural control following concussion", *International journal of sports physical therapy*, vol. 16, no. 5, p. 1222, 2021.

[171] T. Paillard and F. Noé, "Techniques and methods for testing the postural function in healthy and pathological subjects", *BioMed Research International*, vol. 2015, p. 891 390, 2015, ISSN: 2314-6133. DOI: `10.1155/2015/891390`. [Online]. Available: `https://doi.org/10.1155/2015/891390`.

[172] S. A. Bishop, R. T. Dech, P. Guzik, and J. P. Neary, "Heart rate variability and implication for sport concussion", *Clinical Physiology and Functional Imaging*, vol. 38, no. 5, pp. 733–742, 2018. DOI: `https://doi.org/10.1111/cpf.12487`. eprint: `https://onlinelibrary.wiley.com/doi/pdf/10.1111/cpf.12487`. [Online]. Available: `https://onlinelibrary.wiley.com/doi/abs/10.1111/cpf.12487`.

[173] S. Slobounov, W. Sebastianelli, and M. Hallett, "Residual brain dysfunction observed one year post-mild traumatic brain injury: Combined eeg and balance study", *Clinical Neurophysiology*, vol. 123, no. 9, pp. 1755–1761, 2012, ISSN: 1388-2457. DOI: `https://doi.org/10.1016/j.clinph.2011.12.022`.

[174] M. I. Jordan and T. M. Mitchell, "Machine learning: Trends, perspectives, and prospects", *Science*, vol. 349, no. 6245, pp. 255–260, 2015. DOI: `10.1126/science.aaa8415`. eprint: `https://www.science.org/doi/pdf/10.1126/science.aaa8415`. [Online]. Available: `https://www.science.org/doi/abs/10.1126/science.aaa8415`.

[175] A. Pedroni, A. Bahreini, and N. Langer, "Automagic: Standardized preprocessing of big eeg data", *NeuroImage*, vol. 200, pp. 460–473, 2019, ISSN: 1053-8119. DOI: `https://doi.org/10.1016/j.neuroimage.2019.06.046`. [Online]. Available: `https://www.sciencedirect.com/science/article/pii/S1053811919305439`.

[176] Y. Benjamini and Y. Hochberg, "Controlling the false discovery rate - a practical and powerful approach to multiple testing", *J. Royal Statist. Soc., Series B*, vol. 57, pp. 289–300, Nov. 1995. DOI: `10.2307/2346101`.

[177] A. Clouter, K. L. Shapiro, and S. Hanslmayr, "Theta phase synchronization is the glue that binds human associative memory", *Current Biology*, vol. 27, no. 20, pp. 3143–3148, 2017.

[178] J. Mari-Acevedo, K. Yelvington, and W. O. Tatum, "Normal eeg variants", *Handbook of clinical neurology*, vol. 160, pp. 143–160, 2019.

[179] K. Ryu, Y. Choi, J. Kim, Y. Kim, and S. Chio, "Differential frontal theta activity during cognitive and motor tasks", *Journal of integrative neuroscience*, vol. 15, no. 03, pp. 295–303, 2016.

[180] Y.-K. Wang, T.-P. Jung, and C.-T. Lin, "Theta and alpha oscillations in attentional interaction during distracted driving", *Frontiers in behavioral neuroscience*, vol. 12, p. 3, 2018.

[181] G. Manley, A. J. Gardner, K. J. Schneider, *et al.*, "A systematic review of potential long-term effects of sport-related concussion", *British Journal of Sports Medicine*, vol. 51, no. 12, pp. 969–977, 2017, ISSN: 0306-3674. DOI: `10.1136/bjsports-2017-097791`. eprint: `https://bjsm.bmj.com/content/51/12/969.full.pdf`. [Online]. Available: `https://bjsm.bmj.com/content/51/12/969`.

[182] N. S. King and S. Kirwilliam, "Permanent post-concussion symptoms after mild head injury", *Brain Injury*, vol. 25, no. 5, pp. 462–470, 2011. DOI: `10.3109/02699052.2011.558042`.

[183] A. L. Zhang, D. C. Sing, C. M. Rugg, B. T. Feeley, and C. Senter, "The rise of concussions in the adolescent population", *Orthopaedic Journal of Sports Medicine*, vol. 4, no. 8, p. 2 325 967 116 662 458, 2016, PMID: 27579334. DOI: `10.1177/2325967116662458`.

[184] N. Sandel, E. Reynolds, P. E. Cohen, B. L. Gillie, and A. P. Kontos, "Anxiety and mood clinical profile following sport-related concussion: From risk factors to treatment", *Sport Exerc. Perform. Psychol.*, vol. 6, no. 3, pp. 304–323, 2017.

[185] A. R. Sipp, J. T. Gwin, S. Makeig, and D. P. Ferris, "Loss of balance during balance beam walking elicits a multifocal theta band electrocortical response", *Journal of neurophysiology*, vol. 110, no. 9, pp. 2050–2060, 2013.

[186] S. A. Stehle, R. Aubonnet, M. Hassan, *et al.*, "Predicting postural control adaptation measuring eeg, emg, and center of pressure changes: Biovrsea paradigm", *Frontiers in Human Neuroscience*, vol. 16, 2022, ISSN: 1662-5161. DOI: `10.3389/fnhum.2022.1038976`. [Online]. Available: `https://www.frontiersin.org/articles/10.3389/fnhum.2022.1038976`.

[187] N. B. Alexander, "Postural control in older adults", 1994.

[188] R. Marks, J. P. Allegrante, C. R. MacKenzie, and J. M. Lane, "Hip fractures among the elderly: Causes, consequences and control", *Ageing research reviews*, vol. 2, no. 1, pp. 57–93, 2003.

[189] M. Figueiro, L. Gras, R. Qi, P. Rizzo, M. Rea, and M. Rea, "A novel night lighting system for postural control and stability in seniors", *Lighting Research & Technology*, vol. 40, no. 2, pp. 111–126, 2008.

[190] F. B. Horak, "Postural orientation and equilibrium: What do we need to know about neural control of balance to prevent falls?", en, *Age and Ageing*, vol. 35, no. suppl_2, pp. ii7–ii11, Sep. 2006, Number: suppl_2, ISSN: 1468-2834, 0002-0729. DOI: `10.1093/ageing/afl077`. [Online]. Available: `http://academic.oup.com/ageing/article/35/suppl_2/ii7/15654/Postural-orientation-and-equilibrium-what-do-we` (visited on 07/20/2022).

[191] I. Melzer, N. Benjuya, and J. Kaplanski, "Age-related changes of postural control: Effect of cognitive tasks", *Gerontology*, vol. 47, no. 4, pp. 189–194, 2001.

[192] R. J. Peterka, "Sensorimotor integration in human postural control", *Journal of neurophysiology*, vol. 88, no. 3, pp. 1097–1118, 2002.

[193] J. M. Haddad, S. Rietdyk, L. J. Claxton, and J. E. Huber, "Task-dependent postural control throughout the lifespan", *Exercise and sport sciences reviews*, vol. 41, no. 2, pp. 123–132, 2013.

[194] P.-A. Fransson, R. Johansson, A. Hafström, and M. Magnusson, "Methods for evaluation of postural control adaptation", *Gait & posture*, vol. 12, no. 1, pp. 14–24, 2000.

[195] J. He and C.-X. Tian, "Adaptive postural control for a repeated perturbation", in *Proceedings of 18th Annual International Conference of the IEEE Engineering in Medicine and Biology Society*, vol. 5, 1996, 2215–2216 vol.5. DOI: 10.1109/IEMBS.1996.646503.

[196] R. J. Reed-Jones, L. A. Vallis, J. G. Reed-Jones, and L. M. Trick, "The relationship between postural stability and virtual environment adaptation", *Neuroscience letters*, vol. 435, no. 3, pp. 204–209, 2008.

[197] A. E. Edwards, O. Guven, M. D. Furman, Q. Arshad, and A. M. Bronstein, "Electroencephalographic correlates of continuous postural tasks of increasing difficulty", *Neuroscience*, vol. 395, pp. 35–48, 2018, ISSN: 0306-4522. DOI: https://doi.org/10.1016/j.neuroscience.2018.10.040. [Online]. Available: https://www.sciencedirect.com/science/article/pii/S0306452218307103.

[198] S. Slobounov, M. Hallett, S. Stanhope, and H. Shibasaki, "Role of cerebral cortex in human postural control: An eeg study", *Clinical neurophysiology*, vol. 116, no. 2, pp. 315–323, 2005.

[199] R. A. Poldrack, G. Huckins, and G. Varoquaux, "Establishment of best practices for evidence for prediction: A review", *JAMA psychiatry*, vol. 77, no. 5, pp. 534–540, 2020.

[200] D. Scheinost, S. Noble, C. Horien, *et al.*, "Ten simple rules for predictive modeling of individual differences in neuroimaging", *NeuroImage*, vol. 193, pp. 35–45, 2019.

[201] T. A. Woolsey, J. Hanaway, and M. H. Gado, *The brain atlas: A visual guide to the human central nervous system*. John Wiley & Sons, 2017.

[202] S. M. Casillo, D. D. Luy, and E. Goldschmidt, "A history of the lobes of the brain", *World Neurosurgery*, vol. 134, pp. 353–360, 2020.

[203] T. T. Chowdhury, S. A. Fattah, and C. Shahnaz, "Classification of seizure and non-seizure activity in seizure patients using time-frequency domain processing of gamma band eeg signals", in *2017 4th International Conference on Advances in Electrical Engineering (ICAEE)*, 2017, pp. 537–540. DOI: 10.1109/ICAEE.2017.8255414.

[204] V. Harpale and V. Bairagi, "An adaptive method for feature selection and extraction for classification of epileptic eeg signal in significant states", *Journal of King Saud University-Computer and Information Sciences*, vol. 33, no. 6, pp. 668–676, 2021.

[205] R. M. Mehmood, R. Du, and H. J. Lee, "Optimal feature selection and deep learning ensembles method for emotion recognition from human brain eeg sensors", *Ieee Access*, vol. 5, pp. 14 797–14 806, 2017.

[206] B. Faw, "Pre-frontal executive committee for perception, working memory, attention, long-term memory, motor control, and thinking: A tutorial review", *Consciousness and Cognition*, vol. 12, no. 1, pp. 83–139, 2003, ISSN: 1053-8100. DOI: `https://doi.org/10.1016/S1053-8100(02)00030-2`. [Online]. Available: `https://www.sciencedirect.com/science/article/pii/S1053810002000302`.

[207] X. Li, P. Zhou, and A. S. Aruin, "Teager–kaiser energy operation of surface emg improves muscle activity onset detection", *Annals of biomedical engineering*, vol. 35, no. 9, pp. 1532–1538, 2007.

[208] S. Solnik, P. Rider, K. Steinweg, P. DeVita, and T. Hortobágyi, "Teager–kaiser energy operator signal conditioning improves emg onset detection", *European journal of applied physiology*, vol. 110, no. 3, pp. 489–498, 2010.

[209] J. Liu, D. Ying, W. Z. Rymer, and P. Zhou, "Robust muscle activity onset detection using an unsupervised electromyogram learning framework", *PloS one*, vol. 10, no. 6, e0127990, 2015.

[210] P. W. Laksono, T. Kitamura, J. Muguro, K. Matsushita, M. Sasaki, and M. S. Amri bin Suhaimi, "Minimum mapping from emg signals at human elbow and shoulder movements into two dof upper-limb robot with machine learning", *Machines*, vol. 9, no. 3, p. 56, 2021.

[211] R. E. Van Emmerik and E. E. Van Wegen, "On the functional aspects of variability in postural control", *Exercise and sport sciences reviews*, vol. 30, no. 4, pp. 177–183, 2002.

[212] M. C. Hunter and M. A. Hoffman, "Postural control: Visual and cognitive manipulations", *Gait & Posture*, vol. 13, no. 1, pp. 41–48, 2001.

[213] S. F. Donker, M. Roerdink, A. J. Greven, and P. J. Beek, "Regularity of center-of-pressure trajectories depends on the amount of attention invested in postural control", *Experimental brain research*, vol. 181, no. 1, pp. 1–11, 2007.

[214] A. Lott, E. Bisson, Y. Lajoie, J. McComas, and H. Sveistrup, "The effect of two types of virtual reality on voluntary center of pressure displacement", *Cyberpsychology & behavior*, vol. 6, no. 5, pp. 477–485, 2003.

[215] H. Luo, X. Wang, M. Fan, *et al.*, "The effect of visual stimuli on stability and complexity of postural control", *Frontiers in neurology*, vol. 9, p. 48, 2018.

[216] J. V. Jacobs and F. B. Horak, "Cortical control of postural responses", en, *J Neural Transm*, vol. 114, no. 10, pp. 1339–1348, Oct. 2007, ISSN: 0300-9564, 1435-1463. DOI: `10.1007/s00702-007-0657-0`. [Online]. Available: `http://link.springer.com/10.1007/s00702-007-0657-0` (visited on 03/07/2022).

[217] D. A. Perennou, C. Leblond, B. Amblard, J. P. Micallef, E. Rouget, and J. Pelissier, "The polymodal sensory cortex is crucial for controlling lateral postural stability: Evidence from stroke patients", en, *Brain Research Bulletin*, vol. 53, no. 3, pp. 359–365, Oct. 2000, ISSN: 03619230. DOI: `10.1016/S0361-9230(00)00360-9`. [Online]. Available: `https://linkinghub.elsevier.com/retrieve/pii/S0361923000003609` (visited on 04/26/2022).

[218] L. Y.-H., T. P.-F., W. Y.-H., *et al.*, "Reactive postural control deficits in patients with posterior parietal cortex lesions after stroke and the influence of auditory cueing", *American Journal of Physical Medicine and Rehabilitation*, vol. 93, no. 10, pp. 849–859, 2014. DOI: `10.1097/PHM.0000000000000093`.

[219] O. Fasold, M. von Brevern, M. Kuhberg, *et al.*, "Human vestibular cortex as identified with caloric stimulation in functional magnetic resonance imaging", *NeuroImage*, vol. 17, no. 3, pp. 1384–1393, 2002, ISSN: 1053-8119. DOI: `https://doi.org/10.1006/nimg.2002.1241`. [Online]. Available: `https://www.sciencedirect.com/science/article/pii/S1053811902912413`.

[220] T. Stephan, A. Deutschländer, A. Nolte, *et al.*, "Functional mri of galvanic vestibular stimulation with alternating currents at different frequencies", *NeuroImage*, vol. 26, no. 3, pp. 721–732, 2005, ISSN: 1053-8119. DOI: `https://doi.org/10.1016/j.neuroimage.2005.02.049`. [Online]. Available: `https://www.sciencedirect.com/science/article/pii/S1053811905001515`.

[221] F. Herold, K. Orlowski, S. Börmel, and N. G. Müller, "Cortical activation during balancing on a balance board", en, *Human Movement Science*, vol. 51, pp. 51–58, Jan. 2017, ISSN: 01679457. DOI: `10.1016/j.humov.2016.11.002`. [Online]. Available: `https://linkinghub.elsevier.com/retrieve/pii/S0167945716302081` (visited on 03/04/2022).

[222] D. Bolton, "The role of the cerebral cortex in postural responses to externally induced perturbations", en, *Neuroscience & Biobehavioral Reviews*, vol. 57, pp. 142–155, Oct. 2015, ISSN: 01497634. DOI: `10.1016/j.neubiorev.2015.08.014`. [Online]. Available: `https://linkinghub.elsevier.com/retrieve/pii/S0149763415002328` (visited on 03/04/2022).

[223] B. E. Maki and W. E. McIlroy, "Cognitive demands and cortical control of human balance-recovery reactions", en, *J Neural Transm*, vol. 114, no. 10, pp. 1279–1296, Oct. 2007, ISSN: 0300-9564, 1435-1463. DOI: `10.1007/s00702-007-0764-y`. [Online]. Available: `http://link.springer.com/10.1007/s00702-007-0764-y` (visited on 03/07/2022).

[224] R. Goel, R. A. Ozdemir, S. Nakagome, J. L. Contreras-Vidal, W. H. Paloski, and P. J. Parikh, "Effects of speed and direction of perturbation on electroencephalographic and balance responses", *Experimental Brain Research*, vol. 236, no. 7, pp. 2073–2083, 2018, ISSN: 1432-1106. DOI: `10.1007/s00221-018-5284-5`. [Online]. Available: `https://doi.org/10.1007/s00221-018-5284-5`.

[225] J. P. Varghese, R. E. McIlroy, and M. Barnett-Cowan, "Perturbation-evoked potentials: Significance and application in balance control research", en, *Neuroscience & Biobehavioral Reviews*, vol. 83, pp. 267–280, Dec. 2017, ISSN: 01497634. DOI: `10.1016/j.neubiorev.2017.10.022`. [Online]. Available: `https://linkinghub.elsevier.com/retrieve/pii/S0149763417305699` (visited on 04/04/2022).

[226] J. P. Varghese, A. Marlin, K. B. Beyer, W. R. Staines, G. Mochizuki, and W. E. McIlroy, "Frequency characteristics of cortical activity associated with perturbations to upright stability", *Neuroscience Letters*, vol. 578, pp. 33–38, 2014, ISSN: 0304-3940. DOI: `https://doi.org/10.1016/j.neulet.2014.06.017`. [Online]. Available: `https://www.sciencedirect.com/science/article/pii/S0304394014004893`.

[227] T. Hülsdünker, A. Mierau, C. Neeb, H. Kleinöder, and H. Strüder, "Cortical processes associated with continuous balance control as revealed by EEG spectral power", en, *Neuroscience Letters*, vol. 592, pp. 1–5, Apr. 2015, ISSN: 03043940. DOI: `10.1016/j.neulet.2015.02.049`. [Online]. Available: `https://linkinghub.elsevier.com/retrieve/pii/S0304394015001639` (visited on 03/03/2022).

[228] T. Harmony, "The functional significance of delta oscillations in cognitive processing", *Frontiers in Integrative Neuroscience*, vol. 7, 2013, ISSN: 1662-5145. DOI: `10.3389/fnint.2013.00083`. [Online]. Available: `https://www.frontiersin.org/article/10.3389/fnint.2013.00083`.

[229] G. G. Knyazev, "Eeg delta oscillations as a correlate of basic homeostatic and motivational processes", *Neuroscience & Biobehavioral Reviews*, vol. 36, no. 1, pp. 677–695, 2012, ISSN: 0149-7634. DOI: `https://doi.org/10.1016/j.neubiorev.2011.10.002`. [Online]. Available: `https://www.sciencedirect.com/science/article/pii/S0149763411001849`.

[230] R. A. Ozdemir, J. L. Contreras-Vidal, and W. H. Paloski, "Cortical control of upright stance in elderly", *Mechanisms of Ageing and Development*, vol. 169, pp. 19–31, 2018, ISSN: 0047-6374. DOI: `https://doi.org/10.1016/j.mad.2017.12.004`. [Online]. Available: `https://www.sciencedirect.com/science/article/pii/S0047637417302440`.

[231] R. Ibitoye, P. Castro, A. Desowska, *et al.*, "Small vessel disease disrupts eeg postural brain networks in 'unexplained dizziness in the elderly'", *Clinical Neurophysiology*, vol. 132, no. 11, pp. 2751–2762, 2021, ISSN: 1388-2457. DOI: `https://doi.org/10.1016/j.clinph.2021.07.027`. [Online]. Available: `https://www.sciencedirect.com/science/article/pii/S1388245721007069`.

[232] D. Hagemann and E. Naumann, "The effects of ocular artifacts on (lateralized) broadband power in the eeg", *Clinical Neurophysiology*, vol. 112, no. 2, pp. 215–231, 2001, ISSN: 1388-2457. DOI: `https://doi.org/10.1016/S1388-2457(00)00541-1`. [Online]. Available: `https://www.sciencedirect.com/science/article/pii/S1388245700005411`.

[233] Y.-K. Wang, T.-P. Jung, and C.-T. Lin, "Theta and alpha oscillations in attentional interaction during distracted driving", *Frontiers in Behavioral Neuroscience*, vol. 12, 2018, ISSN: 1662-5153. DOI: `10.3389/fnbeh.2018.00003`. [Online]. Available: `https://www.frontiersin.org/article/10.3389/fnbeh.2018.00003`.

[234] S. M. Peterson and D. P. Ferris, "Differentiation in theta and beta electrocortical activity between visual and physical perturbations to walking and standing balance", *eNeuro*, vol. 5, no. 4, 2018. DOI: `10.1523/ENEURO.0207-18.2018`. eprint: `https://www.eneuro.org/content/5/4/ENEURO.0207-18.2018.full.pdf`. [Online]. Available: `https://www.eneuro.org/content/5/4/ENEURO.0207-18.2018`.

[235] R. Goel, S. Nakagome, N. Rao, W. H. Paloski, J. L. Contreras-Vidal, and P. J. Parikh, "Fronto-parietal brain areas contribute to the online control of posture during a continuous balance task", *Neuroscience*, vol. 413, pp. 135–153, 2019, ISSN: 0306-4522. DOI: `https://doi.org/10.1016/j.neuroscience.2019.`

05.063. [Online]. Available: https://www.sciencedirect.com/science/article/pii/S030645221930394X.

[236] O. Bazanova and D. Vernon, "Interpreting eeg alpha activity", *Neuroscience & Biobehavioral Reviews*, vol. 44, pp. 94–110, 2014, Applied Neuroscience: Models, methods, theories, reviews. A Society of Applied Neuroscience (SAN) special issue., ISSN: 0149-7634. DOI: https://doi.org/10.1016/j.neubiorev.2013.05.007. [Online]. Available: https://www.sciencedirect.com/science/article/pii/S0149763413001279.

[237] G. Pfurtscheller and A. Aranibar, "Event-related cortical desynchronization detected by power measurements of scalp eeg", *Electroencephalography and Clinical Neurophysiology*, vol. 42, no. 6, pp. 817–826, 1977, ISSN: 0013-4694. DOI: https://doi.org/10.1016/0013-4694(77)90235-8. [Online]. Available: https://www.sciencedirect.com/science/article/pii/0013469477902358.

[238] W. J. Ray and H. W. Cole, "Eeg alpha activity reflects attentional demands, and beta activity reflects emotional and cognitive processes", *Science*, vol. 228, no. 4700, pp. 750–752, 1985. DOI: 10.1126/science.3992243. eprint: https://www.science.org/doi/pdf/10.1126/science.3992243. [Online]. Available: https://www.science.org/doi/abs/10.1126/science.3992243.

[239] J. J. Foxe, G. V. Simpson, and S. P. Ahlfors, "Parieto-occipital ∼10hz activity reflects anticipatory state of visual attention mechanisms", *NeuroReport*, vol. 9, no. 17, 1998.

[240] R. A. Andersen and C. A. Buneo, "Intentional maps in posterior parietal cortex", *Annual Review of Neuroscience*, vol. 25, no. 1, pp. 189–220, 2002.

[241] V. Wyart and C. Tallon-Baudry, "How ongoing fluctuations in human visual cortex predict perceptual awareness: Baseline shift versus decision bias", *Journal of Neuroscience*, vol. 29, no. 27, pp. 8715–8725, 2009, ISSN: 0270-6474. DOI: 10.1523/JNEUROSCI.0962-09.2009. eprint: https://www.jneurosci.org/content/29/27/8715.full.pdf. [Online]. Available: https://www.jneurosci.org/content/29/27/8715.

[242] H. van Dijk, J.-M. Schoffelen, R. Oostenveld, and O. Jensen, "Prestimulus oscillatory activity in the alpha band predicts visual discrimination ability", *Journal of Neuroscience*, vol. 28, no. 8, pp. 1816–1823, 2008, ISSN: 0270-6474. DOI: 10.1523/JNEUROSCI.1853-07.2008. eprint: https://www.jneurosci.org/content/28/8/1816.full.pdf. [Online]. Available: https://www.jneurosci.org/content/28/8/1816.

[243] T. Solis-Escalante, J. van der Cruijsen, D. de Kam, J. van Kordelaar, V. Weerdesteyn, and A. C. Schouten, "Cortical dynamics during preparation and execution of reactive balance responses with distinct postural demands", *NeuroImage*, vol. 188, pp. 557–571, 2019, ISSN: 1053-8119. DOI: https://doi.org/10.1016/j.neuroimage.2018.12.045. [Online]. Available: https://www.sciencedirect.com/science/article/pii/S105381191832189X.

[244] M. Woldorff, M. Liotti, M. Seabolt, L. Busse, J. Lancaster, and P. Fox, "The temporal dynamics of the effects in occipital cortex of visual-spatial selective attention", *Cognitive Brain Research*, vol. 15, no. 1, pp. 1–15, 2002, Neural Mechanisms of Executive Control in Cognition, ISSN: 0926-6410. DOI: https:

//doi.org/10.1016/S0926-6410(02)00212-4. [Online]. Available: `https://www.sciencedirect.com/science/article/pii/S0926641002002124`.

[245] Y. Zhang, Y. Chen, S. Bressler, and M. Ding, "Response preparation and inhibition: The role of the cortical sensorimotor beta rhythm", *Neuroscience*, vol. 156, no. 1, pp. 238–246, 2008, ISSN: 0306-4522. DOI: `https://doi.org/10.1016/j.neuroscience.2008.06.061`. [Online]. Available: `https://www.sciencedirect.com/science/article/pii/S0306452208009809`.

[246] H. Tan, C. Wade, and P. Brown, "Post-movement beta activity in sensorimotor cortex indexes confidence in the estimations from internal models", vol. 36, no. 5, pp. 1516–1528, 2016. DOI: `10.1523/JNEUROSCI.3204-15.2016`.

[247] A. Pogosyan, L. D. Gaynor, A. Eusebio, and P. Brown, "Boosting cortical activity at beta-band frequencies slows movement in humans", *Current Biology*, vol. 19, no. 19, pp. 1637–1641, 2009, ISSN: 0960-9822. DOI: `https://doi.org/10.1016/j.cub.2009.07.074`. [Online]. Available: `https://www.sciencedirect.com/science/article/pii/S0960982209016996`.

[248] M. Zaepffel, R. Trachel, B. E. Kilavik, and T. Brochier, "Modulations of eeg beta power during planning and execution of grasping movements", *PLOS ONE*, vol. 8, Mar. 2013.

[249] S. Slobounov, C. Cao, N. Jaiswal, and K. M. Newell, "Neural basis of postural instability identified by VTC and EEG", en, *Exp Brain Res*, vol. 199, no. 1, pp. 1–16, Oct. 2009, ISSN: 0014-4819, 1432-1106. DOI: `10.1007/s00221-009-1956-5`. [Online]. Available: `http://link.springer.com/10.1007/s00221-009-1956-5` (visited on 03/25/2022).

[250] A. F. Leuchter, I. A. Cook, T. F. Newton, *et al.*, "Regional differences in brain electrical activity in dementia: Use of spectral power and spectral ratio measures", *Electroencephalography and Clinical Neurophysiology*, vol. 87, no. 6, pp. 385–393, 1993, ISSN: 0013-4694. DOI: `https://doi.org/10.1016/0013-4694(93)90152-L`. [Online]. Available: `https://www.sciencedirect.com/science/article/pii/001346949390152L`.

[251] R. Govindan, A. Massaro, G. Vezina, T. Tsuchida, C. Cristante, and A. du Plessis, "Does relative or absolute eeg power have prognostic value in hie setting?", *Clinical Neurophysiology*, vol. 128, no. 1, pp. 14–15, 2017, ISSN: 1388-2457. DOI: `https://doi.org/10.1016/j.clinph.2016.10.094`. [Online]. Available: `https://www.sciencedirect.com/science/article/pii/S1388245716306411`.

[252] C. S. Sherrington, *The integrative action of the nervous system.* en. New Haven: Yale University Press, 1911. DOI: `10.1037/13798-000`. [Online]. Available: `http://content.apa.org/books/13798-000` (visited on 07/20/2022).

[253] C. Buckley, L. Alcock, R. McArdle, *et al.*, "The Role of Movement Analysis in Diagnosing and Monitoring Neurodegenerative Conditions: Insights from Gait and Postural Control", en, *Brain Sciences*, vol. 9, no. 2, p. 34, Feb. 2019, ISSN: 2076-3425. DOI: `10.3390/brainsci9020034`. [Online]. Available: `https://www.mdpi.com/2076-3425/9/2/34` (visited on 10/05/2022).

[254] A. Mirelman, I. Maidan, H. Bernad-Elazari, *et al.*, "Increased frontal brain activation during walking while dual tasking: An fNIRS study in healthy young adults", en, *Journal of NeuroEngineering and Rehabilitation*, vol. 11, no. 1, p. 85, 2014, ISSN: 1743-0003. DOI: 10.1186/1743-0003-11-85. [Online]. Available: http://jneuroengrehab.biomedcentral.com/articles/10.1186/1743-0003-11-85 (visited on 09/15/2022).

[255] W. Taube, M. Mouthon, C. Leukel, H.-M. Hoogewoud, J.-M. Annoni, and M. Keller, "Brain activity during observation and motor imagery of different balance tasks: An fMRI study", en, *Cortex*, vol. 64, pp. 102–114, Mar. 2015, ISSN: 00109452. DOI: 10.1016/j.cortex.2014.09.022. [Online]. Available: https://linkinghub.elsevier.com/retrieve/pii/S0010945214003153 (visited on 09/15/2022).

[256] K. Caeyenberghs, A. Leemans, C. De Decker, *et al.*, "Brain connectivity and postural control in young traumatic brain injury patients: A diffusion MRI based network analysis", en, *NeuroImage: Clinical*, vol. 1, no. 1, pp. 106–115, 2012, ISSN: 22131582. DOI: 10.1016/j.nicl.2012.09.011. [Online]. Available: https://linkinghub.elsevier.com/retrieve/pii/S2213158212000162 (visited on 10/04/2022).

[257] V. Shenoy Handiru, A. Alivar, A. Hoxha, *et al.*, "Graph-theoretical analysis of EEG functional connectivity during balance perturbation in traumatic brain injury: A pilot study", en, *Human Brain Mapping*, vol. 42, no. 14, pp. 4427–4447, Oct. 2021, ISSN: 1065-9471, 1097-0193. DOI: 10.1002/hbm.25554. [Online]. Available: https://onlinelibrary.wiley.com/doi/10.1002/hbm.25554 (visited on 10/04/2022).

[258] C. E. Little and M. Woollacott, "EEG measures reveal dual-task interference in postural performance in young adults", en, *Experimental Brain Research*, vol. 233, no. 1, pp. 27–37, Jan. 2015, ISSN: 0014-4819, 1432-1106. DOI: 10.1007/s00221-014-4111-x. [Online]. Available: http://link.springer.com/10.1007/s00221-014-4111-x (visited on 10/04/2022).

[259] F. Barollo, M. Hassan, H. Petersen, *et al.*, "Cortical Pathways During Postural Control: New Insights From Functional EEG Source Connectivity", *IEEE Transactions on Neural Systems and Rehabilitation Engineering*, vol. 30, pp. 72–84, 2022, ISSN: 1534-4320, 1558-0210. DOI: 10.1109/TNSRE.2022.3140888. [Online]. Available: https://ieeexplore.ieee.org/document/9672093/ (visited on 07/20/2022).

[260] D. Lehmann, W. Strik, B. Henggeler, T. Koenig, and M. Koukkou, "Brain electric microstates and momentary conscious mind states as building blocks of spontaneous thinking: I. Visual imagery and abstract thoughts", en, *International Journal of Psychophysiology*, vol. 29, no. 1, pp. 1–11, Jun. 1998, Number: 1, ISSN: 01678760. DOI: 10.1016/S0167-8760(97)00098-6. [Online]. Available: https://linkinghub.elsevier.com/retrieve/pii/S0167876097000986 (visited on 07/20/2022).

[261] A. Khanna, A. Pascual-Leone, C. M. Michel, and F. Farzan, "Microstates in resting-state EEG: Current status and future directions", en, *Neuroscience & Biobehavioral Reviews*, vol. 49, pp. 105–113, Feb. 2015, ISSN: 01497634. DOI: 10.1016/j.neubiorev.2014.12.010. [Online]. Available: https://linkinghub.elsevier.com/retrieve/pii/S0149763414003492 (visited on 07/22/2022).

[262] C. M. Michel and T. Koenig, "EEG microstates as a tool for studying the temporal dynamics of whole-brain neuronal networks: A review", en, *NeuroImage*, vol. 180, pp. 577–593, Oct. 2018, ISSN: 10538119. DOI: `10.1016/j.neuroimage.2017.11.062`. [Online]. Available: `https://linkinghub.elsevier.com/retrieve/pii/S105381191731008X` (visited on 10/04/2022).

[263] A. T. Poulsen, A. Pedroni, N. Langer, and L. K. Hansen, "Microstate EEGlab toolbox: An introductory guide", en, Neuroscience, preprint, Mar. 2018. DOI: `10.1101/289850`. [Online]. Available: `http://biorxiv.org/lookup/doi/10.1101/289850` (visited on 07/20/2022).

[264] J. Britz, D. Van De Ville, and C. M. Michel, "BOLD correlates of EEG topography reveal rapid resting-state network dynamics", en, *NeuroImage*, vol. 52, no. 4, pp. 1162–1170, Oct. 2010, ISSN: 10538119. DOI: `10.1016/j.neuroimage.2010.02.052`. [Online]. Available: `https://linkinghub.elsevier.com/retrieve/pii/S105381191000220X` (visited on 07/22/2022).

[265] H. Yuan, V. Zotev, R. Phillips, W. C. Drevets, and J. Bodurka, "Spatiotemporal dynamics of the brain at rest — Exploring EEG microstates as electrophysiological signatures of BOLD resting state networks", en, *NeuroImage*, vol. 60, no. 4, pp. 2062–2072, May 2012, ISSN: 10538119. DOI: `10.1016/j.neuroimage.2012.02.031`. [Online]. Available: `https://linkinghub.elsevier.com/retrieve/pii/S105381191200208X` (visited on 07/22/2022).

[266] J. Duprez, J. Tabbal, M. Hassan, *et al.*, "Spatio-temporal dynamics of large-scale electrophysiological networks during cognitive action control in healthy controls and Parkinson's disease patients", en, *NeuroImage*, vol. 258, p. 119 331, Sep. 2022, ISSN: 10538119. DOI: `10.1016/j.neuroimage.2022.119331`. [Online]. Available: `https://linkinghub.elsevier.com/retrieve/pii/S1053811922004505` (visited on 09/16/2022).

[267] A. Kabbara, W. EL Falou, M. Khalil, F. Wendling, and M. Hassan, "The dynamic functional core network of the human brain at rest", en, *Scientific Reports*, vol. 7, no. 1, p. 2936, Dec. 2017, Number: 1, ISSN: 2045-2322. DOI: `10.1038/s41598-017-03420-6`. [Online]. Available: `http://www.nature.com/articles/s41598-017-03420-6` (visited on 07/20/2022).

[268] J.-P. Lachaux, E. Rodriguez, M. Le Van Quyen, A. Lutz, J. Martinerie, and F. J. Varela, "STUDYING SINGLE-TRIALS OF PHASE SYNCHRONOUS ACTIVITY IN THE BRAIN", en, *International Journal of Bifurcation and Chaos*, vol. 10, no. 10, pp. 2429–2439, Oct. 2000, ISSN: 0218-1274, 1793-6551. DOI: `10.1142/S0218127400001560`. [Online]. Available: `https://www.worldscientific.com/doi/abs/10.1142/S0218127400001560` (visited on 07/21/2022).

[269] R. Pascual-Marqui, C. Michel, and D. Lehmann, "Segmentation of brain electrical activity into microstates: Model estimation and validation", en, *IEEE Transactions on Biomedical Engineering*, vol. 42, no. 7, pp. 658–665, Jul. 1995, ISSN: 0018-9294, 1558-2531. DOI: `10.1109/10.391164`. [Online]. Available: `https://ieeexplore.ieee.org/document/391164/` (visited on 07/21/2022).

[270] M. Xia, J. Wang, and Y. He, "BrainNet Viewer: A Network Visualization Tool for Human Brain Connectomics", en, *PLoS ONE*, vol. 8, no. 7, P. Csermely, Ed., e68910, Jul. 2013, ISSN: 1932-6203. DOI: `10.1371/journal.pone.0068910`.

[Online]. Available: `https://dx.plos.org/10.1371/journal.pone.0068910` (visited on 07/22/2022).

[271] J. R. Andrews-Hanna, J. S. Reidler, J. Sepulcre, R. Poulin, and R. L. Buckner, "Functional-Anatomic Fractionation of the Brain's Default Network", en, *Neuron*, vol. 65, no. 4, pp. 550–562, Feb. 2010, ISSN: 08966273. DOI: `10.1016/j.neuron.2010.02.005`. [Online]. Available: `https://linkinghub.elsevier.com/retrieve/pii/S0896627310000966` (visited on 07/21/2022).

[272] M. E. Raichle, "The Brain's Default Mode Network", en, *Annual Review of Neuroscience*, vol. 38, no. 1, pp. 433–447, Jul. 2015, ISSN: 0147-006X, 1545-4126. DOI: `10.1146/annurev-neuro-071013-014030`. [Online]. Available: `https://www.annualreviews.org/doi/10.1146/annurev-neuro-071013-014030` (visited on 07/21/2022).

[273] M. F. Mason, M. I. Norton, J. D. Van Horn, D. M. Wegner, S. T. Grafton, and C. N. Macrae, "Wandering Minds: The Default Network and Stimulus-Independent Thought", en, *Science*, vol. 315, no. 5810, pp. 393–395, Jan. 2007, ISSN: 0036-8075, 1095-9203. DOI: `10.1126/science.1131295`. [Online]. Available: `https://www.science.org/doi/10.1126/science.1131295` (visited on 07/25/2022).

[274] J.-D. Haynes and G. Rees, "Predicting the Stream of Consciousness from Activity in Human Visual Cortex", en, *Current Biology*, vol. 15, no. 14, pp. 1301–1307, Jul. 2005, ISSN: 09609822. DOI: `10.1016/j.cub.2005.06.026`. [Online]. Available: `https://linkinghub.elsevier.com/retrieve/pii/S0960982205006615` (visited on 07/21/2022).

[275] Y. Kamitani and F. Tong, "Decoding the visual and subjective contents of the human brain", en, *Nature Neuroscience*, vol. 8, no. 5, pp. 679–685, May 2005, ISSN: 1097-6256, 1546-1726. DOI: `10.1038/nn1444`. [Online]. Available: `http://www.nature.com/articles/nn1444` (visited on 07/21/2022).

[276] V. Menon, "Salience Network", en, in *Brain Mapping*, Elsevier, 2015, pp. 597–611, ISBN: 978-0-12-397316-0. DOI: `10.1016/B978-0-12-397025-1.00052-X`. [Online]. Available: `https://linkinghub.elsevier.com/retrieve/pii/B978012397025100052X` (visited on 07/21/2022).

[277] L. Q. Uddin, "Salience processing and insular cortical function and dysfunction", en, *Nature Reviews Neuroscience*, vol. 16, no. 1, pp. 55–61, Jan. 2015, ISSN: 1471-003X, 1471-0048. DOI: `10.1038/nrn3857`. [Online]. Available: `http://www.nature.com/articles/nrn3857` (visited on 07/21/2022).

[278] S. Bray, A. E. Arnold, R. M. Levy, and G. Iaria, "Spatial and temporal functional connectivity changes between resting and attentive states: Connectivity Changes Between Rest and Attention", en, *Human Brain Mapping*, vol. 36, no. 2, pp. 549–565, Feb. 2015, ISSN: 10659471. DOI: `10.1002/hbm.22646`. [Online]. Available: `https://onlinelibrary.wiley.com/doi/10.1002/hbm.22646` (visited on 07/22/2022).

[279] S. M. Szczepanski, M. A. Pinsk, M. M. Douglas, S. Kastner, and Y. B. Saalmann, "Functional and structural architecture of the human dorsal frontoparietal attention network", en, *Proceedings of the National Academy of Sciences*, vol. 110, no. 39, pp. 15 806–15 811, Sep. 2013, ISSN: 0027-8424, 1091-6490. DOI:

10.1073/pnas.1313903110. [Online]. Available: https://pnas.org/doi/full/10.1073/pnas.1313903110 (visited on 07/22/2022).

[280] A. R. Laird, P. M. Fox, S. B. Eickhoff, *et al.*, "Behavioral Interpretations of Intrinsic Connectivity Networks", en, *Journal of Cognitive Neuroscience*, vol. 23, no. 12, pp. 4022–4037, Dec. 2011, ISSN: 0898-929X, 1530-8898. DOI: 10.1162/jocn_a_00077. [Online]. Available: https://direct.mit.edu/jocn/article/23/12/4022/5274/Behavioral-Interpretations-of-Intrinsic (visited on 07/21/2022).

[281] R. Seidler, B. Erdeniz, V. Koppelmans, S. Hirsiger, S. Merillat, and L. Jäncke, "Associations between age, motor function, and resting state sensorimotor network connectivity in healthy older adults", en, *NeuroImage*, vol. 108, pp. 47–59, Mar. 2015, ISSN: 10538119. DOI: 10.1016/j.neuroimage.2014.12.023. [Online]. Available: https://linkinghub.elsevier.com/retrieve/pii/S1053811914010155 (visited on 07/21/2022).

[282] R. Sutter, R. D. Stevens, and P. W. Kaplan, "Continuous electroencephalographic monitoring in critically ill patients: Indications, limitations, and strategies*", *Critical Care Medicine*, vol. 41, no. 4, 2013, ISSN: 0090-3493. [Online]. Available: https://journals.lww.com/ccmjournal/Fulltext/2013/04000/Continuous_Electroencephalographic_Monitoring_in.20.aspx.

[283] V. Alvarez and A. O. Rossetti, "Clinical use of eeg in the icu: Technical setting", *Journal of Clinical Neurophysiology*, vol. 32, no. 6, 2015, ISSN: 0736-0258. [Online]. Available: https://journals.lww.com/clinicalneurophys/Fulltext/2015/12000/Clinical_Use_of_EEG_in_the_ICU__Technical_Setting.8.aspx.

[284] L. M. Moura, M. M. Shafi, M. Ng, *et al.*, "Spectrogram screening of adult eegs is sensitive and efficient", *Neurology*, vol. 83, no. 1, pp. 56–64, 2014, ISSN: 0028-3878. DOI: 10.1212/WNL.0000000000000537. eprint: https://n.neurology.org/content/83/1/56.full.pdf. [Online]. Available: https://n.neurology.org/content/83/1/56.

[285] T. Koenig, U. Smailovic, and V. Jelic, "Past, present and future eeg in the clinical workup of dementias", *Psychiatry Research: Neuroimaging*, vol. 306, p. 111182, 2020, SI: Imaging in neurodegeneration, ISSN: 0925-4927. DOI: https://doi.org/10.1016/j.pscychresns.2020.111182. [Online]. Available: https://www.sciencedirect.com/science/article/pii/S0925492720301542.

[286] V. J. Geraedts, L. I. Boon, J. Marinus, *et al.*, "Clinical correlates of quantitative eeg in parkinson disease", *Neurology*, vol. 91, no. 19, pp. 871–883, 2018, ISSN: 0028-3878. DOI: 10.1212/WNL.0000000000006473. eprint: https://n.neurology.org/content/91/19/871.full.pdf. [Online]. Available: https://n.neurology.org/content/91/19/871.

[287] L. E. Ethridge, L. A. De Stefano, L. M. Schmitt, *et al.*, "Auditory eeg biomarkers in fragile x syndrome: Clinical relevance", *Frontiers in Integrative Neuroscience*, vol. 13, 2019, ISSN: 1662-5145. DOI: 10.3389/fnint.2019.00060. [Online]. Available: https://www.frontiersin.org/articles/10.3389/fnint.2019.00060.

[288] E. Y. Kimchi, A. Neelagiri, W. Whitt, *et al.*, "Clinical eeg slowing correlates with delirium severity and predicts poor clinical outcomes", *Neurology*, vol. 93, no. 13, e1260–e1271, 2019, ISSN: 0028-3878. DOI: `10.1212/WNL.0000000000008164`. eprint: `https://n.neurology.org/content/93/13/e1260.full.pdf`. [Online]. Available: `https://n.neurology.org/content/93/13/e1260`.

[289] F. K. Ciliberti, L. Guerrini, A. E. Gunnarsson, *et al.*, "Ct- and mri-based 3d reconstruction of knee joint to assess cartilage and bone", *Diagnostics*, vol. 12, no. 2, 2022, ISSN: 2075-4418. DOI: `10.3390/diagnostics12020279`. [Online]. Available: `https://www.mdpi.com/2075-4418/12/2/279`.

[290] Y. Zhang and J. M. Jordan, "Epidemiology of Osteoarthritis", en, *Clin. Geriatr. Med.*, vol. 26, no. 3, pp. 355–369, 2010, ISSN: 07490690. DOI: `10.1016/j.cger.2010.03.001`. [Online]. Available: `https://linkinghub.elsevier.com/retrieve/pii/S0749069010000261` (visited on 09/21/2021).

[291] R. Przkora, K. Sibille, S. Victor, *et al.*, "Assessing the feasibility of using the short physical performance battery to measure function in the immediate postoperative period after total knee replacement", *Eur. J. Transl. Myol*, vol. 31, no. 2, Apr. 2021. DOI: `10.4081/ejtm.2021.9673`. [Online]. Available: `https://www.pagepressjournals.org/index.php/bam/article/view/9673`.

[292] M. Cross, E. Smith, D. Hoy, *et al.*, "The global burden of hip and knee osteoarthritis: Estimates from the Global Burden of Disease 2010 study", en, *Ann Rheum Dis*, vol. 73, no. 7, pp. 1323–1330, 2014, ISSN: 0003-4967, 1468-2060. DOI: `10.1136/annrheumdis-2013-204763`. [Online]. Available: `https://ard.bmj.com/lookup/doi/10.1136/annrheumdis-2013-204763` (visited on 09/17/2021).

[293] L. Murphy, T. A. Schwartz, C. G. Helmick, *et al.*, "Lifetime risk of symptomatic knee osteoarthritis", en, *Arthritis Rheum*, vol. 59, no. 9, pp. 1207–1213, 2008, ISSN: 00043591, 15290131. DOI: `10.1002/art.24021`. [Online]. Available: `https://onlinelibrary.wiley.com/doi/10.1002/art.24021` (visited on 09/19/2021).

[294] T. Neogi, "The epidemiology and impact of pain in osteoarthritis", en, *Osteoarthr. Cartil.*, vol. 21, no. 9, pp. 1145–1153, 2013, ISSN: 10634584. DOI: `10.1016/j.joca.2013.03.018`. [Online]. Available: `https://linkinghub.elsevier.com/retrieve/pii/S1063458413007607` (visited on 09/19/2021).

[295] L. Marcucci and C. Reggiani, "Increase of resting muscle stiffness, a less considered component of age-related skeletal muscle impairment", *Eur. J. Transl. Myol*, vol. 30, p. 8982, Jun. 2020. DOI: `10.4081/ejtm.2019.8982`.

[296] F. W. Roemer, S. Demehri, P. Omoumi, *et al.*, "State of the Art: Imaging of Osteoarthritis—Revisited 2020", en, *Radiology*, vol. 296, no. 1, pp. 5–21, 2020, ISSN: 0033-8419, 1527-1315. DOI: `10.1148/radiol.2020192498`. [Online]. Available: `http://pubs.rsna.org/doi/10.1148/radiol.2020192498` (visited on 09/19/2021).

[297] M. D. Crema, F. W. Roemer, M. D. Marra, *et al.*, "Articular Cartilage in the Knee: Current MR Imaging Techniques and Applications in Clinical Practice and Research", en, *Radiographics*, vol. 31, no. 1, pp. 37–61, Jan. 2011, ISSN: 0271-5333, 1527-1323. DOI: `10.1148/rg.311105084`. [Online]. Available: `http://pubs.rsna.org/doi/10.1148/rg.311105084` (visited on 07/05/2021).

[298] R. J. Schmitz, H.-M. Wang, D. R. Polprasert, R. A. Kraft, and B. G. Pietrosimone, "Evaluation of knee cartilage thickness: A comparison between ultrasound and magnetic resonance imaging methods", en, *Knee*, vol. 24, no. 2, pp. 217–223, 2017, ISSN: 09680160. DOI: `10.1016/j.knee.2016.10.004`. [Online]. Available: `https://linkinghub.elsevier.com/retrieve/pii/S0968016016301703` (visited on 09/16/2021).

[299] A. F. M. Hani, D. Kumar, A. S. Malik, R. Razak, and A. Kiflie, "Fusion of multinuclear magnetic resonance images of knee for the assessment of articular cartilage", en, in *2013 35th Annual International Conference of the IEEE Engineering in Medicine and Biology Society (EMBC)*, Osaka: IEEE, Jul. 2013, pp. 6466–6469, ISBN: 978-1-4577-0216-7. DOI: `10.1109/EMBC.2013.6611035`. [Online]. Available: `http://ieeexplore.ieee.org/document/6611035/` (visited on 09/16/2021).

[300] T. M. Link, J. Neumann, and X. Li, "Prestructural cartilage assessment using MRI: Prestructural Cartilage Assessment Using MRI", en, *J. Magn. Reson. Imaging*, vol. 45, no. 4, pp. 949–965, Apr. 2017, ISSN: 10531807. DOI: `10.1002/jmri.25554`. [Online]. Available: `https://onlinelibrary.wiley.com/doi/10.1002/jmri.25554` (visited on 09/16/2021).

[301] D. Ø. Pradsgaard, B. Fiirgaard, A. H. Spannow, C. Heuck, and T. Herlin, "Cartilage Thickness of the Knee Joint in Juvenile Idiopathic Arthritis: Comparative Assessment by Ultrasonography and Magnetic Resonance Imaging", en, *J Rheumatol*, vol. 42, no. 3, pp. 534–540, 2015, ISSN: 0315-162X, 1499-2752. DOI: `10.3899/jrheum.140162`. [Online]. Available: `http://www.jrheum.org/lookup/doi/10.3899/jrheum.140162` (visited on 09/16/2021).

[302] A. Campbell, C. Quatman, L. Schmitt, M. Knopp, and D. Flanigan, "Is Magnetic Resonance Imaging Assessment of the Size of Articular Cartilage Defects Accurate?", en, *J Knee Surg*, vol. 27, no. 01, pp. 067–076, Jul. 2013, ISSN: 1538-8506, 1938-2480. DOI: `10.1055/s-0033-1348404`. [Online]. Available: `http://www.thieme-connect.de/DOI/DOI?10.1055/s-0033-1348404` (visited on 09/16/2021).

[303] T. Petursson, B. Magnusson, B. Helgason, *et al.*, "Bone and muscle assessment in patients undergoing total hip arthroplasty using hu based analysis", *Eur. J. Transl. Myol*, vol. 22, no. 3, pp. 147–152, Sep. 2012. DOI: `10.4081/ejtm.2012.1797`. [Online]. Available: `https://www.pagepressjournals.org/index.php/bam/article/view/bam.2012.3.147`.

[304] L. Esposito, P. Bifulco, P. Gargiulo, *et al.*, "Towards a patient-specific estimation of intra-operative femoral fracture risk.", *Comput Methods Biomech Biomed Engin*, 2018, Total Hip Arthroplasty requires pre-surgical evaluation between un-cemented and cemented prostheses. A Patient with intra-operative periprosthetic fracture and another with a successful outcome were recruited, and their finite element models were constructed by processing CT data, assuming elastic-plastic behavior of the bone as function of the local density. To resemble the insertion of the prosthesis into the femur, a fictitious thermal dilatation is applied to the broach volume. Strain-based fracture risk factor is estimated, depicting results in terms of the total mechanical strain expressed using a simple "traffic lights" color code to provide immediate, concise, and intelligible pre-operative

information to surgeons., ISSN: 1476-8259. DOI: 10.1080/10255842.2018.1508570. [Online]. Available: http://hdl.handle.net/2336/620845.

[305] P. Gargiulo, M. K. Gislason, K. J. Edmunds, *et al.*, "Ct-based bone and muscle assessment in normal and pathological conditions", in *Encyclopedia of Biomedical Engineering*, R. Narayan, Ed., Oxford: Elsevier, 2019, pp. 119–134, ISBN: 978-0-12-805144-3. DOI: https://doi.org/10.1016/B978-0-12-801238-3.99920-3. [Online]. Available: https://www.sciencedirect.com/science/article/pii/B9780128012383999203.

[306] J. Johnston, B. Masri, and D. Wilson, "Computed tomography topographic mapping of subchondral density (CT-TOMASD) in osteoarthritic and normal knees: Methodological development and preliminary findings", en, *Osteoarthr. Cartil.*, vol. 17, no. 10, pp. 1319–1326, 2009, ISSN: 10634584. DOI: 10.1016/j.joca.2009.04.013. [Online]. Available: https://linkinghub.elsevier.com/retrieve/pii/S1063458409001113 (visited on 09/21/2021).

[307] J. H. Kellgren and J. S. Lawrence, "Radiological assessment of Osteo-Arthrosis", en, *Ann. Rheum. Dis.*, p. 9,

[308] S. Ahlbäck, "Osteoarthrosis of the knee. A radiographic investigation.", *Acta Radiol Diagn (Stockh)*, vol. 277, pp. 7–72,

[309] M. Galli, V. De Santis, and L. Tafuro, "Reliability of the Ahlbäck classification of knee osteoarthritis", en, *Osteoarthrit. Cartil.*, vol. 11, no. 8, pp. 580–584, 2003, ISSN: 10634584. DOI: 10.1016/S1063-4584(03)00095-5. [Online]. Available: https://linkinghub.elsevier.com/retrieve/pii/S1063458403000955 (visited on 09/21/2021).

[310] R. W. Wright and The MARS Group, "Osteoarthritis Classification Scales: Interobserver Reliability and Arthroscopic Correlation", en, *J. Bone Jt. Surg.*, vol. 96, no. 14, pp. 1145–1151, 2014, ISSN: 0021-9355, 1535-1386. DOI: 10.2106/JBJS.M.00929. [Online]. Available: https://journals.lww.com/00004623-201407160-00001 (visited on 09/17/2021).

[311] O. J. F. Keenan, G. Holland, J. F. Maempel, J. F. Keating, and C. E. H. Scott, "Correlations between radiological classification systems and confirmed cartilage loss in severe knee osteoarthritis", en, *Bone Joint J*, vol. 102, no. 3, p. 9, 2020.

[312] F. Eckstein, M. P. H. Le Graverand, H. C. Charles, *et al.*, "Clinical, radiographic, molecular and MRI-based predictors of cartilage loss in knee osteoarthritis", *Ann Rheum Dis*, vol. 70, no. 7, p. 1223, 2011. DOI: 10.1136/ard.2010.141382. [Online]. Available: http://ard.bmj.com/content/70/7/1223.abstract.

[313] J. W. MacKay, J. D. Kaggie, G. M. Treece, *et al.*, "Three-dimensional surface-based analysis of cartilage mri data in knee osteoarthritis: Validation and initial clinical application", *J. Magn. Reson.*, vol. 52, no. 4, pp. 1139–1151, 2020.

[314] S. Papernick, R. Dima, D. Gillies, C. Appleton, and A. Fenster, "Reliability and concurrent validity of three-dimensional ultrasound for quantifying knee cartilage volume", *Osteoarthr. Cartil.*, vol. 2, no. 4, p. 100 127, 2020.

[315] R. Kijowski, F. Roemer, M. Englund, C. Tiderius, P. Swärd, and R. Frobell, "Imaging following acute knee trauma", en, *Osteoarthr. Cartil.*, vol. 22, no. 10, pp. 1429–1443, 2014, ISSN: 10634584. DOI: 10.1016/j.joca.2014.06.024. [Online]. Available: `https://linkinghub.elsevier.com/retrieve/pii/S1063458414011443` (visited on 10/25/2021).

[316] F. W. Roemer, R. Frobell, L. S. Lohmander, J. Niu, and A. Guermazi, "Anterior Cruciate Ligament OsteoArthritis Score (ACLOAS): Longitudinal MRI-based whole joint assessment of anterior cruciate ligament injury", en, *Osteoarthr. Cartil.*, vol. 22, no. 5, pp. 668–682, 2014, ISSN: 10634584. DOI: 10.1016/j.joca.2014.03.006. [Online]. Available: `https://linkinghub.elsevier.com/retrieve/pii/S1063458414009984` (visited on 10/26/2021).

[317] Y. Du, R. Almajalid, J. Shan, and M. Zhang, "A novel method to predict knee osteoarthritis progression on mri using machine learning methods", *IEEE Trans Nanobioscience*, vol. 17, no. 3, pp. 228–236, 2018.

[318] A. Tiulpin, S. Klein, S. M. Bierma-Zeinstra, *et al.*, "Multimodal machine learning-based knee osteoarthritis progression prediction from plain radiographs and clinical data", *Sci. Rep.*, vol. 9, no. 1, pp. 1–11, 2019.

[319] F. Liu, Z. Zhou, A. Samsonov, *et al.*, "Deep learning approach for evaluating knee mr images: Achieving high diagnostic performance for cartilage lesion detection", *Radiology*, vol. 289, no. 1, pp. 160–169, 2018.

[320] N. Bien, P. Rajpurkar, R. L. Ball, *et al.*, "Deep-learning-assisted diagnosis for knee magnetic resonance imaging: Development and retrospective validation of mrnet", *PLoS Med.*, vol. 15, no. 11, e1002699, 2018.

[321] A. Tiulpin, J. Thevenot, E. Rahtu, P. Lehenkari, and S. Saarakkala, "Automatic knee osteoarthritis diagnosis from plain radiographs: A deep learning-based approach", *Sci. Rep.*, vol. 8, no. 1, pp. 1–10, 2018.

[322] A. A. Tolpadi, J. J. Lee, V. Pedoia, and S. Majumdar, "Deep learning predicts total knee replacement from magnetic resonance images", *Sci. Rep.*, vol. 10, no. 1, pp. 1–12, 2020.

[323] S. B. Kwon, H.-S. Han, M. C. Lee, H. C. Kim, Y. Ku, *et al.*, "Machine learning-based automatic classification of knee osteoarthritis severity using gait data and radiographic images", *IEEE Access*, vol. 8, pp. 120 597–120 603, 2020.

[324] Y. F. Ramos, S. D. Bos, N. Lakenberg, *et al.*, "Genes expressed in blood link osteoarthritis with apoptotic pathways", *Ann. Rheum. Dis.*, vol. 73, no. 10, pp. 1844–1853, 2014.

[325] J. Li, C.-N. Lan, Y. Kong, S.-S. Feng, and T. Huang, "Identification and analysis of blood gene expression signature for osteoarthritis with advanced feature selection methods", *Front. Genet.*, vol. 9, p. 246, 2018.

[326] T. D. DenOtter and J. Schubert, *Hounsfield Unit*. StatPearls Publishing, Treasure Island (FL), 2020. [Online]. Available: `http://europepmc.org/books/NBK547721`.

[327] QRM, Micro-CT HA Phantom for the calibration of CT-values, `https://www.qrm.de/en/products/micro-ct-ha-phantom/` [Accessed: 02/23/2021].

[328] M. R. Berthold, N. Cebron, F. Dill, *et al.*, "Knime-the konstanz information miner: Version 2.0 and beyond", *SIGKDD Explor*, vol. 11, no. 1, pp. 26–31, 2009.

[329] M. Recenti, C. Ricciardi, K. J. Edmunds, *et al.*, "Healthy aging within an image: Using muscle radiodensitometry and lifestyle factors to predict diabetes and hypertension", *IEEE J Biomed Health Inform*, vol. 25, no. 6, pp. 2103–2112, 2020.

[330] M. Recenti, C. Ricciardi, R. Aubonnet, *et al.*, "Toward predicting motion sickness using virtual reality and a moving platform assessing brain, muscles, and heart signals", *Front. Bioeng. Biotechnol.*, vol. 9, p. 132, 2021.

[331] T. K. Ho, "Random decision forests", in *Proceedings of 3rd international conference on document analysis and recognition*, IEEE, vol. 1, 1995, pp. 278–282.

[332] J. H. Friedman, "Greedy function approximation: A gradient boosting machine", *Ann Stat*, pp. 1189–1232, 2001.

[333] C. Ricciardi, H. Jónsson, D. Jacob, *et al.*, "Improving prosthetic selection and predicting bmd from biometric measurements in patients receiving total hip arthroplasty", *Diagnostics*, vol. 10, no. 10, p. 815, 2020.

[334] M. Recenti, C. Ricciardi, M. Gislason, K. Edmunds, U. Carraro, and P. Gargiulo, "Machine learning algorithms predict body mass index using nonlinear trimodal regression analysis from computed tomography scans", in *Mediterranean Conference on Medical and Biological Engineering and Computing*, Springer, 2019, pp. 839–846.

[335] S. Saeb, L. Lonini, A. Jayaraman, D. C. Mohr, and K. P. Kording, "The need to approximate the use-case in clinical machine learning", *Gigascience*, vol. 6, no. 5, gix019, 2017.

[336] J. A. Buckwalter and H. J. Mankin, "Articular cartilage: Part ii", *Journal of Bone and Joint Surgery*, vol. 79, no. 4, p. 612, Apr. 1997.

[337] A. J. Teichtahl, Y. Wang, A. E. Wluka, *et al.*, "Associations between systemic bone mineral density and early knee cartilage changes in middle-aged adults without clinical knee disease: A prospective cohort study", en, *Arthritis Res Ther*, vol. 19, no. 1, p. 98, 2017, ISSN: 1478-6362. DOI: 10.1186/s13075-017-1314-0. [Online]. Available: http://arthritis-research.biomedcentral.com/articles/10.1186/s13075-017-1314-0 (visited on 11/17/2021).

[338] Y. Zhang, M. Hannan, C. Chaisson, *et al.*, "Bone mineral density and risk of incident and progressive radiographic knee osteoarthritis in women: The framingham study.", *J. Rheumatol.*, vol. 27, no. 4, pp. 1032–1037, 2000.

[339] M. C. Nevitt, Y. Zhang, M. K. Javaid, *et al.*, "High systemic bone mineral density increases the risk of incident knee oa and joint space narrowing, but not radiographic progression of existing knee oa: The most study", *Ann. Rheum. Dis.*, vol. 69, no. 01, pp. 163–168, 2010.

[340] E.-S. Choi, H. D. Shin, J. A. Sim, *et al.*, "Relationship of bone mineral density and knee osteoarthritis (kellgren-lawrence grade): Fifth korea national health and nutrition examination survey", *Clin Orthop Surg*, vol. 13, no. 1, p. 60, 2021.

[341]   B. Vollnberg, T. Koehlitz, T. Jung, *et al.*, "Prevalence of cartilage lesions and early osteoarthritis in patients with patellar dislocation", en, *Eur Radiol*, vol. 22, no. 11, pp. 2347–2356, 2012, ISSN: 0938-7994, 1432-1084. DOI: `10.1007/s00330-012-2493-3`. [Online]. Available: `http://link.springer.com/10.1007/s00330-012-2493-3` (visited on 11/18/2021).

[342]   S. J. Matzat, F. Kogan, G. W. Fong, and G. E. Gold, "Imaging strategies for assessing cartilage composition in osteoarthritis", *Curr Rheumatol Rep*, vol. 16, no. 11, p. 462, 2014.

[343]   M. Nickien, A. Thambyah, and N. D. Broom, "How a decreased fibrillar interconnectivity influences stiffness and swelling properties during early cartilage degeneration", *J Mech Behav Biomed Mater*, vol. 75, pp. 390–398, 2017, ISSN: 1751-6161. DOI: `https://doi.org/10.1016/j.jmbbm.2017.07.042`. [Online]. Available: `https://www.sciencedirect.com/science/article/pii/S1751616117303259`.

[344]   P. J. Watson, T. A. Carpenter, L. D. Hall, and J. A. Tyler, "Cartilage swelling and loss in a spontaneous model of osteoarthritis visualized by magnetic resonance imaging", *Osteoarthr. Cartil.*, vol. 4, no. 3, pp. 197–207, 1996, ISSN: 1063-4584. DOI: `https://doi.org/10.1016/S1063-4584(96)80016-1`. [Online]. Available: `https://www.sciencedirect.com/science/article/pii/S1063458496800161`.

[345]   F. W. Roemer, S. Demehri, P. Omoumi, *et al.*, "State of the art: Imaging of osteoarthritis—revisited 2020", *Radiology*, vol. 296, no. 1, pp. 5–21, 2020.

[346]   T. L. Vincent and A. K. Wann, "Mechanoadaptation: Articular cartilage through thick and thin", *J Physiol*, vol. 597(5), pp. 1271–1281, Mar. 2019.

[347]   J. Folkesson, E. B. Dam, O. F. Olsen, M. A. Karsdal, P. C. Pettersen, and C. Christiansen, "Automatic quantification of local and global articular cartilage surface curvature: Biomarkers for osteoarthritis?", *Magn Reson Med Sci*, vol. 59, pp. 1340–1346, May 2008.

[348]   N. V. Chawla, K. W. Bowyer, L. O. Hall, and W. P. Kegelmeyer, "Smote: Synthetic minority over-sampling technique", *J Artif Intell Res*, vol. 16, pp. 321–357, 2002.

[349]   R. Aubonnet, J. Ramos, M. Recenti, *et al.*, "Toward new assessment of knee cartilage degeneration", *CARTILAGE*, vol. 0, no. 0, p. 19476035221144746, 0, PMID: 36541701. DOI: `10.1177/19476035221144746`. eprint: `https://doi.org/10.1177/19476035221144746`. [Online]. Available: `https://doi.org/10.1177/19476035221144746`.

[350]   S. Koo, G. Gold, and T. Andriacchi, "Considerations in measuring cartilage thickness using mri: Factors influencing reproducibility and accuracy", *Osteoarthritis and cartilage*, vol. 13, no. 9, pp. 782–789, 2005.

[351]   P. Walker and J. Hajek, "The load-bearing area in the knee joint", *Journal of biomechanics*, vol. 5, no. 6, pp. 581–589, 1972.

[352]   J. F. Baker, J. Von Feldt, S. Mostoufi-Moab, *et al.*, "Deficits in muscle mass, muscle density, and modified associations with fat in rheumatoid arthritis", *Arthritis care & research*, vol. 66, no. 11, pp. 1612–1618, 2014.

[353] M. M. Rahman, L. Duerselen, and A. M. Seitz, "Automatic segmentation of knee menisci–a systematic review", *Artificial Intelligence in Medicine*, vol. 105, p. 101 849, 2020.

[354] G. Cai, P. Otahal, F. Cicuttini, *et al.*, "The association of subchondral and systemic bone mineral density with osteoarthritis-related joint replacements in older adults", *Osteoarthritis and Cartilage*, vol. 28, no. 4, pp. 438–445, 2020.

[355] H. Bonakdari, J.-P. Pelletier, F. Abram, and J. Martel-Pelletier, "A machine learning model to predict knee osteoarthritis cartilage volume changes over time using baseline bone curvature", *Biomedicines*, vol. 10, no. 6, p. 1247, 2022.

Appendix A

Supplementary material

A.1 Schizophrenia
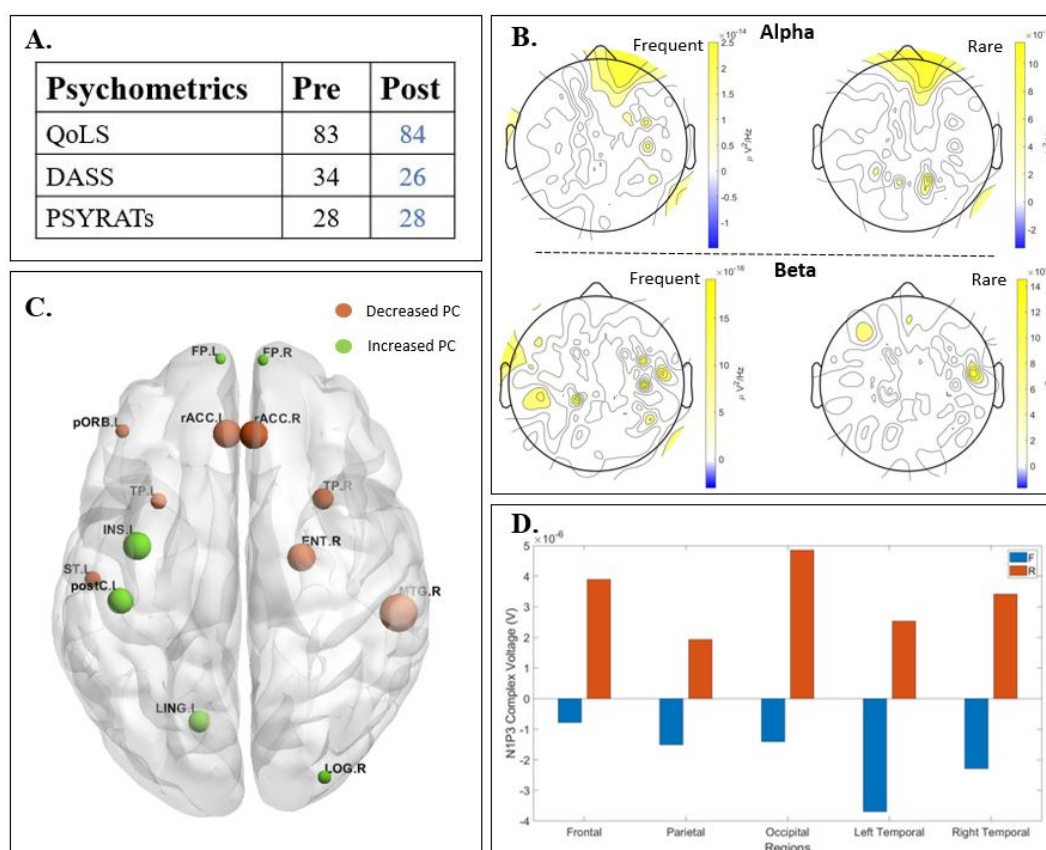
Figure A.1: Results of patient C1 : A. psychometric; B. Scalp-level frequency analysis; C. Source-space connectivity; D. Scalp-level time analysis. The yellow areas in frequency analysis are related to a higher Power Spectral Density (PSD) post-treatment, whereas the blue ones are related to a higher PSD pre-treatment. The size of the node in the connectivity is related to the amount of increase (green) or decrease (orange) participation coefficient (PC) values. The positive bars in time analysis are related to a higher N1-P3 amplitude post-treatment. (QoLS: Quality of Life Scale,DASS: Depression Anxiety Stress Scale ,PSYRATS: Psychotic Symptom Rating Scales)
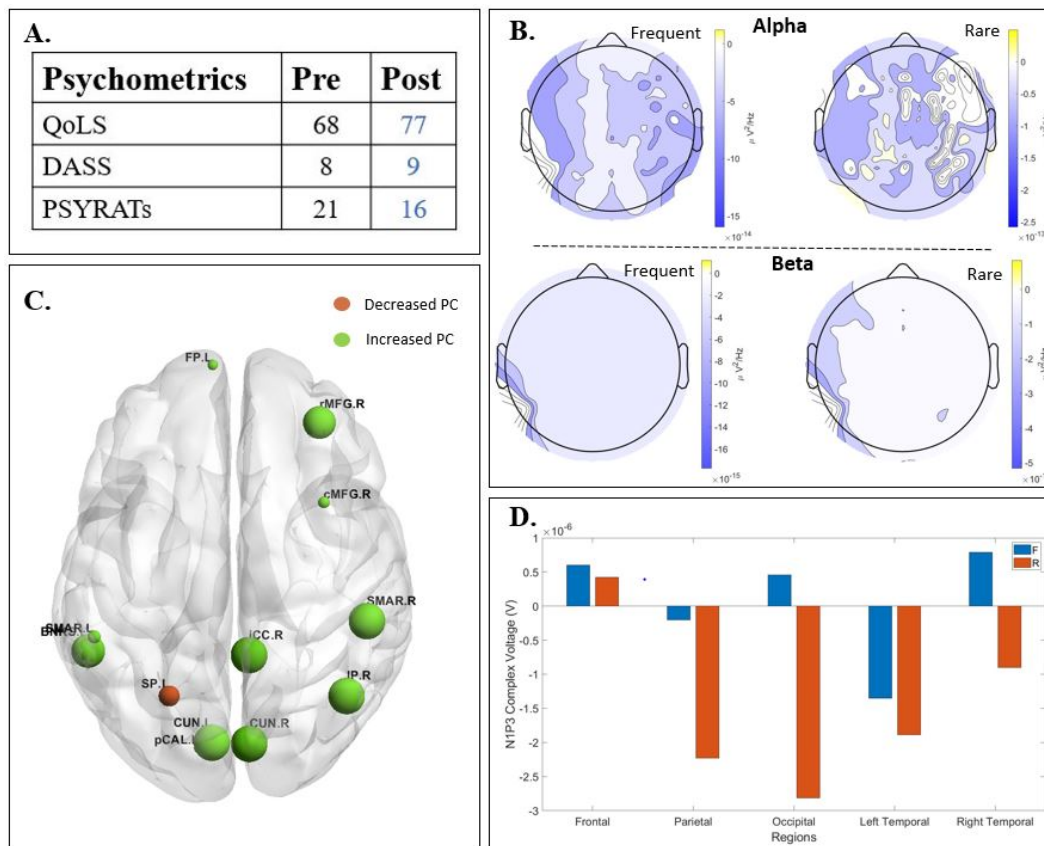
Figure A.2: Results of patient T1 : A. psychometric; B. Scalp-level frequency analysis; C. Source-space connectivity; D. Scalp-level time analysis. The yellow areas in frequency analysis are related to a higher Power Spectral Density (PSD) post-treatment, whereas the blue ones are related to a higher PSD pre-treatment. The size of the node in the connectivity is related to the amount of increase (green) or decrease (orange) participation coefficient (PC) values. The positive bars in time analysis are related to a higher N1-P3 amplitude post-treatment. (QoLS: Quality of Life Scale,DASS: Depression Anxiety Stress Scale ,PSYRATS: Psychotic Symptom Rating Scales)
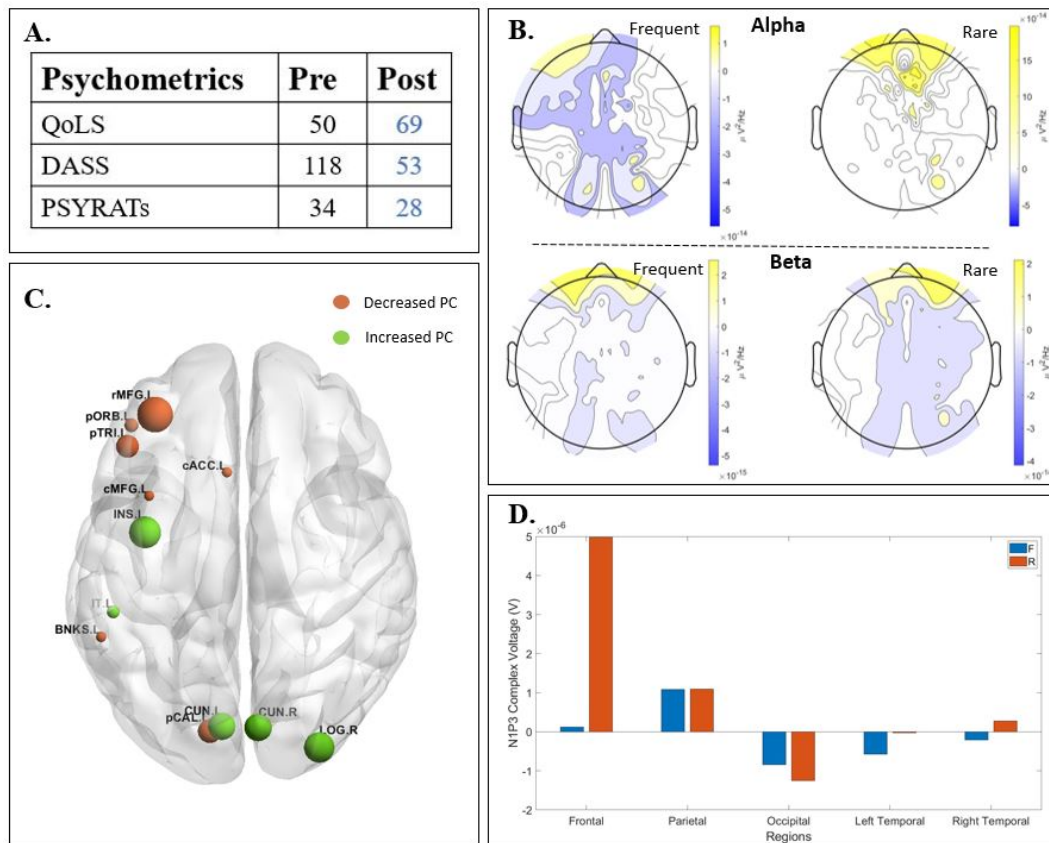
Figure A.3: Results of patient T3 : A. psychometric; B. Scalp-level frequency analysis; C. Source-space connectivity; D. Scalp-level time analysis. The yellow areas in frequency analysis are related to a higher Power Spectral Density (PSD) post-treatment, whereas the blue ones are related to a higher PSD pre-treatment. The size of the node in the connectivity is related to the amount of increase (green) or decrease (orange) participation coefficient (PC) values. The positive bars in time analysis are related to a higher N1-P3 amplitude post-treatment. (QoLS: Quality of Life Scale,DASS: Depression Anxiety Stress Scale ,PSYRATS: Psychotic Symptom Rating Scales)
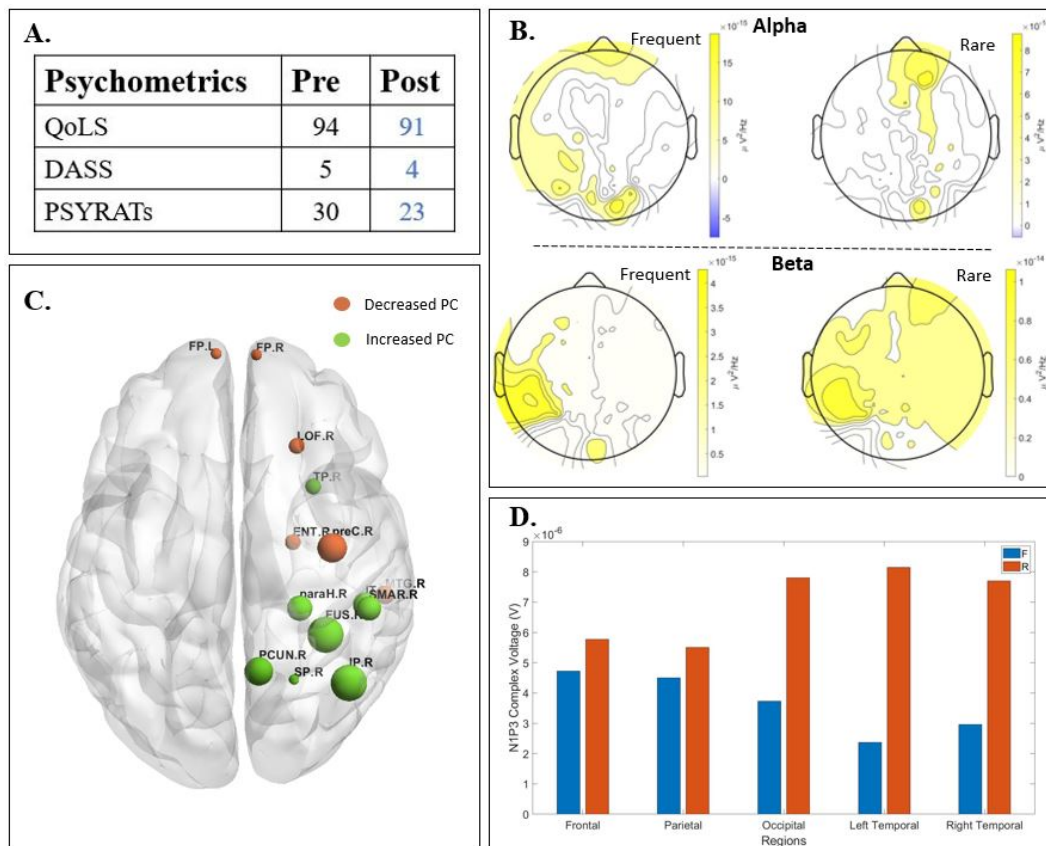
Figure A.4: Results of patient T4 : A. psychometric; B. Scalp-level frequency analysis; C. Source-space connectivity; D. Scalp-level time analysis. The yellow areas in frequency analysis are related to a higher Power Spectral Density (PSD) post-treatment, whereas the blue ones are related to a higher PSD pre-treatment. The size of the node in the connectivity is related to the amount of increase (green) or decrease (orange) participation coefficient (PC) values. The positive bars in time analysis are related to a higher N1-P3 amplitude post-treatment. (QoLS: Quality of Life Scale,DASS: Depression Anxiety Stress Scale ,PSYRATS: Psychotic Symptom Rating Scales)
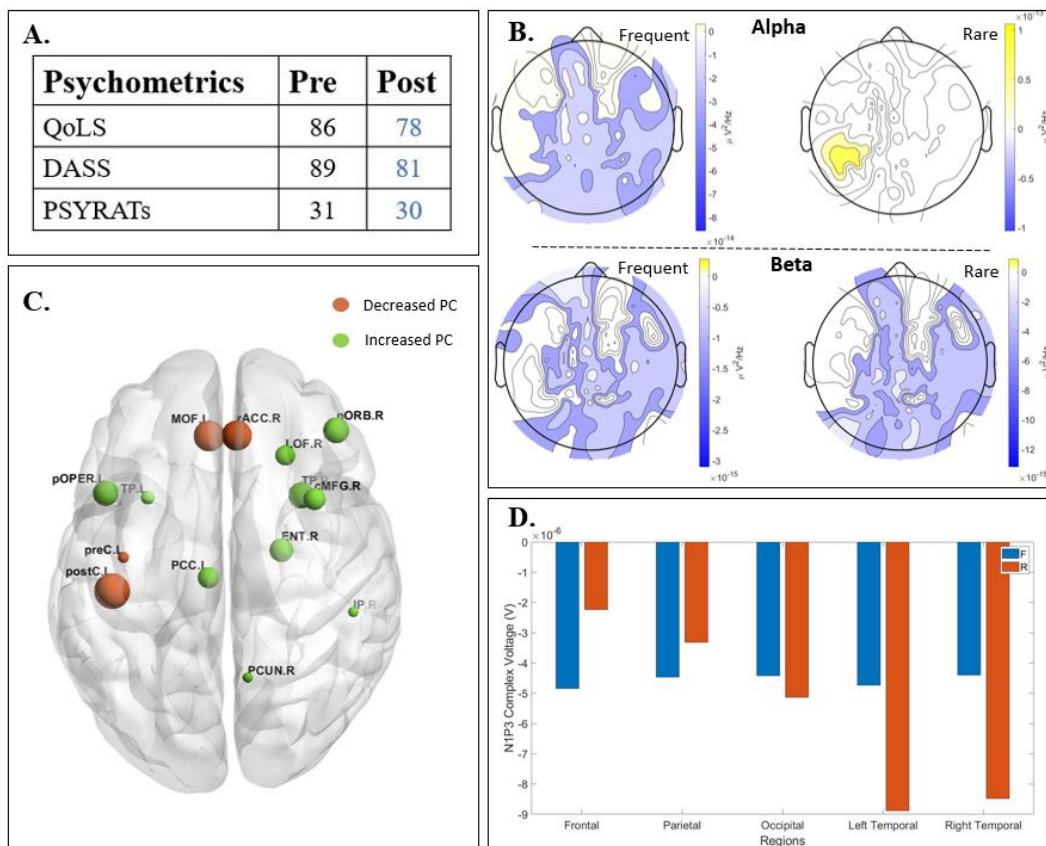
Figure A.5: Results of patient C4 : A. psychometric; B. Scalp-level frequency analysis; C. Source-space connectivity; D. Scalp-level time analysis. The yellow areas in frequency analysis are related to a higher Power Spectral Density (PSD) post-treatment, whereas the blue ones are related to a higher PSD pre-treatment. The size of the node in the connectivity is related to the amount of increase (green) or decrease (orange) participation coefficient (PC) values. The positive bars in time analysis are related to a higher N1-P3 amplitude post-treatment. (QoLS: Quality of Life Scale,DASS: Depression Anxiety Stress Scale ,PSYRATS: Psychotic Symptom Rating Scales)
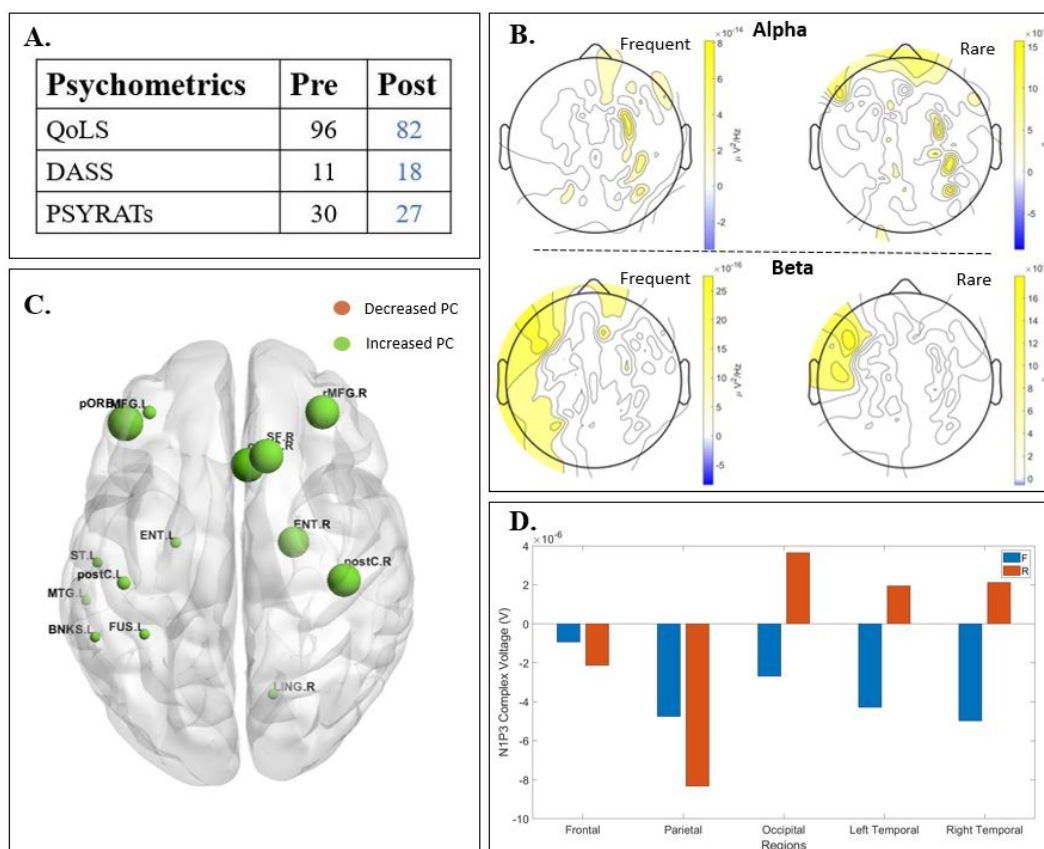
Figure A.6: Results of patient C5 : A. psychometric; B. Scalp-level frequency analysis; C. Source-space connectivity; D. Scalp-level time analysis. The yellow areas in frequency analysis are related to a higher Power Spectral Density (PSD) post-treatment, whereas the blue ones are related to a higher PSD pre-treatment. The size of the node in the connectivity is related to the amount of increase (green) or decrease (orange) participation coefficient (PC) values. The positive bars in time analysis are related to a higher N1-P3 amplitude post-treatment. (QoLS: Quality of Life Scale,DASS: Depression Anxiety Stress Scale ,PSYRATS: Psychotic Symptom Rating Scales)
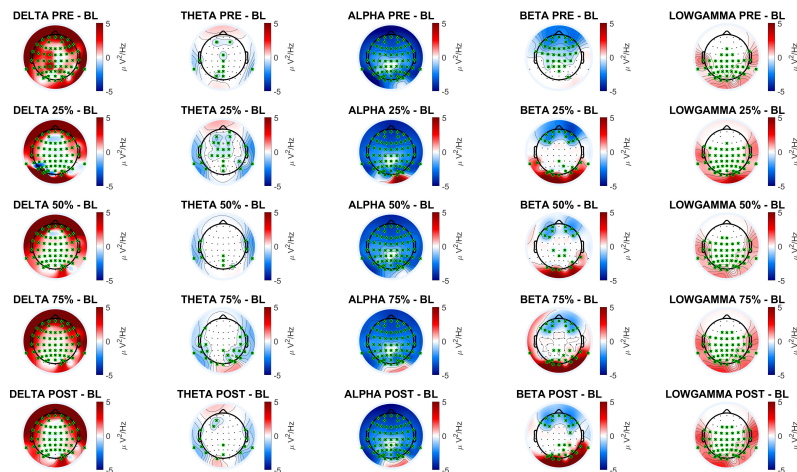
(a) Absolute PSD (1s window) distribution of the global population. The "x" highlighted in green represents significant electrodes after permutation test.
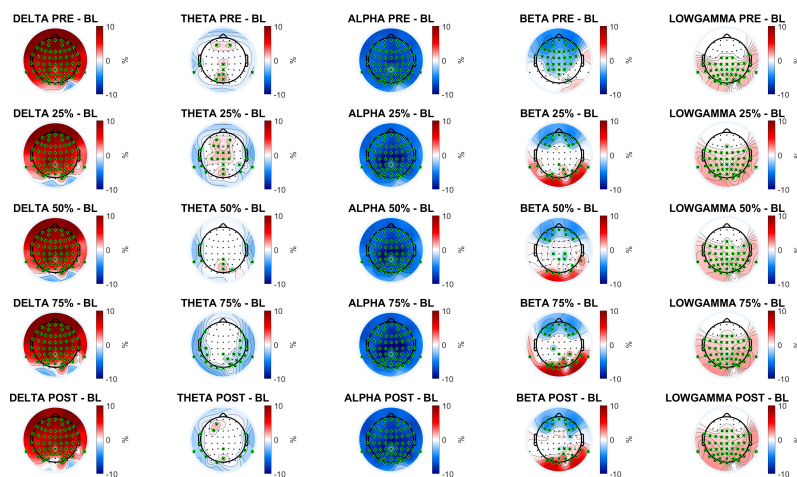
(b) Relative PSD (1s window) distribution of the global population. The "x" highlighted in green represents significant electrodes after permutation test.

Figure A.7: PSD (1s window) distribution of the global population. The "x" highlighted in green represents significant electrodes after permutation test.

A.2   Postural control

A.2.1   Postural control paradigm (BioVRSea) : Towards a neurophysiological signature
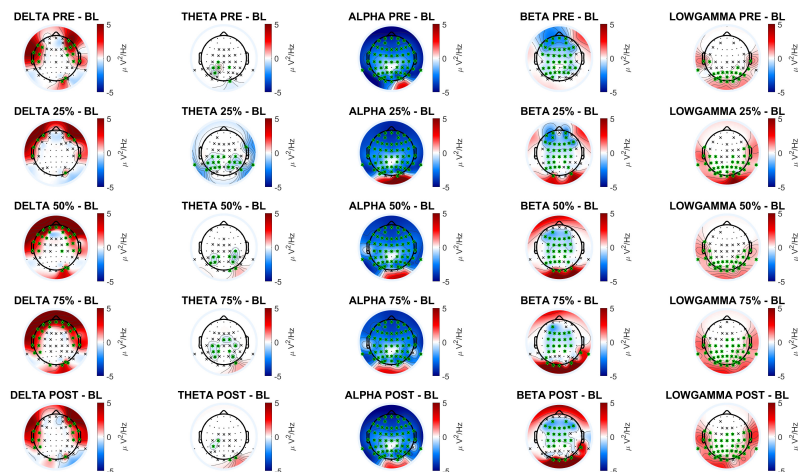
(a) Absolute PSD (2s window) distribution of the global population. The "x" highlighted in green represents significant electrodes after Bonferroni correction.
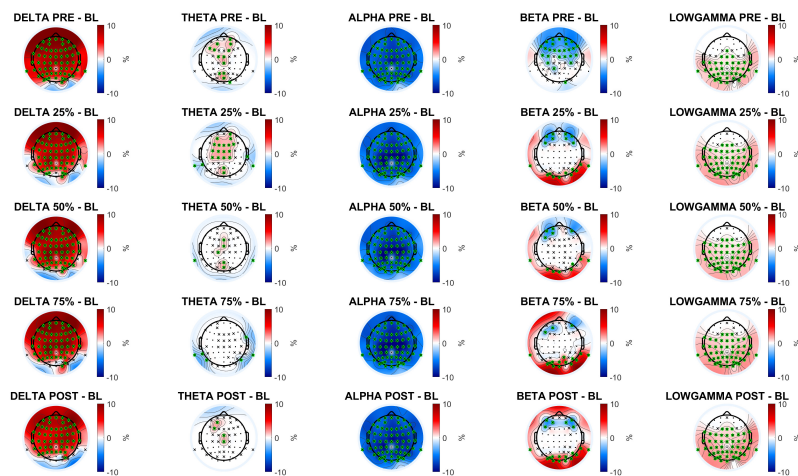
(b) Relative PSD (2s window) distribution of the global population. The "x" highlighted in green represents significant electrodes after Bonferroni correction.

Figure A.8: PSD (2s window) distribution of the global population. The "x" highlighted in green represents significant electrodes after Bonferroni correction.
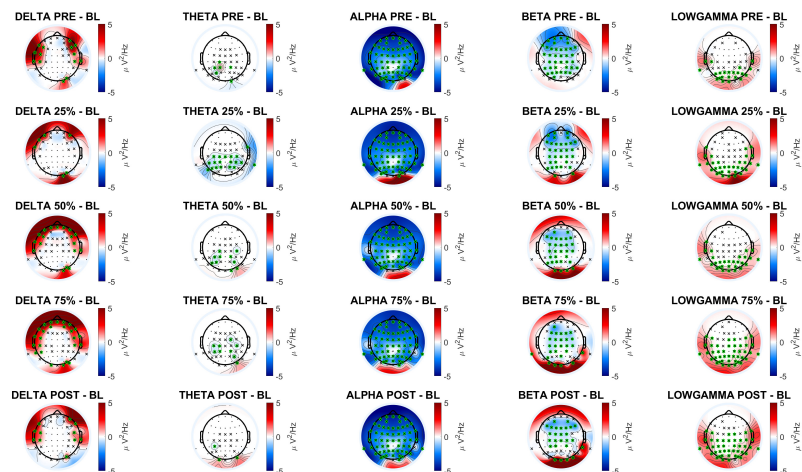
(a) Absolute PSD (4s window) distribution of the global population. The "x" highlighted in green represents significant electrodes after Bonferroni correction.
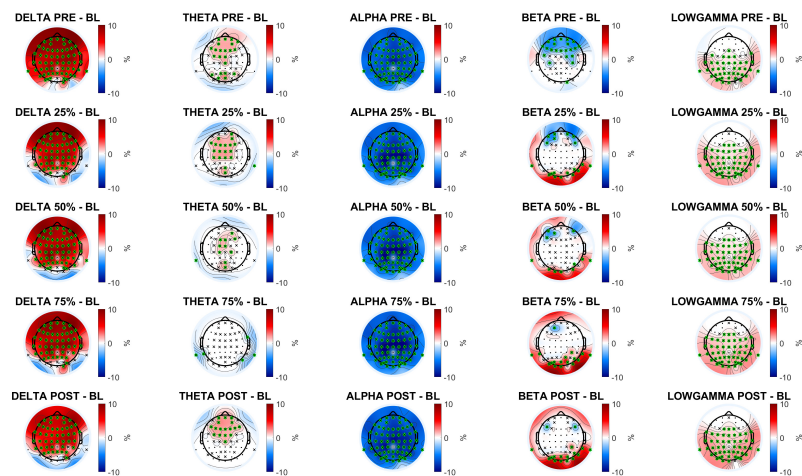
(b) Relative PSD (4s window) distribution of the global population. The "x" highlighted in green represents significant electrodes after Bonferroni correction.

Figure A.9: PSD (4s window) distribution of the global population. The "x" highlighted in green represents significant electrodes after Bonferroni correction.
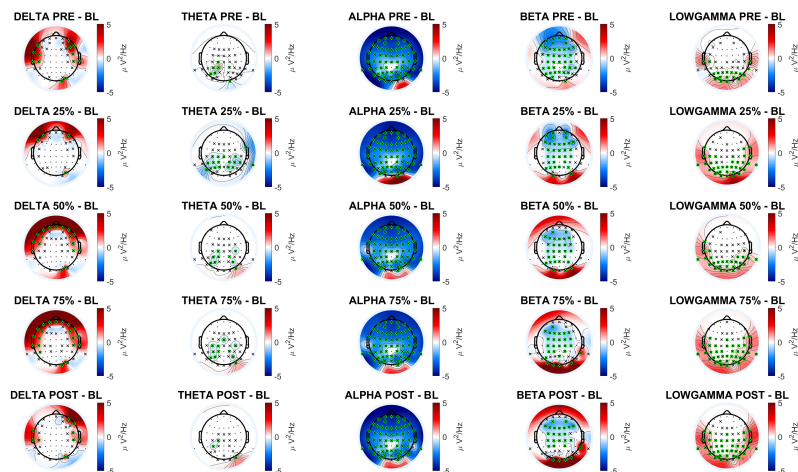
(a) Absolute PSD (8s window) distribution of the global population. The "x" highlighted in green represents significant electrodes after Bonferroni correction.
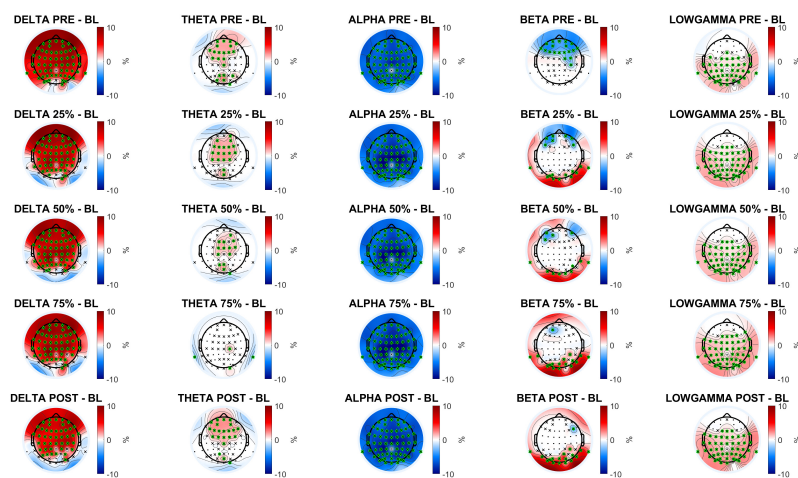
(b) Relative PSD (8s window) distribution of the global population. The "x" highlighted in green represents significant electrodes after Bonferroni correction.

Figure A.10: PSD (8s window) distribution of the global population. The "x" highlighted in green represents significant electrodes after Bonferroni correction.
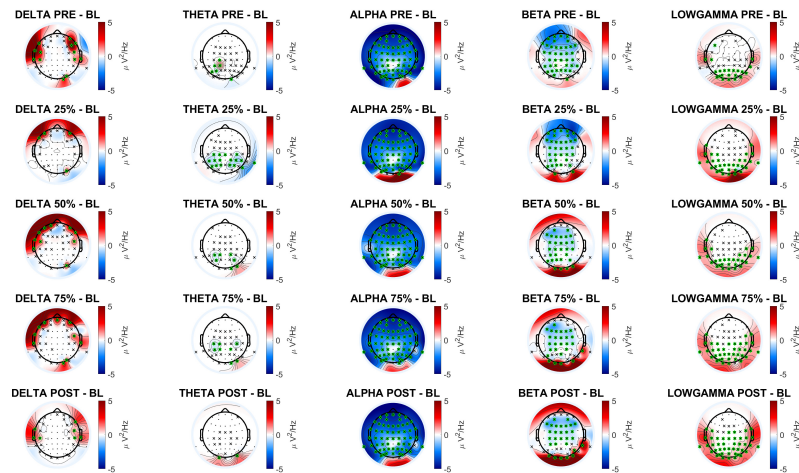
(a) Absolute PSD (16s window) distribution of the global population. The "x" highlighted in green represents significant electrodes after Bonferroni correction.
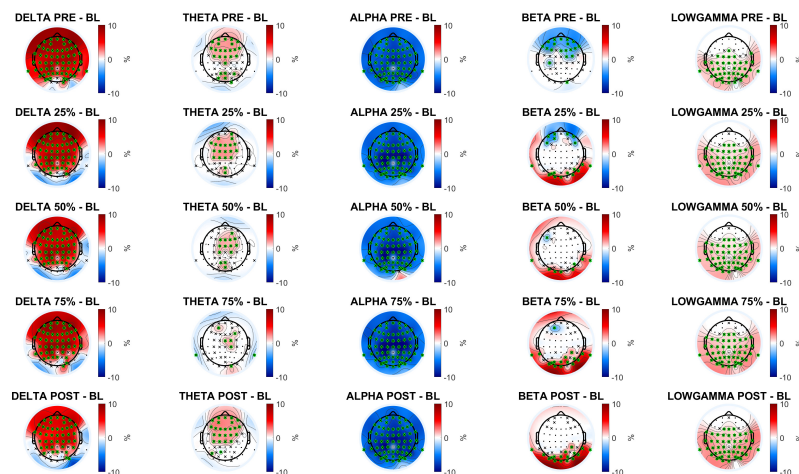
(b) Relative PSD (16s window) distribution of the global population. The "x" highlighted in green represents significant electrodes after Bonferroni correction.

Figure A.11: PSD (16s window) distribution of the global population. The "x" highlighted in green represents significant electrodes after Bonferroni correction.

ABSOLUTE PSD (μV^2/Hz)

Electrodes	DELTA										THETA									
	PRE		25%		50%		75%		POST		PRE		25%		50%		75%		POST	
	AVERAGE	STD	AVERAGE	STD	AVERAGE	STD	AVERAGE	STD	AVERAGE	STD	AVERAGE	STD	AVERAGE	STD	AVERAGE	STD	AVERAGE	STD	AVERAGE	STD
Fp1	-	-	3.08	18.71	9.14	54.60	7.58	27.51	-	-	-	-	-	-	-	-	-	-	-	-
Fpz	-	-	-	-	4.01	20.15	5.68	26.21	-	-	-	-	-	-	-	-	-	-	-	-
Fp2	-	-	-	-	4.83	22.43	6.65	23.92	-	-	-	-	-	-	-	-	-	-	-	-
F7	5.28	27.39	3.83	12.88	5.95	17.79	5.35	13.81	4.58	14.50	-	-	-	-	-	-	-	-	-	-
F3	0.76	7.09	-	-	0.73	5.57	1.05	6.25	-	-	-	-	-	-	-	-	-	-	-	-
Fz	-	-	-	-	-	-	-	-	-	-	-	-	-	-	-	-	-	-	-	-
F4	1.92	18.52	-	-	0.46	5.90	1.21	7.30	0.78	6.05	-	-	-	-	-	-	-	-	-	-
F8	4.30	14.72	3.08	14.43	6.02	20.71	4.19	11.09	5.39	14.44	-	-	-	-	-	-	-	-	-	-
FC5	3.49	24.62	1.06	4.95	2.12	6.59	2.05	5.72	2.02	6.34	-	-	-	-	-	-	-	-	-	-
FC1	-	-	-	-	-	-	-	-	-	-	-	-	-0.51	1.64	-	-	-0.44	1.45	-	-
FC2	-	-	-	-	-	-	-	-	-	-	-	-	-	-	-	-	-0.44	1.31	-	-
FC6	1.78	4.80	1.64	6.41	2.11	6.33	2.67	7.37	2.10	5.39	-	-	-	-	-	-	-	-	-	-
M1	-	-	-	-	-	-	4.22	14.64	-	-	-	-	-1.70	5.42	-	-	-	-	-	-
T7	3.26	7.59	2.76	8.15	2.75	6.99	4.31	7.07	3.75	7.91	-	-	-	-	-	-	-	-	-	-
C3	-	-	-	-	-	-	0.39	1.59	-	-	-	-	-0.47	1.22	-	-	-0.44	1.20	-	-
Cz	-	-	-	-	-	-	-	-	-	-	-	-	-0.21	0.61	-	-	-	-	-	-
C4	-	-	-	-	-	-	0.45	1.85	0.34	2.05	-	-	-0.46	1.33	-0.41	1.33	-0.42	1.25	-	-
T8	2.87	7.49	2.08	6.72	2.27	7.48	3.92	8.04	4.02	8.32	-	-	-	-	-	-	-	-	-	-
M2	-	-	-	-	-	-	4.23	15.56	-	-	-	-	-1.94	5.26	-	-	-	-	-	-
CP5	1.79	18.47	-	-	0.44	2.49	0.67	2.24	0.78	2.90	-	-	-0.83	2.26	-	-	-	-	-	-
CP1	-	-	-	-	-	-	-	-	-	-	0.91	14.33	-0.14	0.35	-0.13	0.36	-0.11	0.47	-	-
CP2	-	-	-	-	-	-	-	-	-	-	-0.05	0.94	-0.13	0.33	-0.11	0.28	-0.10	0.44	-	-
CP6	0.70	5.12	-	-	-	-	0.66	2.60	0.81	2.83	-	-	-0.81	2.15	-	-	-0.67	2.06	-	-
P7	-	-	-	-	-	-	1.48	4.80	1.99	6.50	-	-	-1.31	4.23	-	-	-	-	-	-
P3	-	-	-	-	-	-	-	-	-	-	-0.51	1.75	-0.60	1.49	-0.51	1.49	-0.48	1.61	-	-
Pz	-	-	-	-	-	-	-	-	-	-	-	-	-	-	-	-	-	-	-	-
P4	-	-	-	-	-	-	-	-	-	-	-	-	-0.54	1.39	-0.45	1.31	-0.48	1.39	-	-
P8	-	-	-	-	-	-	1.09	6.29	-	-	-	-	-	-	-	-	-	-	-	-
POz	-	-	-	-	-	-	-	-	-	-	-	-	-	-	-	-	-	-	-	-
O1	-	-	-	-	1.03	4.37	1.17	5.07	1.42	5.51	-	-	-	-	-	-	-	-	-	-
Oz	-	-	-	-	-	-	1.00	5.29	1.31	6.03	-	-	-	-	-	-	-	-	-	-
O2	2.53	8.61	-	-	3.14	8.59	3.35	10.61	-	-	-0.31	4.82	-	-	-0.19	4.21	-	-	-	-
AF7	5.03	20.13	4.70	16.54	11.46	57.82	8.48	22.18	4.28	19.72	-	-	-	-	-	-	-	-	-	-
AF3	-	-	-	-	0.82	14.51	1.93	17.14	-	-	-	-	-	-	-	-	-	-	-	-
AF4	2.05	20.38	-	-	0.99	16.32	3.07	21.16	-	-	-	-	-	-	-	-	-	-	-	-
AF8	7.03	22.03	4.90	16.86	6.71	20.04	7.80	18.23	6.99	19.88	-	-	-	-	-	-	-	-	-	-
F5	2.50	12.91	-	-	3.02	11.82	3.21	11.85	-	-	-	-	-	-	-	-	-	-	-	-
F1	-	-	-	-	-	-	-	-	-	-	-	-	-	-	-	-	-	-	-	-
F2	0.53	6.63	-	-	0.23	4.58	-	-	-	-	-	-	-	-	-	-	-	-	-	-
F6	7.54	71.29	-	-	3.07	15.10	3.85	13.66	2.42	10.29	-	-	-	-	-	-	-	-	-	-
FC3	-	-	-	-	-	-	-	-	-	-	-	-	-	-	-	-	-	-	-	-
FCz	-	-	-	-	-	-	-	-	-	-	-	-	-0.57	1.77	-	-	-0.49	1.53	-	-
FC4	0.44	2.96	-	-	0.41	3.22	0.76	3.38	0.55	3.49	-	-	-	-	-	-	-	-	-	-
C5	1.99	11.64	-	-	1.29	4.63	1.61	6.36	1.55	4.43	-	-	-	-	-	-	-	-	-	-
C1	-	-	-	-	-	-	-	-	-	-	0.11	4.81	-0.25	0.70	-0.22	0.70	-0.21	0.67	-0.26	0.76
C2	-	-	-	-	0.07	1.27	-	-	-	-	-	-	-	-	-	-	-	-	-	-
C6	1.04	11.32	-	-	0.66	7.41	1.07	4.35	1.13	7.51	-	-	-	-	-	-	-	-	-	-
CP3	-	-	-	-	-	-	-	-	-	-	-0.21	3.54	-0.50	1.14	-0.46	1.17	-0.47	1.24	-0.43	1.29
CPz	-	-	-	-	-	-	-	-	-	-	-	-	-	-	-	-	-	-	-	-
CP4	-	-	-	-	-	-	-	-	-	-	-	-	-0.95	2.63	-	-	-	-	-	-
P5	-	-	-	-	-	-	-	-	-	-	0.10	5.30	-0.30	0.76	-0.25	0.77	-	-	-	-
P1	-	-	-	-	-	-	-	-	-	-	-	-	-0.32	1.12	-	-	-	-	-	-
P2	-	-	-	-	-	-	-	-	-	-	-	-	-0.90	2.63	-	-	-	-	-	-
P6	-	-	-	-	-	-	-	-	-	-	-	-	-	-	-	-	-	-	-	-
PO5	-	-	-	-	-	-	-	-	-	-	-	-	-	-	-	-	-	-	-	-
PO3	-	-	-	-	-	-	-	-	-	-	-	-	-	-	-	-	-	-	-	-
PO4	-	-	-	-	-	-	-	-	-	-	-	-	-	-	-	-	-	-	-	-
PO6	3.09	8.39	2.56	8.61	3.47	9.81	3.44	8.74	3.74	9.98	-	-	-	-	-	-	-	-	-	-
FT7	7.21	51.62	2.76	8.24	3.94	10.37	5.01	12.00	4.01	8.39	-	-	-	-	-	-	-	-	-	-
FT8	1.14	5.64	-	-	-	-	1.94	5.37	3.00	8.60	-	-	-1.27	4.30	-	-	-	-	-	-
TP7	1.37	9.25	-	-	-	-	1.93	5.83	2.19	6.43	-	-	-	-	-	-	-	-	-	-
TP8	-	-	-	-	-	-	0.66	4.69	0.99	4.68	-	-	-	-	-	-	-	-	-	-
PO7	-	-	-	-	-	-	-	-	-	-	-	-	-	-	-	-	-	-	-	-
PO8	-	-	-	-	1.18	4.41	1.29	5.47	1.27	5.67	-	-	-	-	0.59	3.02	0.61	3.21	0.90	3.59

ABSOLUTE PSD (μV^2/Hz)

Electrodes	ALPHA										BETA									
	PRE		25%		50%		75%		POST		PRE		25%		50%		75%		POST	
	AVERAGE	STD	AVERAGE	STD	AVERAGE	STD	AVERAGE	STD	AVERAGE	STD	AVERAGE	STD	AVERAGE	STD	AVERAGE	STD	AVERAGE	STD	AVERAGE	STD
Fp1	-4.17	9.43	-3.97	9.40	-3.70	9.37	-3.59	8.66	-4.19	10.10	-2.66	10.97	-2.48	11.18	-	-2	-3	-4	-5	-6
Fpz	-4.14	9.46	-4.11	9.35	-3.89	9.11	-3.82	8.41	-4.24	9.78	-2.04	8.03	-	-	-	-	-	-	-	-
Fp2	-3.85	9.49	-3.99	9.32	-3.71	8.91	-3.62	8.48	-4.06	9.59	-1.98	14.09	-2.86	12.96	-	-	-	-	-	-
F7	-3.50	8.53	-3.28	8.27	-3.06	8.15	-3.00	7.32	-3.64	9.03	-1.12	5.47	-	-	-	-	-	-	-	-
F3	-2.98	6.66	-3.13	6.95	-2.99	6.78	-3.02	6.37	-3.17	7.26	-1.45	3.42	-1.55	3.22	-1.24	3.40	-1.30	4.41	-1.42	3.97
Fz	-3.26	6.81	-3.41	7.25	-3.31	7.04	-3.36	6.71	-3.40	7.41	-1.05	1.70	-0.91	1.71	-0.82	1.59	-0.77	2.03	-0.78	2.01
F4	-3.03	6.79	-3.21	6.87	-3.11	6.68	-3.22	6.47	-3.24	7.18	-1.51	4.43	-1.34	3.25	-1.15	4.71	-1.18	5.02	-	-
F8	-3.43	7.86	-3.37	7.65	-3.10	7.32	-3.41	7.43	-3.47	7.79	-	-	-	-	-	-	-	-	-	-
FC5	-2.43	6.41	-2.52	6.11	-2.28	5.88	-2.38	5.38	-2.63	6.60	-0.53	5.11	-	-	-	-	-	-	-	-
FC1	-1.85	5.43	-2.22	4.80	-2.16	4.68	-2.19	4.49	-2.18	4.91	-0.56	3.05	-0.71	1.21	-0.64	1.22	-0.65	1.52	-0.61	1.54
FC2	-2.14	4.48	-2.24	4.61	-2.20	4.53	-2.25	4.51	-2.24	4.80	-0.75	1.29	-0.65	1.29	-0.65	1.16	-0.63	1.40	-0.63	1.37
FC6	-2.64	5.72	-2.59	5.64	-2.48	5.50	-2.61	5.57	-2.65	6.07	-	-	-	-	-	-	-	-	-	-
M1	-4.49	11.57	-3.90	10.47	-3.60	10.30	-3.32	10.12	-4.23	11.18	-	-	-	-	-	-	-	-	-	-
T7	-2.77	7.62	-2.29	7.46	-	-	-	-	-2.81	7.96	-	-	-	-	-	-	-	-	-	-
C3	-1.48	3.19	-2.00	3.30	-1.90	3.22	-1.99	3.26	-1.77	3.32	-0.59	2.02	-0.69	1.43	-0.64	1.43	-0.73	1.74	-0.37	1.96
Cz	-0.81	1.83	-0.89	1.91	-0.87	1.89	-0.86	1.85	-0.86	1.98	-0.22	0.53	-0.24	0.47	-0.23	0.45	-0.20	0.68	-0.21	0.52
C4	-1.55	3.03	-1.87	3.24	-1.85	3.24	-1.90	3.28	-1.76	3.32	-0.65	1.65	-0.53	2.10	-0.62	1.60	-0.62	1.78	-0.49	1.75
T8	-2.92	6.66	-2.70	6.43	-2.62	6.37	-2.75	6.54	-2.75	6.89	-	-	-	-	-	-	-	-	-	-
M2	-4.48	9.69	-4.16	9.65	-3.72	9.69	-3.21	9.50	-3.78	10.89	-	-	-	-	-	-	2.48	10.49	-	-
CP5	-2.06	4.57	-2.31	4.36	-2.03	4.22	-2.12	4.25	-2.22	4.64	-0.59	4.68	-	-	-	-	-	-	-	-
CP1	-0.02	5.41	-0.56	1.07	-0.55	1.07	-0.54	1.11	-0.48	1.04	0.15	4.89	-0.21	0.40	-0.19	0.41	-0.19	0.56	-0.15	0.44
CP2	-0.32	0.78	-0.42	0.73	-0.41	0.73	-0.39	0.81	-0.40	0.75	-0.14	0.46	-0.16	0.31	-0.17	0.31	-0.13	0.59	-0.16	0.35
CP6	-2.23	4.15	-2.32	4.22	-2.14	4.22	-2.18	4.14	-2.36	4.47	-0.63	3.03	-	-	-	-	-	-	-	-
P7	-3.60	7.83	-3.42	7.65	-2.73	7.57	-2.82	7.70	-3.10	7.81	-	-	-	-	-	-	-	-	-	-
P3	-1.74	3.39	-1.92	3.36	-1.76	3.38	-1.75	3.46	-1.77	3.47	-0.67	1.91	-0.59	1.78	-0.44	1.93	-	-	-	-
Pz	-0.71	1.76	-0.72	1.70	-0.69	1.74	-0.68	1.68	-0.71	1.79	-0.22	0.69	-0.20	0.62	-0.18	0.65	-	-	-	-
P4	-1.88	4.04	-1.94	4.04	-1.83	3.97	-1.84	3.90	-1.87	4.15	-0.61	2.39	-0.53	1.36	-0.50	1.40	-	-	-	-
P8	-4.09	8.54	-3.82	7.81	-3.35	7.76	-3.36	7.82	-3.74	8.21	-	-	-	-	-	-	-	-	-	-
POz	-2.17	5.48	-2.13	5.24	-1.88	5.40	-1.85	5.05	-1.93	5.48	-	-	-	-	-	-	-	-	-	-
O1	-2.80	9.82	-	-	-	-	-	-	-	-	-	-	2.64	8.33	3.25	8.72	6.27	12.85	6.72	15.89
Oz	-2.66	10.22	-	-	-	-	-	-	-	-	-	-	-	-	2.72	9.10	5.91	13.18	5.50	14.95
O2	-1.60	8.47	3.21	68.42	-	-	-1.27	7.80	-1.45	9.11	-	-	1.19	6.43	-	-	-	-	1.79	6.94
AF7	-3.88	9.09	-3.60	9.12	-3.39	9.16	-3.13	8.37	-3.90	9.86	-2.47	7.29	-2.13	8.18	-	-	-	-	-	-
AF3	-3.55	7.87	-3.69	8.13	-3.51	8.00	-3.43	7.31	-3.71	8.55	-2.32	5.23	-2.59	5.75	-1.77	5.84	-1.99	5.80	-1.84	7.41
AF4	-3.49	7.63	-3.61	7.80	-3.46	7.51	-3.48	7.20	-3.62	8.02	-2.01	5.23	-1.86	4.43	-1.18	5.83	-	-	-1.55	5.93
AF8	-3.69	8.48	-3.76	8.66	-3.37	8.29	-3.45	8.31	-3.57	8.83	-	-	-	-	-	-	-	-	-	-
F5	-3.20	7.37	-3.19	7.44	-3.03	7.35	-2.96	6.79	-3.33	7.99	-2.24	7.24	-1.94	9.40	-1.75	7.52	-	-	-1.78	6.98
F1	-3.06	6.70	-3.27	7.12	-3.15	6.90	-3.18	6.56	-3.26	7.31	-1.14	2.15	-1.08	1.96	-0.94	1.99	-0.94	2.59	-0.91	2.39
F2	-3.14	6.66	-3.29	6.95	-3.28	6.76	-3.28	6.53	-3.31	7.18	-1.13	2.05	-0.99	1.89	-0.82	1.88	-0.86	2.29	-0.87	2.36
F6	-2.81	8.60	-3.21	7.07	-3.00	6.84	-3.14	6.80	-3.29	7.42	-1.82	8.30	-2.45	6.78	-	-	-	-	-2.34	8.17
FC3	-1.96	4.99	-2.28	4.79	-2.17	4.64	-2.22	4.46	-2.19	4.98	-0.68	2.60	-0.81	1.65	-0.70	1.89	-0.76	2.43	-0.58	2.27
FCz	-2.37	5.11	-2.55	5.57	-2.48	5.43	-2.52	5.25	-2.51	5.65	-0.75	1.29	-0.69	1.23	-0.62	1.25	-0.63	1.52	-0.62	1.41
FC4	-2.27	4.67	-2.34	4.72	-2.33	4.62	-2.41	4.62	-2.34	4.91	-0.94	2.37	-0.64	3.92	-0.76	2.12	-0.65	2.46	-	-
C5	-2.02	4.85	-2.21	4.74	-1.96	4.49	-2.03	4.42	-2.16	5.16	-	-	-	-	-	-	-	-	-	-
C1	-0.73	2.58	-1.02	1.84	-0.98	1.82	-0.98	1.79	-0.94	1.87	-0.23	1.83	-0.37	0.66	-0.33	0.65	-0.34	0.86	-0.31	0.71
C2	-0.90	1.89	-0.98	1.96	-0.97	1.93	-0.99	1.94	-0.96	2.04	-0.34	0.63	-0.29	0.72	-0.31	0.60	-0.30	0.67	-0.31	0.70
C6	-2.17	4.46	-2.30	4.51	-2.17	4.47	-2.27	4.49	-2.36	4.85	-	-	-	-	-	-	-	-	-	-
CP3	-1.22	3.10	-1.77	3.29	-1.68	3.27	-1.73	3.33	-1.64	3.19	-0.51	2.06	-0.62	1.58	-0.54	1.70	-0.57	1.85	-0.37	1.79
CPz	-	-	-	-	-	-	-	-	-	-	-	-	-	-	-	-	-	-	-	-
CP4	-2.65	5.66	-2.70	5.33	-2.38	5.34	-2.38	5.40	-2.53	5.61	-0.88	4.55	-	-	-	-	-	-	-	-
P5	-0.92	3.05	-1.16	2.08	-1.09	2.11	-1.08	2.12	-1.08	2.14	-0.30	2.18	-0.39	1.05	-0.31	1.10	-0.25	1.46	-	-
P1	-1.12	3.53	-1.21	3.46	-1.16	3.38	-1.14	3.28	-1.18	3.56	-0.18	2.54	-0.31	0.73	-0.28	0.71	-	-	-	-
P2	-2.97	6.73	-2.99	5.93	-2.74	5.95	-2.84	5.95	-2.94	6.13	-0.82	4.30	-	-	-	-	-	-	-	-
P6	-3.50	8.25	-3.32	7.73	-2.88	8.03	-2.74	7.92	-2.77	8.28	-	-	-	-	-	-	-	-	-	-
PO5	-2.76	6.70	-2.74	6.30	-2.37	6.68	-2.29	6.54	-2.32	6.77	-	-	-	-	-	-	-	-	-	-
PO3	-3.19	7.27	-3.08	7.14	-2.71	7.37	-2.71	6.95	-2.93	7.36	-0.65	4.34	-	-	-	-	-	-	-	-
PO4	-3.87	8.53	-3.56	8.55	-3.23	8.55	-3.15	8.35	-3.26	8.91	-	-	-	-	-	-	-	-	-	-
PO6	-3.10	7.68	-2.98	7.45	-2.62	7.18	-2.58	6.50	-3.28	8.13	-	-	-	-	-	-	-	-	-	-
FT7	-3.00	7.57	-3.06	6.70	-2.86	6.55	-2.93	6.62	-3.17	7.03	-	-	-	-	-	-	-	-	-	-
FT8	-3.36	7.23	-2.96	7.03	-2.51	6.86	-2.73	6.57	-2.98	7.43	-	-	-	-	-	-	-	-	-	-
TP7	-3.47	6.68	-2.96	6.44	-2.75	6.60	-2.75	6.66	-3.19	6.95	-	-	-	-	-	-	-	-	-	-
TP8	-3.47	9.26	-3.19	8.43	-2.73	8.54	-	-	-	-	-	-	-	-	-	-	2.68	8.87	4.52	13.51
PO7	-3.85	8.81	-0.88	37.73	-3.09	8.54	-	-	-2.92	8.74	-	-	-	-	-	-	3.05	8.53	-	-
PO8	-	-	-	-	-	-	-	-	-	-	-	-	3.23	8.07	3.43	7.93	5.71	11.45	5.83	12.38

Electrodes	ABSOLUTE PSD (μV²/Hz) LOWGAMMA									
	PRE		25%		50%		75%		POST	
	AVERAGE	STD	AVERAGE	STD	AVERAGE	STD	AVERAGE	STD	AVERAGE	STD
Fp1	-	-	-	-	-	-	-	-	-	-
Fpz	-	-	-	-	-	-	-	-	-	-
Fp2	-	-	-	-	-	-	-	-	-	-
F7	-	-	-	-	-	-	-	-	-	-
F3	-	-	-	-	-	-	-	-	-	-
Fz	-	-	-	-	-	-	-	-	-	-
F4	-	-	-	-	-	-	-	-	-	-
F8	-	-	-	-	-	-	-	-	-	-
FC5	-	-	-	-	-	-	0.12	1.10	0.33	1.51
FC1	-	-	-	-	-	-	-	-	-	-
FC2	-	-	-	-	-	-	0.02	0.13	0.02	0.13
FC6	-	-	0.17	0.77	-	-	0.27	1.01	0.38	1.13
M1	0.37	2.15	0.74	2.49	0.64	2.61	0.91	1.97	0.75	1.97
T7	1.39	3.93	1.68	4.58	1.24	3.53	1.60	4.85	2.05	5.77
C3	-	-	0.04	0.16	-	-	0.04	0.26	0.08	0.28
Cz	-	-	-	-	-	-	0.01	0.08	0.01	0.03
C4	-	-	-	-	-	-	0.05	0.25	0.07	0.28
T8	1.14	4.74	1.10	4.65	0.78	4.00	1.27	4.69	1.86	5.64
M2	-	-	0.40	1.63	0.40	1.89	0.76	2.30	0.52	1.65
CP5	-	-	0.19	0.66	0.20	0.67	0.24	0.83	0.47	1.48
CP1	-	-	-	-	-	-	0.02	0.06	0.02	0.05
CP2	-	-	0.01	0.03	-	-	0.02	0.08	0.01	0.03
CP6	-	-	0.24	0.78	0.22	0.72	0.38	1.28	0.45	1.12
P7	-	-	0.59	3.18	0.48	3.33	0.85	3.70	1.13	3.64
P3	0.06	0.20	0.06	0.16	0.09	0.19	0.14	0.32	0.15	0.27
Pz	0.02	0.08	0.02	0.03	0.02	0.04	0.03	0.08	0.03	0.05
P4	0.14	1.28	0.06	0.21	0.07	0.17	0.13	0.35	0.13	0.23
P8	0.59	2.82	0.73	2.14	0.53	1.77	1.09	3.46	1.11	3.42
POz	0.15	0.40	0.13	0.24	0.13	0.25	0.20	0.36	0.21	0.32
O1	0.58	2.39	0.77	1.91	0.80	1.74	1.28	2.21	1.39	2.74
Oz	1.00	4.48	0.78	1.60	0.79	1.74	1.30	2.59	1.34	2.48
O2	-	-	2.92	34.74	0.44	1.96	0.58	2.27	-	-
AF7	-	-	-	-	-	-	-	-	-	-
AF3	-	-	-	-	-	-	-	-	-	-
AF4	-	-	-	-	-	-	-	-	-	-
AF8	-	-	-	-	-	-	-	-	-	-
F5	-	-	-	-	-	-	-	-	-	-
F1	-	-	-	-	-	-	-	-	-	-
F2	-	-	-	-	-	-	-	-	-	-
F6	-	-	-	-	-	-	-	-	-	-
FC3	-	-	-	-	-	-	-	-	-	-
FCz	-	-	-	-	-	-	0.03	0.13	0.03	0.09
FC4	-	-	-	-	-	-	-	-	-	-
C5	0.28	1.04	0.28	0.67	0.28	0.79	0.31	1.46	0.52	1.49
C1	-	-	-	-	-	-	0.01	0.08	0.02	0.05
C2	-	-	0.02	0.11	-	-	0.02	0.05	0.01	0.06
C6	-	-	0.29	1.09	0.28	0.83	0.35	1.31	0.42	1.25
CP3	-	-	0.03	0.13	-	-	0.05	0.20	0.08	0.20
CPz	-	-	-	-	-	-	-	-	-	-
CP4	0.16	0.76	0.20	0.62	0.28	0.77	0.48	1.69	0.50	1.10
P5	0.06	0.47	0.03	0.09	0.04	0.11	0.05	0.14	0.06	0.13
P1	0.14	1.50	0.01	0.24	0.04	0.11	0.08	0.31	0.06	0.14
P2	0.22	1.14	0.22	0.54	0.22	0.60	0.34	0.80	0.41	0.87
P6	0.21	0.64	0.30	0.52	0.33	0.62	0.51	0.90	0.63	1.39
PO5	0.20	0.63	0.24	0.50	0.27	0.58	0.41	0.88	0.49	1.36
PO3	0.29	1.71	0.16	0.40	0.20	0.43	0.33	0.69	0.32	0.57
PO4	0.37	1.75	0.28	0.66	0.28	0.67	0.48	0.95	0.58	1.26
PO6	-	-	-	-	-	-	0.30	1.58	0.61	1.91
FT7	-	-	0.17	2.00	0.32	1.33	0.43	2.01	0.68	2.36
FT8	-	-	0.97	4.16	-	-	0.76	3.60	1.46	4.02
TP7	-	-	0.96	3.34	0.81	2.82	1.05	3.47	1.27	4.22
TP8	0.38	1.28	0.63	1.19	0.61	1.29	0.82	1.79	1.19	2.52
PO7	0.63	2.27	0.63	2.08	0.50	1.19	0.89	1.60	0.94	2.01
PO8	0.75	2.41	0.73	1.43	0.76	1.39	1.10	2.08	1.16	1.98

Table A.1: Average and standard deviation (over subjects) absolute PSD for each significant electrodes, frequency bands and tasks

RELATIVE PSD (%)

Electrodes	DELTA PRE AVERAGE	STD	25% AVERAGE	STD	50% AVERAGE	STD	75% AVERAGE	STD	POST AVERAGE	STD	THETA PRE AVERAGE	STD	25% AVERAGE	STD	50% AVERAGE	STD	75% AVERAGE	STD	POST AVERAGE	STD
Fp1	10.89	13.43	9.89	13.37	9.79	12.57	10.45	13.99	8.75	12.83	-	-	-	-	-	-	-	-	-	-
Fpz	10.96	12.47	9.19	11.50	8.72	10.63	10.38	12.57	9.09	12.05	-	-	-	-	-	-	-	-	-	-
Fp2	11.20	13.94	9.62	12.46	8.77	11.58	10.40	13.94	9.31	13.00	-	-	-	-	-	-	-	-	-	-
F7	10.63	11.00	9.50	10.40	9.36	12.13	9.67	11.13	9.62	11.78	-	-	-	-	-	-	-	-	-	-
F3	9.39	11.01	8.08	9.98	8.63	9.11	9.55	11.23	8.03	11.22	-	-	-	-	-	-	-	-	-	-
Fz	9.11	9.90	7.96	8.95	8.20	8.04	9.18	10.31	7.74	9.44	-	-	-	-	-	-	-	-	-	-
F4	9.85	10.74	8.09	9.89	8.14	9.05	9.53	11.21	9.40	9.83	-	-	-	-	-	-	-	-	-	-
F8	10.88	11.19	8.90	10.55	9.89	11.87	10.57	11.37	11.09	11.82	-	-	-	-	-	-	-	-	-	-
FC5	8.47	9.84	6.56	9.60	7.23	10.48	7.94	10.29	7.47	11.34	-	-	-	-	-	-	-	-	-	-
FC1	8.63	9.84	7.97	8.79	8.51	8.25	8.88	9.92	7.09	9.62	-	-	1.32	4.54	-	-	-	-	-	-
FC2	9.52	9.70	7.96	8.81	9.03	8.40	9.74	9.48	8.66	9.39	-	-	-	-	-	-	-	-	-	-
FC6	9.35	10.02	7.34	9.92	7.90	10.09	8.95	11.37	8.24	10.20	-	-	-	-	-	-	-	-	-	-
M1	6.82	11.07	3.20	11.12	3.47	10.50	4.37	11.34	4.27	12.23	-	-	-1.90	4.48	-1.78	4.37	-3.09	4.67	-	-
T7	5.60	10.02	3.21	10.43	3.74	10.16	5.68	11.31	5.41	11.72	-	-	-1.74	4.76	-	-	-1.90	4.92	-	-
C3	8.39	10.21	7.93	9.31	9.63	9.30	10.32	9.73	7.68	10.28	-	-	-	-	-	-	-	-	-	-
Cz	9.00	9.68	7.81	8.89	9.04	8.88	9.76	9.99	7.98	9.90	-	-	-	-	-	-	-	-	-	-
C4	9.36	9.39	8.42	9.33	9.38	9.01	10.58	9.71	9.49	9.11	-	-	-	-	-	-	-	-	-	-
T8	5.99	10.47	3.54	10.29	4.00	10.42	6.17	12.33	5.14	11.64	-	-	-1.67	4.66	-1.53	4.46	-1.75	4.99	-1.58	4.76
M2	7.60	13.13	3.74	10.53	4.35	10.45	-	-	4.64	13.07	-	-	-1.69	4.11	-1.70	4.42	-3.15	4.99	-1.64	4.44
CP5	6.92	9.45	5.49	8.93	5.66	8.33	6.38	8.15	6.13	9.48	-	-	-	-	-	-	-	-	-	-
CP1	9.04	10.48	9.94	10.52	10.81	10.57	11.39	10.64	9.00	11.67	-	-	-	-	-	-	-	-	-	-
CP2	8.93	11.11	9.22	10.98	10.01	10.91	10.39	11.55	9.67	10.94	-	-	-	-	-	-	-	-	-	-
CP6	7.19	9.55	5.51	9.22	5.98	8.40	6.52	9.45	6.95	10.48	-	-	-	-	-	-	-1.60	4.56	-	-
P7	5.88	9.86	3.14	9.09	3.78	8.57	3.69	9.39	4.22	11.30	-	-	-	-	-	-	-1.80	4.96	-	-
P3	6.83	8.83	5.11	8.00	5.99	8.30	5.42	8.71	4.64	8.80	-	-	-	-	-	-	-	-	-	-
Pz	6.86	9.83	5.65	8.70	6.39	9.16	6.06	9.64	5.80	10.08	1.47	4.53	-	-	-	-	-	-	-	-
P4	6.89	8.88	5.47	8.38	6.24	8.28	6.02	9.40	5.68	9.69	-	-	-	-	-	-	-	-	-	-
P8	5.54	10.30	3.05	9.92	4.04	9.25	2.88	10.32	4.06	11.67	-	-	-	-	-	-	-2.05	4.70	-	-
POz	3.69	9.23	2.60	8.51	3.73	8.78	-	-	-	-	2.01	4.91	1.62	4.57	-	-	-	-	-	-
O1	-	-	-	-	-	-	-	-	-	-	-	-	-	-	-	-	-1.60	4.81	-	-
Oz	2.62	8.76	-	-	-	-	-	-	-	-	-	-	-	-	-	-	-	-	-	-
O2	4.39	9.41	3.55	11.00	3.90	10.62	4.86	11.45	-	-	0.10	2.86	-	-	-	-	-	-	-	-
AF7	11.34	12.60	10.48	12.63	10.93	13.35	11.02	13.54	10.29	12.67	-	-	-	-	-	-	-	-	-	-
AF3	10.86	12.25	9.85	11.03	9.85	10.94	11.33	12.62	9.61	12.09	-	-	-	-	-	-	-	-	-	-
AF4	10.78	11.14	9.01	10.85	9.03	10.65	10.50	12.26	10.01	10.89	-	-	-	-	-	-	-	-	-	-
AF8	11.97	13.44	10.69	12.59	10.47	13.34	11.83	13.53	11.50	13.14	-	-	-	-	-	-	-	-	-	-
F5	10.59	11.16	9.22	10.92	9.88	10.89	10.22	12.13	9.53	11.93	-	-	-	-	-	-	-	-	-	-
F1	9.38	10.47	7.90	9.18	8.23	8.63	9.10	10.38	7.92	10.74	-	-	-	-	-	-	-	-	-	-
F2	9.44	10.28	7.72	9.29	8.21	8.26	9.14	10.27	8.29	9.26	-	-	-	-	-	-	-	-	-	-
F6	10.98	11.82	9.17	10.58	8.82	11.41	10.69	11.84	10.76	11.22	-	-	-	-	-	-	-	-	-	-
FC3	8.33	10.16	7.33	9.57	8.32	9.05	8.61	10.44	6.67	10.38	-	-	-	-	-	-	-	-	-	-
FCz	8.83	9.46	7.80	8.68	8.63	7.84	8.94	9.49	7.79	9.18	-	-	1.40	4.54	-	-	-	-	-	-
FC4	9.73	9.84	7.96	9.17	8.65	8.69	9.72	10.51	9.13	9.38	-	-	-	-	-	-	-	-	-	-
C5	7.13	9.95	5.64	9.51	6.47	10.00	6.97	9.79	6.44	10.00	-	-	-	-	-	-	-	-	-	-
C1	8.78	10.65	8.92	9.32	9.89	9.34	10.53	9.98	7.59	9.64	-	-	-	-	-	-	-	-	-	-
C2	8.68	9.66	8.53	9.55	10.22	9.42	10.46	10.00	8.58	9.78	-	-	-	-	-	-	-	-	-	-
C6	7.67	9.89	5.65	9.30	6.24	9.98	7.51	10.43	8.16	10.90	-	-	-	-	-	-	-	-	-	-
CP3	8.01	9.85	7.53	9.44	8.42	9.08	8.88	9.21	7.35	9.16	-	-	-	-	-	-	-	-	-	-
CPz	-	-	-	-	-	-	-	-	-	-	-	-	-	-	-	-	-	-	-	-
CP4	5.91	8.84	3.87	8.07	4.59	8.08	3.96	8.93	4.20	9.99	-	-	-	-	-	-	-	-	-	-
P5	7.39	9.19	6.39	8.11	7.13	8.48	6.74	8.88	6.12	9.62	-	-	-	-	-	-	-	-	-	-
P1	-	-	-	-	-	-	-	-	-	-	-	-	-	-	-	-	-	-	-	-
P2	6.51	9.06	4.54	8.98	4.90	8.07	4.49	9.40	4.88	10.13	-	-	-	-	-	-	-1.34	4.17	-	-
P6	-	-	-	-	-	-	-	-	-	-	-	-	-	-	-	-	-	-	-	-
PO5	-	-	-	-	-	-	-	-	-	-	-	-	-	-	-	-	-	-	-	-
PO3	-	-	-	-	-	-	-	-	-	-	-	-	-	-	-	-	-	-	-	-
PO4	4.51	8.65	3.16	9.88	3.25	9.01	-	-	-	-	-	-	-	-	-	-	-	-	-	-
PO6	8.40	10.24	6.55	9.54	6.69	11.11	7.37	10.73	7.55	11.71	-	-	-	-	-	-	-1.35	4.12	-	-
FT7	9.48	9.78	7.25	9.45	7.42	10.34	9.10	11.93	8.39	9.92	-	-	-	-	-	-	-1.68	4.12	-	-
FT8	6.23	9.87	3.67	9.72	3.61	9.02	5.33	9.33	5.31	11.28	-	-	-1.51	4.56	-	-	-1.83	4.58	-	-
TP7	6.76	10.89	4.02	10.25	4.61	9.78	5.40	10.68	5.83	12.44	-	-	-1.66	4.69	-	-	-1.98	4.68	-	-
TP8	4.19	8.12	-	-	-	-	-	-	-	-	-	-	-	-	-	-	-1.66	4.76	-	-
PO7	4.02	8.95	-	-	-	-	-	-	-	-	-	-	-	-	-	-	-	-	-	-
PO8	-	-	-	-	-	-	-	-	-	-	-	-	-	-	-	-	-	-	-	-

RELATIVE PSD (%)

Electrodes	ALPHA										BETA									
	PRE		25%		50%		75%		POST		PRE		25%		50%		75%		POST	
	AVERAGE	STD	AVERAGE	STD	AVERAGE	STD	AVERAGE	STD	AVERAGE	STD	AVERAGE	STD	AVERAGE	STD	AVERAGE	STD	AVERAGE	STD	AVERAGE	STD
Fp1	**-6.38**	**8.13**	**-6.17**	**8.58**	**-6.20**	**8.34**	**-6.62**	**8.43**	**-6.27**	**8.63**	**-4.95**	**10.49**	**-4.17**	**11.21**	**-3.82**	**10.10**	**-**	**-2**	**-3.51**	**10.60**
Fpz	-7.56	8.93	-7.09	9.15	-7.17	8.76	-7.82	9.00	-7.50	9.39	-3.95	8.83	-	-	-	-	-	-	-	-
Fp2	-6.40	8.20	-5.95	8.28	-6.03	8.12	-6.62	8.13	-6.38	8.54	-5.16	10.82	-4.11	9.91	-3.11	9.29	-3.73	10.77	-3.63	10.29
F7	-6.52	7.79	-6.14	7.67	-6.03	7.73	-6.48	7.70	-6.98	7.69	-3.80	7.77	-3.01	7.72	-	-	-	-	-	-
F3	-6.51	8.72	-6.65	8.77	-6.82	8.62	-7.23	8.63	-6.76	8.85	-3.85	8.43	-	-	-2.56	7.75	-	-	-	-
Fz	-7.69	9.65	-8.09	9.60	-8.17	9.54	-8.81	9.87	-8.19	9.82	-2.70	6.40	-	-	-	-	-	-	-	-
F4	-6.94	8.71	-7.00	8.62	-7.06	8.53	-7.90	8.84	-7.43	8.91	-3.81	8.73	-	-	-	-	-	-	-2.98	8.48
F8	-6.76	8.19	-6.24	8.02	-6.60	8.13	-7.13	7.93	-7.29	7.97	-4.01	7.95	-	-	-2.87	8.12	-	-	-3.49	8.94
FC5	-6.36	8.03	-6.10	7.75	-5.94	7.56	-6.60	7.81	-7.06	8.01	-2.64	7.16	-	-	-	-	-	-	-	-
FC1	-7.40	9.79	-8.39	9.69	-8.46	9.66	-8.95	9.84	-7.85	9.73	-2.54	6.54	-	-	-	-	-	-	-	-
FC2	-8.04	9.65	-8.74	9.72	-8.88	9.56	-9.64	9.98	-8.63	9.85	-2.70	6.69	-	-	-	-	-	-	-	-
FC6	-7.05	8.04	-6.83	8.36	-7.01	7.77	-7.71	8.00	-7.66	8.12	-2.83	8.32	-	-	-	-	-	-	-	-
M1	-6.00	7.18	-4.94	7.18	-4.62	6.55	-5.59	7.24	-5.81	7.42	-	-	2.41	7.95	-	-	2.85	8.58	-	-
T7	-5.51	7.02	-5.02	6.73	-4.56	6.67	-5.14	6.81	-6.03	6.76	-	-	-	-	-	-	-	-	-	-
C3	-6.88	9.13	-9.49	9.78	-9.29	9.71	-10.13	9.92	-8.57	9.64	-2.67	7.33	-	-	-	-	-	-	-	-
Cz	-8.45	10.34	-8.90	10.05	-9.18	10.21	-9.84	10.36	-8.94	10.11	-2.21	5.68	-	-	-	-	-	-	-	-
C4	-7.58	8.69	-9.87	10.14	-9.66	9.73	-10.57	10.29	-8.98	9.57	-2.75	7.62	-	-	-	-	-	-	-	-
T8	-5.68	7.24	-5.37	7.19	-5.27	6.79	-6.00	7.22	-6.48	7.71	-	-	-	-	-	-	-	-	-	-
M2	-6.15	7.39	-4.98	6.40	-5.12	6.91	-5.62	7.53	-6.02	7.11	-	-	2.02	7.49	-	-	3.15	9.49	-	-
CP5	-6.55	7.28	-6.89	7.27	-6.20	7.21	-7.04	7.41	-7.99	7.45	-	-	-	-	-	-	-	-	-	-
CP1	-7.02	8.96	-10.11	10.35	-10.11	10.22	-10.64	10.18	-9.10	9.51	-2.77	7.51	-	-	-	-	-	-	-	-
CP2	-7.10	8.86	-9.24	9.89	-9.30	9.87	-9.80	10.13	-8.76	9.52	-2.59	7.05	-	-	-	-	-	-	-	-
CP6	-7.21	7.38	-7.64	7.66	-7.17	7.59	-7.99	8.00	-8.70	7.75	-	-	-	-	-	-	-	-	-	-
P7	-5.95	6.94	-5.68	6.81	-5.08	6.97	-5.72	7.04	-6.91	7.31	-	-	-	-	-	-	-	-	-	-
P3	-7.23	8.02	-7.64	8.02	-7.78	8.40	-7.78	8.28	-7.91	8.41	-	-	-	-	-	-	-	-	-	-
Pz	-7.54	10.15	-7.48	9.33	-7.54	9.51	-7.89	9.74	-7.98	10.23	-	-	-	-	-	-	-	-	-	-
P4	-7.80	9.34	-8.00	8.87	-7.81	9.19	-8.41	9.42	-8.58	9.39	-	-	-	-	-	-	-	-	-	-
P8	-7.06	8.43	-6.98	8.30	-6.41	8.45	-7.00	8.58	-8.09	9.03	-	-	3.52	9.55	-	-	4.19	10.24	-	-
POz	-6.60	9.91	-6.67	9.39	-6.47	9.87	-6.68	9.85	-6.79	10.21	-	-	-	-	-	-	-	-	-	-
O1	-5.89	8.54	-5.64	8.26	-5.32	8.65	-5.51	8.45	-5.85	8.92	-	-	4.30	8.15	3.64	7.56	5.67	8.51	5.12	9.01
Oz	-6.08	9.15	-5.95	9.08	-5.72	9.42	-5.99	9.31	-6.59	9.72	-	-	3.92	8.17	3.15	7.86	5.64	9.28	4.39	9.74
O2	-3.36	5.46	-3.53	6.24	-3.60	6.16	-4.22	5.72	-3.89	6.02	-1.02	6.37	-	-	-	-	-	-	0.18	8.89
AF7	-6.15	7.66	-5.89	7.74	-6.14	7.76	-6.34	7.84	-6.21	7.82	-5.21	9.92	-4.43	10.42	-4.25	10.19	-4.05	10.80	-4.38	10.47
AF3	-6.36	8.45	-6.28	8.73	-6.41	8.62	-6.90	8.78	-6.56	8.74	-5.23	9.96	-4.45	9.38	-3.96	9.39	-4.64	10.27	-4.22	9.89
AF4	-6.92	8.43	-6.75	8.61	-6.91	8.73	-7.71	8.70	-7.18	8.68	-4.77	9.43	-3.22	8.88	-2.88	8.58	-	-	-3.73	9.11
AF8	-6.29	7.76	-5.84	7.84	-5.87	7.65	-6.56	8.02	-6.28	7.60	-5.73	11.24	-4.83	10.90	-4.46	11.01	-4.57	10.88	-5.06	11.23
F5	-5.97	8.34	-5.79	8.22	-5.85	8.04	-6.27	8.14	-6.18	8.07	-5.12	9.27	-3.93	9.79	-4.01	9.58	-3.68	10.27	-4.18	10.02
F1	-7.39	9.34	-7.67	9.47	-7.75	9.26	-8.25	9.40	-7.79	9.57	-3.12	6.96	-	-	-	-	-	-	-	-
F2	-7.62	9.23	-7.86	9.23	-7.93	9.01	-8.63	9.48	-8.08	9.42	-3.01	6.93	-	-	-	-	-	-	-	-
F6	-6.34	8.26	-5.84	8.03	-6.16	8.03	-6.78	8.15	-6.53	8.11	-4.98	9.68	-3.80	9.54	-	-	-3.65	10.05	-4.65	9.55
FC3	-6.69	9.17	-7.58	8.94	-7.63	8.82	-8.07	9.02	-7.19	9.09	-2.83	7.23	-	-	-	-	-	-	-	-
FCz	-7.93	10.08	-8.74	10.00	-8.82	9.91	-9.38	10.18	-8.58	10.09	-2.33	5.92	-	-	-	-	-	-	-	-
FC4	-7.48	8.83	-8.03	9.06	-8.16	8.81	-9.06	9.32	-8.27	8.94	-3.29	7.87	-	-	-	-	-	-	-	-
C5	-6.48	7.74	-6.73	7.46	-6.26	7.45	-6.90	7.58	-7.62	7.75	-	-	-	-	-	-	-	-	-	-
C1	-7.40	9.66	-9.54	9.43	-9.53	9.71	-10.17	9.89	-8.38	9.64	-2.41	6.67	-	-	-	-	-	-	-	-
C2	-7.78	9.70	-9.58	10.31	-9.73	9.93	-10.42	10.31	-8.81	10.33	-2.31	6.60	-	-	-	-	-	-	-	-
C6	-6.80	7.15	-7.27	7.95	-7.24	7.75	-7.90	7.90	-8.24	7.79	-	-	-	-	-	-	-	-	-	-
CP3	-7.08	8.64	-9.29	9.82	-8.90	9.77	-9.62	9.82	-9.01	9.47	-	-	-	-	-	-	-	-	-	-
CPz	-	-	-	-	-	-	-	-	-	-	-	-	-	-	-	-	-	-	-	-
CP4	-6.61	7.43	-6.51	7.10	-6.31	7.37	-6.65	7.27	-7.53	7.56	-	-	-	-	-	-	-	-	-	-
P5	-7.83	8.73	-8.36	8.57	-8.26	8.94	-8.59	8.84	-8.49	9.14	-	-	-	-	-	-	-	-	-	-
P1	-	-	-	-	-	-	-	-	-	-	-	-	-	-	-	-	-	-	-	-
P2	-7.59	8.97	-7.61	8.64	-7.18	9.02	-7.81	9.06	-8.54	9.27	-	-	-	-	-	-	2.85	8.36	-	-
P6	-	-	-	-	-	-	-	-	-	-	-	-	-	-	-	-	-	-	-	-
PO5	-	-	-	-	-	-	-	-	-	-	-	-	-	-	-	-	-	-	-	-
PO3	-	-	-	-	-	-	-	-	-	-	-	-	-	-	-	-	-	-	-	-
PO4	-7.17	9.76	-6.97	9.56	-6.61	9.94	-7.03	10.00	-7.88	10.07	-	-	-	-	-	-	3.94	8.47	3.10	8.76
PO6	-5.96	7.60	-5.45	7.04	-5.30	7.20	-5.77	7.23	-6.82	7.72	-2.47	8.13	-	-	-	-	-	-	-	-
FT7	-6.65	7.68	-6.34	7.70	-6.54	7.46	-7.01	7.68	-7.37	7.63	-2.74	7.96	-	-	-	-	-	-	-	-
FT8	-5.62	7.07	-5.29	6.64	-4.71	6.58	-5.59	6.53	-7.00	7.03	-	-	-	-	-	-	-	-	-	-
TP7	-6.71	7.23	-6.54	7.36	-5.98	7.19	-6.77	7.50	-7.97	7.94	-	-	-	-	-	-	-	-	-	-
TP8	-6.31	7.87	-6.09	7.49	-5.74	7.92	-6.05	7.85	-6.53	8.33	-	-	3.62	7.84	2.93	7.29	4.45	8.55	4.18	9.29
PO7	-6.97	9.56	-6.85	9.31	-6.38	9.87	-6.69	9.84	-7.56	9.87	-	-	3.05	8.39	2.45	7.74	4.79	8.83	3.68	8.77
PO8	-5.39	8.56	-5.21	8.44	-5.02	8.81	-5.29	8.55	-5.43	9.09	-	-	4.03	7.75	3.16	7.45	5.63	8.81	4.94	8.80

Electrodes	RELATIVE PSD (%) LOWGAMMA									
	PRE		25%		50%		75%		POST	
	AVERAGE	STD	AVERAGE	STD	AVERAGE	STD	AVERAGE	STD	AVERAGE	STD
Fp1	-	-	-	-	-	-	-	-	-	-
Fpz	-	-	-	-	-	-	-	-	-	-
Fp2	-	-	-	-	-	-	-	-	-	-
F7	-	-	-	-	-	-	-	-	-	-
F3	-	-	-	-	-	-	-	-	-	-
Fz	-	-	0.38	1.35	0.40	1.11	0.60	1.32	0.64	1.71
F4	-	-	-	-	-	-	-	-	-	-
F8	-	-	-	-	-	-	-	-	-	-
FC5	-	-	0.59	2.23	0.70	2.30	0.83	2.48	0.96	2.72
FC1	0.39	1.35	0.44	1.24	0.56	1.27	0.79	1.69	0.89	2.33
FC2	0.42	1.40	0.53	1.57	0.46	1.32	0.73	1.45	0.72	1.75
FC6	-	-	0.65	2.92	-	-	0.76	2.29	0.89	2.37
M1	0.69	2.53	1.22	3.26	1.14	2.44	1.46	2.23	1.37	2.32
T7	1.35	3.13	1.63	3.40	1.20	3.15	1.37	3.61	1.78	3.65
C3	0.64	2.23	0.97	2.09	0.76	1.82	1.12	2.30	1.20	2.49
Cz	0.43	1.04	0.54	1.04	0.59	1.13	0.71	1.23	0.84	1.63
C4	0.66	2.38	1.12	2.89	0.84	2.10	1.13	2.06	1.12	2.47
T8	1.31	3.44	1.42	3.59	1.27	3.16	1.37	3.76	1.92	3.78
M2	0.50	2.59	0.91	2.80	0.82	2.35	1.27	2.43	1.16	2.06
CP5	1.05	2.89	1.34	2.81	1.12	2.43	1.50	2.50	1.75	2.71
CP1	0.62	1.82	0.85	1.65	0.79	1.66	1.04	1.84	1.03	2.23
CP2	0.61	1.88	0.87	1.95	0.72	1.67	1.08	2.03	1.02	2.19
CP6	1.05	3.17	1.38	3.13	1.22	2.69	1.64	2.73	1.77	2.81
P7	0.90	3.59	1.51	3.56	1.09	3.01	1.66	2.98	1.92	3.22
P3	0.93	1.77	1.17	1.70	1.12	1.59	1.58	2.37	1.70	2.12
Pz	0.64	1.12	0.67	1.08	0.67	1.10	1.03	1.71	1.18	2.07
P4	0.99	1.56	1.12	1.95	1.04	1.48	1.45	1.84	1.59	2.15
P8	1.32	3.37	1.71	3.09	1.30	2.45	1.98	3.05	2.09	3.04
POz	0.96	1.80	0.94	1.37	0.85	1.28	1.29	1.89	1.55	2.52
O1	1.11	2.25	1.62	2.47	1.47	1.88	1.96	2.57	1.97	2.57
Oz	1.29	2.44	1.52	2.41	1.42	1.85	1.88	2.49	2.05	2.90
O2	-	-	0.94	2.28	0.61	2.61	0.62	2.64	-	-
AF7	-	-	-	-	-	-	-	-	-	-
AF3	-	-	-	-	-	-	-	-	-	-
AF4	-	-	-	-	-	-	-	-	-	-
AF8	-	-	-	-	-	-	-	-	-	-
F5	-	-	-	-	-	-	-	-	-	-
F1	-	-	0.29	1.46	-	-	0.53	1.56	0.61	2.09
F2	-	-	0.35	1.76	0.32	1.43	0.54	1.60	0.53	1.84
F6	-	-	-	-	-	-	-	-	-	-
FC3	-	-	0.54	1.82	0.53	1.84	0.80	2.39	0.85	2.58
FCz	0.38	1.01	0.45	1.11	0.48	0.99	0.72	1.39	0.75	1.52
FC4	-	-	0.58	2.42	0.45	1.95	0.75	2.05	0.67	2.05
C5	0.95	2.71	1.21	2.57	1.01	2.39	1.28	2.56	1.58	2.63
C1	0.51	1.39	0.61	1.32	0.67	1.42	0.88	1.74	1.00	2.17
C2	0.56	1.56	0.77	1.80	0.54	1.33	0.90	1.57	0.89	1.71
C6	0.87	3.13	1.25	3.38	1.16	2.44	1.32	2.53	1.39	2.58
CP3	0.83	2.20	1.17	2.09	0.99	2.01	1.37	2.28	1.49	2.22
CPz	-	-	-	-	-	-	-	-	-	-
CP4	1.04	2.39	1.38	2.25	1.30	2.22	1.83	2.80	1.96	2.75
P5	0.84	1.61	0.93	1.39	0.86	1.21	1.28	2.00	1.38	2.00
P1	-	-	-	-	-	-	-	-	-	-
P2	1.10	2.54	1.40	2.38	1.28	2.14	1.81	2.40	1.94	2.65
P6	-	-	-	-	-	-	-	-	-	-
PO5	-	-	-	-	-	-	-	-	-	-
PO3	-	-	-	-	-	-	-	-	-	-
PO4	1.25	2.16	1.24	2.27	1.23	1.71	1.77	2.00	1.93	2.49
PO6	-	-	0.65	2.67	0.77	2.68	0.84	2.71	1.21	2.87
FT7	-	-	0.75	2.87	0.76	2.23	0.76	2.34	0.93	2.46
FT8	0.93	3.12	1.45	3.58	1.29	3.00	1.40	2.76	1.89	3.39
TP7	1.14	3.97	1.57	3.45	1.30	2.90	1.55	3.12	1.90	3.46
TP8	1.11	2.03	1.75	2.67	1.51	1.86	1.99	2.69	2.03	2.65
PO7	1.35	2.54	1.43	2.56	1.34	1.82	1.91	2.12	2.04	2.61
PO8	1.05	2.13	1.37	2.07	1.27	1.85	1.73	2.69	1.89	2.86

Table A.2: Average and standard deviation (over subjects) relative PSD for each significant electrodes, frequency bands and tasks

A.2.2   Brain network dynamics during a complex postural control task

Table A.3: Anatomic regions-of-interest (ROIs) used in the analysis, elaborated from the Desikan Killiany atlas, and their association to RSNs.

Name	Acronym	Associated RSN
bankssts L	l.BSTS	Other
bankssts R	r.BSTS	Other
caudalanteriorcingulate L	l.cACC	DAN
caudalanteriorcingulate R	r.cACC	DAN
caudalmiddlefrontal L	l.cMFG	SAN
caudalmiddlefrontal R	r.cMFG	SAN
cuneus L	l.CUN	VIS
cuneus R	r.CUN	VIS
enthorinal-parahippocampal L	l.ENT	Other
enthorinal-parahippocampal R	r.ENT	Other
superior frontal pole L	l.sFG	Other
superior frontal pole R	r.sFG	Other
fusiform L	l.FUS	VIS
fusiform R	r.FUS	VIS
inferiorparietal L	l.IPL	Other
inferiorparietal R	r.IPL	Other
inferiortemporal L	l.ITG	DAN
inferiortemporal R	r.ITG	DAN
pars-insula L	l.pOPER	DAN
pars-insula R	r.pOPER	DAN
isthmuscingulate L	l.iCC	DMN
isthmuscingulate R	r.iCC	DMN
lateraloccipital L	l.LOG	VIS
lateraloccipital R	r.LOG	VIS
orbitofrontal L	l.LOF	DMN
orbitofrontal R	r.LOF	DMN
lingual L	l.LING	VIS
lingual R	r.LING	VIS
middletemporal L	l.MTG	DAN
middletemporal R	r.MTG	DAN
paracentral L	l.paraC	MOT
paracentral R	r.paraC	MOT
pericalcarine L	l.periCAL	Other
pericalcarine R	r.periCAL	Other
postcentral L	l.postC	MOT
postcentral R	r.postC	MOT
posteriorcingulate L	l.PCC	DMN
posteriorcingulate R	r.PCC	DMN
precentral L	l.preC	MOT
precentral R	r.preC	MOT
precuneus L	l.PCUN	DMN
precuneus R	r.PCUN	DMN

rostralanteriorcingulate L	l.rACC	DMN
rostralanteriorcingulate R	r.rACC	DMN
rostralmiddlefrontal L	l.rMFG	SAN
rostralmiddlefrontal R	r.rMFG	SAN
superiorparietal L	l.SPL	Other
superiorparietal R	r.SPL	Other
superiortemporal L	l.STG	AUD
superiortemporal R	r.STG	AUD
supramarginal L	l.SMAR	SAN
supramarginal R	r.SMAR	SAN
temporalpole L	l.TP	Other
temporalpole R	r.TP	Other
transversetemporal L	l.TT	Other
transversetemporal R	r.TT	Other

ORCID Romain Aubonnet 0000-0002-5395-775X
https://orcid.org/0000-0002-5395-775X